



Title	One dimensional nano-materials as anode materials for Lithium-ion Battery
Author(s)	DE JUAN, Lyn Marie Zarsuela
Citation	北海道大学. 博士(工学) 甲第13342号
Issue Date	2018-09-25
DOI	10.14943/doctoral.k13342
Doc URL	http://hdl.handle.net/2115/82744
Type	theses (doctoral)
File Information	DE_JUAN_Lyn_Marie_Zarsuela.pdf



[Instructions for use](#)

**ONE DIMENSIONAL NANO-MATERIALS AS
ANODE MATERIALS FOR LITHIUM-ION
BATTERY**



Lyn Marie Z. De Juan

Graduate School of Engineering

Hokkaido University

September 2018

ONE DIMENSIONAL NANO-MATERIALS AS ANODE MATERIALS FOR LITHIUM-ION BATTERY



Lyn Marie Z. De Juan

Laboratory of Novel Hybrid Materials Engineering

Division of Materials Science and Engineering

Faculty of Engineering

Hokkaido University

A dissertation submitted to the Graduate School of Engineering of Hokkaido University in
partial fulfillment of the requirements for the degree of
Doctor of Philosophy in Materials Science and Engineering

This dissertation is dedicated to
my husband (Ryan D. Corpuz),
my daughter (Aura Vanya D.J. Corpuz),
and my parents and family...

ACKNOWLEDGMENT

I would like to express my deepest gratitude to my supervisor, Prof. Tetsu Yonezawa, and my mentor, Asst. Prof. Mai Thahn Nguyen, and Asst. Prof. Yohei Ishida, for their kind support, fruitful insights, and shared knowledge and expertise in order for me to complete and finish this work. Prof. Kiyoharu Tadanaga and Asst. Prof. Nataly Carolina Rosero Navarro of the Laboratory of Inorganic Synthesis Chemistry, Division of Applied Chemistry, Hokkaido University, for all the shared knowledge and expertise and fruitful discussions. Prof. Wei-Ren Liu and Irish Valerie B. Maggay, and all of the students in the Energy Optic-electronic Materials Laboratory, Department of Chemical Engineering, Chung Yuan Christian University, Taiwan, for all their help, kind support, and fruitful discussions during my 1 month internship. Mr. T. Tanioka and Ms. R. Kurishiba for their help in taking the TEM images of my samples. Prof. Tomoharu Tokunaga of the Department of Quantum Engineering, Graduate School of Engineering, Nagoya University, for his help in taking the STEM images of my samples. Mr. Hiroki Tsukamoto for all his help, support, and wonderful insights in the day-to-day activities in the laboratory. I would also would like to thank the MEXT Top Global University Scholarship for the financial support during the first two years stay in Sapporo. MEXT Honors Scholarship for the partial financial support during the 1st semester of my 3rd year.

I would also like to thank my labmates in Laboratory of Novel Materials Hybrid Engineering, Department of Materials Science and Engineering, Hokkaido University, who cried, laughed, and celebrated the challenges of life with me. My parents, Ramon C. De Juan, and Isabelita Z. De Juan, and my brothers and sisters, for all they supports and encouragements. And most especially, I would like to thank my husband, Ryan D. Corpuz, for all the support, encouragements, fruitful discussion, and for being my pillar throughout my PhD course, and my daughter, Aura Vanya D.J. Corpuz, for being my inspiration and stress reliever as I finish my PhD.

ありがとうございました。

ABSTRACT

Lithium-ion battery (LIB) have gather much attention due to its wide range of application, e.g. portable devices, portable tools, electronic vehicles, wireless implantable medical devices, and as storage device for renewable energy. However, only 1% of the total energy consumed worldwide can be stored and hence there is a need to further improve the commercially produce LIB. There are several strategies to improve the current state of LIB, and in this research, I will focus on the morphology control, i.e. utilizing 1D material, as anode material for LIB.

There are three type of anode material for LIB, viz. intercalation, alloying, and conversion type. Among these 3, both alloying and conversion type anode material yield high gravimetric and volumetric capacities, however with an expanse of large volumetric change with corresponding structural change that results to pulverization of the anode material during successive charge discharge cycle. The utilization of 1D nanomaterial have several advantage, i.e., 1D morphology that allows 1D flow of e^- and ions for an efficient charge transport, nano-sized dimension and high surface to volume ration that allows for a short Li^+ diffusion length and large Li^+ flux, and small diameter that facilitates strain relaxation.

β -Sn is an alloying type anode material, and upon charge-discharge cycle, different alloys of Li_xSn ($0 < x \leq 4.4$) were formed. Sn can accommodate a maximum of 4.4 Li^+ to form $Li_{22}Sn_5$ with a structural change from tetragonal to cubic during alloying (charge) and vice versa, and large volumetric change of $>250\%$. This large volumetric change and structural change results to the pulverization of Sn during the charge-discharge process and hence been the focus of Chapters 2 and 3 of this dissertation. In these chapters, I propose a new method in the formation of single crystal 1D Sn NRs using chemical synthesis, i.e. feasible for mass

production, as well as examine the electrochemical properties and investigate the cause of the continuous capacity fading of Sn NRs and understand why shorter aspect ratio will yield to a better capacity stability.

1D Sn, specifically, Sn NRs with different aspect ratio, as well as that of the spherical nanoparticles (NPs) were synthesized via chemical synthesis under Chapter 2. Tin (II) acetate ($\text{Sn}(\text{ac})_2$), poly(vinylpyrrolidone) (PVP), and sodium tetrahydroborate (NaBH_4), were utilized as precursor, capping ligand, and reducing agent respectively. On this chapter, three (3) parameters were varied, i.e. synthesis temperature, amount of PVP, and molecular weight (MW) of PVP. It was found that both the synthesis temperature and the amount of PVP (regulates solution viscosity), control the kinetic energy of particles in the solution and thus the preferred attachment along the c-axis, i.e. [001] leaving the {200} on its facets. It was also found that the selective attachment of low kinetic energy particles is due to the higher attraction and adhesion of Sn particles/atoms on higher-surface-energy planes of the nuclei and thus forming a rod like morphology. On the other hand, PVP aids in bridging the particles together rather than act as shape directing agent. The MW of PVP dictates the particle stability and aids in the formation of longer and higher aspect ratio NRs by bridging the particles together along its long polymeric chains bearing repeating functional groups.

The electrochemical properties of the produce Sn NRs with different aspect ratios as well as that of spherical NPs were examined under Chapter 3, wherein the cause of the continuous capacity fading as well as reason for the higher performance of low aspect ratio NRs were determined. The solid-electrolyte interphase (SEI) layer is known to form in the anode material due to higher anode potential of most materials compared to the LUMO of the electrolyte. The type of the formed SEI layer can either improve or further degrade the performance of the anode material. The porous and non-uniform Li_2CO_3 SEI layer, will continuously form and disintegrate during the charge-discharge process to form a thick SEI

layer with a corresponding continuous decomposition of the electrolyte. The formation of thick SEI layer as well as the continuous decomposition of the electrolyte are not favorable and will yield to a continuous capacity fading. On the other hand, LiF-rich SEI layer, is known to improve the ionic (Li^+) conductivity, form a stable SEI layer, and prevents the further degradation of the electrolyte. The difference in the surface energy of each crystallographic planes, aside from utilizing fluoroethylene carbonate as additive in the electrolyte, induces the type of the SEI layer formed, wherein Sn (100) and Sn (001) with yield Li_2CO_3 and LiF rich SEI layers respectively. However, up to date there is still no study that combine the effect of the morphology and formed SEI layer (due to surface crystallographic plane) on the stability of the formed anode material and hence been the focus of Chapter 3. In this chapter, three (3) morphologies were utilized, i.e. high aspect ratio NRs (formed at 0 °C), low aspect ratio NRs (formed at 10 °C), and spherical NPs (formed at 26 °C). The specific surface area of the (001) in low aspect ratio is calculated to be ~9 times that of the high aspect ratio NRs, whereas the spherical particles are composed of {200} surface crystallographic plane. It was found that the chemically synthesized single crystal β -Sn NRs have low surface energy {200} facets with highly active {001} tip is a potential anode material for lithium-ion battery, due to the formation of LiF-rich F containing SEI layer, which is similar to the SEI formed when electrolyte with FEC-additive was used, as indicated by the XPS analysis. The formation of LiF-rich F containing SEI layer is due to higher amount of exposed reactive {001}, i.e. tip of the rod, in low aspect ratio β -Sn NRs. The presence of LiF-rich F-compound agrees well with the impedance test, wherein, low aspect ratio β -Sn NRs have higher Li^+ diffusion by an order of magnitude.

ZnV_2O_4 , a conversion anode material, was also examined on this study. ZnV_2O_4 has a spinel structure of $\text{A}[\text{B}_2]\text{O}_4$, are known to be crystallographically porous with 56 empty tetrahedral sites and 16 empty octahedral sites. However, despite its crystallographically porous

structure, the short distances and coulombic interactions between the guest ions and A- and B-cations prevents the simultaneous occupation of the interstitial sites. Based on several researches, Li^+ could be stored chemically and electrochemically in spinel compounds with a simultaneous reduction of A- and B- cations. There are already existing studies that utilizes ZnV_2O_4 as anode material for LIB. However, 1-D ZnV_2O_4 as well its high current density application (5 A g^{-1} over 1000 cycles) have not yet been studied, and hence been the focus of Chapter 4. In this chapter, 1D porous ZnV_2O_4 were produced via two (2) step fabrication, i.e. hydrothermal to form 1D ZnV_2O_6 followed by calcination to form the 1D porous ZnV_2O_4 . Zinc nitrate ($\text{Zn}(\text{NO}_3)_2 \cdot 6\text{H}_2\text{O}$) and ammonium vanadate (NH_4VO_3) were used as precursors in the hydrothermal process. Dodecyltrimethylammonium bromide (DTAB) was incorporated to reduce the reaction time from 168 h to 24h. It was found that the formed 1D ZnV_2O_4 have a porous structure. However, despite its porous structure, the produced 1D ZnV_2O_4 are still single crystal that have $\{220\}$ facets with wire direction along the $\langle 111 \rangle$. Based on the electrochemical tests, it was found that the porous ZnV_2O_4 NWs have higher specific capacity compared to that of spherical and coral-like morphology, due to the effect of both 1D and porous morphology. In comparison with the previously reported ZnV_2O_4 , the produced porous NWs show better specific capacity and cycling stability with the occurrence of phase transformation until the 35th cycle.

TABLE OF CONTENTS

Chapter 1: General Introduction -----	1
Abstract -----	2
1.1. Why lithium-ion battery? -----	2
1.1.1. Lithium-ion Battery: A history – how it started -----	10
1.1.2. Lithium-ion Battery: How it works -----	16
1.1.3. Lithium-ion Battery: Future and improvements -----	29
1.2. Anode material for LIB -----	32
1.2.1. Alloying anode material for LIB -----	42
1.2.2. Conversion anode material for LIB -----	45
1.2.3. Size and morphology of the anode material for LIB: 1-D nanostructure -----	50
1.3. Summary and Perspective -----	68
1.4. Significance of the study -----	69
1.5. Objective of the study -----	70
References -----	68

Chapter 2: Structural Control Parameters for Formation of Single –

Crystalline β-Sn Nanorods in Organic Phase -----	79
Abstract -----	80
2.1. Introduction -----	80
2.2. Methodology	
2.2.1. Chemicals -----	83
2.2.2. Synthesis of β -Sn Nanorods at Different Temperatures-----	83

2.2.3. Synthesis of β -Sn Nanorods Using Different Amounts and MW of PVP -----	84
2.2.4. Characterizations -----	85
2.3. Results and Discussion	
2.3.1. Structure and Morphology of Sn NPs at Various Synthesis Temperatures ----	86
2.3.2. Growth Direction of Sn NRs and Analysis of Particle Surface -----	89
2.3.3. Discussion on the Temperature-Dependent Growth Mechanism of Sn NR ---	92
2.3.4. Effect of the Capping Agent (PVP) on the Morphology of Sn NPs -----	95
2.3.5. Combined Effect of Temperature and PVP (MW and Amount) on the Formation of Sn NRs -----	102
2.4. Conclusion -----	103
References -----	104

Chapter 3: β-Sn Nanorods with High Surface Energy (001) Tip for LiF- Rich SEI Layer as High-Performance and Stable Anode Material for Lithium Ion Battery-----	106
Abstract -----	107
4.1. Introduction -----	107
4.2. Experimental Section	
3.2.1. Materials Preparation -----	111
3.2.2. Electrochemical Test -----	111
4.3. Results and Discussion	
4.3.1. β -Sn NRs with Different Morphology -----	113
4.3.2. Electrochemical Measurement -----	116
4.3.3. Ex-situ Analysis of Rod-like Morphology -----	123
4.3.4. Mechanism of LiF-rich SEI layer on Low Aspect Ratio NRs -----	128

4.4. Conclusion	130
References	131

Chapter 4: Porous ZnV₂O₄ Nanowires as High-Performance Anode

Material for Lithium-Ion Battery	135
Abstract	135
4.1. Introduction	135
4.2. Experimental Section	
4.2.1. Materials Preparation	139
4.2.2. Characterizations	140
4.2.3. Electrochemical Test	140
4.2.4. Ex-situ Characterizations	142
4.3. Results and Discussion	
4.3.5. Formation of 1D ZnV ₂ O ₄	142
4.3.6. Proposed mechanism in the formation of porous ZnV ₂ O ₄	150
4.3.7. Electrochemical test	151
4.4. Conclusion	160
References	162

Chapter 5: General Conclusion

Appendix I: Supporting information for Chapter 2

Appendix II: Supporting information for Chapter 3

Appendix III: Supporting information for Chapter 4

LIST OF FIGURES

Figure 1.1. -----	4
(a) Forecast and statistics of the world's energy demand until 2050.	
(b) 2015 fuel shares of TPES	
Figure 1.2. -----	6
(a) Comparison of CO ₂ emitted of conventional fuel combustion cars/vehicles vs. EVs that utilizes energy from different electricity sources	
(b) The estimated energy required to produce 1 kWh storage device, vis. battery	
Figure 1.3. -----	7
Comparison of different EES devices:	
(a) specific energy and specific power	
(b) energy density and power density	
Figure 1.4. -----	8
Comparison of volumetric and gravimetric energy density of different rechargeable batteries.	
Figure 1.5. -----	10
(a) Estimated global end-use market of Lithium	
(b) Annual average price of battery grade lithium carbonate per metric ton.	
Figure 1.6. -----	12
Model of a rocking chair battery and the relative charge-discharge voltage profile	

Figure 1.7. ----- **18**

Schematic illustration of the conventional LIB indicating the:

(a) charged and (b) discharged state.

Figure 1.8. ----- **22**

Schematic energy diagrams of:

(a) liquid electrolyte - solid electrodes

(b) solid electrolyte - fluid electrodes without electrode-electrolyte reaction

(c) Li (anode) – LiCoO₂ (cathode) electrodes and their relative energy positions with respect to the HOMO-LUMO of the carbonate-based electrolyte as an example of liquid electrolyte-solid electrodes with electrode-electrolyte reaction

Figure 1.9. ----- **24**

Schematic illustration of:

(a) Charge/discharge potential hysteresis on an ideal insertion electrode material

(b) Potential drop at the end of charge and beginning of discharge cycles.

Figure 1.10. ----- **27**

(a) Schematic illustration of 3D Sn@G-PGNWs

(b) The rate cycle performance of 3D Sn@G-PGNWs

(c-d) TEM images of the Sn@G-PGNWs, (e-f) HRTEM of Sn@G NPs

(g) Cycle performance of the 3D Sn@G-PGNW electrode at current densities of 0.2, 0.5, and 1 A/g for the initial six cycles and then 2 A/g for the subsequent 1000 cycles.

Figure 1.11. ----- **34**

(a) The availability/abundance as a fraction of the earth's crust and the commodity price (USD/lb) of different elements

(b) Calculated gravimetric and volumetric capacities of selected elements.

Figure 1.12. -----	36
<p>(a) Experimental gravimetric (square) and volumetric (star) capacities of different compounds vs their half-cell potentials</p> <p>(b) Rate capability of different compounds</p>	
Figure 1.13. -----	38
<p>Schematic illustration of how different types of electrode materials stores Li^+</p>	
Figure 1.14. -----	39
<p>Crystal structure of materials that schematically illustration how Li^+ was stored by:</p> <p>(a) intercalation (graphite), (b) intercalation ($\text{Li}_4\text{Ti}_5\text{O}_{12}$), (c) alloying (Silicon), (d) conversion (SnO_2), (e) sample voltage hysteresis of different compounds.</p>	
Figure 1.15. -----	45
<p>(a) Schematic illustration of the coating design on mesoporous Si microparticles (pSiMPs) and the structure evolution during the charge/discharge cycles</p> <p>(b) TEM images of impregnating C-coating</p> <p>(c) TEM images of non-filling C-coating</p> <p>(d) initial 1000 galvanostatic cycles of the pSiMPs with different coatings</p>	
Figure 1.16. -----	49
<p>(a) TEM image of the SnO_2 NW indicating the reaction front, i.e. dislocation cloud, which separates the lithiated and the unreacted SnO_2 part</p> <p>(b-e) EDPs of the different sections of the SnO_2 NW,</p> <p>(f) HRTEM image of the lithiated part showing the Sn NPs dispersed in an amorphous matrix</p> <p>(g) schematic illustration of Li^+ diffusion flux</p>	

Figure 1.17. -----	53
Schematic diagrams of Li^+ and e^- transport on 0-D (a-c) and 1-D (d-e) NPs	
Figure 1.18. -----	54
Schematic illustration of the pulverization and the aggregation of β -Sn NPs with respect to particle size.	
Figure 1.19. -----	55
Schematic illustration of the advantages of using 1-D NPs.	
Figure 1.20. -----	57
(a) SEM image of the SiNP@C	
(b) STEM image of the SiNP@C with the corresponding EDAX elemental mapping for C, O, and Si	
(c) Cross-sectional SEM image of the SiNP@C indicating that C shell and the Si NPs comprised core	
(d) cycling performance of SiNP@C measured at 3C rate	
Figure 1.21. -----	58
(a) TEM image of Sn@C encapsulated in hollow carbon fiber	
(b) Elemental mapping of (a) where blue = carbon and yellow = Sn	
(c) Cycle test of at a cycling rate of 0.5 C	
(d) Capacities at different C-rate	
Figure 1.22. -----	60
(a) Schematic illustration of NWs directly grown on the current collector	
(b) SEM image of the grown Si NWs	
(c) Voltage profiles at various C-rates	
(d) Cycle rate at C/20 of Si NWs directly grown on SS substrate	

Figure 1.23. ----- **62**

(a) Schematic diagram of a single nanowire electrode device for *in-situ* probing the actual optical image of the single nanowire electrode device:

(b) with and (c) without Si/a-Si nanowire/LiCoO₂ electrodes

Figure 1.24. ----- **63**

(a) Schematic illustration of the nanoscale electrochemical device

TEM images of:

(b) initial straight NW

(c) meniscus on the ionic liquid-based electrolyte (ILE) wetted NW

(d-s) screen shots indicating the changes observed during lithiation with respect to time

(p-s) high-magnification image of the progressive migration of the reaction front, and the swelling and twisted morphology of the lithiated part

Figure 1.25. ----- **65**

(a) HAADF image of a partially lithiated SnO₂ NW

(b) corresponding SAED pattern taken with the [010] zone axis

(c) atomic resolution HAADF image from the partially lithiated area of (a) with EELS analysis as inset

(d) strain map with the [100] direction in (c)

(e) atomic resolution HAADF image from the fully lithiated area of (a)

(f) atomic resolution HAADF image of the surface step induced by lithiation

Figure 1.26. ----- **67**

(a-b) Direct observation of lithiation of SnO₂ (a) with and (b) without twin boundary (TB) defect, with electron diffraction of the reaction front shown at the right

(c) HAADF of the lithiated are of sample with TB and its corresponding EELS maps of O, Sn, and Li

(d-e: left) atomic scale HAADF and strain analysis

(d-e: right) of SnO₂ NW (d) with and (e) without TB defect

(f-g) DFT simulation of (f) atomic structure model to investigate the Li intercalation induced TB defect and (g) strain associated with Sn-Sn bond change induced by one (1) or two (2) Li insertion.

Figure 2.1. ----- **86**

(a) XRD pattern of Sn particles produced at different synthesis temperatures

(b) Interval plot of particle size versus synthesis temperature

Figure 2.2. ----- **89**

TEM images of the nanoparticles formed after 15 min reaction time at various synthesis temperatures

Figure 2.3. ----- **91**

(a) HAADF-STEM image of the tip of a Sn nanorod; inset is the TEM image.

(b) Magnified image of the area shown in (a) that corresponds to the (020).

(c) Stacked β -Sn unit cell indicating the (020) plane with respect to the [001] growth direction.

(d-e) SAED patterns along sand at the tip of a NR respectively.

Figure 2.4. ----- **92**

Wulff-constructed equilibrium shape of β -Sn with respect to the surface Energies

Figure 2.5. -----	97
<p>(a-d) TEM image of the particles prepared using different amounts of PVP: (a) 0.3073, (b) 1.5364, (c) 3.0728, and (d) 6.1456 g.</p> <p>(e) Interval plot of the particle size vs amount of PVP (95% CI for mean size)</p>	
Figure 2.6. -----	99
<p>(a-c) TEM image of the particles produced using PVP of (a) 10000 MW, (b) 40000 MW, and (c) 630 000 MW</p> <p>(d) Interval plot of the particle size vs MW of PVP</p>	
Figure 2.7. -----	102
<p>(a) A PVP-coated single nanoparticle</p> <p>(b) high MW PVP attached to two or more nanoparticles due to its long polymeric chain</p> <p>(c) HR-TEM image of the rod-like morphology synthesized at $-15\text{ }^{\circ}\text{C}$</p>	
Figure 3.1. -----	114
<p>TEM images of the nanoparticles formed at different synthesis temperatures: (a) $0\text{ }^{\circ}\text{C}$, (b) $10\text{ }^{\circ}\text{C}$, and (c) $26\text{ }^{\circ}\text{C}$</p>	
Figure 3.2. -----	116
<p>The calculated XRD based micro-strains of each crystallographic planes of spherical, low aspect ratio, and high aspect ratio β-Sn NPs for different crystal planes</p>	
Figure 3.3. -----	118
<p>Cyclic voltammograms at a scan rate of $0.1\text{ mV}\cdot\text{s}^{-1}$ between 0.1 and 3.0 V vs Li/Li⁺: (a) high aspect ratio and (b) low aspect ratio β-Sn NRs.</p>	

Figure 3.4. ----- **121**

- (a) Cyclic test of high and low aspect ratio β -Sn NRs and spherical β -Sn electrodes
- (b-c) Charge-discharge curve of (b) high and (c) low aspect ratio β -Sn NRs electrodes using 0.2C with voltage window of 0.1 V to 3.0 V
- (d) rate performance of high (red) and low (black) aspect ratio β -Sn NRs electrodes

Figure 3.5. ----- **122**

- (a) Nyquist plot after the 3rd discharge with the inset of the equivalent circuit model for the determination of the resistance values
- (b) relationship between real resistance (Z') and inverse square root of angular speed ($\omega^{-1/2}$) low frequency region, of the high and low aspect ratio β -Sn NRs.

Figure 3.6. ----- **124**

- (a, b) TEM images (a) high and (b) low aspect ratio NRs after the 3rd discharge
- (c, d) SAED pattern of (c) high and (d) low aspect ratio NRs after the 3rd discharge

Figure 3.7. ----- **127**

- XPS analysis of (a-f) low and (g-l) high aspect ratio NRs before cycling (a-c,g-i), and after 3rd discharge (d-f, j-l)

Figure 3.8. ----- **130**

- (a) SAED analysis of β -Sn NRs indicating the growth direction and surface planes
- (b) The type of SEI layer compound formed on the surface of β -Sn NRs with respect to the surface crystallographic plane
- (c-d) schematic illustrations of the SEI layer formed on (c) high and (d) low aspect ratio β -Sn NRs.

Figure 4.1. -----	141
(a) Schematic diagram of HS Flat Cell	
(b) The chemical formula of the CMC and SBR binders used.	
Figure 4.2. -----	143
XRD patterns of the samples synthesized in the presence of DTAB: after hydrothermal (blue) and after calcination (red)	
Figure 4.3. -----	144
TEM images of the 1D ZnV ₂ O ₄ : (a) whole 1D ZnV ₂ O ₄ , (b) tip of the 1D ZnV ₂ O ₄ , (c) along the wire, (d) SAED of the 1D ZnV ₂ O ₄ with inset of the examined area	
Figure 4.4. -----	146
(a) Two-dimensional crystal structure of ZnV ₂ O ₄ illustrating the distribution of Zn (blue), V (yellow), and O (red) atoms viewed along the [220]	
(b and c) HAADF-STEM images of the rod indicating the distance between the (b) lattice fringes, i.e. 2.97 Å, corresponding to the (220) plane and (c) the distribution of the atoms at the surface of the rod .	
(d) ABF-STEM image of (c)	
Figure 4.5. -----	148
XPS spectra of porous ZnV ₂ O ₄ NWs: (a) wide scan, and narrow scans of (b) V 2p, (c) Zn 2p, and (d) O 1s	
Figure 4.6. -----	154
Electrochemical test of porous ZnV ₂ O ₄ NWs:	
(a) charge/discharge profile with a current density of 1 A g ⁻¹	
(b) rate performance	
(c-d) voltage-capacity profiles associated with (c) charge/discharge profile with a current density of 1 A g ⁻¹ and (d) various current rates	

Figure 4.7. -----	155
Plots of dQ/dV of the porous ZnV_2O_4 NWs cycled at 1 A g^{-1} at different cycle number	
Figure 4.8. -----	156
Nyquist plot of the porous ZnV_2O_4 : fresh cell (red), after 10 cycles (black), and after 100 cycles (blue) in the frequency range of 10^{+5} to 0.01 Hz	
Figure 4.9. -----	158
(a) CV curves of porous ZnV_2O_4 at different scan rates from 0.05 to 1.0 mV s^{-1} with voltage window of 0.01 – 3.0 V	
(b) $\log(v) - \log(i)$ plot of (a).	
Figure 4.10. -----	159
(a) SEM image of the porous ZnV_2O_4 NWs after 100 cycles	
(b-d) The corresponding EDS mapping for (b) Zn, (c) V, and (d) O, and EDS spectrum with inset of the atomic %	
Figure 4.11. -----	160
Charge/discharge profiles (current density of 5 A g^{-1}) of ZnV_2O_4 with different morphologies: (red) porous NWs, (blue) spherical, (black) and coral-like	

LIST OF TABLES

Table 1.1. -----	8
Comparison of rechargeable battery cell properties	
Table 1.2. -----	30
LIB component deficiencies and the necessary improvement of the currently produced LIBs	
Table 2.1. -----	85
Summary of Experimental Conditions to Investigate the Effect of Temperature, Amount and MW of PVP in the Formation of Sn NR	
Table 2.2. -----	88
Summary of the Particle Sizes of the Produced Nanoparticles under Different Synthesis Conditions, and PVP Quantities and MW	
Table 3.1. -----	122
Calculated resistivity values (top) and diffusion coefficient (bottom) in Figure 3.5a and 3.5b respectively.	
Table 3.2. -----	128
Corresponding XPS binding energy (eV) of low and high aspect ratio NRs before cycling and after the 3 rd discharge	

LIST OF SCHEMES

Scheme 2.1. -----	94
Formation Mechanism of β -Sn Nanoparticles with Different Morphologies (Spherical Nanoparticles and Nanorods) with Respect to Temperature	
Scheme 3.1. -----	113
Preparation of the CR2032 Li half-cell and the chemical structures of the binder (CMC and SBR) used	
Scheme 3.2. -----	115
The formation of the different aspect ratio of β -Sn NPs with respect to the synthesis temperature	
Scheme 4.1. -----	151
Mechanism in the formation of porous ZnV_2O_4 with different morphologies with respect to the calcination condition.	

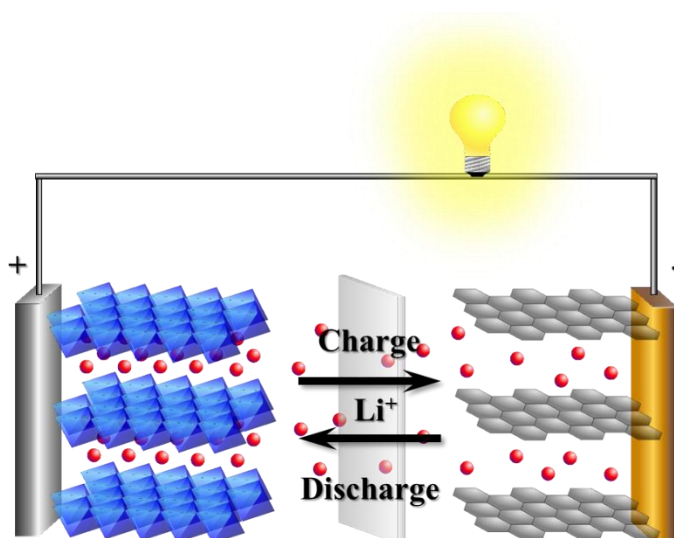
LIST OF ABBREVIATIONS

0D	0-Dimensional (spherical)
1D	1-Dimensional
AAO	Anodized Alumina
ABF-STEM	Annular Bright-Field
AFM	Atomic Force Microscopy
BMS	Battery Management System
CE	Coulombic Efficiency
CMC	Carboxymethyl Cellulose
CV	Cyclic Voltammetry
CVD	Chemical Vapor Deposition
DFT	Density functional theory
DI water	Deionized water
DMC	Dimethyl Carbonate
DOD	Depth of Discharge
DTAB	Dodecyl Trimethylammonium Bromide
EC	Ethylene Carbonate
EDS	Energy Dispersive X-ray Spectroscopy
EE	Energy Efficiency
EELS	Electron Energy Loss Spectroscopy
EES	Electrical Energy Storage
E_g	Electrolyte window
EV	Electric vehicles
F	Faraday's constant (96485.33289 C mol ⁻¹)
FEC	Fluoroethylene Carbonate
FTIR	Fourier Transform Infrared Spectroscopy
HAADF-STEM	High Angle Annular Dark Field- Scanning Transmission Electron Microscopy
HOMO	Highest Occupied Molecular Orbital
HR-TEM	High Resolution Transmission Microscopy
I_i	Ionic current
ILE	Ionic liquid-based Electrolyte
JCPDS	Joint Committee on Powder Diffraction Standards
KS6	synthetic graphite with lateral size of 6 μm (d ₉₀)
LIB	Lithium-ion Battery
LUMO	Lowest Unoccupied Molecular Orbital
MW	Molecular Weight
NP	Nanoparticle
NR	Nanorod
NT	Nanotube
NW	Nanowide

OCP	Open Circuit Potential
P	Pressure
PC	Propylene Carbonate
PVD	Physical Vapor Deposition
PVP	Poly(vinylpyrrolidone)
Q	total charge per unit weight
R_b	internal battery resistance
SAED	Selected Area Electron Diffraction
SBR	Styrene-Butadiene Rubber
SEI	Solid-Electrolyte Interphase
SEM	Scanning Electron Microscopy
SOC	State of Charge
STEM	Scanning Transmission Electron Microscopy
Super P	6 nm Carbon Black
T	Temperature
TB	Twin Boundary
TEM	Transmission Electron Microscopy
TMO	Ternary Transition Metal Oxides
V	Volume
VC	Vinylene Carbonate
V_{ch}	Charge Voltage
V_{dis}	Discharge Voltage
VE	Voltage Efficiency
V_{oc}	Open-circuit voltage
XPS	X-ray photoelectron Spectroscopy
XRD	X-ray Diffraction
Z'	Real resistance
Z''	Imaginary Resistance
ΔG_r	Gibbs free energy
ΔS_r	change in the vibrational and configurational entropies of ion insertion and extraction
ΔU_r	change in the internal energy
ΔV_r	change in volume
μ_A	Potential of Anode
μ_C	Potential of Cathode
ω^{-1/2}	inverse square root of the angular speed at low frequency region

CHAPTER 1

GENERAL INTRODUCTION



Abstract	2
1.1. Why lithium-ion battery?	2
1.1.1. Lithium-ion Battery: A history – how it started	10
1.1.2. Lithium-ion Battery: How it works	16
1.1.3. Lithium-ion Battery: Future and improvements	29
1.2. Anode material for LIB	32
1.1.1. Alloying anode material for LIB	42
1.1.2. Conversion anode material for LIB	45
1.1.3. Size and morphology of the anode material for LIB:	
1-D nanostructure	50
1.3. Summary and Perspective	68
1.4. Significance of the study	69
1.5. Objective of the study	70
References	71

Abstract

The general introduction for the topics of this dissertation are presented in this chapter. The current state of lithium-ion batteries in the world market, its advantages over other storage devices, how it works, the current problem associated with its safety issues, and other relevant related literatures on how to improve the capacity and the stability of LIBs by using 1-D alloying and conversion type anode materials has been reviewed. The summary, research perspective, and limitations of this research are provided at the end of this chapter allow the reader to have an insight on the future of LIBs as a promising energy storage device for renewable energy and EVs.

1.1 Why Lithium-ion battery (LIB)?

Global warming and the continuous increase in the energy demand are currently the two most popular debatable environmental issues. The energy production of 14 TW in 2010 is foreseen to double by 2050, i.e. 130,000 TWh or equivalent to 10^{10} tons of oil every year [1], to meet the energy demand due to the continuous industrialization and increase in population as shown in Figure 1.1 (a). However, the increase in the energy consumption means an increase in CO₂ emission, i.e. for every hour, the consumed 10^6 TOE equates to 3×10^6 tons of CO₂ emitted [1]. Per the International Energy Agency (IEA), CO₂ emission was doubled from 1973 to 2015, i.e. 15,458 Mt to 32,294 Mt of CO₂ respectively [2]. Hence to address the increasing

energy demand without increasing the CO₂ emission, renewable energy and electric vehicles (EV) becomes the global imperative [2]. Based on the fuel shares of the total primary energy supply (TPES) of IEA last 2015, only ~20% of 13,647 Mtoe are from the renewable energy [1] as shown in Figure 1.1 (b). The often-used renewable energies such as wind, solar, tidal, biomass, and geothermal, are all have intermittent operations and not mature enough compared to the vast majority of electrical energy supplier, i.e. fossil fuel, to supply the necessary energy. There are still several issues that are still needed to be addressed in-order for the renewable energy to fully operates, and one of which is the suitable energy-storage system. EVs on the other hand are also not mature enough to replace the conventional fuel combustion cars / vehicles to have an environmental impact, despite the fact that they are expected to be eco-friendly. As shown in Figure 1.2 (a), the CO₂ emission of EVs are comparable with that of the conventional fuel combustion cars / vehicles due to energy consumption which utilizes electricity produced from burning coals / natural gas, and the production of the energy storage devices (battery) as shown in Figure 1.2 (b). To annihilate the CO₂ emission from the electricity production, renewable energy should be utilized as indicated by the drastic reduction of CO₂ emission of EVs that utilizes 100% hydrothermal. On the other hand, for the battery production, it has been revealed that to make a 1 kWh battery, more than 400 kWh energy from electricity (from burning fossil fuel) is necessary which equates to a total of about 75 kg of emitted CO₂

[3]. Hence, to have an environmental impact, batteries should be stable enough to run beyond hundreds of cycles.

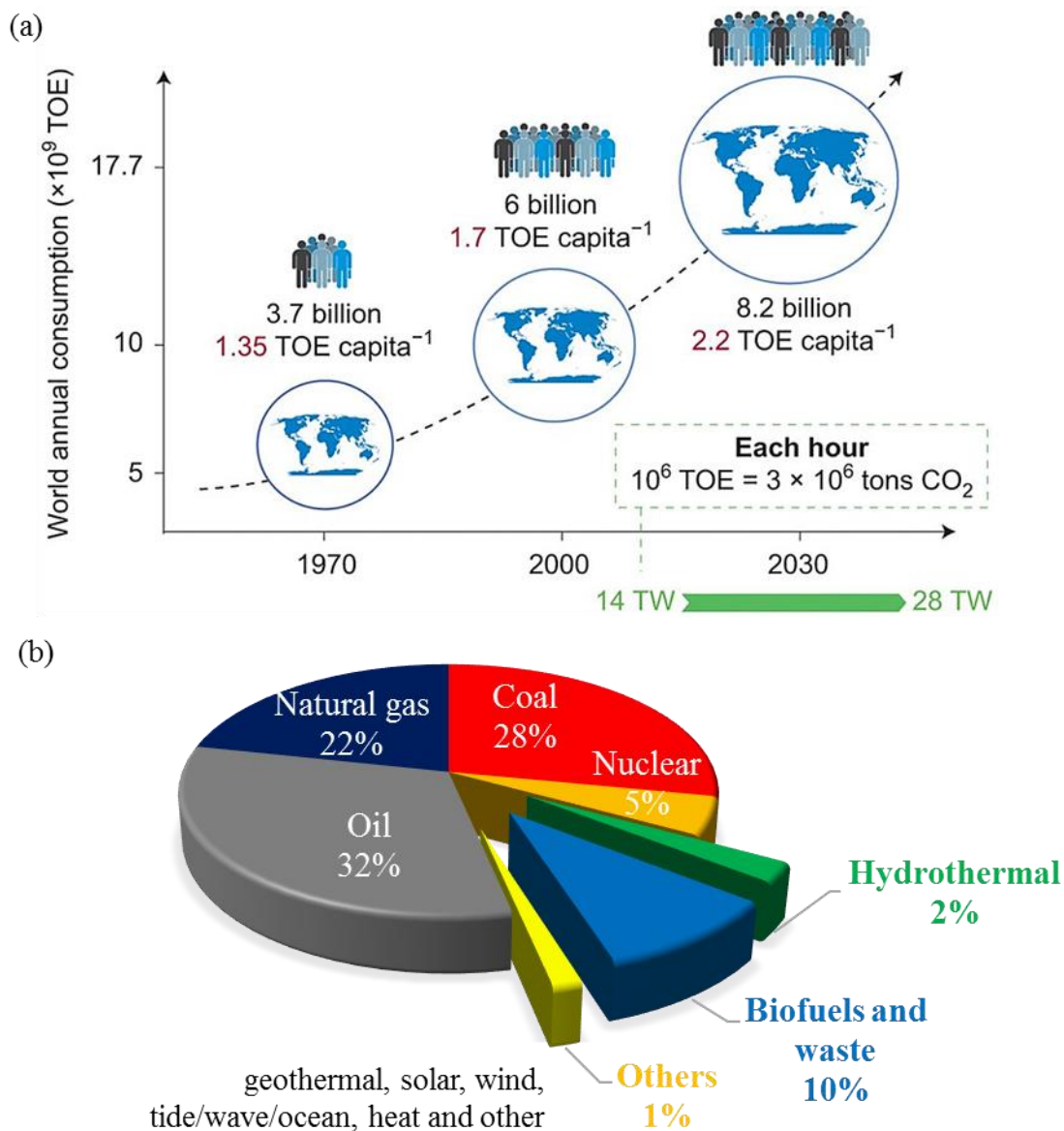


Figure 1.1. (a) Forecast and statistics of the world's energy demand until 2050. Reproduce with permission from [1]. Copyright 2014 Macmillan Mexico/Haide Ortiz Ortiz, Mario Enrique Ramirez Ruiz. (b) 2015 fuel shares of TPES [2].

For the electrical energy storage (EES) devices of high end applications such as storage devices for renewable energies and EVs, high specific energy and specific power are required. The specific energy and specific power indicates the total energy and power per unit weight, wherein, for a specific amount energy, the higher the specific power and specific energies, the lighter the EES device as shown in Figure 1.3 (a). Due to fast response time, SMES, capacitors, and supercapacitors have low specific energy but with high specific power, and hence it is more suitable for power quality applications for electric power delivery. On the other hand, fuel cells and TES have high specific energy with low specific power, while flywheel, flow batteries, and other conventional batteries have average specific energy and specific power. The promising high specific energy and specific power of LIBs however explains its current wide range of application and development. LIBs also have high energy density and high-power density as shown in Figure 1.3 (b), which satisfies the requirements for portable devices, and shows a promising potential for EVs and other small-scale applications. For most of EES applications, the size is also one of the most important parameters that should be considered, i.e. the smaller the volume / density of the EES devices, the higher the power density and energy density for a certain amount of energy. On the other hand, among other rechargeable batteries, LIBs are advantageous in terms of both gravimetric and volumetric densities as shown in Figure 1.4 and Table 1.1. These promising features of LIBs can be attributed to its mass and density, i.e. 6.94 *amu* and 0.53 g/cm³ respectively, which is the

lightest and smallest amongst all metal, and its reduction potential, i.e. -3.04 V (SHE) which is the most negative. Other advantage of LIBs as shown in Table 1.1 includes: (a) the rate of discharge, i.e. the ability of the battery to lose their charge over time, is much lower than other rechargeable battery, (b) priming is no longer required for the 1st charge process, and (c) there is no memory effect as that of the Ni-Cad cells that requires the periodic discharge and hence the battery maintenance [1, 3-15].

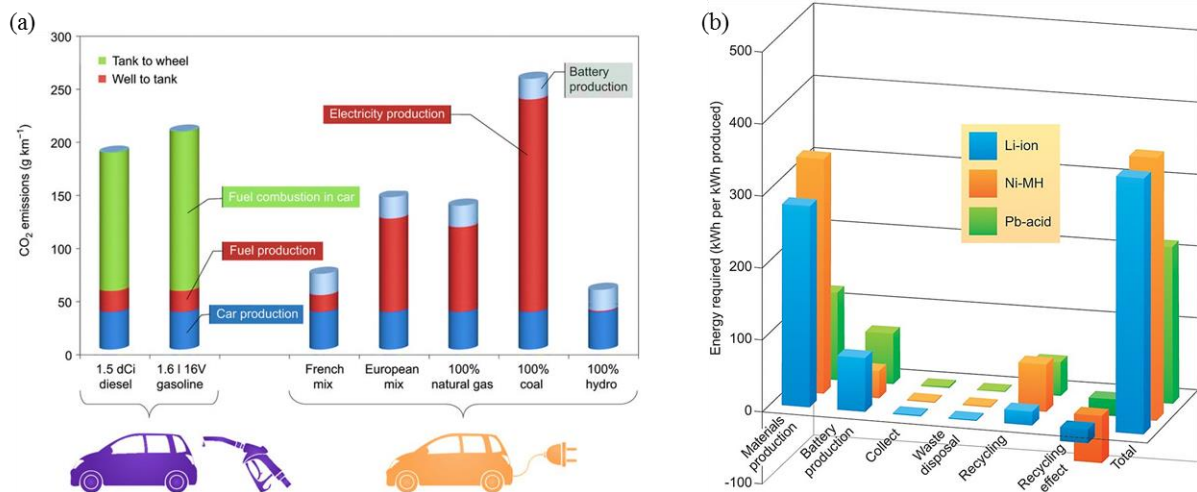


Figure 1.2. (a) Comparison of CO₂ emitted of conventional fuel combustion cars/vehicles vs. EVs that utilizes energy from different electricity sources, and (b) the estimated energy required to produce 1 kWh storage device, vis. battery. Reproduce with permission from [1].

Copyright 2014 Macmillan Publishers Limited.

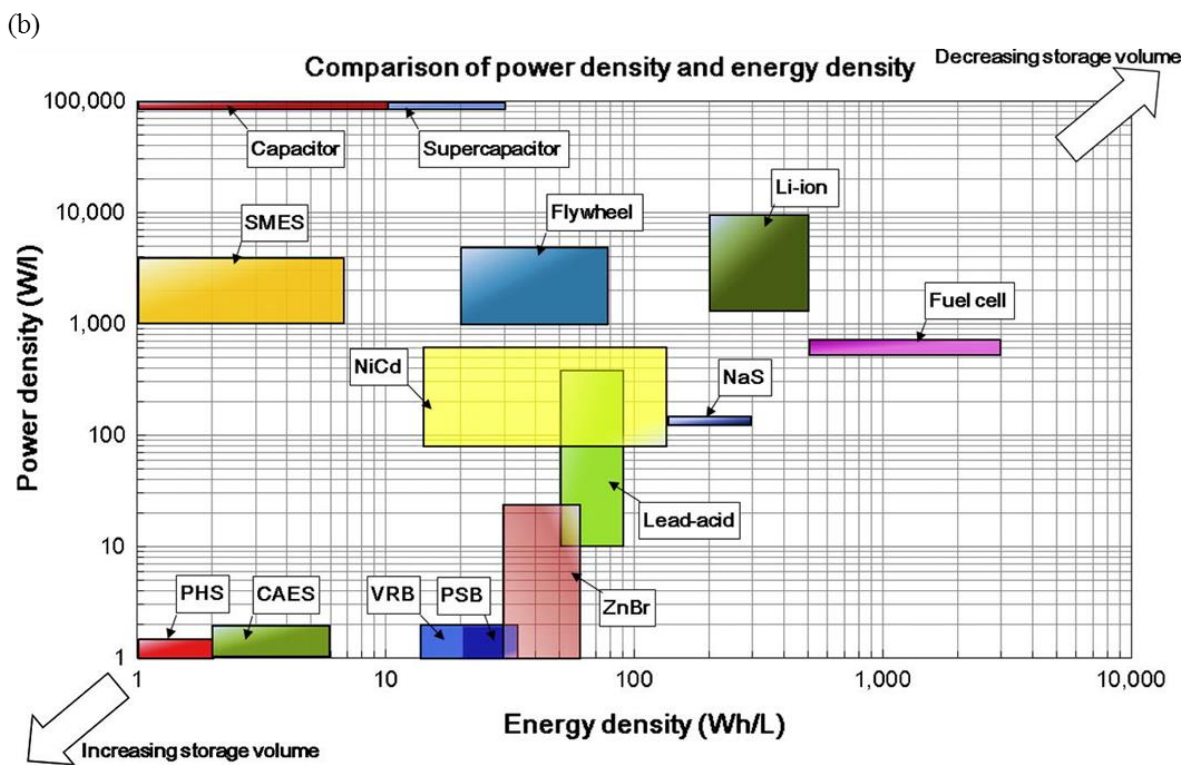
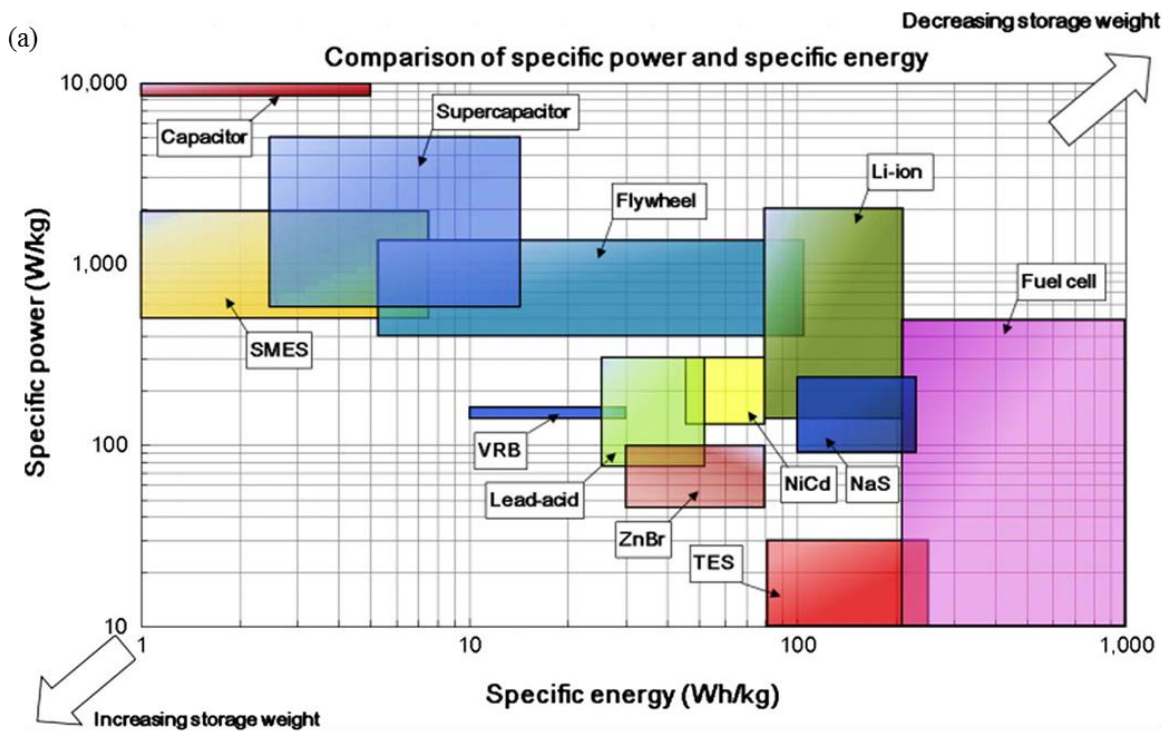


Figure 1.3. Comparison of (a) specific energy and specific power, and (b) energy density and power density, of different EES devices. Reproduce with permission from [3]. Copyright 2014

Elsevier Ltd.

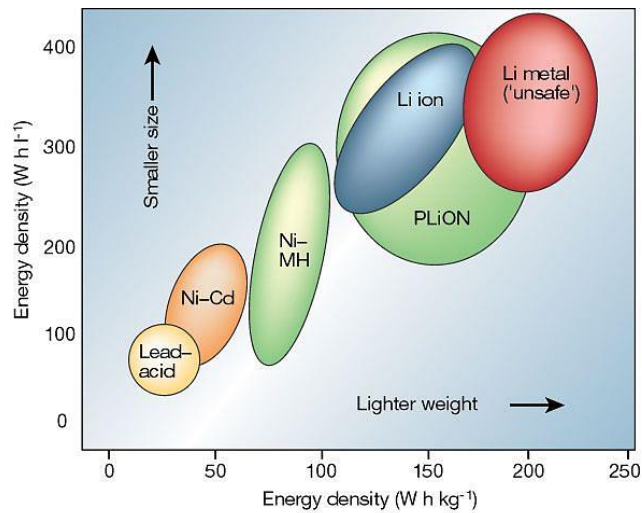


Figure 1.4. Comparison of volumetric and gravimetric energy density of different rechargeable batteries. Reproduce with permission from [4]. Copyright 2001 Macmillan Magazines Ltd.

Table 1.1. Comparison of rechargeable battery cell properties [5].

	Lead Acid	Nickel Cadmium, Ni-Cd	Nickel Metal Hydride, Ni-MH	Li-ion	Li-Poly	LiFe
Voltage, V	2	1.2	1.2	3.6-3.7	3.6-3.7	3.3
Specific Energy, Wh/Kg	35	45	70	167	110	100
Cycle Life	400	500-1000	400-1000	300-1000	300-1000	>1000
Life, years @ one charge/day	1	2	2	1+	1+	3
Charging Time, hours	8	1.5	4	2-6	2-6	1-3
Self-Discharge Rate, %/month	10-20	30	30-35	3	3	3
Safety	No BMS	Good	Good	Poor	Avg	Good
High Temp Performance	Good	Good	Good	Avg	Avg	Good
Cold Temp (0°F) Charge	Good	Fair	Fair	0-45°F	0-45°F	0-45°F
Cold Temp (0°F) Discharge	Good	Good	Poor	Avg-Good	Avg-Good	Good
Memory Effect	No	Yes	Little	No	No	No

The versatility of LIBs attracts wide range of applications from portable electronics, EVs, to grid applications that requires dozens of watt-hours, kilowatt-hours, to megawatt-hours respectively. However, promising as it is, LIBs shows several disadvantages such as safety issues from the immature technology, applied current limitation, and the transportation restrictions, aging which is dependent on the number of charge-discharge cycles, and most especially the cost and materials' abundance [1-14]. Lithium can be viewed as gold of the next century [3] due to its limited abundance, cost, and at the same time usefulness. Per U.S. geological survey of the commodity of lithium as of January 2018, almost half, i.e. 46%, of the utilized Li were allocated for the battery production (Figure 1.5 a), and due to the in-demand production of LIBs, the annual average price of the battery grade lithium carbonate increases dramatically from US\$ 8,650.00 to US\$ 13,900.00 per metric ton (Figure 1.5 b). Though the price of lithium increases, the continuous exploration led to the substantial increases of lithium resources to more than 53 million tons worldwide, i.e. 6.8 million tons from the U.S. and ~47 million tons in other countries such as Argentina, Bolivia, Chile, China, Australia, Canada, Congo, Russia and Serbia, Czechia, Zimbabwe, Spain, Mali, Brazil and Mexico, Portugal, and Austria [16]. These disadvantages however served stepping stone to hone and to have a continuous development of LIBs to meet the requirements of high energy storage devices needed to help our environment.

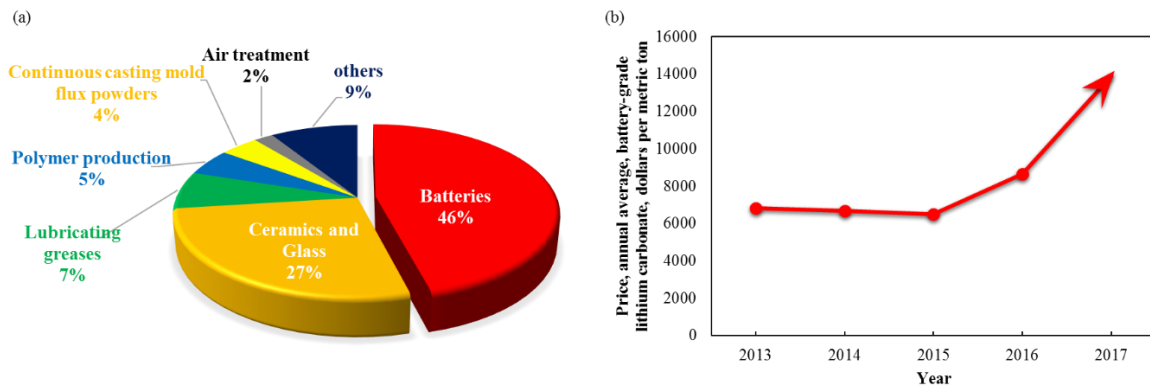


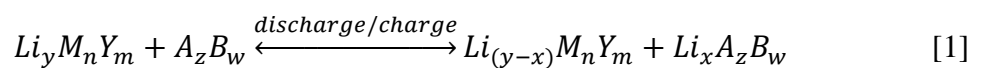
Figure 1.5. (a) Estimated global end-use market of Lithium, and (b) annual average price of battery grade lithium carbonate per metric ton. [16]

1.1.1 Lithium-ion Battery: A history – how it started

G.N. Lewis began the research for LIBs as early as 1912, while the breakthrough on the stability of lithium battery (primary battery) started in 1958 by Harris. He noticed the stability of Li-metal in several non-aqueous (aprotic) electrolytes, viz. fused salts, liquid SO_2 , and lithium salt, dissolved in organic solvent, e.g. LiClO_4 in propylene carbonate ($\text{C}_4\text{H}_6\text{O}_3$). He observed that the formation of passivation layer on the Li metal hinders its direct contact, and hence chemical reaction, with the electrolyte, and at the same time still allows ionic transport [17, 18]. These researches pave way to the fabrication and the commercialization of lithium battery in late 1960s [18]. However, not until 1991 where rechargeable LIBs (secondary battery) have been first manufactured and commercialized by Sony. The idea of a secondary battery (rechargeable battery) in which the lithium ion (Li^+) moves from the cathode (positive) to the anode (negative) and vice versa, often called rocking chair battery, was inspired by the

work of Armand in Stanford in the late 1970s, where he deals with the properties of Prussian blue (iron cyanide bronzes $M_{0.5}Fe(CN)_3$). This research opened the door to the discovery of the other reversible insertion of guest species, i.e. ions, organic molecules, and organometallics, into a host lattice while maintaining its structural features and at the same time exhibits new physical properties [18-20].

The malfunctioning operations and the serious safety hazard due to the reactivity of the alkali metal that led to the passivation and instability phenomena at its interface restricts the initial commercialization of LIBs [20]. Lithium metal are very unstable, i.e. air- and water-sensitive, and very flammable. Upon rapid charging of LIBs using lithium metals as anode, lithium dendrites form on the anode that causes short circuit in the LIBs which in turn overheat and ignite, thus limits its application [5-14, 21]. One approach to mitigate this problem is to replace the lithium metal in the cathode with non-metallic compound, $Li_yM_nY_m$, to store and exchange large quantities of Li^+ , rather than the conventional Li plating and stripping, and use another non-metal Li-accepting compound, A_zB_w , in the anode. The Li^+ “rock” from one side to the other, i.e. cathode to anode and vice versa, as show in equation [1] and Figure 1.6, and hence termed as “rocking chair battery” [20].



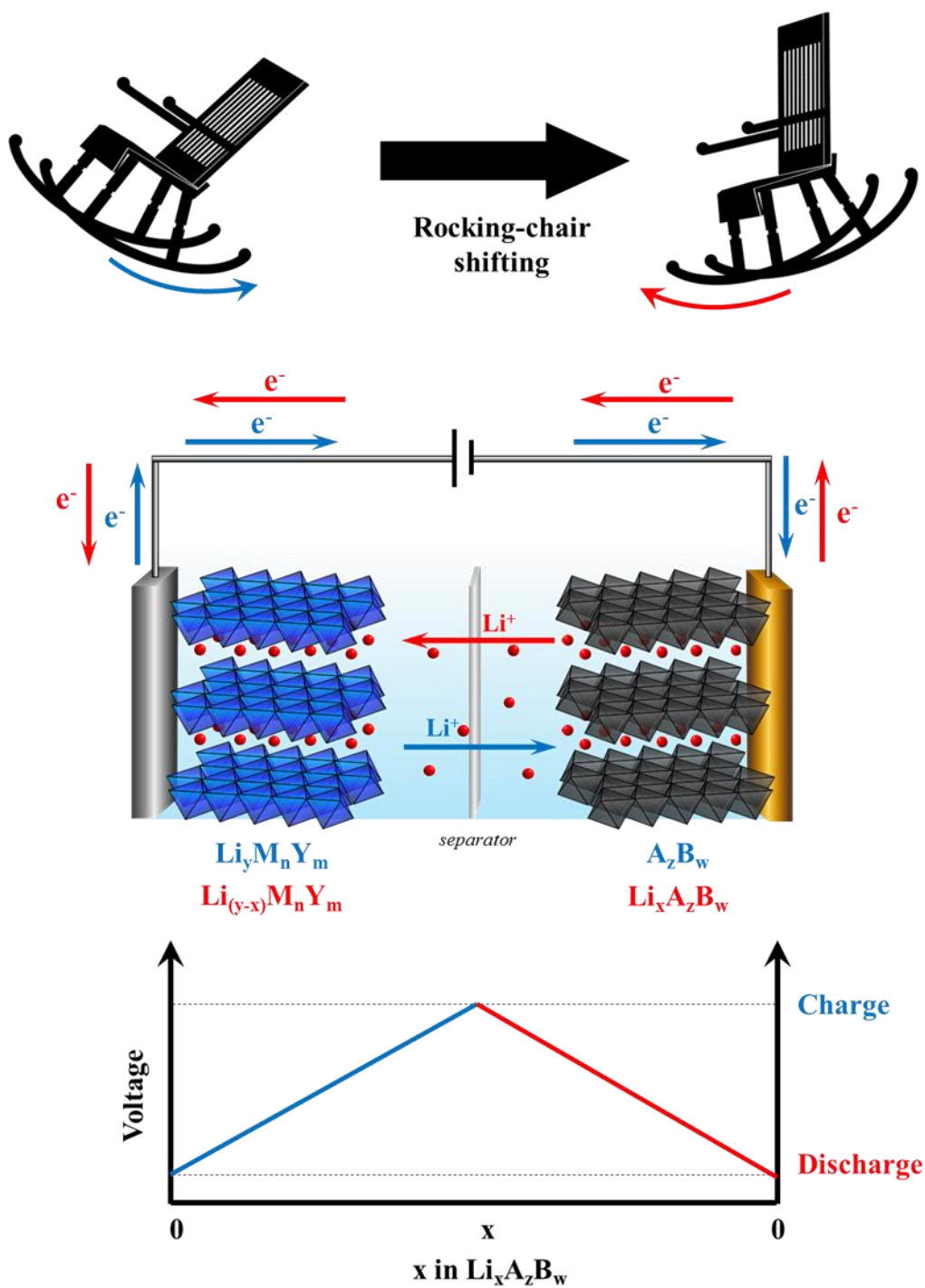
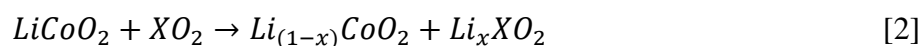


Figure 1.6. Model of a rocking chair battery and the relative charge-discharge voltage profile.

Scrosati et al., shows the feasibility of a stable rocking chair battery in 1979 by using non-metallic cathode material, i.e. LiWO_2 or $\text{Li}_6\text{Fe}_2\text{O}_3$, and non-metallic Li-accepting anode

material, i.e. TiS_2 , WO_3 , NbS_2 or V_2O_5 . In this work, they use a typical organic electrolyte, i.e. lithium perchlorate (LiClO_4) in propylene carbonate (PC). Their work shows a reasonable high open-circuit voltage, and good charge-discharge efficiency for over 60 cycles. However, the fabrication was complicated and requires a two-step procedure. Also, the potential range was only 0.8 to 2.1 V, where the charge voltage was limited to about 2.2 V and the discharge voltage was about 1.6 V, and both electrodes featured high molecular weights. Furthermore, both LiWO_2 and $\text{Li}_6\text{Fe}_2\text{O}_3$ have low specific capacity and have slow Li^+ diffusion. Though, this work was characterized to have high cost, low energy density, and low rate capability battery, they were able to establish an important principle in rocking chair battery [19, 20, 22]. In the early 1980s, Goodenough laboratory had found a seminal discovery of using transition metal oxide, vis. LiCoO_2 , as cathode material to reversibly deintercalate and reintercalate Li^+ at relatively high potential, while limiting the voltage to prevent the oxidation/degradation of the electrolyte. They also found that combining Ni or Co with Mn, Al, Fe, etc., can have a similar effect. This discovery led to the adoption of LiCoO_2 , as cathode material of Sony's LIBs in 1991 and made John Goodenough the inventor of LIB [19, 23]. On the other hand, in 1981, Hunter of Eveready Laboratories, discovered $\lambda\text{-MnO}_2$ (spinel structure), that form LiMn_2O_4 (spinel structure) with Li, which has a similar property as that of LiCoO_2 . This material was also commercialized for a number of succeeding higher rate battery application [19, 24]. In 1987, Auburn and Barberio, on the other hand utilized LiCoO_2 as cathode material and a Li-

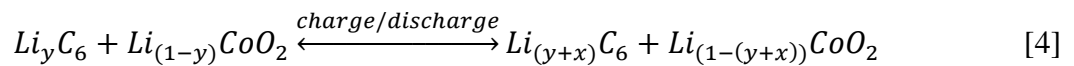
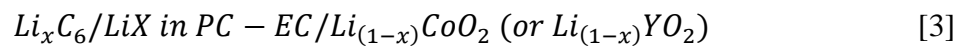
accepting or Li-sink, pristine anode compound XO_2 , vis. WO_2 or MoO_2 , to examine and show the feasibility of rocking chair cell: MoO_2 (or WO_2)/ $LiPF_6$ -PC/ $LiCoO_2$, following the reaction in equation [2], where $X = W$ or Mo . However, the slow Li^+ diffusion on both electrodes limits the charge-discharge rates [20, 25].



Thus, finding a suitable anode material is a bit more challenging than cathode material [19].

The Li insertion in Graphite, the most common and commercially produced anode material, on the other hand has been studied as early as 1955 by A. Harrold and was confirmed when R. Juza and V. Wehle synthesized LiC_6 in 1965 [26-28]. The electrochemical process where lithium can reversibly intercalate in the graphite matrix however was established by J. O. Besenhard and G. Eichinger in 1976 [26, 29-30]. They proposed that graphite can be use as anode material for lithium cell while using Li salt dissolved in either propylene carbonate (PC) or dimethyl sulphoxide (DMSO) as electrolyte. However, the lack of suitable electrolyte restricts its application until M. Armand and M. Duclot's work and patent in 1981 regarding the PEO-polymer electrolyte [26, 31]. On the other hand, the work of Basu of Bell Laboratories [32], and Yazami and Touzain [33] of University of Grenoble in 1983 further proved the Li^+ intercalation on graphite and other carbonaceous compounds. While the work and patent by Yoshino et al. of Asahi Kasei (Japanese supplier of battery separators) made a pivotal discovery

of using petroleum coke, a low temperature carbon as anode material in LIB. The basic battery cell equation and electrochemical reaction are shown in equation [3] and [4], where LiX is a lithium salt, vis. LiClO₄, PC-EC is a solution of propylene carbonate (PC) and ethylene carbonate (EC) that serves as the solvent, and Y is a transition metal, vis. Ni or Mn [20, 34-35]. This work regarded Akira Yoshino as the true inventor of the LIB [19]. While Nagaura and Tazawa coined the term “Lithium ion rechargeable battery” to refer to Yoshino’s work [19, 35]. Hence, the novelty of the work of Yoshino et al. open the door to more improvements in cyclability, energy density, and cost [20].



However, the drawback of carbonaceous compounds is the chemical reaction with the electrolyte and thus the formation of solid-electrolyte interface (SEI) layer. The formation of SEI layer was caused by the degradation of the electrolyte and hence controlling the formation of the SEI layer is necessary in the stability and the applicability of the used anode material and thus the produced LIBs.

LIB has been first commercialized since 1991, but the need for further improvement on both properties and safety are still on-going and thus a lot of researched has been done to address these issues.

1.1.2 Lithium-ion Battery: How it works

From Lithium-rocking chair battery (1980s) to lithium-ion battery (1990s), the general idea of a single battery cell is merely the subsequent transfer of Li^+ from anode to cathode and vice versa. A battery can either be one (single) or more (parallel or series) interconnected electrochemical cells, which releases current at a voltage for a time Δt . To increase the output current I , and the time Δt to deplete the stored energy, it is either enlarge the area of the electrodes or connect the single cells in parallel. On the other hand, to increase the desired power, $P=IV$, the single cells should be connected in series [36, 37]. Multiple battery cells are integrated into a module and thus to a battery pack, e.g. an 85-kWh battery pack in a typical Tesla car contains 7104 single battery cells [37].

The basic design and operating principle of the current single-cell LIB as shown in Figure. 1.7, is still similar to that of the rocking chair battery and the initial commercially produced LIB by Sony for almost three (3) decades ago, although various kinds of electrode,

electrolyte, and separator materials have been explored and considered. The components of the LIBs are composed of two (2) electrodes, vis. anode and cathode, which is separated by either solid or liquid electrolyte and were connected externally to an external electrical supply. In a battery with solid electrolytes, the electrodes used are typically either gaseous or liquid electrodes. In solid electrodes however, though solid electrolytes, vis. polymer gel or ceramics electrolytes, can still be used, solid-solid interaction is problematic and might be feasible if the electrolyte is a polymer or the electrodes are thin. Nevertheless, solid electrodes typically use liquid electrolyte and is being kept apart by a permeable separator, usually a microporous polymer membrane, that can traverse both electrolytes and ions. Each cell of the battery stores electrical energy from the consecutive conversion of electrical energy to chemical energy and vice versa. The commercially produced LIBs are in “discharge state”, i.e. no energy has been stored. Initially, the cathode material, usually a spinel material containing Li^+ , cannot easily release Li^+ to produce e^- , and hence an external force, vis. electric current, is used to drive the reaction. This process is called “charging” where Li^+ moves from cathode to anode internally via the electrolyte, while electrons were forced to move in the same direction through the external electrical supply; and thus, converts electrical energy to chemical energy. The released e^- are being stored electrochemically in the battery in the form of chemical energy. The difference in the potential of the anode (reductant) and the cathode (oxidant) materials vs Li allow the spontaneous redox reaction to do the work. This process is called “discharging”,

wherein Li^+ moves from the anode to cathode spontaneously, while at the same time releases e^- [15, 36-39].

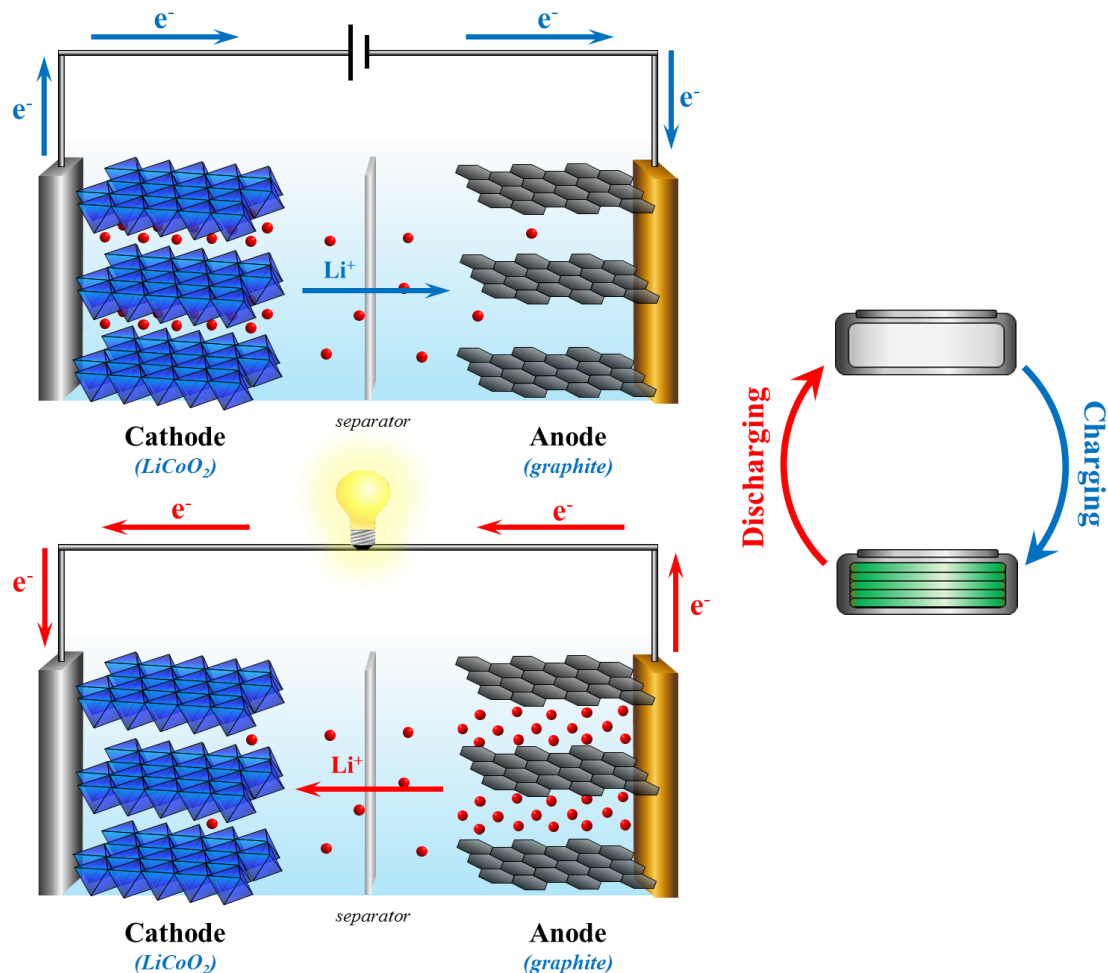


Figure 1.7. Schematic illustration of the conventional LIB indicating the (a) charged and (b) discharged state.

The practical performance of the LIBs are evaluated by the following parameters: specific energy / energy density, specific power / power density, volumetric energy, specific capacity, rate of charge/discharge, cyclability, and safety / abuse tolerance, and working potential. Specific energy (Wh/kg) and energy densities (Wh/L) are correspond to the

gravimetric and volumetric energies respectively, wherein the gravimetric / volumetric specific capacities (Ah/kg / Ah/L) are multiplied by the operating battery voltage (V). Specific power (W/kg) and power density (W/L) corresponds to the gravimetric and volumetric power respectively, which is calculated by multiplying the specific energy / energy densities by scan rate (V/sec) divided by the applied voltage (V) [15, 36-37]. The specific power and power densities can be improved by utilizing nanostructured electrodes with large surface area and short solid-state transport distance [15, 23]. The specific capacity indicated the amount of charge, which is related to the amount e^- and Li^+ , that can be stored reversibly in the electrodes, with respect to the weight of the active material. Cyclability indicates how stable the capacities are during the charge / discharge process before the capacity / energy drops significantly, i.e. 80% of its initial reversible value, and lose the ability to store power. The rate of charge/discharge refers to how fast the battery can be charged and discharged, typically called the C-rate, e.g. at 1 C, the battery can release/store its maximum capacity in 1 hour, 2 C for 30 mins, etc. The cyclability, hence the cycle life of the battery, is greatly affected by the depth of discharge (DOD), state of charge (SOC), operating temperature, rate of charge/discharge, and the type of materials used which is related to the battery chemistry. To enhance the cyclability and the shelf life of the battery, DOD cycles should be shallow, SOC swings should be less, and high operating temperature and rate of charge/discharge should be avoided [4, 15, 36-37].

The typical LIBs used for portable devices such as mobile phones that utilizes carbonaceous

anode can be fully charged after 1-4 hours, however, for EVs, it may take even longer time. To increase the charging time of EVs using a special charging device, it can be charged to a certain low SOC at high rate of charge, i.e. high current/time. Safety is one of the issues underlying LIBs from the dendrite formation to the thermal runaway. Typical battery cells/modules/packs are equipped with battery management systems (BMS) to prevent the thermal runaway by detecting and isolating the problematic cell. Abuse tolerance on the other hand is one of the critical requirement to be addressed before engaging the battery to the end-users, esp. EVs, for safety precautions. Abuse evaluations of the batteries includes mechanical (mechanical shock and drop, roll-over, nail penetration, and immersion in water), thermal (radiant heat, thermal stability, overheat, and extreme cold test), and electrical (short circuit, overcharge, and alternative current exposure) abuse to determine the batteries' tolerance [37]. The working potential or the electrochemical potential varies with the type of material and hence its electronic configuration [15, 40].

On the other hand, the open-circuit voltage, V_{OC} , of the cell as shown in Figure 1.8 and equation (5), is known as the working potential. It is the difference between the electrochemical potentials of the anode (μ_A) and cathode (μ_C) where e is the magnitude of the electronic charge.

$$V_{OC} = (\mu_A - \mu_C)/e \quad [5]$$

The “window” of the electrolyte or the top of the anion-p bands of the cathode limits the open-circuit voltage. The electrolyte window, E_g , is the energy between the lowest unoccupied molecular orbital (LUMO) and the highest occupied molecular orbital (HOMO) of the liquid electrolyte as shown in Figure 1.8 (a), or the energy between the bottom of the conduction band and the top of the valence band of the solid electrolyte as shown in Figure 1.8 (b). The electrode materials should be selected such that μ_A and μ_C lies below the LUMO and above the HOMO of the electrolyte respectively, hence to prevent the electrode-electrolyte reaction. The electrode-electrolyte reaction and thus the formation of the SEI layer occurs when μ_A is above the electrolyte LUMO as shown in Figure 1.8 c, by the reduction of the electrolyte to form the passivating film, SEI layer, at the surface of the anode material, in this case, the Li metal. Likewise, if μ_C is lower than the HOMO of the electrolyte, the electrolyte will be oxidized at the surface of the cathode and thus form an SEI layer. If the formed SEI layer is stable enough, it can act as a barrier to prevent the further degradation of the electrolyte at the surface of the electrode [15, 36]. Normally, SEI layers formed only at the anode since the electrolyte HOMO are normally above μ_C .

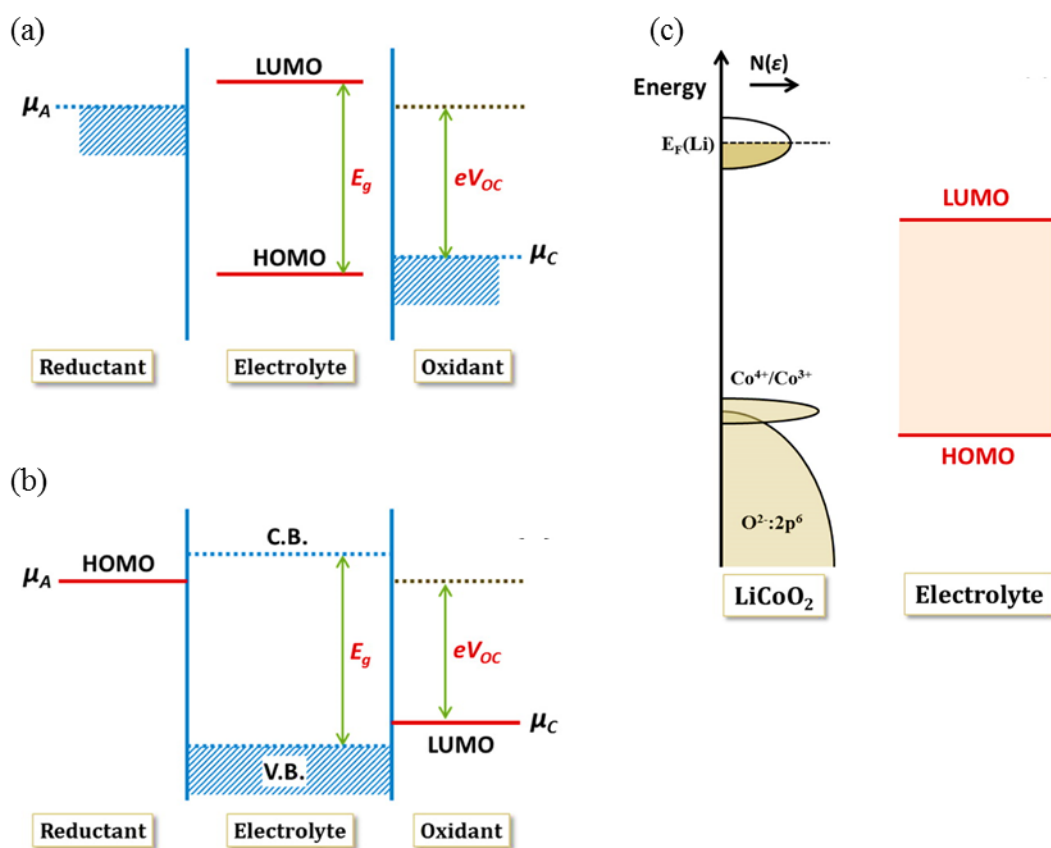


Figure 1.8. Schematic energy diagrams of: (a) liquid electrolyte - solid electrodes and (b) solid electrolyte - fluid electrodes without electrode-electrolyte reaction, and (c) Li (anode) – LiCoO₂ (cathode) electrodes and their relative energy positions with respect to the HOMO-LUMO of the carbonate-based electrolyte as an example of liquid electrolyte - solid electrodes with electrode-electrolyte reaction. Reproduced with permission from ref [36]. Copyright 2013 American Chemical Society.

Aside from electrochemical window of the electrolyte, the achievable voltage of the cathode is also a factor of the p -electron band of anions. However, lowering μ_C , to increase the working voltage, below the top of the anion- p bands, which usually have an energy above

the electrolyte HOMO, i.e. 4.3 eV below μ_A (Li), is not possible. Hence, the LiMO_2 structure is preferable and are commonly used cathode material compared to that of the LiMS_2 structure whose top of O-2p bands and S-3p bands of the layered oxides and sulfides resides ~ 4.0 eV and ~ 2.5 eV below μ_A (Li) respectively. On the other hand, the top of the O-2p bands of the oxide host can be lowered to more than 5 eV below μ_A (Li), by replacing the oxide ion with polyanion, e.g. LiNiPO_4 . However, too high voltage, for high voltage applications, is not preferable for the current organic carbonate electrolytes since it can be decomposed at a $V > 5\text{V}$ and hence should be replaced / substituted. [15, 23, 36, 37, 41]

The internal battery resistance, R_b , to the ionic current, $I_i = I$ varies the both the charge and discharge voltage from the V_{OC} . The discharge voltage, V_{dis} , is reduced by a polarization, $\eta_{dis} = I_{dis}R_b$, while in order to reverse the reaction, the charge voltage, V_{ch} , is increased by an overvoltage, $\eta_{ch} = I_{ch}R_b$ from the V_{OC} as indicated by equations (6) and (7), where q represents the state of charge. [15, 36-37]

$$V_{dis} = V_{OC} - \eta(q, I_{dis}) \quad [6]$$

$$V_{ch} = V_{OC} + \eta(q, I_{ch}) \quad [7]$$

The polarization and overvoltage can be attributed to the observed hysteresis between the charge and discharge curves, and the potential drop between the end of charge and the beginning of the discharge potential as shown in Figure 1.9 a and b.

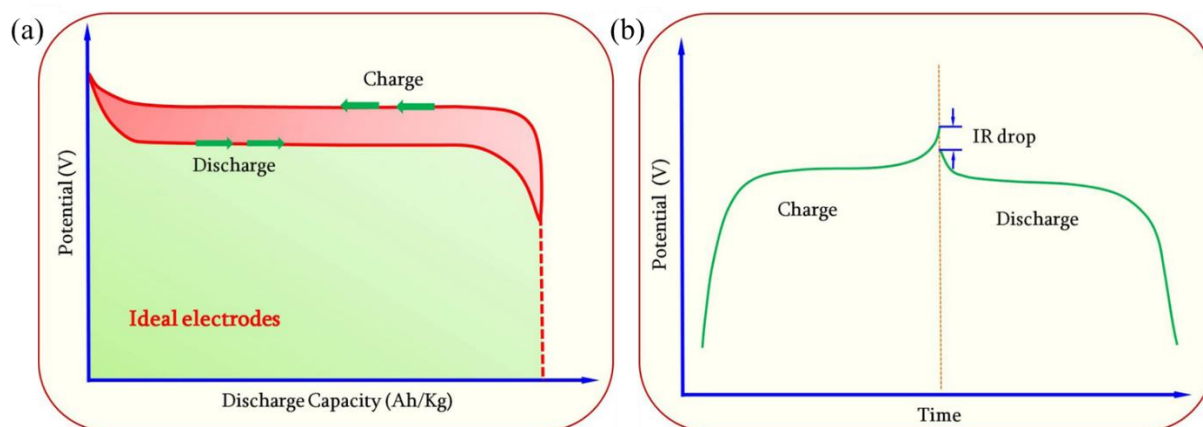
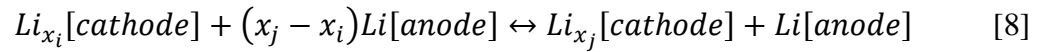


Figure 1.9. Schematic illustration of: (a) charge/discharge potential hysteresis on an ideal insertion electrode material, (b) potential drop at the end of charge and beginning of discharge cycles. Reproduce with permission from [15]. Copyright 2015 Elsevier Ltd.

The general reaction associated with the lithium insertion and extraction during the charge/discharge process is shown in equation (8) where x_i and x_j corresponds to the solubility limits of the intercalation reaction. The electrochemical reaction associated by the release of the stored chemical energy correspond to the change in the Gibbs free energy, equation (9) of the system, where T , P , ΔV_r , ΔS_r , and ΔU_r are the thermodynamic properties corresponding to the temperature, pressure, change in volume, change in the

vibrational and configurational entropies of ion insertion and extraction, and change in the internal energy respectively. The terms $P\Delta V_r$ and $T\Delta S_r$ are of the order of 10^{-5} and 10^{-2} eV respectively, and hence can be assumed negligible. ΔU_r on the other hand, can be approximated as 2-3 eV to evaluate the ΔG_r of the reaction. Since at constant T and P , the chemical potential μ is related with the partial molar quantity of the Gibbs free energy G , the equilibrium cell voltage between the two (2) electrodes can be estimated by using equation (10), where F is the *Faraday* constant [15, 36, 37, 40].



$$\Delta G_r = \Delta H_r - T\Delta S_r = \Delta U_r + P\Delta V_r - T\Delta S_r \quad @ \text{ constant } T \text{ and } P \quad [9]$$

$$V(x) = \frac{-\Delta G}{(x_j - x_i)F} \quad [10]$$

On the other hand, the efficiency of the cell to store energy at a fixed current, $I = dq/dt$, is shown in equation (11), where Q is the total charge per unit weight, i.e. gravimetric capacity (Ah kg⁻¹), or per volume, i.e. volumetric capacity (Ah L⁻¹). Q is dependent of I , where $Q(I)$ refers to the cell capacity per given I , since at high currents, the diffusion of ions across the electrode/electrolyte interface becomes limited. The diffusion-limited loss of the capacity at high current is theoretically reversible without the effect of the irreversible capacity loss due to the change in the electrode volume and electrode-electrolyte reaction [36, 37].

$$\% \text{ efficiency} = 100 \times \frac{\int_0^{Q_{dis}} V_{dis}(q) dq}{\int_0^{Q_{ch}} V_{ch}(q) dq} \quad [11]$$

The reversible diffusion-limited capacity loss was clearly shown on the study by Qin et al, wherein they examine the electrochemical performance of 3D porous graphene networks anchored with 5-30 nm Sn NPs encapsulated with graphene shell of about 1 nm (3D Sn@G-PGNWs) as shown in Figure 1.10 a. The rate and rate cycle performance of the 3D Sn@G-PGNWs up to 10 C were analyzed in the potential window of 0.005 to 3.0 V, and showed a reversible, durable and stable gravimetric capacity at different charge/discharge rates as shown in Figure 1.10 b. The 3D Sn@G-PGNWs is stable enough to combat the large volumetric expansion of Sn (electrode) and the electrode-electrolyte reaction. The formation of the stable solid-electrolyte interface (SEI) on the graphene shell surface on the 1st cycle, that causes the irreversible capacity loss, prevents the direct contact of Sn with the electrolyte and maintain the structural integrity of the Sn@G NPs during the subsequent cycles [42].

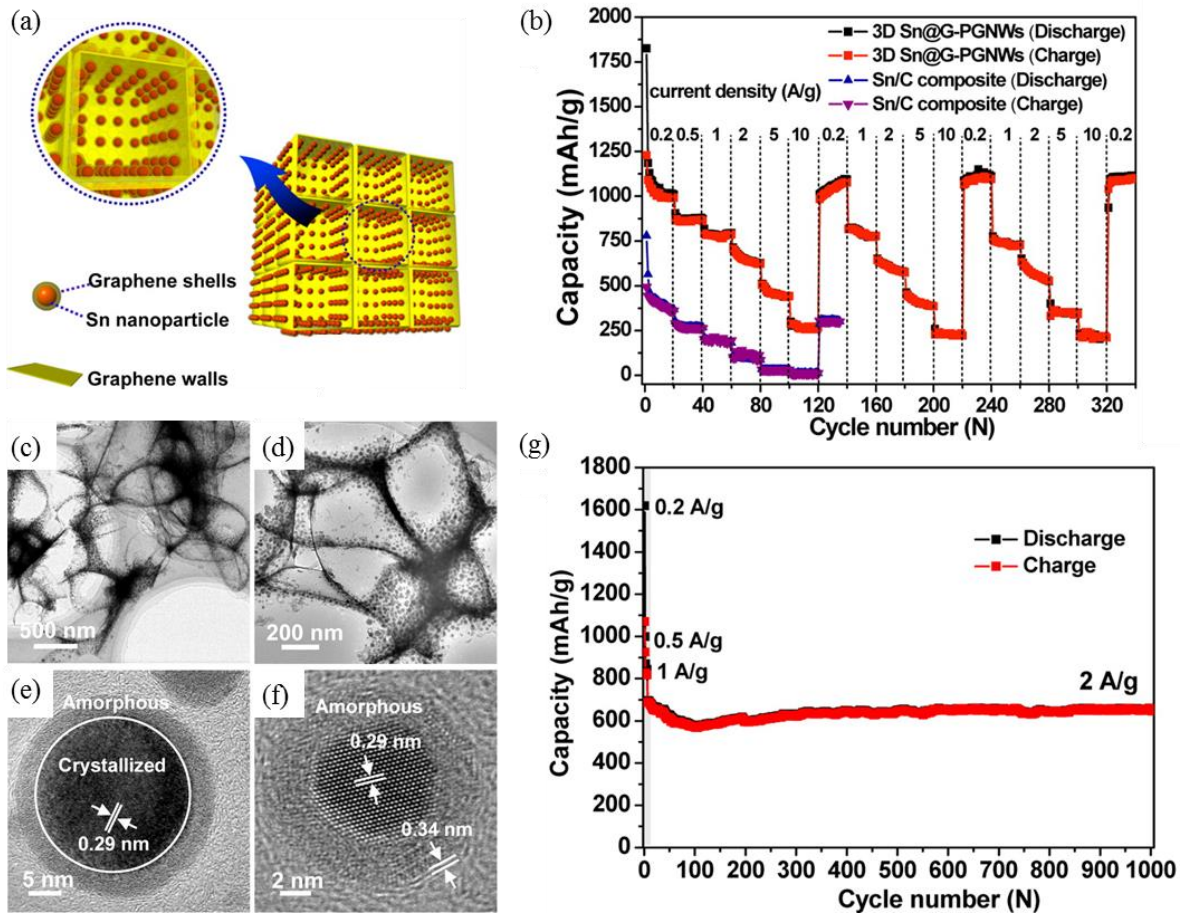


Figure 1.10. (a) schematic illustration of 3D Sn@G-PGNWs, and (b) the rate cycle performance of 3D Sn@G-PGNWs, (c-d) TEM images of the Sn@G-PGNWs, (e-f) HRTEM of Sn@G nanoparticles, and (g) cycle performance of the 3D Sn@G-PGNW electrode at current densities of 0.2, 0.5, and 1 A/g for the initial six cycles and then 2 A/g for the subsequent 1000 cycles. Reproduced with permission from ref [42]. Copyright 2014 American Chemical Society.

The Coulombic efficiency on the other hand of a single cycle corresponds to the capacity fade due to the irreversible capacity lost associated with the SEI formation, degradation of the

electrolyte, and the volumetric change and pulverization of the electrode material. The percent Coulombic efficiency can be calculated as shown in equation (12). [36]

$$\% \text{ Coulombic efficiency} = 100 \times \frac{Q_{dis}}{Q_{ch}} \quad [12]$$

The theoretical specific capacity (gravimetric, Q_{theo} , mAh/g) of an active electrode material can be estimated based on the involved electrochemical reactions with Li^+ and can be estimated as shown in equation (13), where x is the number of electrons associated with the reaction, F is the Faraday's constant equal to 96,485.33289(59) C/mol, n is the number of moles of the electroactive component that reacts/interacts with Li^+ , and M is the molecular weight of the electroactive material. Sample calculation for the specific theoretical capacities of both carbon (anode) and LiCoO_2 (cathode) with reversible chemical reaction with Li^+ are shown in equations (14) and (15) respectively [37].

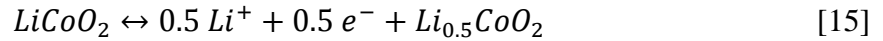
$$Q_{theo} = xF/nM \quad [13]$$



$$Q_{theo, c} = (1) \left(96485.33289 \frac{\text{C}}{\text{mol}} \right) / (6) \left(12.01 \frac{\text{g}}{\text{mol}} \right)$$

$$\text{where: } 3600 \text{ C} = 1 \text{ A h}$$

$$Q_{theo, c} = 371.9332 \text{ mAh/g}$$



$$Q_{theo, LiCoO_2} = (0.5) \left(96485.33289 \frac{C}{mol} \right) / (1) \left(97.87 \frac{g}{mol} \right)$$

$$Q_{theo, LiCoO_2} = 136.924 \text{ mAh/g}$$

The actual specific capacity and hence the energy density of LIBs are always lower than the estimated (calculated), hence one should also consider not only the integration of the electrode materials but also other factors such as binders, conductive enhancers, separators, electrolytes, current collectors, case, tabs, as well as the BMS [37].

1.1.3 Lithium-ion Battery: Future and improvements

Lithium-ion battery is a promising storage device for high energy and high power application such as for EVs and renewable energy storage devices aside from its current application such as portable electronic devices. However, though LIB shows exceptional properties, its applicability in high energy applications are restricted due to its current design and hence further improvements are necessary as shown in Table 1.2.

Table 1.2. LIB component deficiencies and the necessary improvement of the currently produced LIBs. [19, 36, 37]

LIB components	Deficiencies	Possible / necessary improvements
anode (negative electrode) e.g. carbon	low volumetric and gravimetric capacity (Ah/L and Ah/g)	replace carbon with another material with: <ol style="list-style-type: none"> 1. high energy efficiency (coulombic efficiency and voltage efficiency) 2. good power capability 3. low irreversible capacity 4. low cost 5. low to almost no specific capacity and cell voltage loss
anode-electrolyte interface	<ol style="list-style-type: none"> 1. causes low coulombic efficiency of the anode material due to the formation of SEI layer 2. causes cell impedance 	<ol style="list-style-type: none"> 1. coatings and functional binders on the anode material should be improved to protect the surface during large volume changes 2. electrolyte additives to improve the quality of the SEI layer 3. use nanostructured material to increase the surface area and hence the Li⁺ diffusion 4. use particles with specific surface crystallographic plane that can direct the type of SEI compound formed
separator	conductive particles and lithium dendrites can penetrate and hence causes short circuit	improve the coatings of the separator to improve the penetration of ion (Li ⁺) flux, salt diffusion, and fluid flow, and hinders or can chemically bind with Li dendrites

LIB components	Deficiencies	Possible / necessary improvements
cathode-electrolyte interface	<ol style="list-style-type: none"> limits the operating voltage due to the degradation of the carbonaceous electrolyte at $V > 5V$ causes low coulombic efficiency of the anode material due to the formation of CEI (cathode-electrolyte interface) layer 	<ol style="list-style-type: none"> Change the electrolyte used to a material/solution that will not disintegrate at high voltage coatings and functional binders on the anode material should be improved to protect the surface during large volume changes electrolyte additives to improve the quality of the SEI layer
cathode (positive electrode) e.g. lithiated transition metal oxide or phosphate	<ol style="list-style-type: none"> low volumetric and gravimetric capacity (Ah/L and Ah/g) limited charging voltage 	replace lithiated transition metal oxide or phosphate with another material with: <ol style="list-style-type: none"> high energy efficiency (coulombic efficiency and voltage efficiency) good power capability low irreversible capacity low cost low to almost no specific capacity and cell voltage loss high charging voltage \rightarrow replacing oxide with a polyanion
metal collectors e.g. Cu and Al foil	<ol style="list-style-type: none"> add additional cost and weight (should be thick enough to provide adequate electrical and thermal conductivity) 	<ol style="list-style-type: none"> Use perforated or expanded metal collectors which are normally for primary lithium battery and secondary aqueous battery

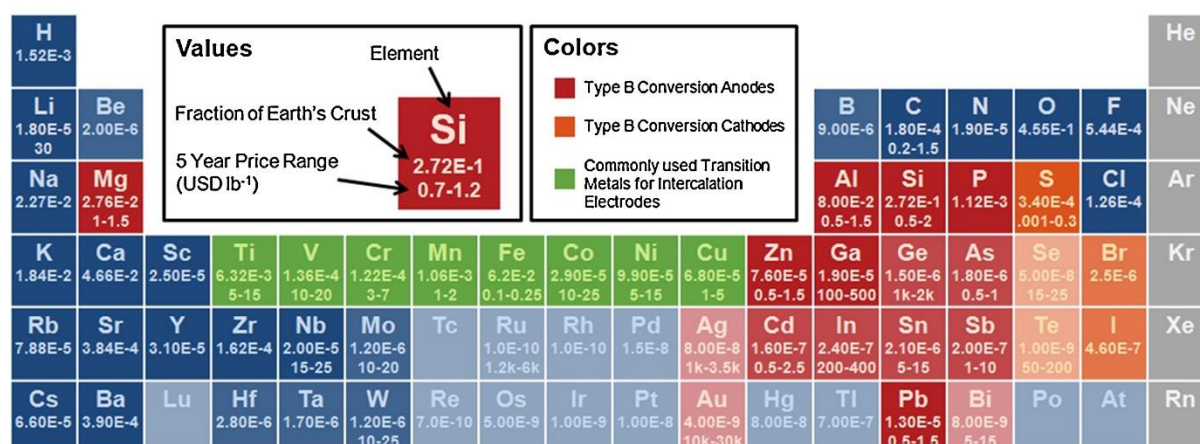
1.2 Anode material for LIB

The anode is responsible to store majority if not all of the Li^+ that migrated from the cathode to store the charge during the charging process. The anode material should be capable of storing a large amount of Li^+ to have high specific energy. However, incorporating large amount of Li^+ into the anode structure can result to a large volumetric change and hence the energy efficiency (EE) of the selected material should also be considered. The EE is greatly affected by Coulombic efficiency (CE) and voltage efficiency (VE). Both VE and CE depends on the following: (a) electrode material's property (e.g. specific surface area, particle size, porosity, coating thickness, etc.) and coating formulation (e.g. mass loading, amount of conductive carbon, etc.) that influences the formed of SEI layer and hence the resistance during cycling, (b) electrode material's mechanical stability (e.g. aging effect, type of formed SEI layer, structure or phase change, and cracking/pulverization) upon subsequent charge/discharge cycle, (c) electrode material's ability to store Li^+ (e.g. intercalate, alloying, and conversion type), and (d) operating conditions (e.g. temperature, voltage range, and charge/discharge rate) [19]. Hence, a mechanically stable with good capacity and cyclability anode material should be considered, as well as the cost and abundance of the material on the earth's crust.

The relative commodity price of each element and its abundance, as indicated by the fraction of the earth's crust, is shown in Figure 1.11 a. This table clearly illustrates how one type of material can greatly affect the price of the produced battery, e.g. Mn is cheaper than Co, and hence the produced battery utilizing the said materials. On the other hand, the abundance of each elements indicates if the said materials will become limited or scarce in the long run/future, though the actual availability still depends on the supply and demand of the material. Among the different conversion type anode materials that can be use, as indicated by the red color, Si is the most abundant and has the lowest price [43]. Though the process and the cost it takes to produce the pure compound should also be considered. On the other hand, Figure 1.11 b shows the different gravimetric and volumetric theoretical capacities of element that has been examine as electrode material. Among these materials, as expected, using Li^+ as anode material yield to the highest gravimetric and volumetric capacities. However, utilizing Li as anode material is undesirable due to the formation of dendrites that causes short circuit which in turn overheat and ignite [7-14]. Among the other elements, Si is comparable with that of lithium in terms of both gravimetric and volumetric capacities. P resides next to Si, though due to safety issues such as toxicity, and flammability upon in contact with air [44] restricts its applicability. Ge and In also have promising gravimetric and volumetric capacities, however, both are known to be expensive and hence undesirable [15]. On the other hand, Sn has lower gravimetric capacity compared to Si, P, Ge, and In, but with comparable volumetric capacity.

The lower gravimetric capacity of Sn, a heavy metal, can be attributed to its high molecular weight. Since its volumetric capacity is comparable with other metals, Sn is one of the promising anode material for high power density and energy density applications such as portable devices, EVs, and other small device applications [4].

(a) Availability



(b) Charge Capacity

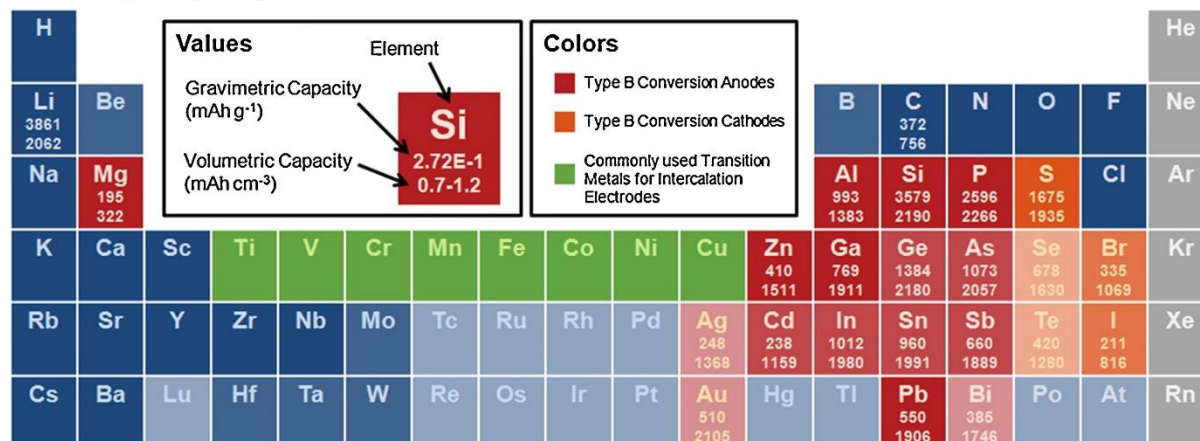


Figure 1.11. (a) The availability/abundance as a fraction of the earth's crust and the commodity price (USD/lb) of different elements, and the (b) calculated gravimetric and volumetric capacities of selected elements. Reproduce with permission from [43]. Copyright 2014 Elsevier Ltd.

Anode material is not only limited to a single element or metal, and hence metal oxides and distinct types of ceramic compounds have also been considered, e.g. SnO_2 , $\text{Li}_4\text{Ti}_5\text{O}_{12}$, Fe_2O_3 , etc. Experimental gravimetric and volumetric capacities of some these compounds are shown in Figure 1.12 a. Though Si still has the highest gravimetric capacity next to that of Li, several ceramic compounds such as ZnMn_2O_4 , SnO_2 , MnO , Fe_2O_3 , and CuO show promising and much higher experimental volumetric capacity than that of Li and hence Si. The rate capability of these compounds are shown in Figure 1.12 b, wherein the black arrow corresponds to the approximated rate of 1C [45]. It can be observed that the relative capacity decreases as the rate of charge/discharge increases, and hence was attributed to the reversible diffusion-limited capacity loss [36]. Even though Si and P have higher theoretical capacity than that of Sn, Sn has better relative capacity at approximately 1C rate of charge/discharge. On the other hand, some oxide and ceramic type compounds, vis. $\text{Li}_4\text{Ti}_5\text{O}_{12}$ and anatase, have better rate capability than the others. Though oxides and ceramic type compounds have low electronic and ionic conductivity, and thus requires high amount of conductive carbon to compensate for the low electronic conductivity, some groups show enhanced rate stability if the material is in the form of composites [45-48]. It is also evident in Figure 1.12 that some material have higher and better Li^+ storage and rate capabilities than the other and hence can be attributed to other factor, vis. how the material can store the Li^+ .

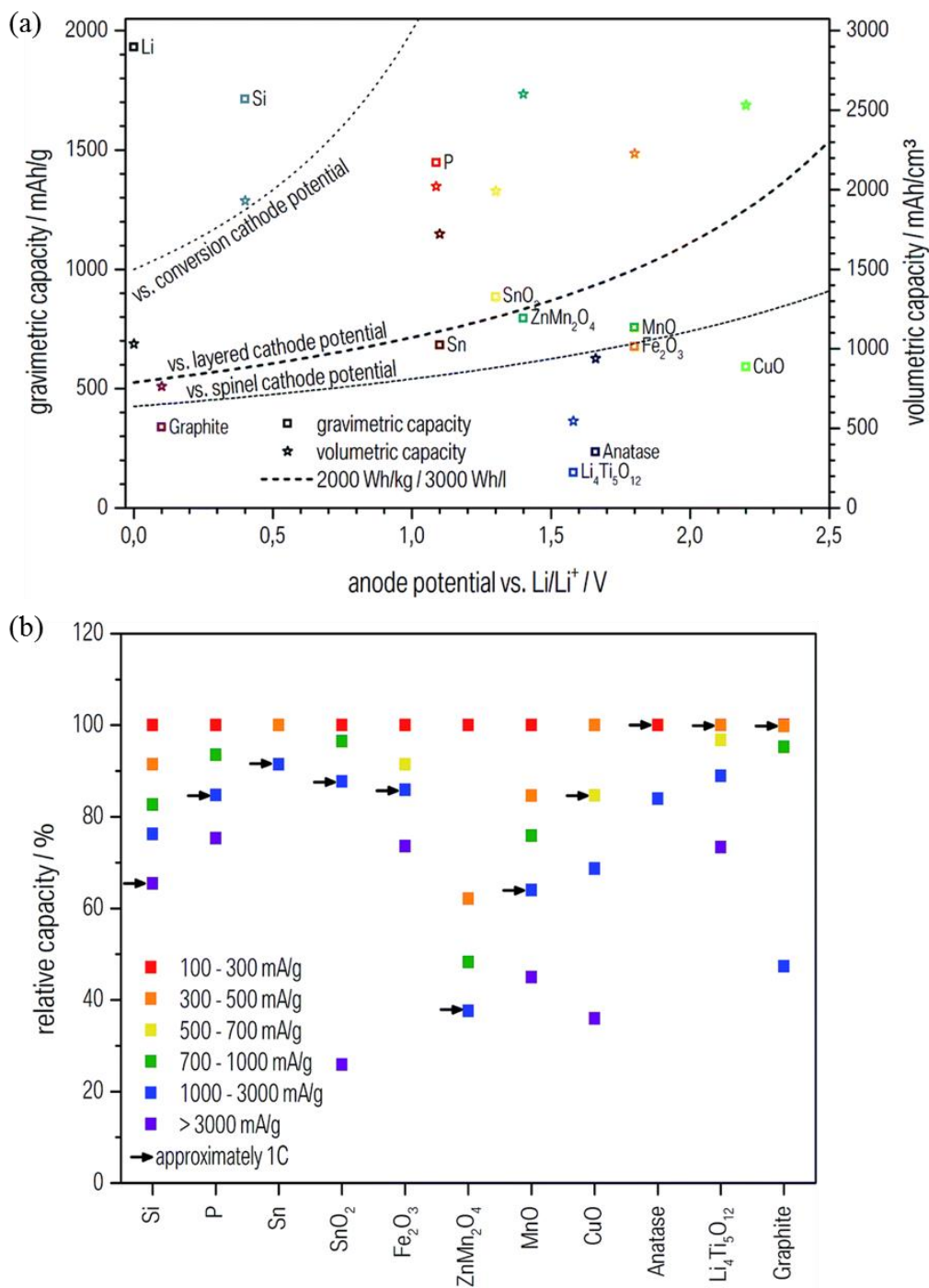


Figure 1.12. (a) Experimental gravimetric (square) and volumetric (star) capacities of different compounds vs their half-cell potentials, (b) rate capability of different compounds. Reproduce with permission from [45]. Copyright 2017 The Royal Society of Chemistry.

The anode materials can be classified in three (3) groups depending on how it stores Li^+ , such as intercalating, alloying, and conversion type of material as shown in Figure 1.13 and 1.14. Intercalating materials, as the term implies, stores Li^+ through insertion in between the layers of the material, e.g. graphene and titanium oxides as shown in Figure 1.13 and Figure 1.14 a and b. The materials also experience minimal structural change, wherein the increase in the inter-layer distance or in-plane movement were kept within a limit of below 25%, e.g. graphene experience only 10% expansion whereas $\text{Li}_4\text{Ti}_5\text{O}_{12}$ has smaller cell volume than its delithiated counterpart [43, 45, 49-51]. Intercalation materials also have an advantage of having small voltage hysteresis, i.e. the difference between lithiation and delithiation potential as shown in Figure 1.13 and Figure 1.14 e [15, 36, 45, 52]. However, since Li^+ can only insert in-between planes, intercalating compounds can only accommodate few amount of Li^+ per host atom and hence, have low gravimetric ($< 500 \text{ mA h g}^{-1}$) and volumetric ($< 1500 \text{ mA h cm}^{-3}$) capacities.

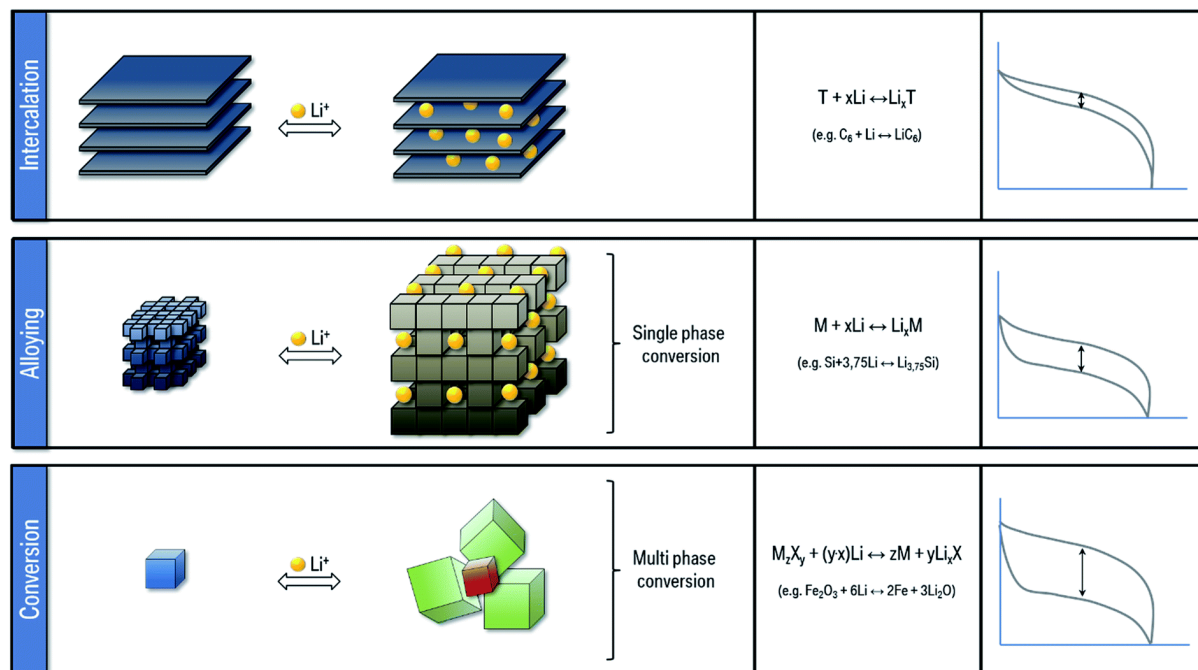


Figure 1.13. Schematic illustration of how different types of electrode materials stores Li^+ .

Reproduce with permission from [45]. Copyright 2017 The Royal Society of Chemistry.

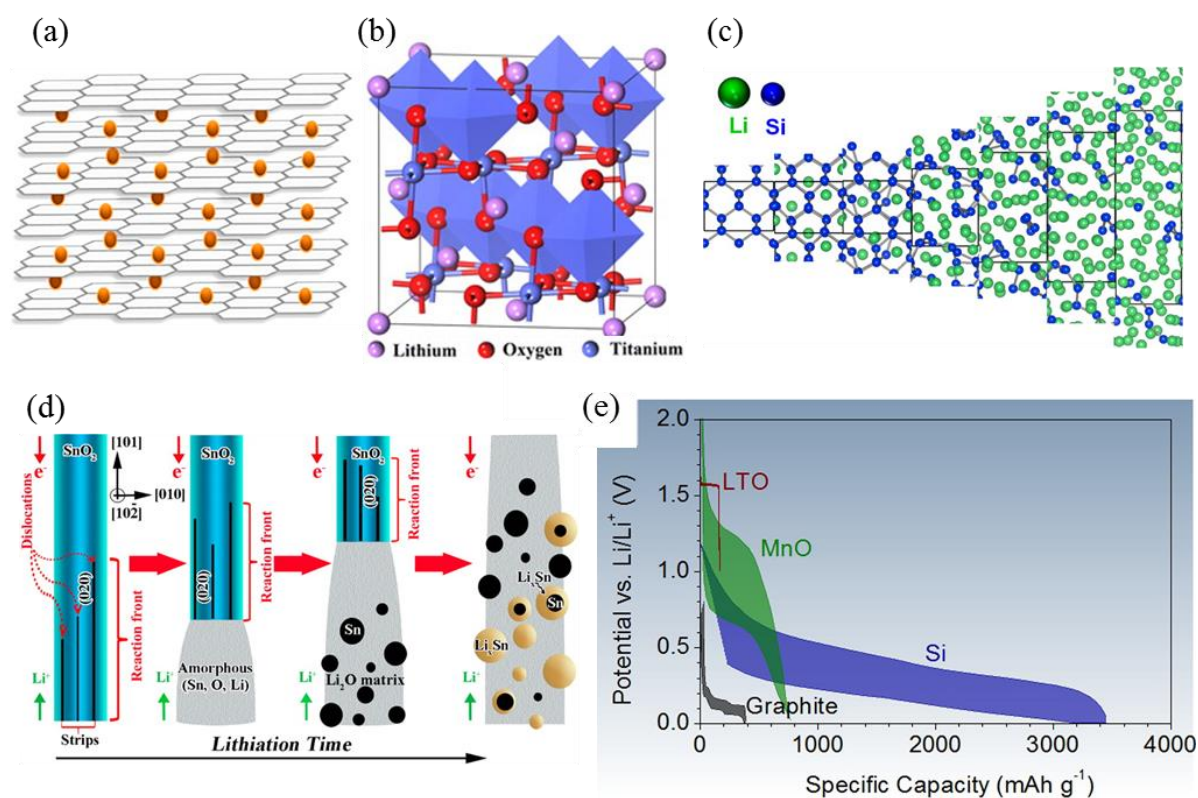


Figure 1.14. Crystal structure of materials that schematically illustration how Li⁺ was stored by: (a) intercalation (graphite). Reproduce with permission from [50] Copyright 2014 American Chemical Society; (b) intercalation (Li₄Ti₅O₁₂). Reproduce with permission from [51] Copyright 2016 American Chemical Society, (c) alloying (Silicon). Reproduce with permission from [53] Copyright 2012 American Chemical Society, (d) conversion (SnO₂). Reproduce with permission from [52] Copyright 2013 American Chemical Society, and (e) sample voltage hysteresis of different compounds. Reproduce with permission from [43] Copyright 2014 Elsevier Ltd.

Graphite is widely known as the most common and commercially produced anode material, due to its numerous advantage: (a) graphite, a semi-metal, has high electrical conductivity, i.e. $10^{-3} \text{ S cm}^{-1}$, (b) between C and LiC_6 the theoretical capacity is 372 mAh g^{-1} , (c) LiC_6 , a metal, has high ionic conductivity, i.e. $10^{-3} \text{ S cm}^{-1}$, and (d) the potential of carbon with respect to Li metal is only 0.15 - 0.25 V. Low potential range can indicate that there is a room to increase the operating voltage of the battery [26, 33, 45, 50]. It has a lamellar structure, wherein van der Waals forces act between its planes. Since this force is weak, different molecules, ions, or atoms can penetrate between its planes under certain conditions, and thus increasing the c-axis forming the graphite intercalated compound (GIC) [33]. However, when Li^+ intercalates, there is a weak coulombic interaction between the lithium guest layer (Li^+) and the negative charge distributed along the graphene layers (C_n^-), hence a space to accommodate large solvent molecules is still available [50, 54-55]. Due to the promising properties of carbonaceous compounds, other carbon-based materials, e.g. hard carbon, soft carbon, graphene, carbon nanotubes (CNTs), fullerene, etc., are also being studied and considered, though the theoretical capacities of the said compounds are still unavailable [45]. Among these compounds, graphene is expected to have a promising property. The reaction mechanism is similar to that of graphite, wherein six (6) C atoms can store one (1) Li^+ on both sides of a single graphene layer, and thus, the theoretical capacity is expected to be around 740 mA h g^{-1} (almost twice of that of graphite). However, single graphene layer is hard to stabilize

and hence, most reported graphene are stack of two (2) or more layers, that resulted a much lower capacity. Graphene and CNTs also has low packing density that makes it difficult to prepare and hence unsuitable for high energy and power density applications compare to that of graphite. [45, 50, 54, 56-57].

Another type of Li^+ storage is the conversion type of materials as shown in Figure 1.13 and 1.14. As the word implies, it converts the material from one compound to the other upon lithiation. Conversion type material stores large amount of lithium into their crystal structure and hence undergo structural changes that can in some cases completely rearrange all the atoms. This phenomenon is evident in the large voltage hysteresis of this type of materials, though others are much larger than the others, e.g. Si vs MnO in Figure 1.14 e. The difference can be associated to the degree of conversion and hence the type of compound. Conversion type of material can further be classified into two (2) namely the single- and multi-phase materials which are designated as alloying and conversion type materials respectively on the succeeding paragraphs. Alloying, due to its single phase conversion has smaller voltage hysteresis compared to that of the conversion type (multi-phase) materials. Lithium on the otherhand, is considered as alloying type of material since it has a single-phase before and after lithiation, and it has large volumetric change. Though the actual volume increase strongly depends on the amount of extra lithium used [45].

1.2.1 Alloying material as anode material for LIBs

Alloying materials are characterized as materials that has single-phase compound before and after lithiation and hence conversion reaction, and can accommodate large amount of Li^+ by forming a metallic bond. Most alloying materials are metals and semi-metals under group 13 (IIIa), 14 (IVa), and 15 (Va) of the periodic table. These metals and semi-metals forms an intermetallic or Zintl-phases with Li^+ [45, 58-60]. Elements under the same group, has almost equal number of reacting Li atoms per host atom, e.g. group 14 (IV a) elements, vis. Si, Ge, and Sn, can all store 4.4 Li^+ (Li_{22}M_5 , where M = Si, Ge, Sn). However, under the same group, from top to bottom, the atomic weight increases, so as the molar volume and the delithiation potential [45] The increase in the atomic weight with constant amount of stored Li^+ explains the difference in the gravimetric capacities and the comparable volumetric capacities of elements under the same group. As an example, group 14 (IVa) elements, vis. Si, Ge, and Sn, have 4200 mA h g^{-1} (9786 mA h cm^{-3}), 1625 mA h g^{-1} (8645 mA h cm^{-3}), and 994 mA h g^{-1} (7216 mA h cm^{-3}) gravimetric (volumetric) capacities respectively [43, 45, 61].

The most common alloying compounds fall under group 14 (IVa) of the periodic table, vis. Si, Ge, and Sn. Among it advantages are high volumetric and gravimetric capacities for high specific energy and energy density applications. These elements also has high average delithiation voltage, i.e. 0.4, 0.5, and 0.6 V vs Li/Li^+ , than that of commercial graphite, i.e. 0.05

V vs Li/Li⁺, where Li⁺ dendrites can easily form at high current density. Having a high average delithiation voltage indicates that the cut-off voltage can be increased to prevent the formation of Li dendrites and hence improve LIB safety [61-64]. These alloying elements are also known to have relative low delithiation voltage compared to that of the less strain and more stable anode material, vis. Li₄Ti₅O₁₂, resulting to a high working voltage and energy density [15, 61, 65]. However promising as it is, the large accommodation of Li⁺ also correspond to a large volumetric expansion, e.i. 420, 370, 260 % for Si, Ge, and Sn respectively. This large volumetric expansion results to the cracking and pulverization of the anode material and hence led to poor cyclability and rapid capacity loss during charge/discharge cycle. To address this issue, several studies were conducted such as carbon coating, alloying with electroactive metals, and varying the morphology. Since carbon is known to have be safe and have stable capacity, coating / encapsulating the alloying elements with carbon can help buffer the large volumetric change associated with lithiation. Qin, et. al., successfully coat Sn NPs with graphene and further encapsulate it inside the graphene matrix by a simple CVD process as shown in Figure 1.10 a, c-f. Based on their electrochemical test as shwon in Figure 1.10 b, g, the 3D Sn@G-PGNWs have a remarkable electrochemical performance due to the encapsulation of Sn with graphene shell that buffer large volumetric change and the graphene wall that prevents the direct contact of Sn with the electrolyte that can cause the further electrolyte decomposition [42]. Lu et. al. on the other hand, compare Si NPs that are coated

with C shell (impregnation coating) and that of encapsulating Si NPs into a carbon matrix that leave internal void space of Si for volume expansion (non-filling coating) as shown in Figure 1.15. Based on their result, non-filling coating has better integrity and electrochemical performance since the carbon coating hinders the electrolyte penetration and minimize the electrode-electrolyte contact area while retaining the internal pore space for Si expansion [66]. However, incorporating C also adds up to the capacity of the anode material and hence several studies did not account the amount of carbon to the declared capacity [45]. On the other hand, aside from incorporating C into the active material, varying the morphology also possesses several advantages and hence can mitigate the large volumetric change associated with the alloying type anode materials. The effect of variation in the morphology will be further discuss in the succeeding paragraphs.

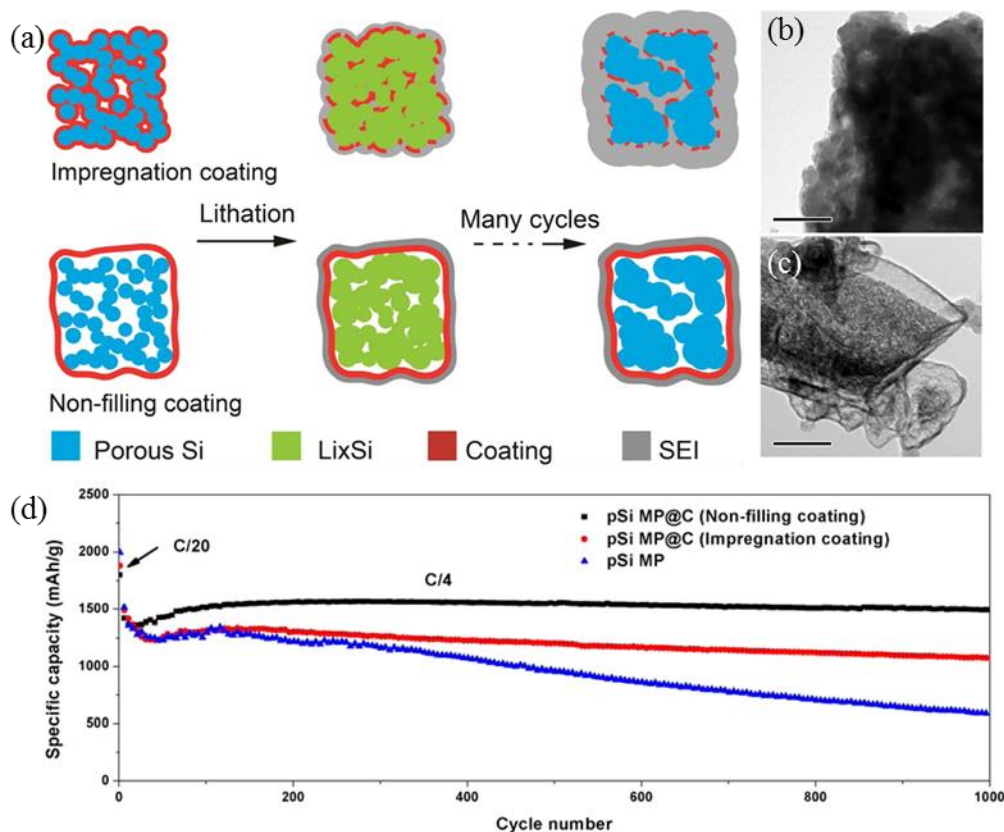
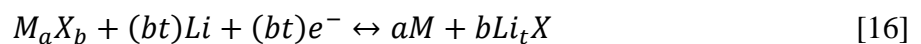


Figure 1.15. (a) Schematic illustration of the coating design on mesoporous Si microparticles (pSiMPs) and the structure evolution during the charge/discharge cycles, TEM images of (b) impregnating C-coating and (c) non-filling C-coating, and (d) initial 1000 galvanostatic cycles of the pSiMPs with different coatings. Reproduce from [66]. Copyright 2015 American Chemical Society.

1.2.2 Conversion material as anode material for LIBs

Multi-phase conversion type anode material, also known as conversion type, reacts with lithium according to equation (16), where M is a transition metal, X is anion such as O, P,

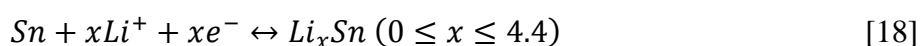
N, etc., and t is the formal oxidation state of X . These materials exhibit a theoretical capacity ranging from 650 to 1000 mA h g⁻¹, which is still much higher than the theoretical capacity of the commercially produced graphite, though less than that of the alloying type materials. The high-capacity of conversion type of anode material can be attributed to both the ability to transfer more than 1 e⁻ per metal atom, wherein oxides can typically exchange 2-3 electrons, during the redox reaction. However, compare to the alloying compounds, conversion compounds have lower gravimetric capacities, but with higher volumetric capacities and smaller volumetric change. [45, 67-68].



Conversion type anode materials are known to have average delithiation (operating) voltage in the range of 1-2.2 V, that are much higher than those of intercalating and alloying type of anode material. Though it possesses several advantages, the following disadvantage should be addressed and considered: (a) high band gaps that results to high insulative property and hence causes poor electronic conductivity, (b) poor ionic conductivities, (c) high voltage hysteresis between lithiation and delithiation, (d) poor cyclability due to both complete structural reorganization and volumetric expansion during lithiation/delithiation cycle, (e) low 1st cycle

coulombic efficiency, and (f) has evolving voltage-capacity curves upon successive charge-discharge process due to the evolving shape and compounds formed [45, 58, 69].

SnO₂ is one of the conversion materials that attracted much attention due to its comparatively low operating voltage with theoretical capacity of 782 mA h g⁻¹ [45, 70]. The total uptake of Li⁺ is 8.4, i.e. 4 from the conversion reaction with oxygen and 4.4 from the alloying with Sn as shown in equation [17] and [18] respectively. Although classified as conversion type of material, equation [17] is irreversible and hence only the active Sn particles is in-charge of the capacity. The very high irreversible initial capacity of more than 2100 mA h g⁻¹ that can be obtained at 100 mA g⁻¹ can be attributed to the large initial Li⁺ uptake due to the formation of Li₂O matrix [45].



The formation of the irreversible Li₂O matrix was verified by Nie et al. [71] in Figure 1.14 d and Huang et al. [72] in Figure 1.16. The schematic illustration (Figure 1.14 d) of the lithiation of SnO₂ based on the atomic-scale observation indicates that during lithiation, Sn NPs that are embedded in the Li₂O matrix is responsible for the reversible Li⁺ uptake [71]. This

phenomenon was also observed by Huang et al. (Figure 1.16) in their in-situ analysis of the electrochemical lithiation of SnO₂. They observed that during lithiation of a single crystal SnO₂ NW, the reaction front was indicated by the dislocation cloud, while the lithiated part is composed of amorphous Li₂O matrix containing Sn and Li_xSn compound, vis. Li₁₃Sn₅ based on their EDP analysis. The formation of Sn embedded in Li₂O matrix were clearly shown in Figure 1.16 F.

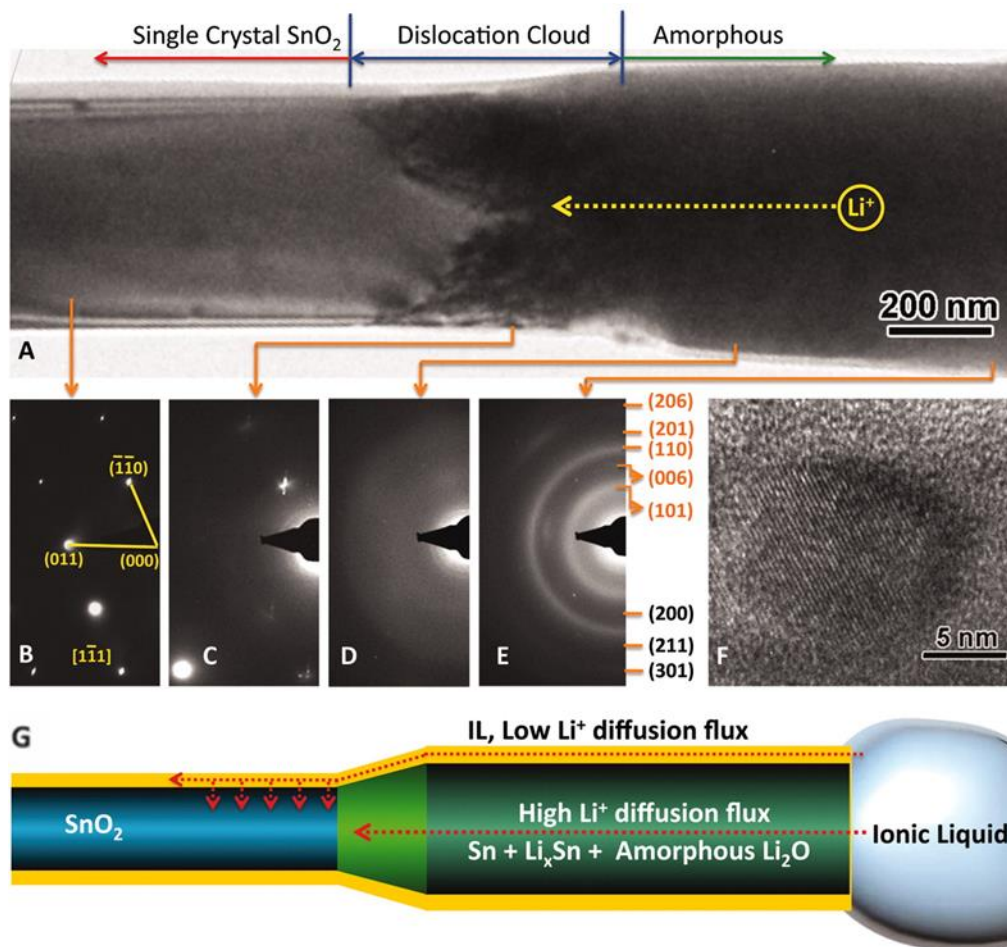


Figure 1.16. (a) TEM image of the SnO₂ NW indicating the reaction front, i.e. dislocation cloud, which separates the lithiated and the unreacted SnO₂ part, (b-e) EDPs of the different sections of the SnO₂ NW, (f) HRTEM image of the lithiated part showing the Sn NPs dispersed in an amorphous matrix, and (g) schematic illustration of Li⁺ diffusion flux from ionic liquid to the SnO₂ NW. Reproduce from [72]. Copyright 2010 American Association for the Advancement of Science.

1.2.3 Size and morphology of the anode material for LIB: 1-D nanostructured

The crystal structure, physical properties (e.g. specific capacity, electrical conductivity, mechanical stability, etc.) and chemical properties (e.g. intercalation, reversibility, reactivity, etc.) are among the several factors that are being considered in selecting the type of electrode material. However, the performance of the electrode does not only depend on the innate property of the material but also on the size and shape (morphology) of the material being used. The morphology and the crystallinity of the material can greatly influence the electrochemical property, e.g. rate of lithiation-delithiation, capacity, and cyclability, due to the effect of both the structure and the exposed surface crystallographic planes that interact with the electrolyte. The rate of the lithiation and delithiation strongly depend upon the Li^+ diffusivity and e^- flow in the material [73-74]. The Li^+ diffusion in a material depends on both diffusion coefficient and diffusion length and hence the diffusion time is represented by equation [19].

$$\tau = L_{\text{Li}^+}^2 / D_{\text{Li}^+} \quad [19]$$

Where L_{Li^+} is the diffusion length and D_{Li^+} is the diffusion coefficient. The D_{Li^+} depends merely on the nature of the material while L_{Li^+} depends on the size of the material [73, 75], hence the smaller the material the easier and the lesser time it takes for Li^+ to diffuse. An example of which is rutile TiO_2 which is known to have a very low to almost negligible Li^+ diffusion

coefficient ($10^{-15} \text{ cm}^2 \text{ s}^{-1}$) at room temperature. However, based on the work conducted by Hu et al., when rutile TiO_2 size was decreased to 5-15 nm, it can accommodate ~ 0.7 Li per rutile TiO_2 , i.e. there is a full loading of lithium (Li_xTiO_2 , $x < 1$), even in subsequent lithiation-delithiation cycles [73, 76-77]. The higher the amount of Li^+ a sample can accommodate, means higher specific capacity. In the study conducted by Cheng et al., they found that using NiO nanoparticles can deliver more energy than that of the sub-micron particles [78]. On the other hand, miniaturization of the electrode material also means having a larger surface to volume ratio and thus larger electrode-electrolyte interface that allows higher charge-discharge rate [73, 79-81]. Wang et al., compared different morphologies of CuO NPs. They reported that leaf-like CuO and oatmeal-like CuO NPs have good initial capacities, i.e. 536.8 and 637.7 mA h g^{-1} respectively due to the ease of Li^+ diffusion associated with large CuO-electrolyte surface area compared to that of CuO hollow spheres with 467.7 mA h g^{-1} initial capacity. However, the decrease in the capacities after 55 cycles to ~ 500 and $\sim 260 \text{ mA h g}^{-1}$ of leaf-like CuO and oatmeal-like CuO NPs respectively is associated with the ineffective buffering of large volumetric change upon charge-discharge cycles [82]. Small spherical NPs are also known to have large surface area to volume ratio that leads to the larger electrode-electrolyte contact area. Though large electrode-electrolyte contact area accommodates large Li^+ flux [83], it also triggers the secondary reaction involving electrolyte decomposition and the formation of the SEI layer. The formation of SEI film in the graphite anode is undesirable since it inhibits

graphite exfoliation, and irreversibly consumes Li^+ supplied by the cathode that results to capacity loss and thus low coulombic efficiency [82, 84]. Though SEI is known to be formed due to the decomposition of the electrolyte and the consumption of Li^+ , it can either be detrimental or beneficial to the anode material depending on the type and structure formed [85].

In general, the smaller the material the faster the Li^+ can diffuse. However, its applicability in electrode material is a different story. Aside from the formation of SEI layer, using smaller material, vis. 0-D, limits its performance due to: (a) hindering or slowing down Li^+ diffusion and e^- transfer due to Li^+/e^- random walk in the electrode material as shown in Figure 1.17, (b) cracking and pulverization due to large volumetric expansion leading to poor cyclability and battery life [86], (c) reducing electrical conductivity due to loose contacts and/or voids in-between particles [73], and (d) having higher electrode-electrolyte surface area that yields to secondary reaction involving electrolyte decomposition and formation of SEI layer that irreversibly consumes Li^+ [73].

Using bare or carbon coated 0-D particles, the Li^+/e^- can move along the grain boundaries, recombination site, and/or particle-particle interface, or through the carbon binders or coatings respectively, leading to poor ionic and electronic transport, thus limiting the electron collection efficiency in the current collector [73, 74].

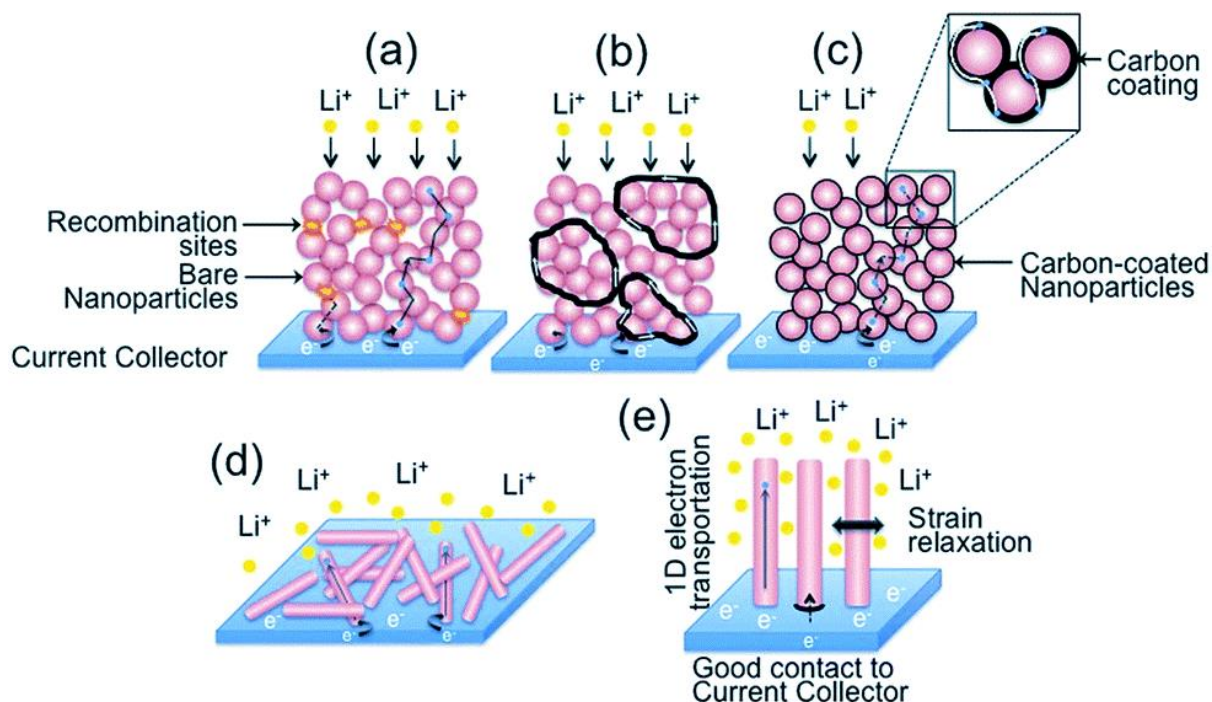


Figure 1.17. Schematic diagrams of Li^+ and e^- transport on 0-D (a-c) and 1-D (d-e) NPs.

Reproduce with permission from [73]. Copyright 2015 The Royal Society of Chemistry.

0-D NPs, or spherical NPs, are the easiest morphology to produce and are known to be the most stable structure among materials since it has the lowest particle total surface energy [87], and thus several studies have been conducted as its applicability as anode material in LIB. However, it was found that using spherical NPs, there is a poor cyclability due to the cracking and pulverization of the NPs upon successive charge and discharge cycles. Based on the study conducted by Wang et al. on the pulverization of β -Sn upon successive charge and discharge cycles, they found that cracks already occur on micrometer-sized β -Sn spherical particles after lithiation and then pulverizes after delithiation. On the other hand, as shown in Figure 1.18, a

particle with nanometer size that is >50 nm does not crack after the first delithiation but still pulverizes after delithiation. While particles with less than 50 nm, does not crack nor pulverizes as it is, it tends to aggregate to form larger particles upon successive charge and discharge cycles. These large particles will soon crack/pulverize in the succeeding cycles. The formation of cracks and pulverization of the particles are due to the large volumetric change, i.e. $\sim 250\%$ for β -Sn, experienced by the particles during the charge-discharge cycles [86].

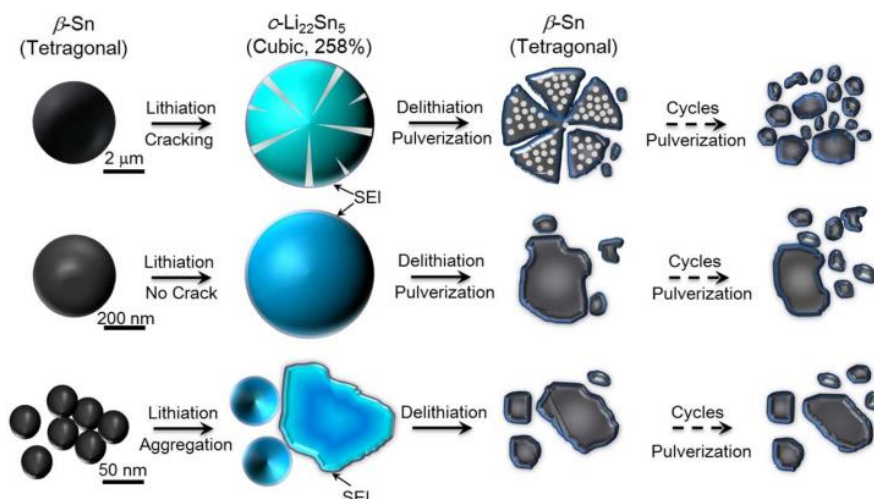


Figure 1.18. Schematic illustration of the pulverization and the aggregation of β -Sn NPs with respect to particle size. Reproduce with permission from [86]. Copyright 2014 The Electrochemical Society.

To mitigate the problems associated with spherical NPs, 0-D, one promising approach is to vary the morphology, i.e. using a 1-D structure such as nanorods (NRs), nanowires (NWs), nanofibers, and nanotubes (NTs). As schematically illustrated by Song et al. as shown in Figure

1.19, using 1-D NPs have several advantages over other morphologies such as: (a) short Li^+ diffusion length due to its nanometer sized dimensions, especially in radial direction, (b) large Li^+ flux that reduces the charge-discharge rate due to large surface area to volume ratio, (c) direct e^- transfer due to its 1-D geometry, (d) can buffer large volumetric change by facilitating strain relaxation due to the effect of its small sized diameter, and (e) morphological advantage in *in-situ* electrochemical probing where the structural change as well the degradation of the material can be observed [61, 83, 85, 88-101].

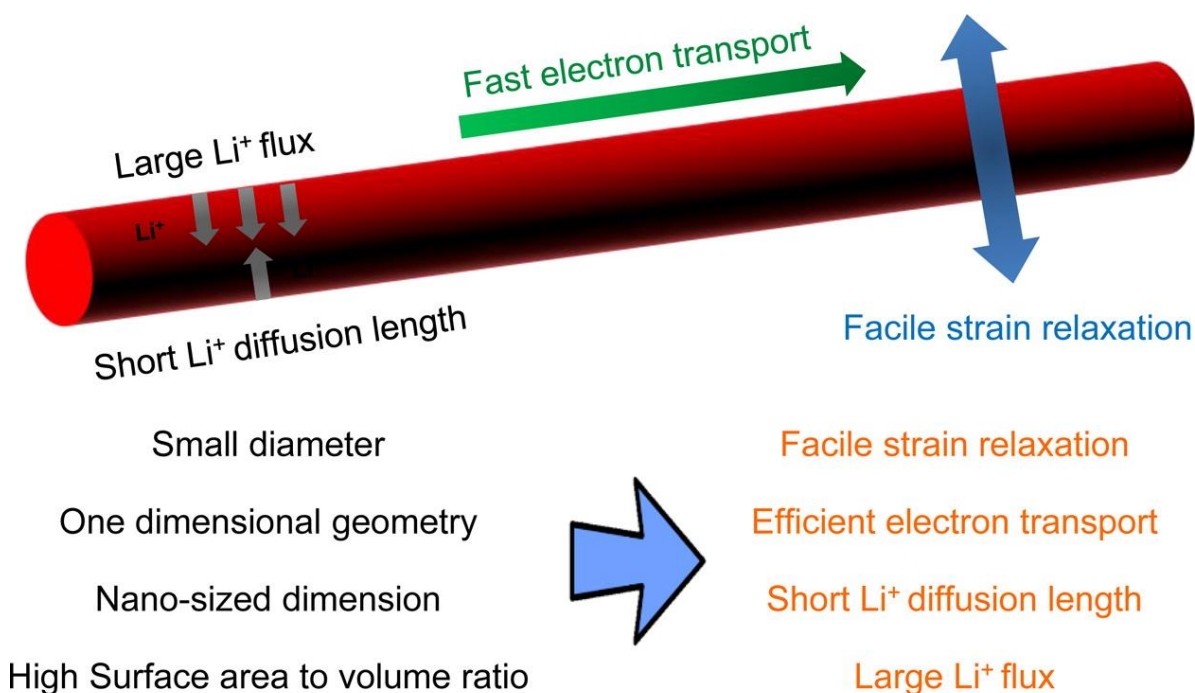


Figure 1.19. Schematic illustration of the advantages of using 1-D NPs. Reproduce with permission from [83]. Copyright 2014 American Chemical Society

In general, 1D can facilitate strain relaxation by restraining the stress accumulated along the radial direction with stress relief due to ample internal space. While the intertwined structure can improve the charge-transfer process and thus improve the rate performance [97]. Several studies had been done that proved that 1-D nanostructure improves the cyclability of the produced anode material. It can either be 0D NPs encapsulated in 1D nanofibers or formed 1D nanostructures, e.g. NRs, NWs, and nanotubes (NTs). Hwang et al. work shows that encapsulating Si NPs in C nanofiber (SiNP@C) using coaxial electrospinning technology as shown in Figure 1.20, can address and solve the issues with Si as anode material, e.g. pulverization, poor Si-C contact, and unstable SEI layer. The SiNP@C exhibit excellent cyclability, wherein only 1% initial capacity lost after 300 cycles even at high C-rate, i.e. 3C [98].

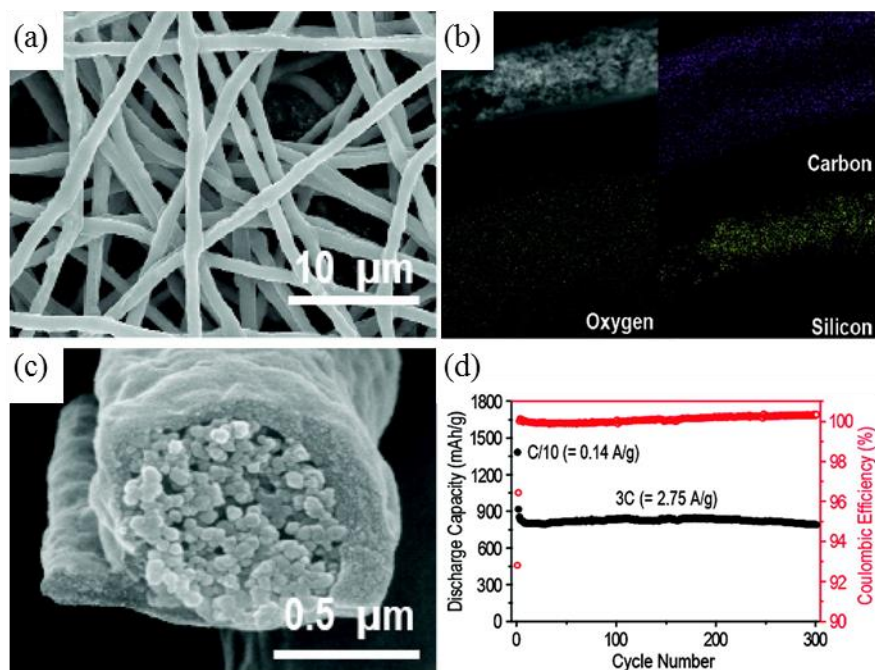


Figure 1.20. (a) SEM image of the SiNP@C; (b) STEM image of the SiNP@C with the corresponding EDAX elemental mapping for C, O, and Si; (c) Cross-sectional SEM image of the SiNP@C indicating that C shell and the Si NPs comprised core; and (d) cycling performance of SiNP@C measured at 3C rate. Reproduce with permission from [98]. Copyright 2012 American Chemical Society.

On a similar study, Yu et al, showed that Sn@C encapsulated in hollow carbon fiber as shown in Figure 1.21, has a much better reversible capacity of 737 mA h g^{-1} even after 200 cycles at 0.5C rate compared to that commercially produced Sn NPs. Even at various discharge rate of 1C, 3C, 5C, it can deliver 650 , 550 , and 480 mA h g^{-1} capacities respectively. The improved cyclability was attributed to its special morphology, which is almost similar to the work of Qin et al. as shown in Figure 1.10, wherein the hollow carbon fiber acts as a “buffer zone” that

accommodates large volumetric change of Sn during the charge-discharge process, while the C-shell that coats the Sn particles prevented the aggregation of Sn [99].

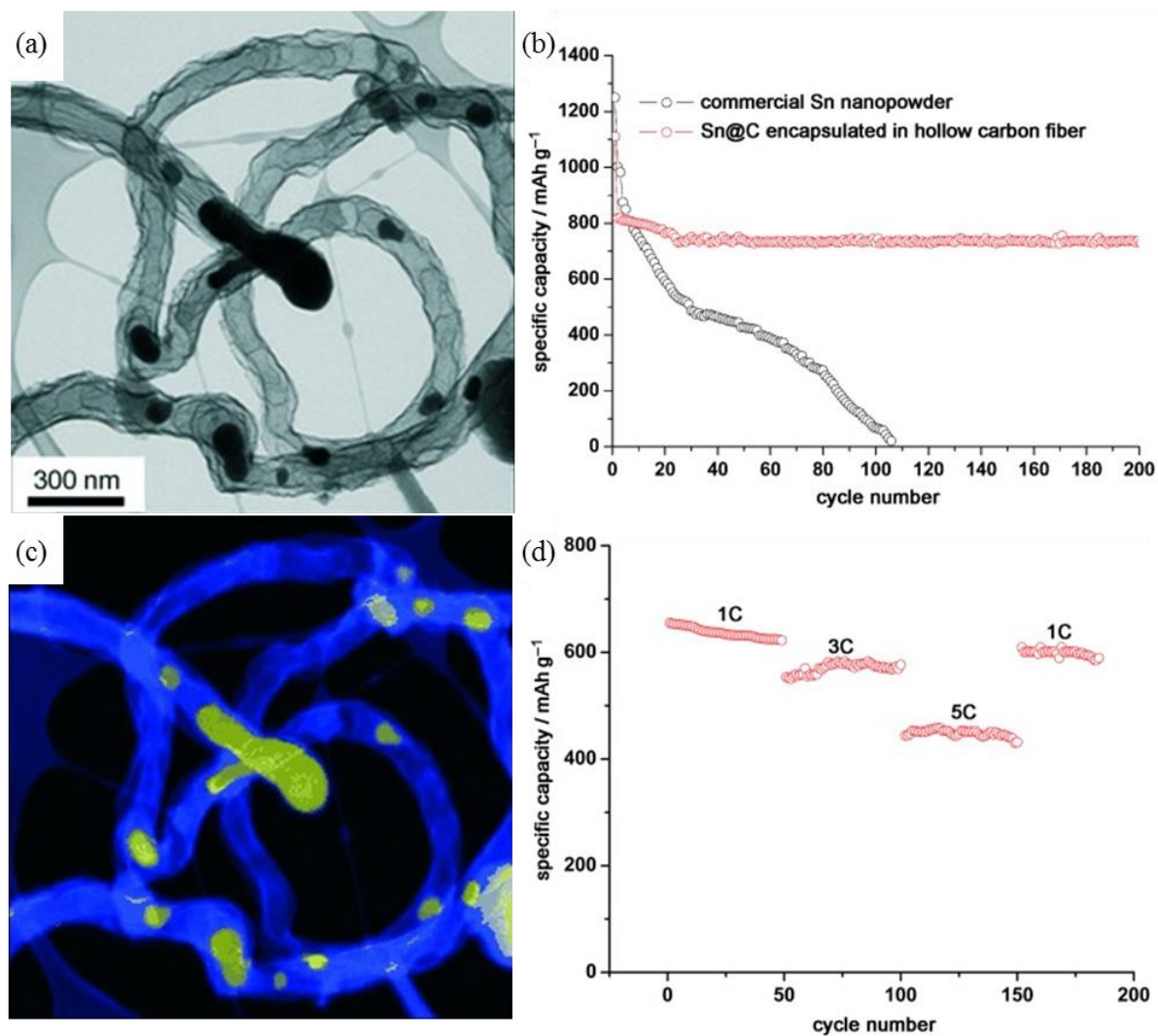


Figure 1.21. (a) TEM image of Sn@C encapsulated in hollow carbon fiber; (b) elemental mapping of (a) where blue = carbon and yellow = Sn; (c) cycle test of Sn@C encapsulated in hollow carbon fiber at a cycling rate of 0.5 C; and (d) discharge capacities of Sn@C encapsulated in hollow carbon fiber at different C-rate. Reproduced with permission from [99].

Copyright 2009 Wiley-VCH Verlag GmbH & Co. KGaA, Weinheim.

Chan et al. however, showed that producing 1D NPs directly grown in the current collector can further improve the properties of the anode material in addition to the outstanding characteristics of 1D nanoparticles. Particles directly grown on the current collector correspond to the good contact and enhanced electron transport of the NWs to the current collector. In addition, the conductive carbons and binders, which contributes to the additional weight of the electrode, is no longer needed. In their experiment, they grow Si NWs on stainless steel (SS) substrate using vapour-solid-liquid method using Au catalyst, as shown in Figure 1.22 a and b. Based on electrochemical test (Figure 1.22 c and d) of Si NWs directly grown on SS substrate, the sample displayed high capacities at different C-rates. At 1C, it exhibits $>2100 \text{ mA h g}^{-1}$ capacity which is almost 5 times larger than that of the commercially produced graphite. On the other hand, the charge-discharge cycle was observed to be almost constant at 3193 mA h g^{-1} (2nd discharge) on the succeeding cycles [100], though they were only able to check until 10 cycles.

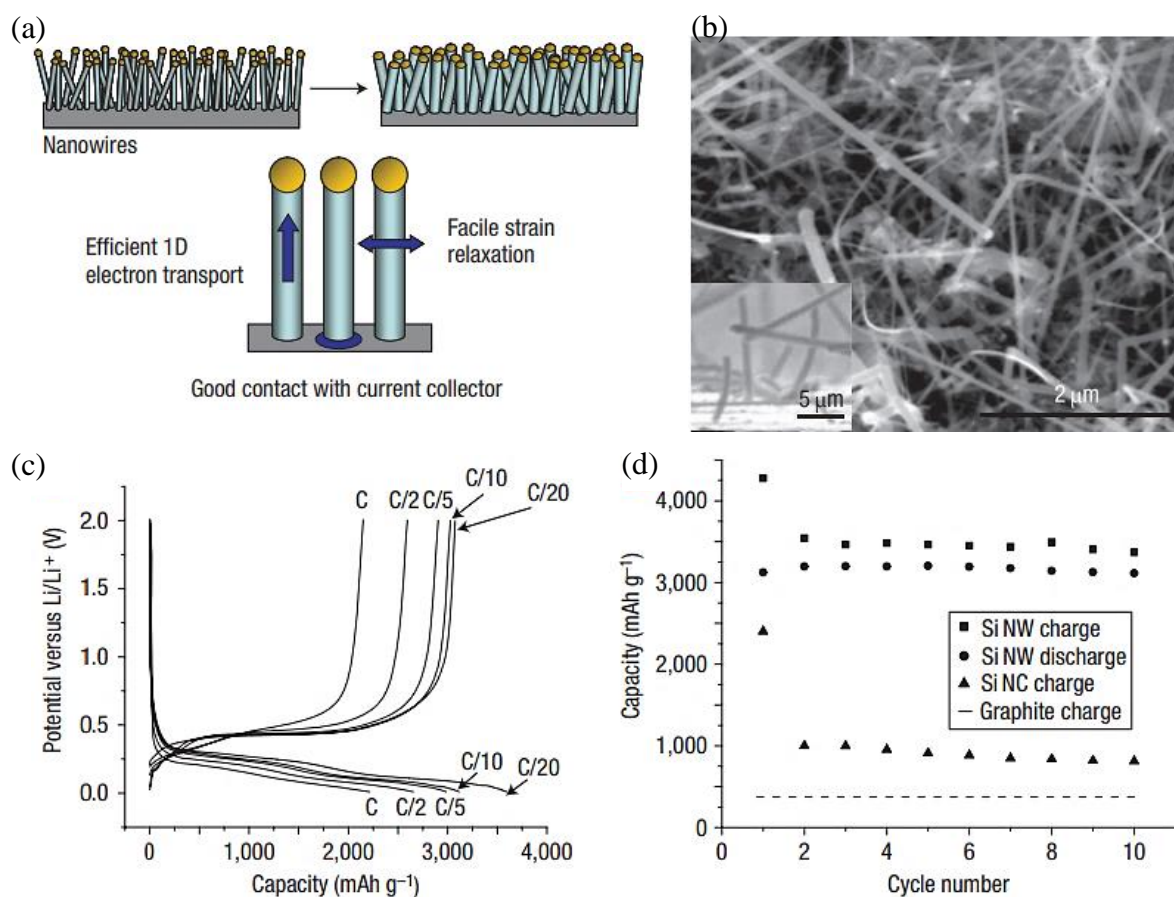


Figure 1.22. (a) Schematic illustration of NWs directly grown on the current collector; (b) SEM image of the grown Si NWs; and (c) voltage profiles at various C-rates and (d) cycle rate at C/20 of Si NWs directly grown on SS substrate. Reproduce with permission from [100].

Copyright 2008 Nature Publishing Group.

The *in-situ* electrochemical probing of 1-D NPs, as one of the advantages of 1-D NPs, is a promising technique to understand the underlying phenomena occurring on the material during charge-discharge cycles. To better understand the capacity decay and the structural instability of electrode materials, several *in-situ* probing had been used such as TEM, Raman spectroscopy, XRD, NMR, etc. [71, 72, 100-111] These *in-situ* probing can directly (real time)

observe the volume expansion, changes/evolution in the structure, dimension and crystallinity (phase), cracking/pulverization, decay, and atomic variations of the electrode material. In the work of Mai et al., they examine the changes associated with charge-discharge cycles on both vanadium oxide NW and Si NW. In their work, to better understand the effect of lithiation and delithiation on the wire structure, they fabricated an in-situ probing device, wherein binders and conductive carbons were not added as shown in Figure 1.23. By observing a single NW, they found that vanadium oxide NW has a reversible structure that is maintained under shallow discharge state, however, the conductivity can no longer be recovered after deep charging. This can clearly indicate that a permanent structural change occurs when a large amount of Li^+ intercalates into the vanadium oxide layered structure. On the other hand, *c*-Si NW with *a*-Si shell indicates large volumetric expansion, i.e. ~400% upon Li^+ insertion and extraction that resulted to the pulverization and capacity fading [72].

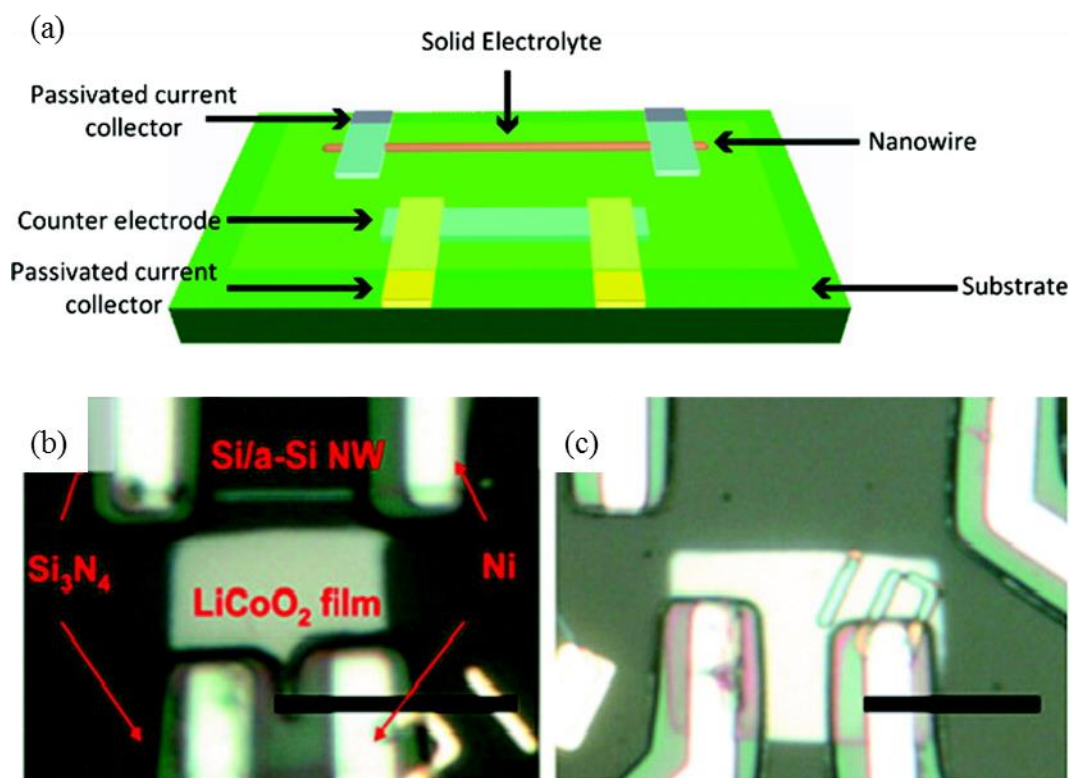


Figure 1.23. (a) Schematic diagram of a single nanowire electrode device for *in-situ* probing, and the actual optical image of the single nanowire electrode device (b) with and (c) without Si/a-Si nanowire/LiCoO₂ electrodes, where the scale bar is 10 μm. Reproduce with permission from [96]. Copyright 2010 American Chemical Society.

On the other hand, Huang et al., observed the electrochemical lithiation of a single SnO₂ nanowire electrode using a nanoscale electrochemical device as schematically illustrated in Figure 1.24 a. They use LiCoO₂ and ionic liquid-based electrolyte (ILE) as counter electrode (cathode) and electrolyte respectively. On their work, they were able to record how Li⁺ propagates, reacts and causes the volumetric change in SnO₂ NW as indicated by the screen shots shown in Figure 1.24 b-s. Initially, the SnO₂ NW is straight as indicated by Figure 1.24 b,

and upon in contact with the ILE, the NW shows a meniscus indicating the electrolyte take-up surrounding the NW. After charging for 1860 s, the NW has 60% elongation with 45% radial expansion, which accounted to the 240% volume expansion of the NW [72].

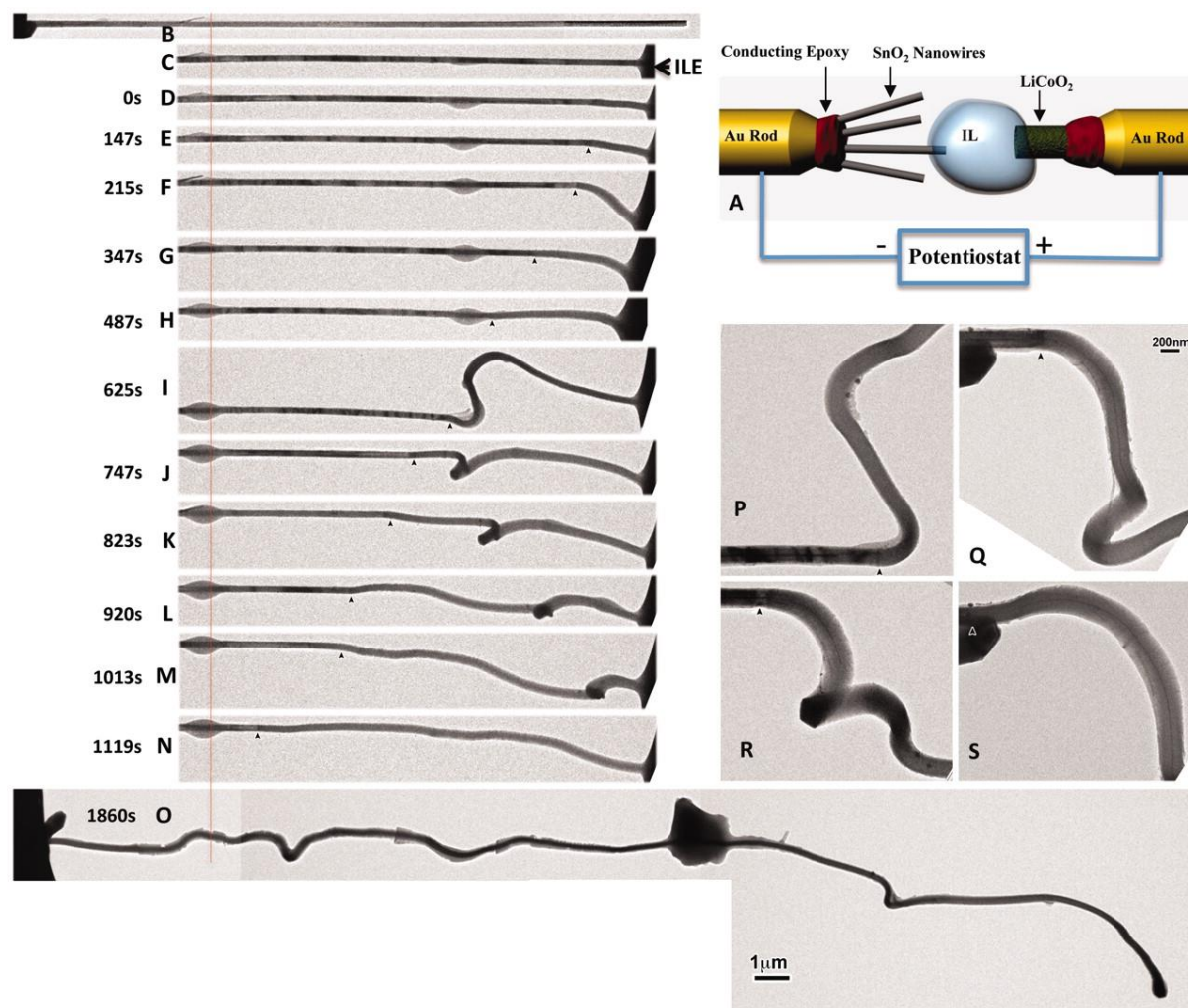


Figure 1.24. (a) Schematic illustration of the nanoscale electrochemical device, TEM images of (b) initial straight NW, (c) meniscus on the ionic liquid-based electrolyte (ILE) wetted NW, (d-s) screen shots indicating the changes observed during lithiation with respect to time, (p-s) high-magnification image of the progressive migration of the reaction front, and the swelling

and twisted morphology of the lithiated part. The red line from (b) to (o) marks the reference point to track the changes in the NW, while the arrowheads in (e-s) indicates the chemical reaction (lithiation) front. The big particle at the middle of the NW in (o) is an island of formed gel (viscous) ILE due to long electron beam exposure during the recording. Reproduce from [72]. Copyright 2010 American Association for the Advancement of Science.

Though in situ TEM is a splendid tool in understanding the morphology change and structure evolution, the works of Nie et al. [71, 111] show a magnificent atomistic analyses and mechanisms of the dynamic lithiation of a single SnO₂ NW. They found that after lithiation, collateral dark stripes and surface defects were formed as indicated by Figure 1.25. The lithiation stripes are parallel to the (200) lattice plane as indicated by the SAED analysis shown in Figure 1.25 b. The HAADF and EELS analysis, Figure 1.25 c and inset respectively, of the partially lithiated SnO₂ NW show that Li is present in the lithiated stripes and that the Li⁺ diffusion along the [001] direction in the (200) plane is favored compared to other direction. The strain mapping (Figure 1.25 d) clearly indicates that these lithiation stripes are highly strained. The strained area was highlighted in the highly lithiated stripes (Figure 1.25 e). It was characterized as mixed dislocation, i.e. edge dislocation ($1/2[1\bar{1}1]$) + screw dislocation ($1/2[\bar{1}11]$ or $1/2[111]$), with Burger vector of $[0\bar{1}0]$ or $[101]$. Hence it was determined that the slip has $[0\bar{1}0](101)$ character since $[101](10\bar{1})$ is likely to stay in the lattice near

the surface. This further explain the formation of surface step in the lithiated NW as shown in

Figure 1.25 f [71].

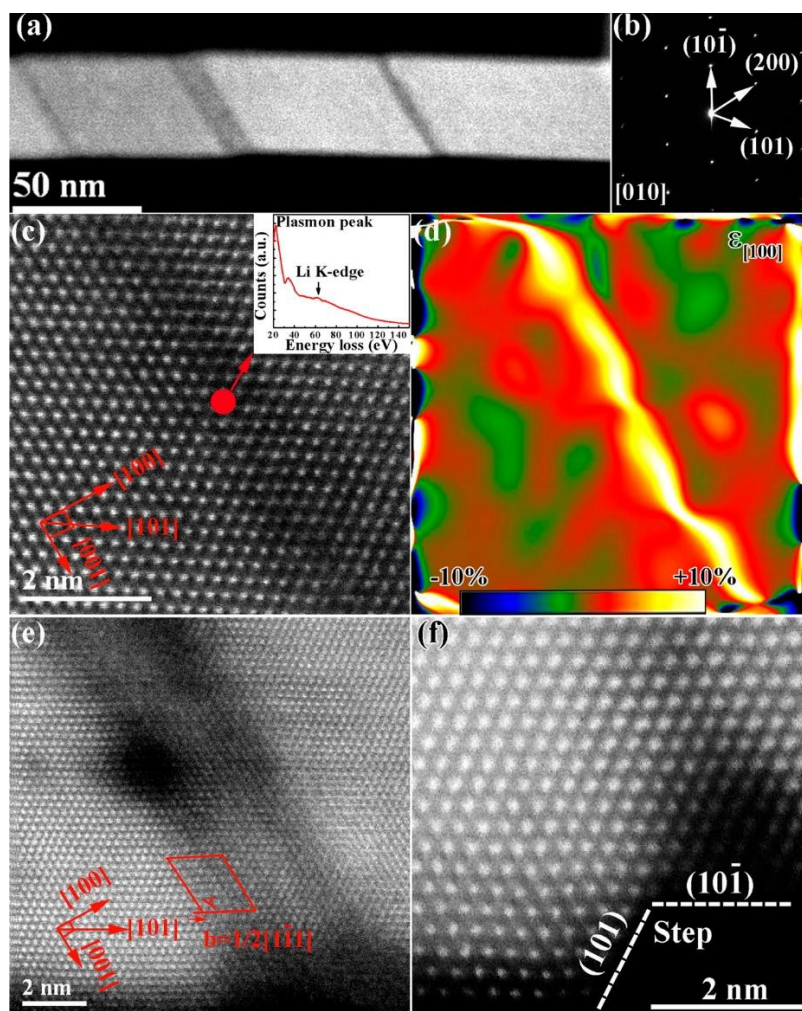


Figure 1.25. (a) HAADF image of a partially lithiated SnO_2 NW, (b) corresponding SAED pattern taken with the $[010]$ zone axis, (c) atomic resolution HAADF image from the partially lithiated area of (a) with EELS analysis as inset, (d) strain map with the $[100]$ direction in (c), (e) atomic resolution HAADF image from the fully lithiated area of (a), and (f) atomic resolution HAADF image of the surface step induced by lithiation. Reproduce with permission from [71]. Copyright 2013 American Chemical Society.

On the other hand, Nie et al. also compare how lithiation occurs in SnO₂ NWs with and without TB defect as shown in Figure 1.26. The TB defect was observed under TEM (Figure 1.26 a-b) and was emphasized using strain analysis (Figure 1.26 d-e). Based on their work, they found that Li⁺ are more concentrated in the TB defect than the highly ordered structure as indicated by the EELS maps in Figure 1.26 c. This agrees well with their discrete Fourier transform (DFT) analysis (Figure 1.26 f-g), which indicates that the preferred site of the Li⁺ is on/near the (10 $\bar{1}$) TB. On the other hand, their DFT analysis also explains the large contrast change in STEM of TB and (200) planes, which is merely due to the large expansion in the Sn-Sn distance along the [100] direction and perpendicular to the TB direction as shown in Figure 1.26 g.

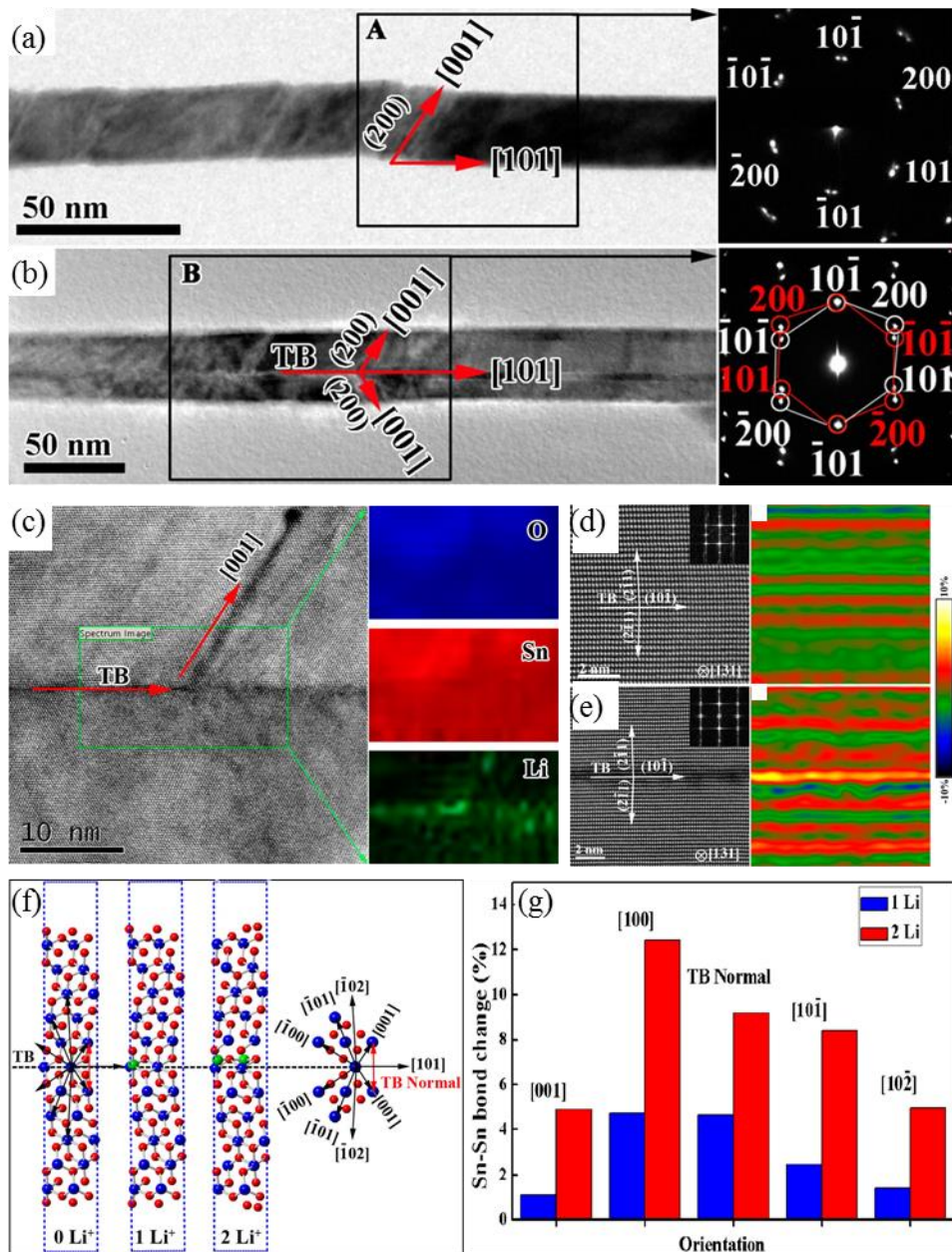


Figure 1.26. Direct observation of lithiation of SnO₂ (a) with and (b) without twin boundary (TB) defect, with electron diffraction of the reaction front shown at the right; (c) HAADF of the lithiated are of sample with TB and its corresponding EELS maps of O, Sn, and Li; atomic scale HAADF (d-e left) and strain analysis (d-e right) of SnO₂ NW (d) with and (e) without TB defect, DFT simulation of (f) atomic structure model to investigate the Li intercalation induced

TB defect and (g) strain associated with Sn-Sn bond change induced by one (1) or two (2) Li insertion. Reproduce with permission from [111]. Copyright 2015 American Chemical Society.

1.3 Summary and Perspective

LIB is a very promising storage device with wide range of applications due to its exhibited high energy and power compared to the other storage devices. However, the optimum design of LIB to unveil its full energy and power is yet to be determined, and hence a lot of researches have been done to explore the possibility of replacing the existing commercially produced LIB. One of the approach is to improve the anode material which is responsible to store the Li^+ and hence the accumulated charge that attributed to the total capacity of the produced LIB. Several materials have been considered, such as intercalating, alloying, and conversion type of materials; one has greater advantage than the other with respect to the property being considered such as cycle stability, specific capacity, and the type of SEI layer formed. In this study, we explore the effectiveness of the 1-D NP using both alloying (Chapter 3) and conversion (Chapter 4) type of material as anode material for LIB.

1.4 Significance of the Study

This study deals with the formation and application of 1D nanomaterials as anode materials for Lithium-ion battery. Though there are already a lot of researches that deals with

1D nanomaterial, the understanding on the continuous capacity fading of 1D Sn nanomaterial is still unknown, while that of the formation and applicability of 1D ZnV_2O_4 as anode material for LIB has not yet been explored and hence been the focus of this study.

There has not been much study that deals with 1D Sn nanomaterial as anode material for LIB. Most of the study that has been done deals with SnO_x instead of metallic Sn to combat the large volumetric change that greatly degrades the electrode. Tokur et al.,⁸⁹ compare the spherical particle with that of the 1D Sn. Based on their result, 1D Sn have better specific capacity compared to that of the spherical particles. However, the capacity still continuously fades throughout the cycles despite its 1D morphology, and they were not able to determine the main cause. In this study, we also compare the electrochemical property of the spherical NPs with that of the 1D Sn, i.e. Sn NRs, with different aspect ratio. However, the single crystal property of the formed NRs with {200} facets and <001> growth direction, allow us to deduce the cause of the continuous capacity fading of 1D Sn nanomaterial, hence been the focus of this study. We believe that this finding can contribute to better understand what occurs in 1D Sn as anode material for LIB.

On the other hand, ZnV_2O_4 , a spinel compound is one of the potential anode material for LIB. Different morphologies have already been studied by other researchers to evaluate its applicability as anode material for LIB. However, the formation and the applicability of 1D ZnV_2O_4 as anode material has not yet been explored. In addition to 1D morphology, formation

of a porous structure is also desirable due to the large surface area that increases the Li^+ flux. This further improves its applicability at high current density applications, and hence been the focus of this study. This study is also the first that evaluate ZnV_2O_4 at high current density of 5 A g^{-1} for 1000 cycles. We believe that this study show a possible route in the formation of porous 1D ZnV_2O_4 via two-step process and the applicability of formed porous 1D ZnV_2O_4 as anode material for LIB.

1.5 Objective of the Study

The objective of this study is to evaluate the electrochemical performance of 1D nanomaterials, vis. Sn (alloying type) and ZnV_2O_4 (conversion type), as anode material for LIB.

- To find a possible route in the formation of 1D Sn and ZnV_2O_4 .
- To understand the formation mechanism governing the reaction in the formation of 1D nanomaterial, vis. Sn and ZnV_2O_4 .
- To evaluate the applicability of the formed 1D Sn and ZnV_2O_4 as anode material for LIB.
- To understand what occurs on the 1D Sn and ZnV_2O_4 that contributes to its improved electrochemical properties.

References

1. Larcher, D.; Tarascon, J-M., Towards greener and more sustainable batteries for electrical energy storage, *Nature Chemistry*, **2015**, 7, 19-29
2. International Energy Agency *Key World Energy Statistics 2017* (IEA, 2017); available at <https://www.iea.org/publications/freepublications/publication/KeyWorld2017.pdf>.
3. Luo, X.; Wang, J.; Dooner, M.; Clarke, J., Overview of current development in electrical energy storage technologies and the application potential in power system operation, *Applied Energy*, **2015**, 137, 511-536
4. Tarascon, J-M.; Armand, M., Issues and challenges facing rechargeable lithium batteries, *Nature*, **2001**, 414, 359-367
5. Walker, W., Short Course on Lithium-ion Batteries: Fundamentals, Thermal Performance and Understanding Thermal Runaway, NASA Thermal Fluids and Analysis Workshop 2015 available at: <https://ntrs.nasa.gov/archive/nasa/casi.ntrs.nasa.gov/20160010460.pdf>
6. Li, L.; Basu, S.; Wang, Y.; Chen, Z.; Hundekar, P.; Wang, B.; Shi, J.; Shi, Y.; Narayanan, S.; Koratkar, N., Self-healing-induced healing of lithium dendrites, *Science*, **2018**, 359, 1513-1516
7. Kwon, E.; Lim, H.-S.; Sun, Y.-K., Suh, K.-D., Improved rate capability of lithium-ion batteries with Ag nanoparticles deposited onto silicon/carbon composite microspheres as an anode material, *Solid State Ionics*, **2013**, 237, 28-33
8. Shin, H.-C.; Liu, M., Three-Dimensional Porous Copper-Tin Alloy Electrodes Rechargeable Lithium Batteries, *Adv. Funct. Mater.*, **2005**, 15 (4), 582-586
9. Ren, Y.; Shen, Y.; Lin, Y.; Nan, C.-W., Direct observation of lithium dendrites inside garnet-type lithium-ion solid electrolyte, *Electrochem. Commun.*, **2015**, 57, 27-30
10. Liu, C.-J.; Xue, F.-H.; Huang, H.; Yu, X.-H.; Xie, C.-J.; Shi, M.-S.; Cao, G.-Z.; Jung, Y.-G.; Dong, X.-I., Preparation and Electrochemical properties of Fe-Sn (C) Nanocomposites as Anode for Lithium-ion Batteries, *Electrochim. Acta*, **2014**, 129, 93-99
11. Liu, C.-J.; Huang, H., Cao, G.-Z.; Xue, F.-H; Camacho, R. A. P.; Dong, X. I., Enhanced Electrochemical Stability of Sn-Carbon Nanotube Nanocapsules as Lithium-Ion Battery Anode, *Electrochim. Acta*, **2014**, 376-382
12. Zou, P.; Wang, Y.; Chiang, S.-W.; Wang, X.; Kang, F.; Yang, C., Directing lateral growth of lithium dendrites in micro-compartmented anode arrays for safe lithium metal batteries, *Nat. Commun.*, **2018**, 9, 464 (1-9)
13. Cheng, X.-B.; Zhao, M.-Q.; Chen, C.; Pentecost, A.; Maleski, K.; Mathis, T.; Zhang, X.-Q., Zhang, Q; Jiang, J.; Gogotsi, Y., Nanodiamonds suppress the growth of lithium dendrites, *Nat. Commun.*, **2017**, 8, 336 (1-9)
14. Jana, A.; Garcia, R. E., Lithium dendrite growth mechanisms in liquid electrolyte, *Nano Energy*, **2017**, 41, 552-565

15. Liu, C.; Neale, Z. G.; Cao, G., Understanding electrochemical potentials of cathode materials in rechargeable batteries, *Mater. Today*, **2016**, 19 (2), 109-123
16. U.S. Geological Survey, Mineral Commodity Summaries, January 2018: Lithium, available at: <https://minerals.usgs.gov/minerals/pubs/commodity/lithium/mcs-2018-lithi.pdf>.
17. Harris, W.S., Ph.D. Thesis, University of CA, Berkeley, 1958
18. Julien, C.; et al., *Lithium Batteries*, Springer International Publishing Switzerland, **2015**; Chapter 2, 29-68
19. Blomgren. G. E., The Development and Future of Lithium Ion Battery, *J. Electrochem. Soc.*, **2017**, 164 (1), A5019-A5025
20. Scrosati, B., Lithium Rocking Chair Batteries: An Old Concept?, *J. Electrochem. Soc.*, **1992**, 139 (10), 2776-2781
21. Hu, R. Z.; Liu, H.; Zeng, M. Q.; Liu, J. W.; Zhu, M., Progress on Sn-based thin-film anode materials for lithium-ion batteries, *Chinese Science Bulletin*, volume 57, 32, 2012, pp.4119-4130
22. Lazzari, M.; Scrosati, B., A Cyclable Lithium Organic Electrolyte Cell Based on Two Intercalation Electrodes, *J. Electrochem. Soc.*, **1980**, 127, 773-774
23. Mizushima, K.; Jones, P. C.; Wiseman, P. J.; Goodenough, J. B., Li_xCoO_2 ($0 < x \leq 1$): A New Cathode Material for Batteries of High Energy Density, *Mat. Res. Bull.*, **1980**, 15, 783-789
24. Hunter, J. C., Preparation of a New Crystal Form of Manganese Dioxide: λ - MnO_2 , *J. Solid State Chem.*, **1981**, 39, 142-147
25. Auborn, J. J.; Barberio, Y. L., Lithium Intercalation Cells Without Metallic Lithium: $\text{MoO}_2/\text{LiCoO}_2$ and $\text{WO}_2/\text{LiCoO}_2$, *J. Electrochem. Soc.*, **1987**, 134 (3), 638-641
26. Mauger, A.; Julien, C. M., Critical review on lithium-ion batteries: are they safe? Sustainable?, *Ionics*, **2017**, 23, 1933-1947
27. Herold, A., Recherches sur les composes dinsertion du graphite, *Bulletin de la Société chimique de France*, **1955**, 7-8, 999-1012
28. Juza, R.; Wehle, V., Lithium-graphit-einlagerungsverbindungen, *Naturwissenschaften*, **1965**, 52 (20), 560-560
29. Besenhard, J. O.; Eichinger, G., High energy density lithium cells: Part I. Electrolytes and anodes, *J. Electroanal. Chem.*, **1976**, 68, 1-18
30. Eichinger, G.; Besenhard, J. O., High energy density lithium cells: Part II. Cathodes and complete cells, *J. Electroanal. Chem.*, **1976**, 72, 1-31
31. Armand, M. B.; Duclot, M., Electrochemical generators for producing current and new materials for their manufacture, *U.S. Pat. 4,303,748*, **1981**
32. Basu, S., Ambient temperature rechargeable battery, *U.S. Pat. 4,423,125*, **1983**

33. Yazami, R.; Touzain, P., A reversible graphite-lithium negative electrode for electrochemical generators, *J. Power Sources*, **1983**, 9, 365-371
34. Yoshino, A.; Sanechika, K.; Nakajima, T., Secondary Battery, *U.S. Pat. 4,668,595*, **1987**
35. Nagaura, T.; Tazawa, K., Lithium-Ion Rechargeable Battery, *Prog. Batteries Sol. Cells*, **1990**, 9, 20
36. Goodenough, J. B.; Park, K., The Li-Ion Rechargeable Battery: A Perspective, *J. Am. Chem. Soc.*, **2013**, 135, 1167-1176
37. Deng, D., Li-ion batteries: basics, progress, and challenges, *Energy Sci. Eng.*, **2015**, 3 (5), 385-418
38. Thackeray, M. M.; Wolverton, C.; Isaacs, E. D., Electrical energy storage for transportation – approaching the limits of, and going beyond, lithium-ion batteries, *Energy Environ. Sci.*, **2012**, 5, 7854-7863
39. Pfleging, W., A review of laser electrode processing for development and manufacturing of lithium-ion batteries, *Nanophonics*, **2018**, 7(3), 549-573
40. Islam, M. S.; Fisher, C. A. J., Lithium and sodium battery cathode materials: computational insights into voltage, diffusion and nanostructure properties, *Chem. Soc. Rev.*, **2014**, 43, 185-204
41. Kim, Y.; Park, K.-S.; Song, S.-H.; Han, J.; Goodenough, J. B., Access to M^{3+}/M^{2+} Redox Couples in Layered $LiMS_2$ Sulfides ($M = Ti, V, Cr$) as Anodes for Li-ion Battery, *J. Electrochem. Soc.*, **2009**, 156 (8), A703-A708
42. Qin, J.; He, C.; Zhao, N.; Wang, Z.; Shi, C.; Liu, E.-Z.; Li, J., Graphene Networks Anchored with Sn@Graphene as Lithium Ion Battery Anode, *ACS Nano*, **2014**, 8(2), 1728-1738
43. Nitta, N.; Wu, F.; Lee, J. T.; Yushin, G., Li-ion battery materials: present and future, *Mater. Today*, **2015**, 18 (5), 252-264
44. Uses and properties of Phosphorous, Royal Society of Chemistry, 2017, available at: <http://www.rsc.org/periodic-table/element/15/phosphorus>
45. Andre, D.; Hain, H.; Lamp, P.; Maglia, F.; Stiaszny, B., Future high-energy density anode materials from an automotive application perspective, *J. Mater. Chem. A*, **2017**, 5, 17174-17198
46. Kim, H.; Cho, J., Superior Lithium Electroactive Mesoporous Si@Carbon Core-Shell Nanowires for Lithium Battery Anode Material, *Nano Lett.*, **2008**, 8(11), 3688-3691
47. Yao, Y.; McDowell, M. T.; Ryu, I.; Wu, H.; Liu, N.; Hu, L.; Nix, W. D.; Cui, Y., Interconnected Silicon Hollow Nanospheres for Lithium-Ion Battery Anodes with Long Cycle Life, *Nano Lett.*, **2011**, 11(7), 2949-2954
48. Yi, R.; Dai, F.; Gordin, M. L.; Chen, S.; Wang, D., Microsized Si-C Composite with Interconnected Nanoscale Building Blocks as High-Performance Anodes for Practical Application in Lithium-Ion Batteries, *Adv. Energy Mater.*, **2013**, 3(3), 295-300

49. Deng, D.; Kim, M. G.; Lee, J. Y.; Cho, J., Green energy storage materials: Nanostructured TiO₂ and Sn-based anodes for lithium-ion batteries, *Energy Environ. Sci.*, **2009**, 2, 818–837
50. Yamada, Y.; Usui, K.; Chiang, C. H.; Kikuchi, K.; Furukawa, K.; Yamada, A., General Observation of Lithium Intercalation into Graphite in Ethylene-Carbonate-free Superconcentrated electrolyte, *ACS Appl. Mater. Interfaces*, **2014**, 6, 10892-10899
51. Fang, Z.-K.; Zhu, Y. R.; Yi, T. F.; Xie, Y., Li₄Ti₅O₁₂-LiAlO₂ Composite as High Performance Anode Material for Lithium-Ion Battery, *ACS Sustainable Chem. Eng.*, **2016**, 4, 1994-2003
52. Nie, A.; Gan, L.-Y.; Cheng, Y.; Asayesh-Ardakani, H.; Li, Q.; Dong, C.; Tao, R.; Mashayek, F.; Wang, H.-T.; Schwingenschlögl, U.; Klie, R. F.; Yassar, R. S., Atomic-Scale Observation of Lithiation Reaction Front in Nanoscale SnO₂ Materials, *ACS Nano*, **2013**, 7 (7), 6203-6211
53. Chan, M. K. Y.; Wolverton, C.; Greeley, J. P., First Principle Simulations of the Electrochemical Lithiation and Delithiation of Faceted Crystalline Silicon, *J. Am. Chem. Soc.*, **2012**, 134 (35), 14362-14374
54. Winter, M.; Besenhard, J. O., Lithiated Carbons, Handbook of Battery Materials, Wiley, New York, **1999**, Part III. Chapter 5, 383-418
55. Lundgren, C. A.; Xu, K.; Jow, T. R.; Allen, J.; Zhang, S. S., Lithium-Ion Batteries and Materials, *Springer Handbook of Electrochemical Energy 1st ed*, Breitkopf, C.; Swider-Lyons, K., **2017**, XXVI, 1016, ISBN: 978-3-662-46656-8
56. Kaskhedikar N. A.; Maier, J., Lithium Storage in Carbon Nanostructures, *Adv. Mater.*, **2009**, 21(25–26), 2664–2680
57. Su, D. S.; Schlögl, R., Nanostructured Carbon and Carbon Nanocomposites for Electrochemical Energy Storage Applications, *Chem. Sus. Chem.*, **2010**, 3(2), 136–168
58. Nitta, N.; Yushin, G., High-Capacity Anode Materials for Lithium-Ion Batteries: Choice of Elements and Structures for Active Particles, *Part. Part. Syst. Char.*, **2014**, 31(3), 317–336
59. McDowell, M. T.; Lee, S. W.; Nix, W. D.; Cui, Y., 25th Anniversary Article: Understanding the Lithiation of Silicon and Other Alloying Anodes for Lithium-Ion Batteries, *Adv. Mater.*, **2013**, 25(36), 4966–4985
60. Obrovac, M. N.; Chevrier, V. L., Alloy Negative Electrodes for Li-Ion Batteries, *Chem. Rev.*, **2014**, 114(23), 11444–11502
61. Li, W.; Sun, X.; Yu, Y., Si-, Ge-, Sn-Based Anode Materials for Lithium-ion Batteries: From Structure Design to Electrochemical Performance, *Small Methods*, **2017**, 1, 1600037 (1-22)
62. Agubra, V.; Fergus, J., Lithium ion Battery Anode Aging Mechanism, *Materials*, **2013**, 6, 1310-1325

63. Wen, J.; Yu, Y.; Chen, C., A Review on Lithium-Ion Batteries Safety Issues: Existing Problems and Possible Solutions, *Mater. Express.*, **2012**, 2 (3), 197-212
64. Maruyama, H.; Nakano, H.; Ogawa, M.; Nakamoto, M.; Ohta, T.; Sekiguchi, A., Improving battery safety by reducing the formation of Li dendrites with the use of amorphous silicon polymer anodes, *Sci. Rep.*, **2015**, 5, 13219 (1-9)
65. Zaghbi, K.; Simoneau, M.; Armand, M.; Gauthier, M., Electrochemical study of $\text{Li}_4\text{Ti}_5\text{O}_{12}$ as negative electrode for Li-ion polymer rechargeable batteries, *J. Power Sources*, **1999**, 81-82, 300-305
66. Lu, Z.; Liu, N.; Lee, H.-W.; Zhao, J.; Li, W.; Li, Y.; Cui, Y., Non-filling Carbon coating of porous Silicon Micrometer-Sized Particles for High-Performance Lithium Battery Anodes, *ACS Nano*, **2015**, 9 (3), 2540-2547
67. Courtel, F.; Duncan, H.; Abu-Lebdeh, Y., Beyond Intercalation: Nanoscale-Enabled Conversion Anode Materials for Lithium-Ion Batteries, in *Nanotechnology for Lithium-Ion Batteries*, ed. Y. Abu-Lebdeh and I. Davidson, Springer, US, **2013**, pp. 85–116
68. Poizot, P.; Laruelle, S.; Grugeon, S.; Dupont, L.; Tarascon, J.-M., Nano-sized transition-metal oxides as negative-electrode materials for lithium-ion batteries, *Nature*, **2000**, 407(6803), 496–499
69. Cabana, J.; Monconduit, L.; Larcher, D.; Palacín, R. M., Beyond Intercalation-Based Li-Ion Batteries: The State of the Art and Challenges of Electrode Materials Reacting Through Conversion Reactions, *Adv. Mater.*, **2010**, 22(35), E170–E192
70. Feng, L.; Xuan, Z.; Ji, S.; Min, W.; Zhao, H.; Gao, H., Preparation of SnO_2 Nanoparticles and Performance as Lithium-ion Battery Anode, *Int. J. Electrochem. Sci.*, **2015**, 10, 2370-2376
71. Nie, A.; Gan, L.-Y.; Cheng, Y.; Asayesh-Ardakani, H.; Li, Q.; Dong, C.; Tao, R.; Mashayek, F.; Wang, H.-T.; Schwingenschlögl, U.; Klie, R. F.; Yassar, R. S., Atomic-scale Observation of Lithiation Reaction Front in Nanoscale SnO_2 Materials, *ACS Nano*, **2013**, 7 (7), 6203-6211
72. Huang, J. Y.; Zhong, L.; Wang, C. M.; Sullivan, J. P.; Xu, W.; Zhang, L. Q.; Mao, S. X.; Hudak, N. S.; Liu, X. H.; Subramanian, A.; Fan, H.; Qi, L.; Kushima, A.; Li, J., In Situ Observation of the Electrochemical Lithiation of a Single SnO_2 Nanowire Electrode, *Science*, **2010**, 330, 1515-1520
73. Roy, P.; Srivastava, K., Nanostructured anode materials for lithium ion battery, *J. Mater. Chem. A*, **2015**, 3, 2454-2484
74. Bruce, P. G.; Scrosati, B.; Tarascon J.-M., Nanomaterials for Rechargeable Lithium Batteries, *Angew. Chem. Int. Ed.*, **2008**, 47, 2930-2946
75. Wang, Y.; Li, H.; He, P.; Hoson, E.; Zhou, H., Nano active materials for lithium-ion batteries, *Nanoscale*, **2010**, 2, 1294-1305

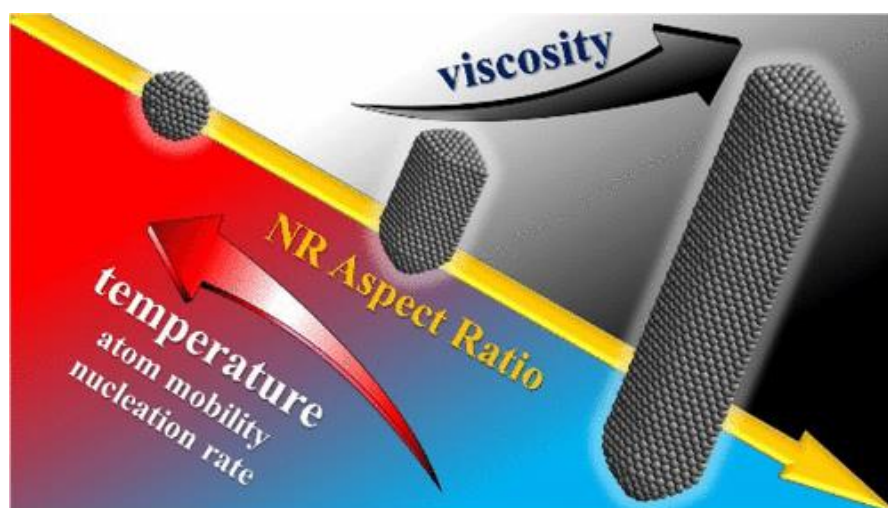
76. Jiang, C.; Hosono, E.; Zhou, H., Nanomaterials for lithium ion batteries, *Nano Today*, **2006**, 1 (4), 28-33
77. Hu, Y.-S.; Kienle, L.; Guo, Y.-G.; Maier, J., High Lithium Electroactivity of Nanometer-Sized Rutile TiO₂, *Adv. Mater.*, **2006**, 18, 1421-1426
78. Cheng, M.-Y.; Ye, Y.-S.; Chiu, T.-M.; Pan, C.-J.; Hwang, B.-J., Size effect of nickel oxide for lithium ion battery anode, *J. Power Sources*, **2014**, 253, 27-34
79. Aricò, A. S.; Bruce, P.; Scrosati, B.; Tarascon, J.-M.; Schalkwijk, W. V., Nanostructured materials for advanced energy conversion and storage devices, *Nat. Mater.*, **2005**, 4, 366-377
80. Armstrong, M. J.; O'Dwyer, C.; Macklin, W. J.; Holmes, J. D., Evaluating the performance of nanostructured materials as lithium-ion battery electrodes, *Nano Res.*, **2014**, 7(1), 1-62
81. Goriparti, S.; Miele, E.; De Angelis, F.; Di Fabrizio, E.; Zaccaria, R. P.; Capiglia, C., Review on recent progress of nanostructured anode materials for Li-ion batteries, *J. Power Sources*, **2014**, 257, 421-443
82. Wang, C.; Li, Q.; Wang, F.; Xia, G.; Liu, R.; Li, D.; Li, N.; Spendelow, J. S.; Wu, G., Morphology-Dependent Performance of CuO Anodes via Facile and Controllable Synthesis for Lithium-ion Batteries, *ACS Appl. Mater. Interfaces*, **2014**, 6, 1243-1250
83. Song, T.; Hu, L.; Paik, U., One-Dimensional Silicon Nanostructure for Li Ion Batteries, *J. Phys. Chem. Lett.*, **2014**, 5, 720-731
84. Guo, Y.-G.; Hu, J.-S.; Wan, L.-J., Nanostructure Materials for Electrochemical Energy Conversion and Storage Devices, *Adv. Mater.*, **2008**, 20, 2878-2887
85. De Juan, L. M. Z.; Maggay, I. V. B.; Nguyen, M. T.; Liu, W.-R.; Yonezawa, Y., β -Sn Nanorods with Active (001) Tip Induced LiF-Rich SEI Layer for Stable Anode Material in Lithium Ion Battery, *ACS Appl. Nano. Mater.*, DOI:10.1021/acsanm.8b00664
86. Wang, J.; Fan, F.; Liu, Y.; Jungjohann, K. L.; Lee, S. W.; Mao, S. X.; Liu, X.; Zhu, T., Structural Evolution and Pulverization of Tin Nanoparticles during Lithiation-Delithiation Cycling, *J. Electrochem. Soc.*, **2014**, 161 (11), F3019-F3024
87. De Juan, L. M. Z.; Nguyen, M. T.; Yonezawa, T.; Tokunaga, T.; Tsukamoto, H.; Ishida, Y., Structural Control Parameters for Formation of Single-Crystalline β -Sn Nanorods in Organic Phase, *Cryst. Growth Des.*, **2017**, 17, 4554-4562
88. Huang, L.; Wei, Q.; Sun, R.; Mai, L., Nanowire electrodes for advance lithium ion batteries, *Front. Energy Res.*, **2014**, 2, 43 (1-13)
89. Tokur, M.; Algul, H.; Uysal, M.; Cetinkaya, T.; Alp, A.; Akbulut, H., Electrolytic coating of Sn nano-rods on nickel foam support for high performance lithium ion battery anodes, *Surf. Coat. Technol.*, **2016**, 288, 62-68
90. Wang, B.; Luo, B.; Li, X.; Zhi, L., The dimensionality of Sn anodes in Li-ion batteries, *Materials Today*, **2012**, 15 (12), 544-552

91. Dasgupta, N. P.; Sun, J.; Liu, C.; Britzman, S.; Andrews, S. C.; Lim, J.; Gao, H.; Yan, R.; Yang, P., 25th anniversary article: semiconductor nanowires-synthesis, characterization, and applications, *Adv. Mater.*, **2014**, 26, 2137–2184
92. Chan, C. K.; Peng, H.; Liu, G.; Mcilwrath, K.; Zhang, X. F.; Huggins, R. A.; Cui, Y., High-performance lithium battery anodes using silicon nanowires, *Nat. Nanotechnol.*, **2008**, 3, 31–35
93. Szczech, J. R.; Jin, S., Nanostructured silicon for high capacity lithium battery anodes, *Energy Environ. Sci.*, **2011**, 4, 56–72
94. Huang, J.Y.; Zhong, L.; Wang, C. M.; Sullivan, J. P.; Xu, W.; Zhang, L. Q.; Mao, S. X.; Hudak, N. S.; Liu, X. H.; Subramanian, A.; Fan, H.; Qi, L.; Kushima, A.; Li, J., In situ observation of the electrochemical lithiation of a single SnO₂ nanowire electrode, *Science*, **2010**, 330 (6010), 1515–1520
95. Mai, L. Q.; Wei, Q. L.; Tian, X. C.; Zhao, Y. L.; An, Q. Y., Electrochemical nanowire devices for energy storage, *IEEE Trans. Nanotechnol.*, **2014**, 13, 10–15
96. Mai, L.; Dong, Y.; Xu, L.; Han, C., Single nanowire electrochemical devices, *Nano Lett.*, **2010**, 10, 4273–4278
97. Ying, H.; Han, W.-Q., Metallic Sn-Based Anode Materials: Application in High-Performance Lithium-Ion and Sodium-Ion Batteries, *Adv. Sci.*, **2017**, 4, 1700298 (1-21)
98. Hwang, T. H.; Lee, Y. M.; Kong, B.-S.; Seo, J.-S.; Choi, J. W., Electrospun Core-Shell Fibers for Robust Silicon Nanoparticle-Based Lithium Ion battery Anodes, *Nano Lett.*, **2012**, 12 (2), 802-807
99. Yu, Y.; Gu, L.; Wang, C.; Dhanabalan, A.; Aken, P. A.V.; Maier, J., Encapsulation of Sn@carbon Nanoparticles in Bamboo-like Hollow Carbon Nanofibers as an Anode Material in Lithium-Based Batteries, *Angew. Chem. Int. Ed.*, **2009**, 48, 6485-6489
100. Chan, C. K.; Peng, H.; Liu, G.; McIlwrath, K.; Zhang, X. F.; Huggins, R. A.; Cui, Y., High-performance lithium battery anodes using silicon nanowires, *Nat. Nanotechnol.*, **2008**, 3, 31-35
101. Huang, L.; Wei, Q.; Sun, R.; Mai, L., Nanowire electrodes for advanced lithium batteries, *Front. Energy Res.*, **2014**, 2, 43 (1-13)
102. Mai, L.; Dong, Y.; Xu, L.; Han, C., Single nanowire electrochemical devices, *Nano Lett.*, **2010**, 10, 4273–4278
103. Li, J.; Dahn, J., An in situ x-ray diffraction study of the reaction of Li with crystalline Si, *J. Electrochem. Soc.*, **2007**, 154, A156–A161
104. Wang, X.-J.; Chen, H.-Y.; Yu, X.; Wu, L.; Nam, K.-W.; Bai, J.; Li, H.; Huang, X.; Yang, X.-Q., A new in situ synchrotron X-ray diffraction technique to study the chemical delithiation of LiFePO₄, *Chem. Commun.*, **2011**, 47, 7170–7172

105. Bhattacharyya, R.; Key, B.; Chen, H.; Best, A. S.; Hollenkamp, A. F.; and Grey, C. P., In situ NMR observation of the formation of metallic lithium microstructures in lithium batteries, *Nat. Mater.*, **2010**, 9, 504–510
106. Blanc, F.; Leskes, M.; Grey, C. P., In situ solid-state NMR spectroscopy of electrochemical cells: Batteries, supercapacitors, and fuel cells, *Acc. Chem. Res.*, **2013**, 46, 1952–1963
107. Hu, Y.-Y.; Liu, Z.; Nam, K.-W.; Borkiewicz, O. J.; Cheng, J.; Hua, X.; Dunstan, M. T.; Yu, X.; Wiaderek, K. M.; Du, L.-S.; Chapman, K. W.; Chupas, P. J.; Yang, X.-Q.; Grey, C. P., Origin of additional capacities in metal oxide lithium-ion battery electrodes, *Nat. Mater.*, **2013**, 12, 1130–1136
108. Ogata, K., Salager, E., Kerr, C. J., Fraser, A. E., Ducati, C., Morris, A. J., Hofmann, S.; Grey, C. P., Revealing lithium-silicide phase transformations in nano-structured siliconbased lithium ion batteries via in situ NMR spectroscopy, *Nat. Commun.*, **2014**, 5, 3217 (1-11)
109. Lee, S.; Oshima, Y.; Hosono, E.; Zhou, H.; Kim, K.; Chang, H. M.; Kanno, R.; Takayanagi, K., In situ TEM observation of local phase transformation in a rechargeable LiMn₂O₄ nanowire battery, *J. Phys. Chem. C*, **2013**, 117, 24236–24241
110. Liu, X. H.; Huang, J. Y., In situ TEM electrochemistry of anode materials in lithium ion batteries, *Energy Environ. Sci.*, **2011**, 4, 3844–3860
111. Nie, A.; Gan, L.-Y.; Cheng, Y.; Li, Q.; Yuan, Y.; Mashayek, F.; Wang, H.; Klie, R.; Schwingenschlögl, U.; Yassar, R. S., Twin Boundary-Assisted Lithium Ion Transport, *Nano Lett.*, **2014**, 15, 610-615

CHAPTER 2

STRUCTURAL CONTROL PARAMETERS FOR FORMATION OF SINGLE-CRYSTALLINE β -SN NANORODS IN ORGANIC PHASE



Cryst. Growth Des., 2017, 17, 4554-4562

Abstract	80
2.1. Introduction	80
2.2. Methodology	
2.2.1. Chemicals	83
2.2.2. Synthesis of β -Sn Nanorods at Different Temperatures.....	83
2.2.3. Synthesis of β -Sn Nanorods Using Different Amounts and MW of PVP ----	84
2.2.4. Characterizations	85
2.3. Results and Discussion	
2.3.1. Structure and Morphology of Sn NPs at Various Synthesis Temperatures ----	86
2.3.2. Growth Direction of Sn NRs and Analysis of Particle Surface	89
2.3.3. Discussion on the Temperature-Dependent Growth Mechanism of Sn NR ----	92
2.3.4. Effect of the Capping Agent (PVP) on the Morphology of Sn NPs	95
2.3.5. Combined Effect of Temperature and PVP (MW and Amount) on the Formation of Sn NRs	102
2.4. Conclusion	103
References	104

Abstract

For the first time, investigation on the effect of lowering the synthesis temperature below room temperature (10 to -10 °C) and increasing the viscosity of the reaction solution at certain temperatures has been used to trigger the formation of single-crystalline β -Sn nanorods (NRs) in a chemical synthesis using an organic solvent. These two parameters govern the energy of the particles in the solution, thereby mediating the selective attachment to the nuclei and the preferential growth of Sn along the c-axis. The length and aspect ratio of the NRs were inversely proportional to the synthesis temperature and directly proportional to the viscosity of the reaction solution. In addition, we found that poly(vinylpyrrolidone) with a high molecular weight aided the formation of longer and higher aspect ratio NRs via the bridge flocculation effect.

2.1. Introduction

Nanorods (NRs) are one-dimensional (1D) nanomaterials and are promising especially in the field of electronics, energy storage, e.g., as anode materials in lithium ion batteries (LIB), and as gas sensing materials.¹ This is due to their high surface-to-volume ratio, ease of electrolyte penetration and electron conduction, and facilitation of strain relaxation, that further improve both the mechanical and electrical properties.²⁻⁴ Various synthetic procedures have been employed to produce NRs, such as template assisted chemical vapor deposition (CVD),¹ physical vapor deposition (PVD),^{5,6} electrochemical deposition,^{3,7} solvothermal methods,⁸ and chemical synthesis.⁹ Theoretically, the shape of the nanomaterial represents the minimum total surface energy of the material, which is a function of the different crystallographic planes at the particle surface. A material with an anisotropic crystal structure, i.e., the side and basal planes have a considerable difference in surface energy, may grow to have an anisotropic morphology. For example, if the basal plane has a higher surface energy than that of the side

planes, the growth of the basal plane is preferential to minimize the total surface energy, hence formation of the rod-shaped morphology.^{2,10-12} β -Tin (β -Sn) is an anisotropic material with a tetragonal crystal structure and an I41/amd space group.¹⁰ Because of the anisotropy of Sn, Hsu and Lu used a template-free PVD process to grow Sn nanowires with {200} facets.⁵ On the other hand, Tokur et al. were able to produce Sn NRs using an electrolytic coating on nickel foam at room temperature, wherein NR growth was accompanied by a change in peak current density.⁷ The template supported electrochemical deposition method has been used to synthesize segmented nanowires containing Sn for studying the use of Sn as nanosolder.^{13,14} Gao et al. synthesized Sn NRs for lead-free solder material using electrodeposition in nanoporous templates, i.e., anodized alumina (AAO).¹³ Using a similar method, Zhou et al. prepared segmented Cu/Sn nanowires for an in situ TEM study of interface propagation during a metallurgical reaction.¹⁴ This template-directed method can be used to control the size, shape, and elemental multiple segment of the formed NRs; however, methods in removing the template could harm the formed NRs, and thus a chemical synthesis of Sn NRs is preferable.¹⁵ In producing NRs under chemical synthesis, the type and concentration of the ligand have often been considered as the major factors that dictate the produced morphology. Ligands or capping agents are thought to modify the surface energy and kinetic attachment of precursors (atoms, clusters, and ions) to nuclei, leading to anisotropic growth and thus the ability to dictate the shape of the produced nanomaterial.^{11,16-18} However, when Sn was synthesized using chemical reduction of metal salts at high temperatures (100–160 °C), spherical β -tin nanoparticles (NPs) were formed regardless of the amount of stabilizing agent used.¹⁹⁻²² This is due to the lower melting point (232 °C for bulk Sn, and 177 °C for 11 nm Sn NPs),²¹ meaning the spherical morphology is the most stable structure for Sn NPs obtained via high-temperature chemical reduction. To alter the morphology of Sn formed by a chemical synthesis, besides addition of a ligand/capping agent, decreasing the temperature is necessary.¹⁶ However, only the influence

of the type and concentration of capping species has been investigated, and the effect of temperature on the growth of anisotropic Sn NPs has not been studied so far. While some studies employed low temperature synthesis, they were not able to discuss its effect on the formed NRs. Cui et al. synthesized β -Sn in an aqueous solution of tin sulfate at room temperature; they reported that the concentration of the sodium dodecyl sulfate (SDS) capping ligand was the most important parameter in the formation of β -Sn NRs. They demonstrated the SDS-mediated NP agglomeration mechanism. At insufficient ligand concentrations, the SDS did not completely cover the Sn NPs and nuclei, so they merged to form large spherical Sn particles. In contrast, enough or excess amounts of SDS allowed for the adsorption of SDS on certain crystalline surfaces. This helped to reorient and grow the low-surface-energy planes via free SDS exchange between the solution and the NR surface.²³ Gu et al. also synthesized β -Sn and Sn/In NRs using SDS as a capping agent in DI water, but instead of synthesizing at room temperature, low temperature synthesis, i.e., 0 °C, was utilized. On this study, the authors investigated the effect of the stirring speed and the rate of injection of NaBH₄ in the aspect ratio of the formed NRs.¹⁵ So far, the formation of Sn NRs has not been reported using a chemical synthesis in an organic solvent, nor with respect to the influence of temperature and viscosity of the reaction solution. In the present study, for the first time, we propose a sub-room temperature synthesis to form Sn NRs based on the reduction of tin(II) acetate in propanol by sodium tetrahydroborate (NaBH₄), in the presence of the polymer stabilizing agent poly(vinylpyrrolidone) (PVP). Various low synthesis temperatures, from -15 to 26 °C, and solution viscosities attained using different PVP amounts, were systematically studied to understand their influence on the formation of the rod-like Sn morphology. We found that the formation of β -Sn NRs was induced by lowering the reaction temperature and increasing the viscosity of the reaction solution, with the aid of the bridging flocculation effect of PVP. Both temperature and viscosity regulate the kinetic energy of the particles (cations, atoms, and

clusters) in the solution and thus play an important role in controlling the reduction rate of the tin salt, preferential growth, and shape formation of the Sn particles. Furthermore, the change in the length and aspect ratio of the produced Sn NRs were compared according to the solution viscosity by using different amounts and molecular weights (MW) of PVP at the same synthesis temperature. We could attribute the formation of longer and higher aspect ratio NRs to the bridging flocculation effect of PVP. Therefore, the longer the polymeric chain, the higher the chance it will attach to more particles that it can bridge together to form longer NRs with higher aspect ratios.

2.2. Methodology

2.2.1. Chemicals

Tin(II) acetate, Sn(ac)₂ (97% purity), and NaBH₄ (95% purity) were purchased from Wako, Japan. PVP K15 (MW 10 000) and K90 (MW 630 000) with 95% purity were purchased from Tokyo Chemical Industry Co., Ltd. (TCI). PVP K30 (MW 40 000) was purchased from Junsei, Japan. 1-Propanol (99.5% purity) was also purchased from Junsei and dehydrated using molecular sieves (3A 1/16) before use. All other chemicals were used without further purification.

2.2.2. Synthesis of β -Sn Nanorods at Different Temperatures

The chemical synthesis of Sn NRs was conducted in a two-necked round bottom flask (200 mL) under Ar using an air-free Schlenk line technique. Sn(ac)₂, PVP, NaBH₄, and 1-propanol were used as the Sn precursor, capping agent, reducing reagent, and solvent, respectively. In a typical synthesis, 3.0728 g of PVP K90 (MW 630,000) and 0.36 g of Sn(ac)₂ were added consecutively to 50 mL of 1-propanol in a two-necked flask and dissolved for 15

min and 1 h under vigorous stirring, respectively. The flask was then cooled using a low-temperature pairstirrer (EYELA, PSL-1400) to different temperatures: 26, 10, 5, 0, -10, and -15 °C. A total of 0.5775 g of NaBH₄ was dispersed in 10 mL of 1-propanol in another three-necked 100 mL flask under Ar and was cooled to 0 °C. This mixture was then added to the PVP-Sn(ac)₂ solution and allowed to react for 15 min. The as-synthesized solution was purified three times through further dispersion in 1-propanol (at -35 °C) with a 1:10 volumetric ratio of the as-synthesized solution to 1-propanol, and centrifugation at 15 000 rpm for 30 min at -5 °C.

2.2.3. Synthesis of β -Sn Nanorods Using Different Amounts and MW of PVP

Similar synthesis procedures were performed at 0 °C. To investigate the effect of the amount of PVP, various amounts were used: 0.3073, 1.5364, 3.0728, and 6.1456 g, corresponding to 2.76, 13.82, 27.65, and 55.29 mmol, respectively of the PVP K90 monomer with MW of 630 000. When the effect of the MW of PVP was studied, 3.0728 g of PVP with different MWs (10,000, 40,000, and 630,000) were used, corresponding to PVP K15, K30, and K90, respectively.

Table 2.1 summaries the experimental conditions for investigating the influence of temperature, and the amount and molecular weight of PVP.

Table 2.1. Summary of Experimental Conditions to Investigate the Effect of Temperature, Amount and Molecular Weight (MW) of Poly(vinylpyrrolidone) (PVP) in the Formation of Sn Nanorods.

Synthesis parameters	Parameter of Interest		
	Temperature effect	Amount of PVP	MW of PVP
Temperature	-10, 0, 10, 26 °C	0 °C	0 °C
PVP MW (type)	630000 (K90)	630000 (K90)	630000 (K90), 40000 (K30), 10000 (K15)
Amount of PVP (unit: 3.0728 g)	×1	×1/10, ×1/2, ×1, ×2	×1

2.2.4. Characterization

The crystalline and phase structures of the produced NRs were characterized using X-ray diffraction (XRD, Rigaku Miniflex II X-ray diffractometer, Cu K α radiation, $\lambda = 1.5418$ Å). The mean crystalline size was estimated based on the Scherrer formula. The chemical states of Sn on particle surface were characterized using X-ray photoelectron spectroscopy (XPS, JEOL photoelectron spectrometer (ESCA), JPS-9200, monochromatic Al- K α). The morphology of the produced NRs was examined using a transmission electron microscope (TEM, JEOL JEM-2000FX, 200 kV, and JEM-2010, 200 kV), while the crystal growth and surface plane were analyzed using a scanning transmission electron microscope (STEM, JEOL JEM-ARM200F, 200 kV). In determining the equilibrium shape of β -Sn, the Wulff construction was performed with the aid of the online Wulffman software.²⁴

2.3. Results and Discussion

2.3.1. Structure and Morphology of Sn NPs at Various Synthesis Temperature

The crystalline and phase structures of the as-synthesized Sn NPs at different synthesis temperature (-15 to 26 °C) are shown in Figure 2.1. It is evident that for all synthesis temperatures from 0 to 26 °C, β -Sn particles with a tetragonal crystal structure (JCPDS 04-0673) were formed. However, as the synthesis temperature were further reduced to -10 °C and -15 °C, SnO, SnO₂, and/or unreacted tin(II) acetate were observed aside from β -Sn (Figures 2.1 and S2.1).

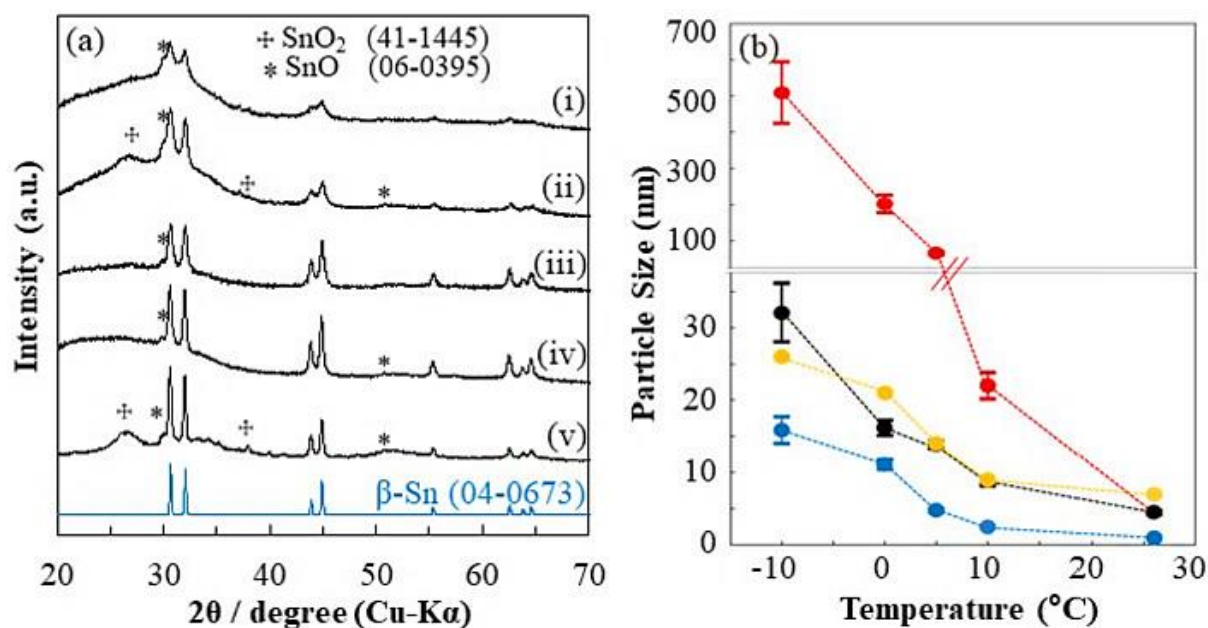


Figure 2.1. (a) XRD pattern of Sn particles produced at different synthesis temperatures: (i) 26 °C, (ii) 10 °C, (iii) 5 °C, (iv) 0 °C, and (v) -10 °C[§]. (b) Interval plot of particle size versus synthesis temperature (95% confidence interval (CI) for mean size) where the red, black, blue, and yellow lines correspond to length, diameter, aspect ratio, and mean crystalline size of the produced particles, respectively; [§] number of particles counted was only ~ 10 .

The presence of tin oxides was due to the byproduct produced during the ongoing reduction of Sn as it was being purified with 1-propanol. During the reaction of tin(II) acetate and NaBH₄ in 1-propanol, Sn²⁺ is reduced to Sn⁰. However, at the low temperatures of -10 °C and -15 °C, the reduction occurred more slowly than at 0 °C, 5 °C, 10 °C, and 26 °C, and hence the 15 min reaction time was not enough to complete the reduction of tin(II) acetate. During the purification process, the ongoing reaction of Sn(ac)₂ and the existence of oxygen resulted in the formation of tin oxides and unreacted Sn(ac)₂. As shown in Figure S2.1, when the synthesis was conducted at -15 °C for 15 min reaction time, the obtained XRD peaks correspond to tin(II) acetate and tin oxides. As the reaction time was prolonged, the peaks that correspond to Sn(ac)₂ and/ or tin oxides disappeared, and all obtained peaks correspond to β-Sn clearly observed after 44 h reaction. Likewise, when the reaction was prolonged at -10 °C, we observed the same phenomenon (Figure S2.2). On the basis of the TEM images (Figure S2.3), as the reaction time increases from 15 min to 5 h, the relative amount of spherical particles (~2.6 nm) decreases.

As the synthesis temperature increases from 0 to 26 °C, the XRD peaks become broader (Figure 2.1a), indicating that the mean crystalline size of the produced particles becomes smaller (Table 2.2, Figure 2.1b). On the basis of the TEM image (Figure 2.2), it can be confirmed that the broadening of the XRD peaks from 0 to 26 °C was due to the decrease in the particles size (i.e., length and diameter). At room temperature, i.e., at 26 °C, spherical Sn NPs with a mean diameter of 4.5 nm were obtained. When the synthesis was conducted at 10 °C, Sn NRs (8.5 nm in diameter and 22.0 nm in length) with a low aspect ratio of 2.5 started to form. At 0 °C, longer Sn NRs with a higher aspect ratio of 11.1 were obtained (Figures 2.2d and S4). However, at -10 °C, fewer NRs were observed and had an aspect ratio of 15.8. When the synthesis was conducted at -10 °C, aside from the formation of few β-Sn NRs, a noticeable

increase in the formation of 2.6 nm spherical SnO_x/unreacted Sn(ac)₂ NPs were observed; the byproduct formed during the purification process becomes prominent. When the synthesis temperature was further reduced to -15 °C (below this is not possible since PVP will become insoluble in 1-propanol), formation of single crystal β-Sn NRs was not observed, and the majority of the particles formed were the 2.6 nm spherical SnO_x/unreacted Sn(ac)₂ NPs attributed to the purification byproduct (Figures 2.2f and S2.1). Increasing the reaction time to 44 h to complete the reduction and growth of Sn, the byproducts disappeared and Sn NRs with an aspect ratio of 22.9 were observed (inset of Figure 2.2f).

Table 2.2. Summary of the Particle Sizes of the Produced Nanoparticles under Different Synthesis Conditions, and Poly(vinylpyrrolidone) (PVP) Quantities and Molecular Weights (MW).

Experimental conditions	d_{TEM}^a			d_{XRD} (nm)	
	Diameter (nm)	Length (nm)	Aspect Ratio		
Temperature effect (°C)	26	4.5 ± 2.1	-	1	7
	10	8.5 ± 2.4	22.0 ± 15.6	2.5 ± 1.2	9
	5	13.8 ± 4.0	66.7 ± 33.4	4.8 ± 1.9	14
	0	16.2 ± 7.8	202.1 ± 174.3	11.1 ± 5.0	21
	-10 ^b	32.0 ± 6.5	508.6 ± 136.1	15.8 ± 3.0	27
	-15 ^c	42.9 ± 13.1	971.6 ± 398.1	22.9 ± 7.8	48
PVP amount (unit: 3.0728 g)	×2 ^b	25.4 ± 12.4	489.5 ± 204.3	21.2 ± 9.7	23
	×1	16.2 ± 7.8	202.1 ± 174.3	11.1 ± 5.0	21
	×1/2	13.6 ± 7.3	149.2 ± 150.0	9.7 ± 4.9	19
	×1/10	9.3 ± 2.2	21.2 ± 13.1	2.56 ± 1.0	19
MW of PVP	K15	8.4 ± 2.1	15.8 ± 7.6	1.9 ± 0.9	5
	K30	14.8 ± 6.7	58.3 ± 50.8	3.8 ± 1.9	16
	K90	16.2 ± 7.8	202.1 ± 174.3	11.1 ± 5.0	21

^a d_{TEM} is particle size measured using TEM images; d_{XRD} is the mean crystalline size estimated from XRD line broadening based on the Scherrer formula using the Sn (200) peak. ^b Number of particles counted was only ~10. ^c The NRs measured was obtained after 44 h reaction time.

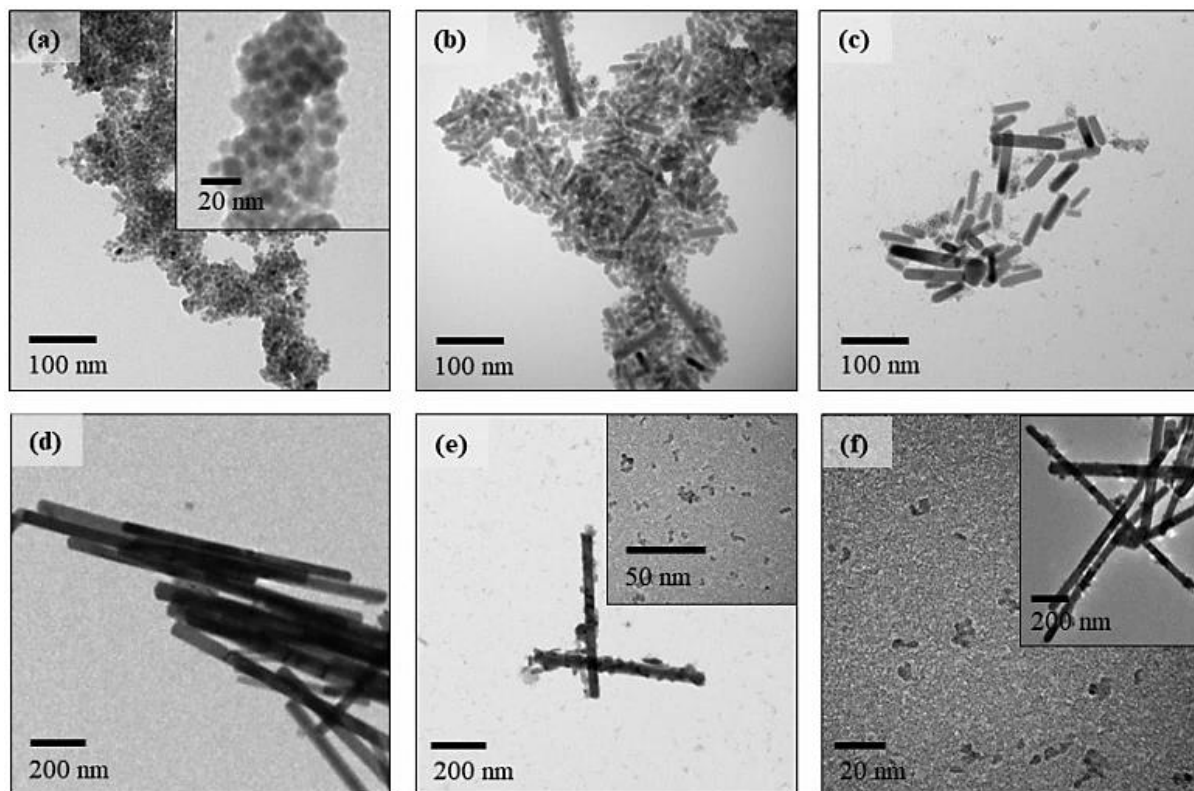


Figure 2.2. TEM images of the nanoparticles formed after 15 min reaction time at various synthesis temperatures: (a) 26, (b) 10, (c) 5, (d) 0, (e) -10 , and (f) -15 °C. Inset of (a) shows high magnification image of Sn particles obtained at 15 °C and inset of (f) shows Sn nanorods obtained after 44 h reaction time at -15 °C.

2.3.2. Growth Direction of Sn NRs and Analysis of Particle Surface

The crystal structure of Sn NRs with respect to their growth direction was analyzed using high-angle annular dark-field (HAADF) STEM images of the tip (Figure 2.3a), and selected area diffraction (SAED) patterns along the rod (Figure 3d) and the tip (Figure 2.3e) of a β -Sn NR synthesized at 0 °C. Both STEM-HAADF and SAED results indicate that the formed β -Sn NRs have single crystal structure. The result clearly indicates that the surface of the single crystal NR was composed of atoms that were stacked in a hexagonal arrangement as shown in Figure 2.3b, which corresponds to the arrangement of atoms at (020) as shown in Figure 2.3c. It can also be observed that the Sn NR grew along the [001] direction (c-axis) of the tetragonal

structure of β -Sn, while the sides of the NRs are composed of $\{200\}$ planes (Figure 2.3a). This observation is in good agreement with the results obtained by other researchers using different synthesis methods, such as vapor–solid growth,⁵ electrochemical deposition,⁷ and aqueous solution synthesis.²³ This phenomenon can be explained by the difference in the surface energy of each crystallographic plane of β -Sn. For β -Sn with a tetragonal unit cell, (100) has the lowest surface energy.²⁵ On the basis of the constructed Wulff image of β -Sn (Figure 2.4), with reference to the surface energies of each crystallographic plane, the lowest energy (100) plane is at its facets. In order for a particle to be stabilized, the total surface energy should be at its minimum, i.e., the majority of its surface should be composed of low-surface-energy planes, and in the case of β -Sn, the surface should be composed of $\{200\}$. This is in good agreement with the structure and morphology of the formed NRs with growth occurring along the [001] direction and facets of $\{200\}$ planes.

β -Sn is known for being susceptible to oxidation upon contact with air and thus β -Sn nanoparticles normally have a core–shell structure, i.e., tin oxide coated β -Sn nanoparticles.²⁶ We observed a similar core–shell structure in HAADF image (inset of Figure 2.3a). Low contrast of the shell indicates a surface oxide layer with thickness of 3–7 nm. The oxide layer appeared amorphous in HAADF and SAED analysis (Figure 2.3). We further analyzed the surface layer of Sn NRs with XPS. The narrow scan for Sn 3d (Figure S2.5) can be deconvoluted to three curves of Sn, Sn^{2+} in SnO, and Sn^{4+} in SnO_2 with $3d_{5/2} / 3d_{3/2}$ peak positions at 484.21 eV/492.665 eV, 486.589 eV/ 494.614 eV, and 488.627 eV/496.577 eV, respectively. The spin–orbit splitting energies were 8.46, 8.03, and 7.95 eV for Sn, Sn^{2+} , and Sn^{4+} components respectively, which is near the reported values corresponding to Sn, SnO, and SnO₂ respectively.²⁷ Sn^{2+} (in SnO) was the main component of the Sn 3d spectrum of the particle surface followed by Sn^{4+} (in SnO_2). The curve for metallic Sn was also observed as a

minor contribution of Sn 3d spectrum, suggesting that the surface oxide layer is very thin. This XPS result is in good agreement with the surface tin oxide layer observed in the inset of Figure 2.3a.

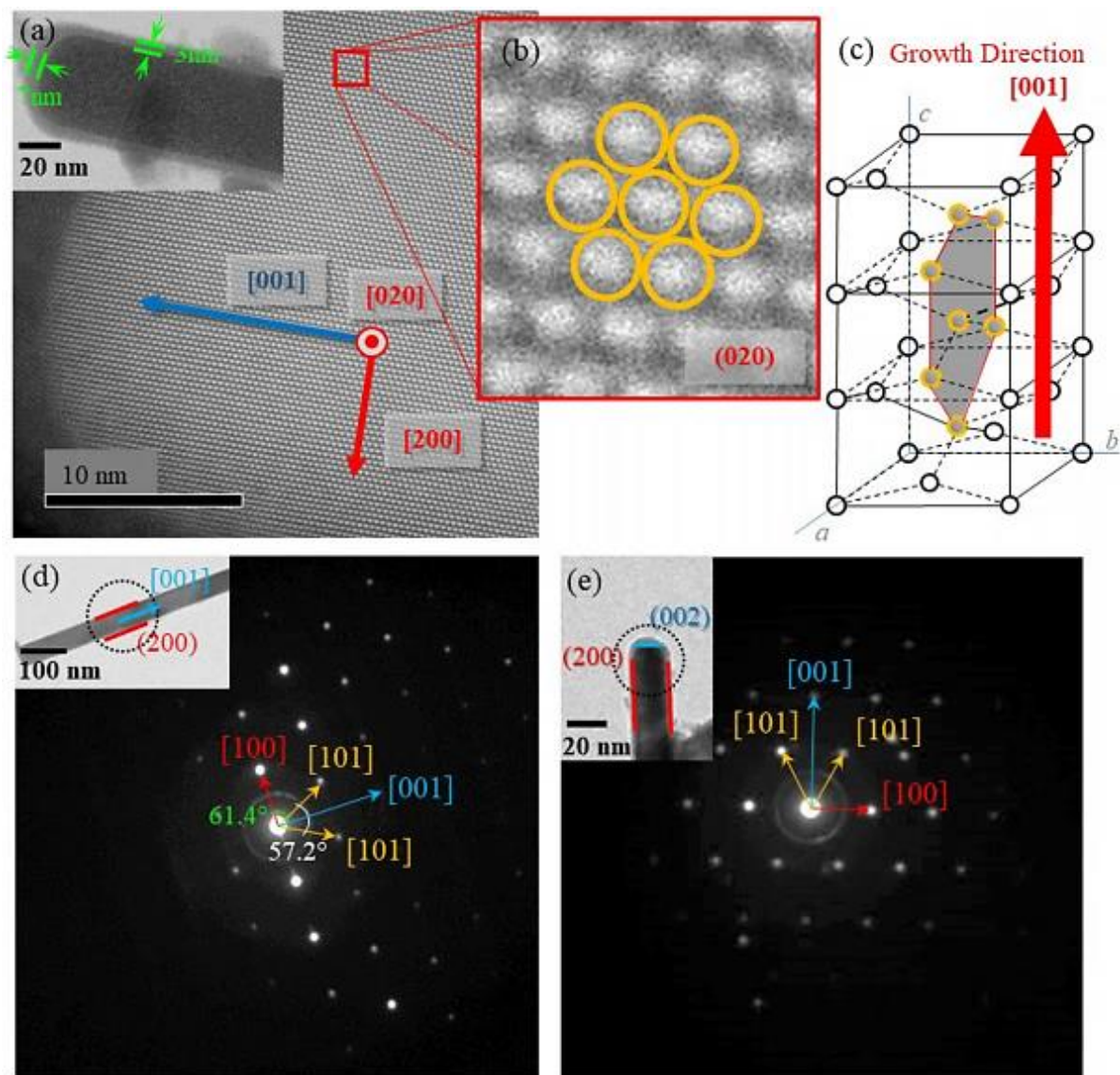


Figure 2.3. (a) HAADF-STEM image of the tip of a Sn nanorod; inset is the TEM image. (b) Magnified image of the area shown in (a) that corresponds to the (020). (c) Stacked β -Sn unit cell indicating the (020) plane with respect to the [001] growth direction. Panels (d) and (e) are SAED patterns along and at the tip of a NR respectively.

Surface oxides are usually inappropriate in most metal NP applications such as solder materials²⁸ where the absence of surface oxides was required for complete nanosolder melting of Sn/Ag NRs.^{13,28} On the other hand, when Sn was used as anode materials for lithium ion batteries (LIBs), Courtney and Dahn showed that oxides do not have a negative effect. They found that oxides irreversibly react first with lithium to form lithia (Li_2O) before forming an alloy with β -Sn. During delithiation process, only β -Sn will be reformed, and the irreversible lithia “matrix” helps keep the electrode particles mechanically connected together, i.e., “glue” the Sn particles together.²⁹

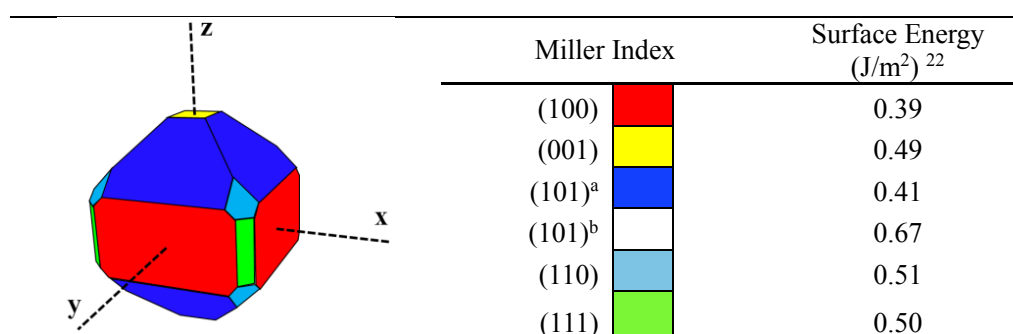


Figure 2.4. Wulff-constructed equilibrium shape of β -Sn with respect to the surface energies.

2.3.3. Discussion on the Temperature-Dependent Growth Mechanism of Sn NRs

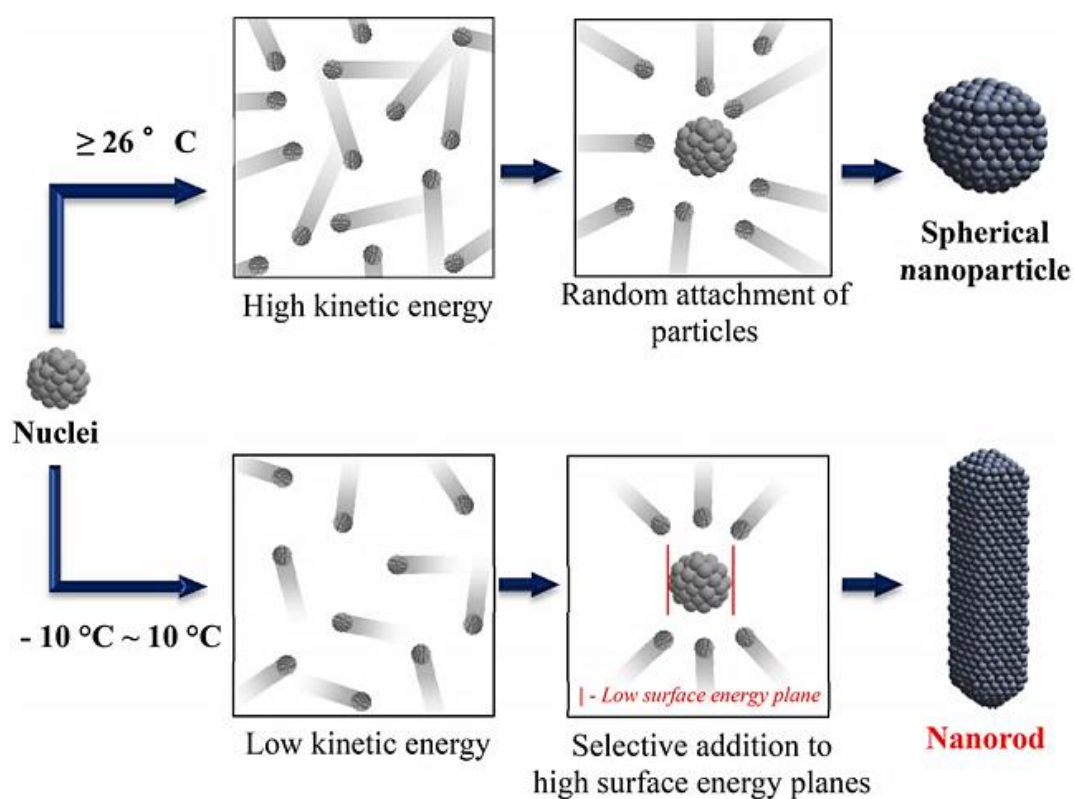
The reaction temperature is the determining factor of the metal precursor reduction rate and the Brownian motion of nuclei, atoms, cations, and molecules (hereafter called particles) in the reaction solution. A change in Brownian motion changes the kinetics of the addition of metal atoms toward different crystal facets of the growing nuclei, thus directing the growth of the Sn NPs toward different shapes. In particular, the addition of metal atoms to high energy surfaces is preferred to reduce the total surface energy of the produced NPs. Analysis of the β -Sn NR in Figure 2.3 reveals that the NR grew along the $[100]$ direction, leaving the lowest surface energy plane at its facets. Therefore, the synthesis temperature can greatly affect the

nucleation and growth process of Sn NPs.

The low reaction temperature-induced NR formation is explained in Scheme 2.1. In general, the reduction of the tin salt is more robust at higher temperatures in terms of producing the saturation condition for nucleation. This leads to a larger number of nuclei being formed and less precursor being left for NP growth, and consequently the size of the resulting Sn NPs is smaller. The lower the reaction temperature, the lower the tin salt reduction rate. As a result, fewer nuclei form and the higher availability of precursor for particle growth can be expected to produce larger Sn particles. This is the reason why we obtained smaller particles (4.4 nm spherical NPs) when the synthesis was performed at 26 °C, but at lower reaction temperatures (10 °C, 5 °C, 0 °C, -10 °C, and -15 °C), larger particles were found (NRs with diameters 8.5 nm, 13.8 nm, 16.2 nm, 32.0 and 43.9 nm, and mean lengths of 22.0 nm, 66.7 nm, 202.1 nm, 508.6 and 971.6 nm, respectively). Moreover, the reaction temperature relates to the kinetic energy, and thereby Brownian motion of the particles in solution, which regulates the selective growth of the nuclei. In particular, particles have higher kinetic energy at high temperatures, move relatively faster and thus can randomly attach to the nuclei regardless of the surface energy of the crystallographic planes. This enhances the random attachment during the particle growth. These effects resulted in Sn NPs with a spherical morphology obtained in the synthesis at 26 °C. On the other hand, particles with low kinetic energy preferentially attach to high-surface-energy planes to minimize the total surface energy of the nuclei. Therefore, lowering the synthesis temperature (10 °C to -10 °C) directed the growth of Sn along the c-axis with the formation of {200}, the plane with the lowest surface energy, as its facet. As a result, the lower the synthesis temperature, the longer the Sn NRs (higher aspect ratio) with preferential growth along the c-axis were formed, as shown in Figure 2.2. It can also be observed that lowering the synthesis temperature, the standard deviation of the particle size increases as shown in Table

2.2, which indicates the decrease in the uniformity of the growth of particles as the synthesis temperature decreases. This decrease in growth uniformity can be attributed to both the decrease in reduction speed and the mobility and hence the kinetics of the particles that dictates its preferential attachment.

Scheme 2.1. Formation Mechanism of β -Sn Nanoparticles with Different Morphologies (Spherical Nanoparticles and Nanorods) with Respect to Temperature.



However, at a very low synthesis temperature of -15°C , the formation of fine SnO_x /unreacted $\text{Sn}(\text{ac})_2$ NPs (2.6 nm) was observed in the absence of single crystal Sn NRs after 15 min reaction time. We think that such a low temperature significantly decelerates the reduction of Sn and makes the reaction solution highly viscous (PVP solidifies just below -15°C), and thus reduces both the reduction rate and the interaction between the produced Sn particles. This prevented the growth and formation of crystalline Sn NRs, and hence only

SnO_x/unreacted Sn(ac)₂ NPs were formed. Longer reaction time was needed for the reduction of Sn to occur and to form the single crystal β-Sn NRs at very low temperature as evident with formation of Sn NRs after a 44 h reaction at −15 °C (Appendices A.1 and A.2f). Those SnO_x/unreacted Sn(ac)₂ NPs were observed to form at the same time as Sn NRs for other synthesis temperatures (5 °C and −10 °C), but their relative population decreased with an increase in temperature.

2.3.4. Effect of the Capping Agent (PVP) on the Morphology of Sn NPs

In the absence of the PVP capping ligand, when Sn²⁺ was reduced to form Sn⁰, the Sn NPs grew over time and agglomerated to form big particles with spherical or irregular shapes even at very low temperatures (−25 °C, Figure S2.6) due to the Ostwald ripening effect.³⁰ Therefore, besides the synthesis temperature, PVP plays an important role in the formation and morphology of chemically synthesized NPs. PVP stabilized the produced NPs and thus prevented their coalescence and growth. Moreover, we note that without PVP, the reaction solution was inviscid compared to the solutions containing PVP. Because the motion of particles in the solution not only depends on temperature but on the viscosity of the solution as well, the presence of PVP may help mediate particle growth as it dictates the viscosity. Therefore, we varied the viscosity of the reaction solution by varying the amount and the MW of PVP at 0 °C to investigate the influence of PVP on the morphology of Sn.

To determine the influence of PVP concentration on NR formation, various amounts of PVP (0.3073, 1.5364, 3.0728, and 6.1456 g) were used, which correspond to one tenth (× 1/10), half (× 1/2), standard (× 1), and double (× 2) the amounts of the standard quantity of PVP (3.0728 g). It was found that varying the amount of PVP also yielded particles with β-Sn crystal structure together with some minor peaks that correspond to SnO (Figure S2.7). In addition, as

the amount of PVP increases from 0.3073 g ($\times 1/10$) to 3.0728 g ($\times 1$), longer and higher aspect ratio NRs was obtained (Figure 2.5). However, with a further increase in the amount of PVP ($\times 2$), a few NRs with an aspect ratio of 25.4 were formed (Figure 2.5), while there was an increase in the number of small NPs. The increase of the average aspect ratio from 11.1 to 25.4 as the amount of PVP increased from one ($\times 1$) to double ($\times 2$) the amount of the standard PVP quantity was not due to the formation of longer and higher aspect ratio NRs; rather, this was due to the fewer small aspect ratio NRs produced. These observed phenomena were similar to the formation of Sn NRs and small NPs when the synthesis temperature was reduced from 0 to -10 °C. On the other hand, using one tenth of the standard amount of PVP at 0 °C, the NRs produced have an aspect ratio of 2.6, which is similar to that of the NRs produced when the synthesis temperature was conducted at 10 °C using the standard amount of PVP. Since this result is similar to the effect of synthesis temperature, it is expected that the change in the morphology was also caused by the Brownian motion of the particles in solution that dictates their kinetic energy.

The Brownian motion of particles in the solution is not only a function of temperature but also of viscosity, to which particle movement is inversely proportional. Varying the amount of PVP in the solution greatly varies its viscosity (Figure 2.5e). Using different amounts of PVP, i.e., 0.3073, 1.5364, 3.0728, and 6.1456 g, created solutions with viscosities of 2.4, 41.9, 149.1, and 777.0 cP, respectively (green in Figure 2.5e). An increase in the viscosity decreases the mobility of the particles and thus their kinetic energy, and vice versa. Hence, at higher quantities of PVP (higher solution viscosity), longer NRs with higher aspect ratios were formed. The trend of the particle size with viscosity mirrors the trend seen with temperature as shown in Figure S2.8.

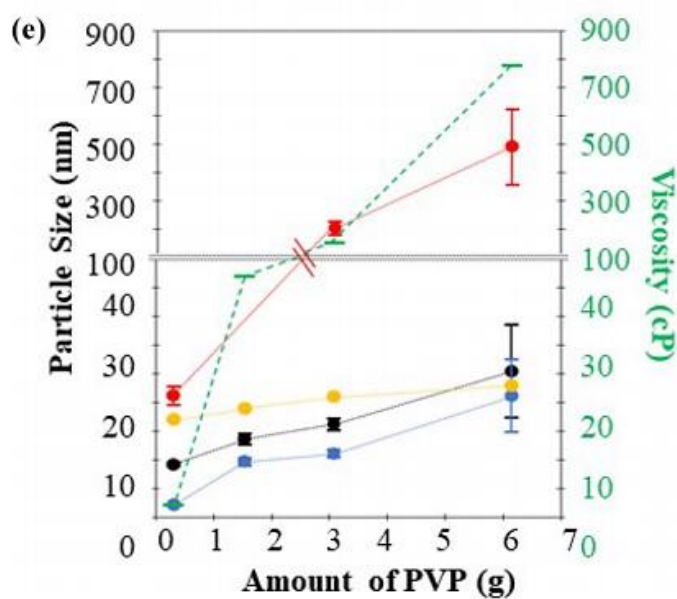
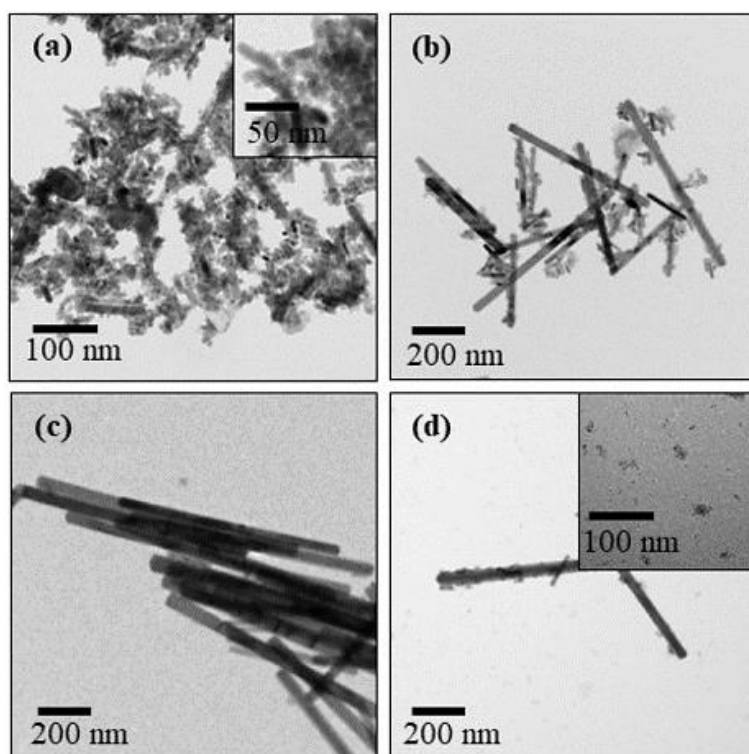


Figure 2.5. TEM image of the particles prepared using different amounts of poly(vinylpyrrolidone) (PVP): (a) 0.3073, (b) 1.5364, (c) 3.0728, and (d) 6.1456 g. (e) Interval plot of the particle size vs amount of PVP (95% CI for mean size) where the green, red, black, blue, and yellow lines correspond to the viscosity of the solution, the length, diameter, aspect ratio, and mean crystalline size of the produced sample, respectively, when using different amounts of PVP.

However, as with too low reaction temperature, too viscous solution also hinders the interaction between particles and hence their growth. That is the reason why using double the amount of PVP ($\times 2$) resulted in fewer NRs and a larger number of spherical 2.6 nm particles. On the other hand, in a less viscous solution, it is expected that the particles will move relatively fast compared to those in a viscous solution and hence will have a higher energy. High energy particles upon collision will not have a preferred attachment and thus form small aspect ratio rods or spherical morphology; this is evident in the samples obtained using 0.3073 g of PVP. This is similar to what occurred when the synthesis temperature was increased, from 10 to 26 °C.

The viscosity of the solution can be altered not only by using different amounts of PVP but also by varying its MW. Increasing the MW of PVP while using the same amount in the synthesis produced a solution with a higher viscosity (Figure S2.8) due to the longer polymeric chains. To further prove the effect of solution viscosity on the growth and morphology of the produced NPs, the capping agent MW was varied using different types of PVP, i.e., K15 (10 000 MW), K30 (40 000 MW), and K90 (630 000 MW). The synthesis was conducted at 0 °C using the standard amount of PVP (3.0728 g). When different types of PVP with different MW were used, β -Sn were formed (Figure S2.9). However, as the MW of PVP increases, the sharpness of the XRD peaks also increase, indicating an increase in the mean crystalline size of the produced β -Sn (Table 2.2). This is consistent with the TEM results of the produced NRs; as the PVP MW increased from 10 000, 40 000, to 630 000, noticeable increase in the lengths (from 15.8 nm, 58.3 nm, to 202.1 nm, respectively) and aspect ratios (from 1.9, 3.8, to 11.1, respectively) were observed (Figure 2.6). On the other hand, the change in the mean diameter of the produced NRs was less significant (8.4 nm, 14.8 nm, to 16.2 nm) as the MW of PVP increased from 10 000, 40 000, to 630 000 respectively. This indicates that high viscosity and

low temperature promote the selective growth of Sn along the c-axis.

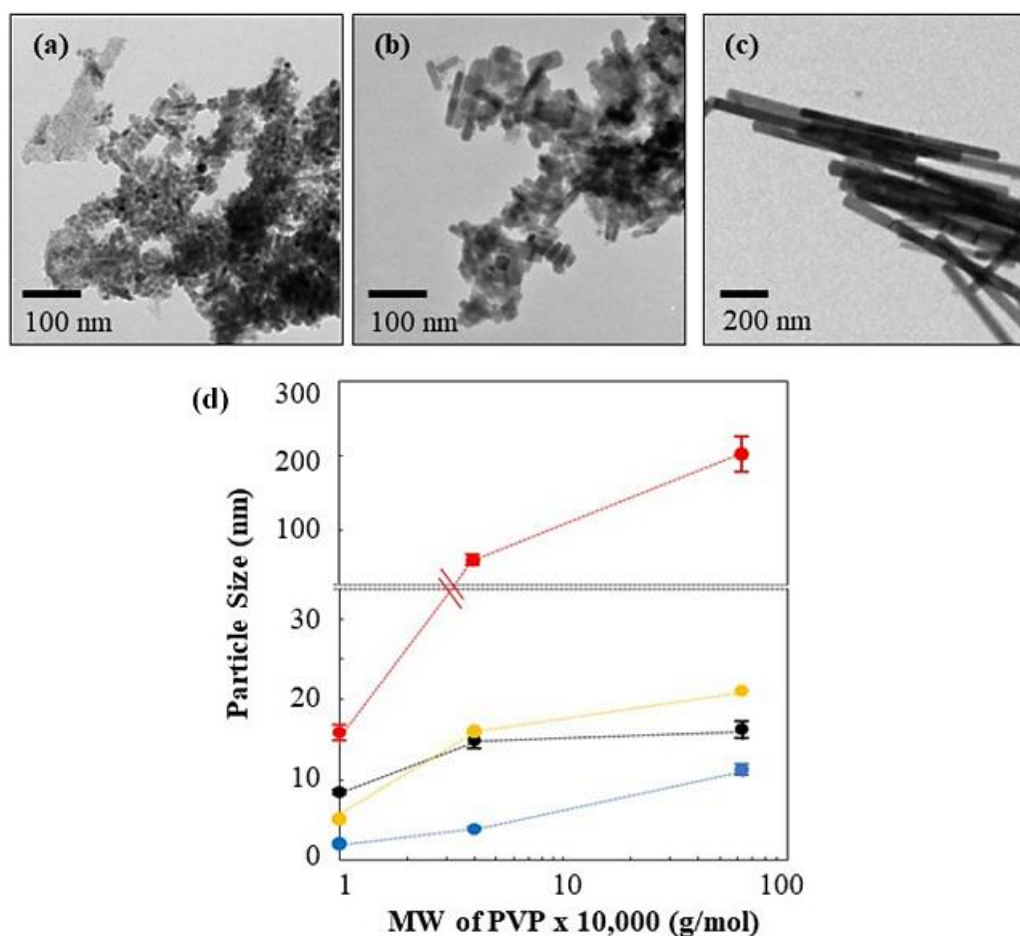


Figure 2.6. TEM image of the particles produced using PVP of (a) 10 000 MW, (b) 40 000 MW, and (c) 630 000 MW. (d) Interval plot of the particle size vs MW of PVP (95% confidence interval, CI, for mean size), where the red, black, blue, and yellow line corresponds to length, diameter, aspect ratio, and mean crystalline size of the particles, respectively.

The increase in the aspect ratio with solution viscosity accompanying the increasing MW of PVP, agrees with the proposed mechanism in Scheme 2.1. However, it was observed that even though 3.0728 g of K15 PVP has a higher viscosity than that of 0.3073 g of K90 PVP at 0 °C, the former produced NRs with a lower aspect ratio of 1.9, compared with the latter case which had an aspect ratio of 2.3. Therefore, other factor, vis., polymeric chain length or

number of repeating units, aside from the solution viscosity contribute to the formation of NRs.

According to the study on Au NRs by Bakshi,¹⁶ as the hydrocarbon chain of the ionic ligand increased, from C12TAB to C16TAB, the aspect ratio of the produced Au NRs also increased from 2 to 3 to 20 respectively, and thus the length of the NRs depends on the surfactant alkyl chain length. In this context, the longer the chain length, the stronger the hydrophobic interaction, which produces a more compact bilayer. This prevents the freshly produced atoms from nucleating, allowing only the ends of the NRs to grow.¹⁶ CTAB has a worm-like micellar structure, i.e., a polar headgroup and hydrocarbon tail, that serves as a solution template to produce rod-like structures.¹⁶ SDS is another capping agent with worm-like micellar structure that is being utilized to form NRs via free SDS exchange mechanism. In this mechanism, as discussed by Cui et al., particle surface can adsorb the free SDS on certain crystalline plane and thus form a rodlike morphology.²³ However, on this study unlike CTAB and SDS, PVP, which has a repeating unit consisting of a pyrrolidone unit attached to a vinyl group, has a “tail and loop” attachment to the particle. The number of repeating units in PVP corresponds to the chain length, which greatly affects how PVP molecules coat and sterically stabilize the NPs. According to the study by Song et al.¹⁸ the influence of PVP on the shape control of Ag NPs was due to both adsorption and steric effects. As capping/stabilizing agent, molecules of PVP adsorb on the surfaces of the particles/atoms and thus stabilize and prevent the further growth and aggregation of the formed NPs (Figure 2.7a). Particles that are sterically stabilized are completely protected by PVP, so further aggregation is prevented due to steric hindrance. Theoretically, as the chain length (i.e., the MW of PVP) increases, the better the coverage and protection due to the long hydrocarbon chain providing a thicker protective layer. However, too great an increase in the MW of the ligand has a negative effect on its stabilizing ability. Since high MW ligands have longer polymeric chains, they can intertwine and attach

to two or more particles (Figure 2.7b). When two or more particles are attached to a single PVP molecule, these particles are bridged together, and hence this is termed the “bridge flocculation” effect.³¹ The change in the aspect ratio of the NRs was partly caused by the change in the MW of PVP and hence the number of repeating units per molecule of PVP. The number of repeating units, i.e., ~90, ~360, and ~5668, corresponds to PVP with a MW of 10 000 (K15), 40 000 (K30), and 630 000 (K90), respectively. The number of repeating units corresponds to the number of functional groups, which is proportional to the number of particles it can attach to and bridge together. Hence K90 PVP, which has highest MW, can bridge higher numbers of particles and thus form larger particles, i.e., longer and higher aspect ratio NRs. To some extent, the bridge flocculation effect can be observed when the synthesis temperature was reduced to as low as $-15\text{ }^{\circ}\text{C}$ at 15 min reaction time and high MW PVP was used. Single-crystalline Sn NRs were not observed, but small Sn and SnO₂ NPs with different crystal orientations aggregated to form some rod-like morphologies (Figures 2.7c and S2.10). At such a low temperature and high MW of PVP, the small fine particles can be bridged together into a rod-like aggregate but may not have enough energy and time for reorientation to form single-crystalline Sn NRs and thus longer reaction time was needed. Ascencio (Univ. Nacional Autonoma de Mexico, private communication, 2008)³² observed with electron microscopy that particles could align their lattice fringes before coagulating to form single particles without grain boundaries. At $0\text{ }^{\circ}\text{C}$, different MW of PVP all yielded a rod-like morphology and the only difference was the resulting aspect ratio of the produced NR. Therefore, the formation of the rod-like morphology was mainly attributed to the synthesis temperature and solution viscosity; varying the amount and MW of PVP greatly affects the preferred attachment of particles, whereas the bridge flocculation effect of PVP aids the formation of longer and higher aspect ratio NRs.

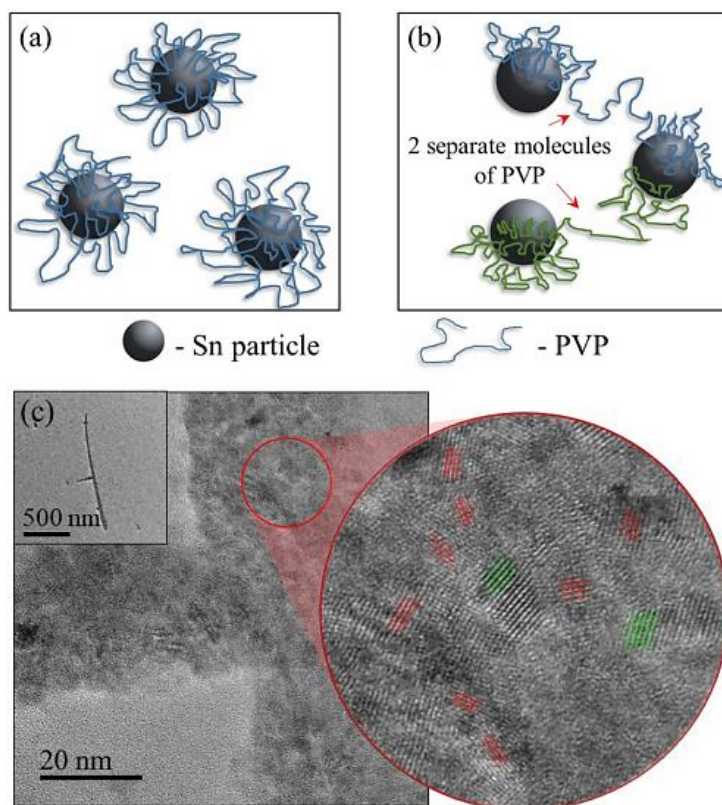


Figure 2.7. (a) A PVP-coated single nanoparticle, and (b) high MW PVP attached to two or more nanoparticles due to its long polymeric chain. (c) HR-TEM image of the rod-like morphology synthesized at $-15\text{ }^{\circ}\text{C}$, with a low magnification TEM image of the whole rod-like particle in the inset, where the green and red lines correspond to SnO₂ (110) and Sn (200) lattice fringes, respectively.

2.3.5. Combined Effect of Temperature and PVP (MW and Amount) on the Formation of Sn NRs

In general, depending on the synthesis temperature and solution viscosity, particles in contact can have a preferred attachment according to the particle's energy to form NRs. PVP as a protective agent can stabilize the NRs via adsorption on their surface and provide a high viscosity for supporting the anisotropic growth along the c-axis. Moreover, PVP with long polymeric chains and repeating functional groups can have an additional effect, bridging particles together during the growth process to form a single particle. In the case of low-

temperature synthesis, i.e., 10 °C to -10 °C, both the alignment of the lattice orientation and the preferred attachment of the particles was affected by the Brownian motion and thus the particle kinetic energy. The low kinetic energy of the particles will not only affect their preferred attachment but also the formation of a single crystal structure. If particles in contact have enough energy to rotate and align lattice orientation, they can form a single crystal NRs, like in the case of the particles synthesized at -10 °C and above. However, if they do not have enough energy, population, and time, i.e., synthesized at -15 °C for 15 min, particles in contact will not form a single crystal but can form a rod like aggregates of small NPs owing to the bridge flocculation effect (Figure 2.7c). Therefore, in formation of single-crystalline NRs, temperature and viscosity play a key role via their effect on the particle kinetic energy that dictates the preferred attachment and the degree it can rotate to align its crystal lattice. On the other hand, PVP is an important parameter that can aid in the stabilization and formation of longer and higher aspect ratio NRs due to its long polymeric chain that bridge particles together to form a single particle.

2.4. Conclusion

β -Sn, which has an anisotropic crystal structure, can form a rodlike morphology. However, having an anisotropic structure does not guarantee the formation of the rod-like morphology in the solution synthesis of Sn NPs. We demonstrated that synthesis parameters such as the temperature and amount and type of PVP used triggered the formation of Sn NRs. We proved that both temperature and the amount of PVP, of which the latter regulates viscosity, control the kinetic energy of particles in the solution. These factors can induce the formation of rod-like β -Sn via promoting the preferential growth along the c-axis. Alternatively, the MW of PVP dictates particle stability and aids in the formation of longer and higher aspect ratio NRs. The selective attachment of low kinetic energy particles is due to the higher attraction

and adhesion of Sn particles/atoms on higher-surface-energy planes of the nuclei. The preferred attachment resulted in a rod-like morphology, leaving the low-surface-energy planes, i.e., {200}, on its facets. PVP also prevents further particle growth via steric stabilization, and bridges particles together by its long polymeric chains bearing repeating functional groups. The higher the MW of the PVP the longer the polymeric chains, and hence the PVP can attach and bridge more particles together to form longer NRs. Both high MW of PVP and low synthesis temperatures, but enough to provide the necessary energy for selective crystallographic attachment and lattice realignment, are necessary to form single crystalline NRs with a high aspect ratio.

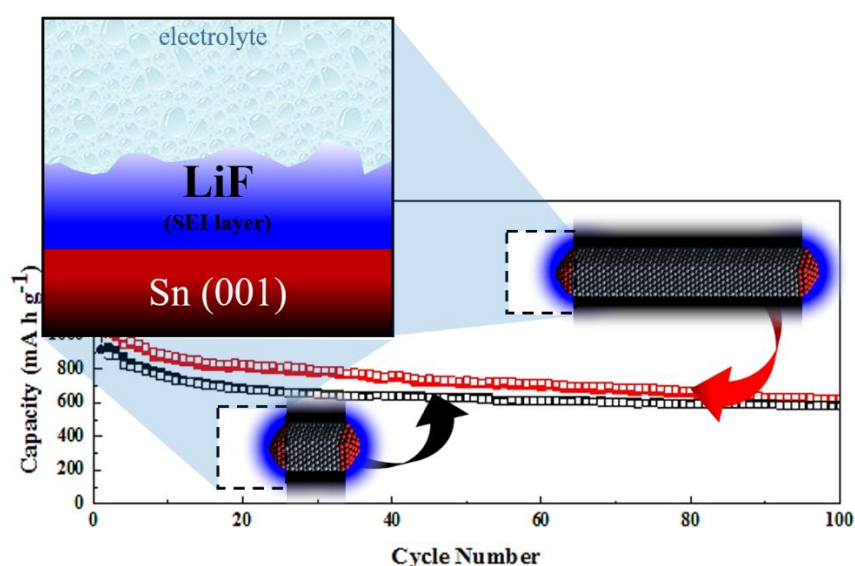
References

1. Vallejos, S.; Selina, S.; Annanouch, F.E.; Grácia, I.; Llobet, E.; Blackman, C., “Aerosol assisted chemical vapour deposition of gas sensitive SnO₂ and Au-functionalised SnO₂ nanorods via a non-catalysed vapour solid (VS) mechanism”, *Sci. Rep.*, **2016**, 6, 28464
2. Roy, P.; Srivastava, K. J., “Nanostructured anode materials for lithium ion batteries”, *Mater. Chem. A.*, **2015**, 3, 2454-2484
3. Choi, N.S.; Yao, Y.; Cui, Y.; Cho, J., “One dimensional Si/Sn – based nanowires and nanotubes for lithium-ion energy storage materials”, *J. Mater. Chem.*, **2011**, 21, 9825-9840
4. Mackay, D., Janish, M., Sahaym, U., Kotula, P., Jungjohann, K., Carter, B., Norton, G., “Template-free electrochemical synthesis of tin nanostructures”, *J. Mater. Sci.*, **2014**, 49, 1476-1483
5. Hsu, Y.J.; Lu, S.Y., “Vapor–Solid Growth of Sn Nanowires: Growth Mechanism and Superconductivity”, *J. Phys. Chem. B*, **2005**, 109, 4398-4403
6. Stagon, S., Huang, H., “Controllable growth of aluminum nanorods using physical vapor deposition”, *Nanoscale Res. Lett.*, **2014**, 9, 400
7. Tokur, M.; Algul, H.; Uysal, M.; Cetinkaya, T.; Alp, A.; Akbulut, H., “Electrolytic coating of Sn nano-rods on nickel foam support for high performance lithium ion battery anodes” *Surf. Coat. Technol.*, **2016**, 288, 62-68
8. Chen, S.; Wang, M.; Ye, J.; Cai, J.; Ma, Y.; Zhou, H.; Qi, L., “Kinetics-controlled growth of aligned mesocrystalline SnO₂ nanorod arrays for lithium-ion batteries with superior rate performance”, *Nano Res.*, **2013**, 6, 243-252
9. Liu, X.; Zhang, F.; Huang, R.; Pan, C.; Zhu, J., “Capping Modes in PVP-Directed Silver Nanocrystal Growth: Multi-Twinned Nanorods versus Single-Crystalline Nano-Hexapods”, *Cryst. Growth Des.*, **2008**, 8, 1916- 1923
10. Al-Salman, R.; Sommer, H.; Brezesinski, T.; Janek, “Template-Free Electrochemical Synthesis of High Aspect Ratio Sn Nanowires in Ionic Liquids: A General Route to Large-Area Metal and Semimetal Nanowire Arrays?” *J. Chem. Mater.*, **2015**, 27, 3830-3837

11. Vollath, D., Nanoparticles-Nanocomposite-Nanomaterials: An introduction for beginners; Wiley-VCH Verlag GmbH & Co., KGaA: Gemany, **2013**; Chapter 5, pp. 79-83
12. Sohn, J.I.; Hong, W.K.; Lee, S.; Lee, S.; Ku, S.; Ku, J.; Park, Y.J.; Hong, J.; Hwang, S.; Park, K.H.; Warner, J.; Cha, S.N.; Kim, J.M., "Surface energy-mediated construction of anisotropic semiconductor wires with selective crystallographic polarity", *Sci. Rep.*, **2014**, *4*, 5680.
13. Bakshi, M. S., "How Surfactants Control Crystal Growth of Nanomaterials", *Cryst. Growth Des.*, **2016**, *16*, 1104-1133
14. Koczur, K.; Mourdikoudis, S.; Polavarapu, L.; Skrabalak, S., "Polyvinylpyrrolidone (PVP) in nanoparticle synthesis", *Dalton Trans.*, **2015**, *44*, 17883-17905
15. Song, Y.J, Wang, M., Zhang, X.Y., Wu, J.Y., Zhang, T., "Investigation on the role of the molecular weight of polyvinyl pyrrolidone in the shape control of high-yield silver nanospheres and nanowires", *Nanoscale Res. Lett.*, **2014**, *9*, 17
16. Shirai, H.; Nguyen, M.T.; Ishida, Y.; Yonezawa, T., "A new approach for additive-free room temperature sintering of conductive patterns using polymer-stabilized Sn nanoparticles", *J. Mater. Chem. C*, **2016**, *4*, 2228-2234
17. Chee, S.S.; Lee, J.H., "Synthesis of tin nanoparticles through modified polyol process and effects of centrifuging and drying on nanoparticles", *Trans. Nonferrous Met. Soc. China*, **2012**, *22*, s707-s711
18. Jo, Y.H.; Jung, I.; Choi, C.S.; Kim, I.; Lee, H.M., "Synthesis and characterization of low temperature Sn nanoparticles for the fabrication of highly conductive ink", *Nanotechnology*, **2011**, *22*, 225701-225709
19. Chee, S.; Lee, J., "Reduction synthesis of tin nanoparticles using various precursors and melting behavior", *Electron. Mater. Lett*, **2012**, *8*, 587-593
20. Cui, Q.; Rajathurai, K.; Jia, W.; Li, X.; Gao, F; Lei, Y.; Gu, Z., "Synthesis of Single Crystalline Tin Nanorods and Their Application as Nanosoldering Materials", *J. Phys. Chem. C*, **2010**, *114*, 21938-21942
21. R. Edwin García; John Blendell (2014), "Equilibrium Wulff Shape Generator," <https://nanohub.org/resources/wulffman>. (DOI: 10.4231/D3C53F234)
22. Qiao, R., Lucas, I. T., Karim, A., Syzdek, J., Liu, X., Chen, W., Persson, K., Kostecki, R., Yang, W., "Distinct Solid-Electrolyte-Interphases on Sn (100) and (001) Electrodes Studied by Soft X-Ray Spectroscopy", *Adv. Mater. Interfaces*, **2014**, *1*, 1300115-1300121.
23. Komari, H.M.; Naseri, M. G.; Saion, E., "A Novel Research on Behavior of Zinc Ferrite Nanoparticles in Different Concentration of Poly(vinyl pyrrolidone) (PVP)", *Metals*, **2014**, *4*, 118-129
24. Myers, D., *Surfaces, Interfaces, and Colloids: Principles and Applications, Second Edition*, John Wiley & Sons, Inc., **1999**, ISBNs: 0-471-23499-0 (Electronic), Chapter 10, pp. 214-252
25. Vollath, D., Nanoparticles-Nanocomposite-Nanomaterials: An introduction for beginners; Wiley-VCH Verlag GmbH & Co., KGaA: Gemany, **2013**; Chapter 3, pp. 21-38

CHAPTER 3

β -Sn NANORODS WITH ACTIVE (001) TIP INDUCED LiF-RICH SEI LAYER FOR STABLE ANODE MATERIAL IN LITHIUM ION BATTERIES



Abstract	107
3.1.Introduction	107
3.2.Experimental Section	
3.2.1. Materials Preparation	111
3.2.2. Electrochemical Test	111
3.3.Results and Discussion	
3.3.1. β -Sn NRs with Different Morphology	113
3.3.2. Electrochemical Measurement	116
3.3.3. Ex-situ Analysis of Rod-like Morphology	123
3.3.4. Mechanism of LiF-rich SEI layer on Low Aspect Ratio NRs	128
3.4.Conclusion	130
References	131

Abstract

β -Sn nanorod (NR) with (200) facets and (001) tip is a potential anode material in lithium ion battery (LIB) due to its good cycle stability that can retain ~ 600 and 550 mA h g^{-1} after 100 cycles using 0.2 C for high and low aspect ratios, respectively. The high stability compared to that of spherical nanoparticles can be attributed to the combination of the nanorod morphology that buffers large volumetric change, and the LiF-rich F-containing surface electrolyte interface (SEI) layer that allows for a stable SEI layer, a good ionic and electronic contact. The lower SEI resistivity and high Li^+ diffusivity of low aspect ratio β -Sn NRs resulted in a better cyclability compared to high aspect ratio β -Sn NRs. In addition, low aspect ratio β -Sn NRs have more specific surface area of highly reactive (001) surface, *i.e.*, the tip of the rod, that produces a LiF-rich F-containing SEI layer.

3.1. Introduction

Industrialization and the growing demand for renewable energy require high-performance energy storage devices. Among these storage devices, lithium-ion batteries (LIBs) have attracted much attention, due to its high energy density, high voltage, lightweight, and long life application.¹⁻⁸ However, the commercially produced LIBs that utilizes carbon as anode material restricts its application. The high specific capacity of β -Sn, 994 mA h g^{-1} ($7262 \text{ mA h cm}^{-3}$), that forms an alloy with Li^+ ($\text{Li}_{4.4}\text{Sn}$) made it as an alternative anode material to replace graphite in LIBs. However, the declining of capacities during repeated cycling due to large volumetric change, *i.e.*, $>250\%$, and the consumption of Li in continuous formation of unstable solid electrolyte interphase (SEI) restricts its application.¹⁻⁹ To mitigate the mechanical instability of β -Sn, the use of 1D nanostructure has been extensively studied due to (a) high surface to volume ratio that allows the large Li^+ flux, short Li^+ diffusion, and buffers the large volumetric change (b) the efficient e^- transfer along the length of the rod, and (c) strain

relaxation.^{4,7,8,10-15} Based on the study conducted by Tokur *et al.*, β -Sn nanorods (NRs) have better reversible capacity and cycle stability compared to that of spherical nanoparticles (NPs).⁴ However, it can be observed that the capacity of β -Sn NRs still continuously decreases during the charge-discharge process. Hence, other factors that greatly affect the stability of the anode material should be considered, *vis.* (SEI), to prevent the capacity fading.

In LIBs, SEI layer is formed via the decomposition and/or reduction of electrolyte on any anode materials.^{5,16,17} Depending on the type of SEI layer compound formed, it can either stabilize the anode material or further degrade the electrolyte and consumes additional Li^+ that leads to capacity fading. In general, the SEI layer composes of alkyl carbonates, oxide, ethers, ester, polymeric compounds, and F-containing compounds with Li^+ uptake. The structure and composition of the SEI layer can dictate its Li^+ permeability and electronic conductivity that greatly affect the resistivity of the cell. However, with succeeding charge-discharge cycle, the large volumetric change of the anode material can cause the SEI layer to crack.¹⁶ Therefore, the SEI layer formed on the surface of the anode material should be stable enough to prevent continuous electrolyte decomposition, adhere well, and flexible enough to withstand large volume expansion of the anode material upon charge-discharge cycles, and have high ionic and electronic conductivities.^{5,16-20} In order to improve the quality of the SEI layer, the addition of electrolyte additives, *vis.* fluoroethylene carbonate (FEC) and vinylene carbonate (VC), are being considered. The addition of FEC, a good oxidizing agent, have removed highly oxidized carbon compounds and made a thinner SEI layer during delithiation (an oxidation process where SEI layer forms) in the nano-Sn electrode.^{5,6} According to Markevich *et al.*, the formation of the thin surface film in Si anodes using FEC additive is due to the higher amount of: (a) LiF compared to other F-containing compounds, (b) polymeric oxygen-free organic species than organic and inorganic carbonates, alkoxides, and oxygen-containing polymers,

and (c) $\text{Li}_x\text{PO}_y\text{F}_z$ compared to Li_xPF_y .¹⁸ Seo *et al.* examined the effect of addition of FEC or VC in both the electrochemical performance and formed SEI layer on Sn anodes. The addition of VC results in a high concentration of poly(VC) that results in the cell's high impedance; while the incorporation of FEC contains low concentrations of poly(FEC) but higher concentrations of Li_2CO_3 and LiF .² According to Jaumann *et al.*, the high film resistance for the Li^+ migration on the SEI layer using VC as an additive is likely due to the absence of the defects in the film structure, LiF . FEC derived SEI, on the other hand, have excellent Li^+ conductivity due to the presence of LiF nanocrystals. Thus, the benefits of incorporating electrolyte additives on the cell's capacity retention are merely due to its effect in the formed SEI layer that favors the formation of LiF (in the case of FEC) which contributes to the Li^+ migration through the SEI layer while maintaining the stability and integrity of the SEI layer. Based on several studies on the formed SEI layer on the active materials, aside from the electrolyte additives, the surface crystallographic planes of the active material plays an important role in the composition and structure of the formed SEI layer.^{1,2,21} The work of Qiao *et al.* showed that the SEI layer formed at low surface energy (100) of β -Sn mainly consists of porous Li_2CO_3 with electrolyte uptake. The SEI layer on high surface energy (001) of β -Sn, on the other hand, is a layer of LiF and organic molecules with a small amount of carbonate and electrolyte buried inside.¹ This is because the active (001) surface enabled the decomposition of the electrolyte, LiPF_6 , to form LiF which in turn passivated the active β -Sn surface whereas the porous Li_2CO_3 did not hinder the further decomposition of the electrolyte. However, their study did not cover the Hence, controlling the surface crystallographic planes of the β -Sn anode can be crucial for the cycle stability via fine engineering of the SEI composition and structure. So far, the cycle stability of both crystallographic planes in the form of nanomaterials has not been investigated and hence been the focus of this study.

We have successfully grown single crystalline β -Sn NRs with various controllable aspect ratios with (001) tip and (200) facets via below room temperature synthesis in our previous study.²² Varying the aspect ratios can help change the specific surface area ratio between the active (001) and non-active (100) surfaces, *i.e.*, lower aspect ratio NRs have higher specific area of the active (001) plane than that of the higher aspect ratio NRs. It should be noted that the spherical β -Sn NPs formed at room temperature have (200), *i.e.* the lowest surface energy plane, as the facets. Thus, using β -Sn NRs with different aspect ratio and spherical β -Sn NPs allows us to address the capacity cycle instability of β -Sn by the combined effect of the rod-like morphology and the preferential formation of LiF in (001) crystallographic plane.

In this study, we investigated the electrochemical performance and characterized the LiF-rich F-containing compound SEI layer of single crystal β -Sn NRs with different aspect ratio using an electrolyte with VC-additive. The 1D nanostructure of the formed β -Sn NRs improves both the electrochemical and mechanical stability compared to that of spherical β -Sn NPs. The different aspect ratios of single crystalline β -Sn NRs with (200) facets and (001) tip were utilized in this study to explore the combine effect of the rod-like morphology and the active (001) surface crystallographic plane that can interact with the electrolyte during the charge-discharge process to form LiF-rich F containing SEI layer. The use of electrolyte with VC additive instead of FEC is to exclude the interference of the FEC additive effect on the preferential formation of LiF. Thus, the formation of LiF is merely attributed to the existence of (001) active surface on β -Sn NRs. We demonstrated that instead of the length of the rod, the huge surface area of the (001) active crystal facets of the low aspect ratio NRs, which induces the formation of LiF, is the key factor for the cycle stability of β -Sn NRs.

3.2. Experimental Section

3.2.1. Materials Preparation

β -Sn NRs with different aspect ratio were produced by varying the synthesis temperature, i.e. 0 °C, and 10 °C and 26 °C for high and low aspect ratio NRs respectively, following our previous work.²² Tin(II) acetate ($\text{Sn}(\text{ac})_2$, Wako, Japan), poly(vinyl pyrrolidone, K90 (PVP, M. W. = 360000, TCI, Japan), sodium tetrahydroborate (NaBH_4 , Wako Japan), and 1-propanol (1-PrOH, Junsei) were used as precursors, capping ligand, reducing agent, and solvent respectively. 3.0728 g of PVP K90 and 0.36 g of $\text{Sn}(\text{ac})_2$ were dissolved consecutively in 50 mL 1-PrOH in a 200 mL two-neck round bottom flask and allowed the solution to cool to the desired temperature using a low-temperature pair-stirring machine. In another 15 mL three-neck round-bottom flask, 0.5775 g NaBH_4 was dispersed in 10 mL 1-PrOH and cooled using an ice bath. After the desired temperature was reached, the two solutions were combined and allowed to react for 5 hours while maintaining the necessary temperature constant. The product was purified three times by dispersing the as-synthesized solution in 1-PrOH followed by centrifugation at 15000 rpm for 30 min. The produced NRs were dried in a vacuum oven overnight to remove the excess solvent.

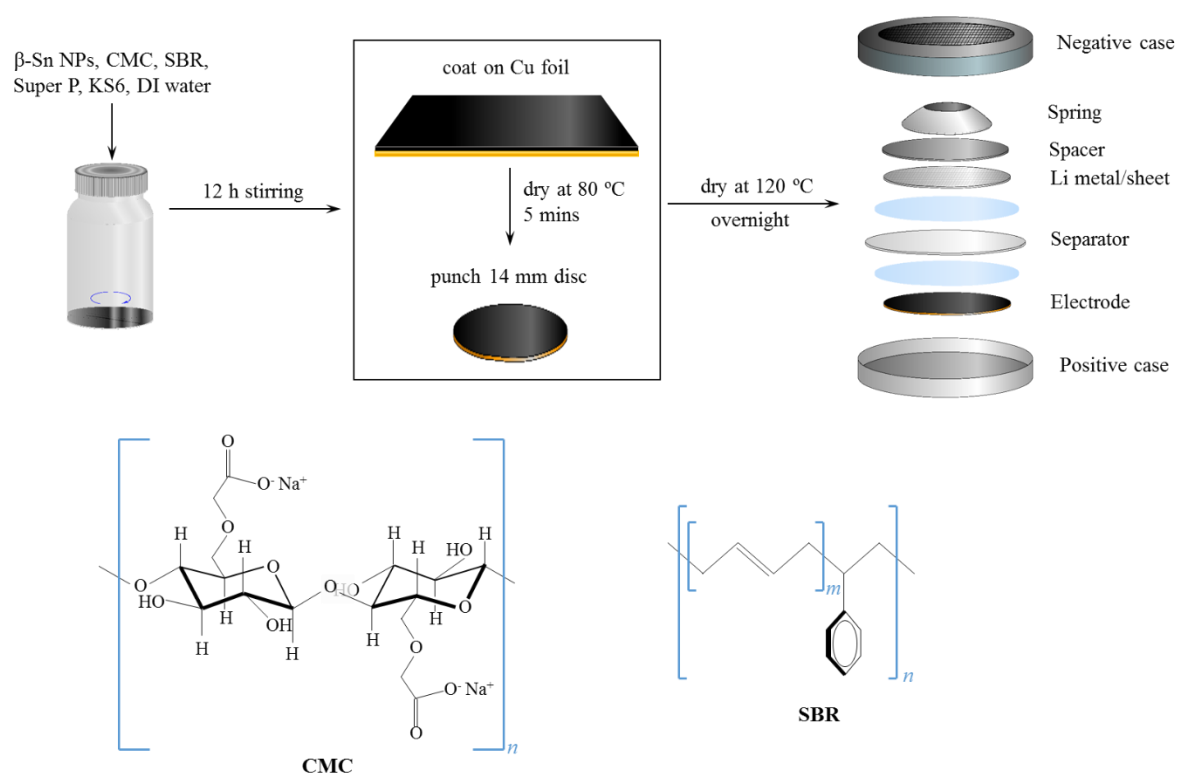
3.2.2. Electrochemical Test

The electrochemical test was conducted using CR2032 Li half-cell with lithium metal disk as the counter electrode (Scheme 3.1). The β -Sn NRs electrode, which served as the working electrode, was prepared by coating a slurry containing of 60 w/w% active material, 25 w/w% KS6 (synthetic graphite with lateral size of 6 μm (d_{90}), Timcal®), 5 w/w% Super P (6 nm Carbon black, Timcal®), 6 w/w% carboxymethyl cellulose (CMC), and 4 w/w% styrene-butadiene rubber (SBR, Asahi Chemicals) onto a 10 μm copper foil. The electrode was dried at 80 °C for 5 min before it was cut into 14 mm disk. It was then completely dried under vacuum

at 120 °C overnight to remove the residual water. The coin cell battery was assembled in an Ar-gas filled glove box with H₂O and O₂ content < 0.5 ppm. Celgard membrane disk (Celgard[®] 2325), and LiPF₆ in ethylene carbonate and ethyl methyl carbonate (EC:EMC 1:1 v/v %) + 2% vinylene carbonate (VC) were used as separator and electrolyte respectively. Both the discharge/charge test and C-rate test were analyzed using AcuTech System in the voltage range of 0.01 V and 3.0 V at room temperature, while the cyclic voltammogram (CV) was measured by CH Instruments Analyzer CHI6273E at a scan rate of 0.1 mV s⁻¹ between 0.01 V and 3.0 V.

The use of 25 and 5 w/w% KS6 and Super P respectively was to improve the quality, i.e. coating coverage and adhesion, of the slurry on the Cu foil. As shown in Figure S3.1, using 20 w/w% Super P in the absence of KS6 resulted in a flaked coating, i.e. cracks were formed after the first drying at 80 °C. While using 25 and 5 w/w% KS6 and Super P respectively greatly improves the coating coverage. It is known that utilizing a large amount of conductive agent and binders for active materials that undergo drastic volume change and with poor conductivity can improve electrical conductivity, facilitate electron transport between the active material and the current collector, i.e. Cu foil, and enhance capacity stability.²³⁻²⁵ However, the improved cycle stability of our experiment is not due to the amount of conductive agent added. Sn is known to have poor cycle stability, even after adding 25 and 5 w/w% KS6 and Super P, spherical Sn NPs still exhibits poor cycling stability, hence the stability of the produced Sn NRs can be attributed to other factors, which will be further discussed under the results and discussion.

Scheme 3.1. Preparation of the CR2032 Li half-cell and the chemical structures of the binder (CMC and SBR) used.



3.2.3. Ex-situ Characterizations

To analyze what occurs in the electrode during the discharge process, the working electrodes were analyzed after coating and after 2.5 cycles. The coin cells were opened inside the Ar-gas filled glove box with H₂O and O₂ content < 0.5 ppm to obtain the working electrodes which were washed several times with dimethyl carbonate (DMC, Alfa Aesar) to remove the excess electrolyte. The phase structures of the working electrodes after coating and after 2.5 cycles were characterized and compared using X-ray diffraction (XRD, Rigaku Miniflex II X-ray diffractometer, Cu K α radiation, $\lambda = 1.5418 \text{ \AA}$). The chemical states of Sn, C, O, and Li on particle surface were characterized using X-ray Photoelectron Spectroscopy (XPS, JEOL photoelectron spectrometer (ESCA), JPS-9200, monochromatic Al-K α). The morphology of the produced electrode was examined using both scanning electron microscope (SEM, JEOL

JSM-6510LA) and transmission electron microscope (TEM, JEOL JEM-2000FX, 200 kV).

3.3. Results and Discussion

3.3.1. β -Sn NRs with Different Morphology

Varying the synthesis temperature, *i.e.*, 26 °C to 0 °C, yields to different morphologies of β -Sn, as shown in Figure 3.1, due to the effect of both the reduction rate and the particle's mobility in the solution as shown in scheme 3.2 as we have reported in our previous paper.²² When the synthesis was conducted at 26 °C, spherical NPs of 4.5 nm were obtained, while low aspect ratio, 2.5, NRs ($d = 8.5$ nm, $l = 22.0$ nm) was formed when the synthesis temperature decreases to 10 °C. A further decrease in the synthesis temperature, *i.e.* at 0 °C, longer and higher aspect ratio NRs, 11.1, ($d = 16.2$ nm, $l = 202.1$) was obtained. Herein we refer to the β -Sn NRs produced at 0, 10 and 26 °C as high aspect ratio NRs, low aspect ratio NRs, and spherical NPs respectively. The formed β -Sn NRs have a single crystal structure that grows along the [001] direction with (200) facets.²²

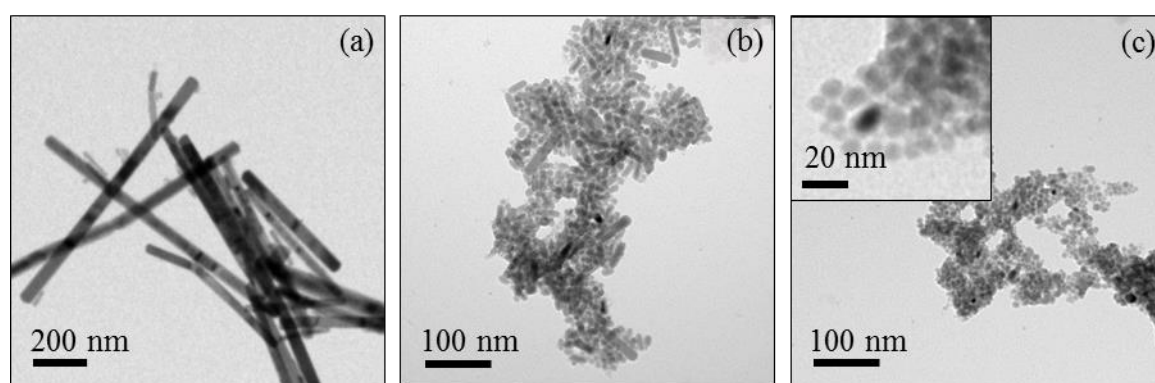
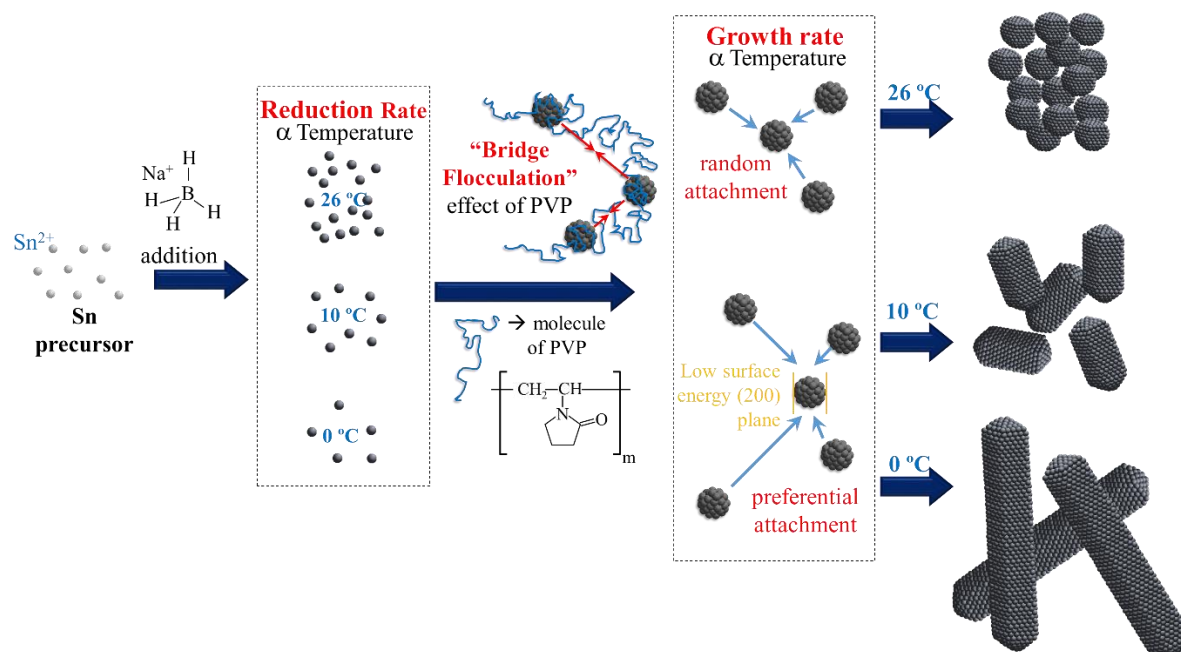


Figure 3.1. TEM images of the nanoparticles formed at different synthesis temperatures: (a) 0 °C, (b) 10 °C, and (c) 26 °C.

Scheme 3.2. The formation of the different aspect ratio of β -Sn NPs with respect to the synthesis temperature.



The micro-strain of the produced β -Sn NPs was analyzed using curve fitting in HighScore Plus v3.0 as shown in Figure 3.2. It was observed that the calculated micro-strain of the produced NRs decreases dramatically from spherical and from low aspect ratio to high aspect ratio β -Sn NRs for each of the crystallographic planes. The decrease in the micro-strain can be attributed to the decrease in the crystallographic defect as indicated by the single crystal property of the produced β -Sn NRs. The decrease in the initial crystallographic defect and thus the micro-strain of the particles is one of the factors that can mitigate the large volume expansion and induces strain relaxation,²⁶ and thus β -Sn NRs, as 1D NP, is expected to have better cycle stability as anode material for LIB.

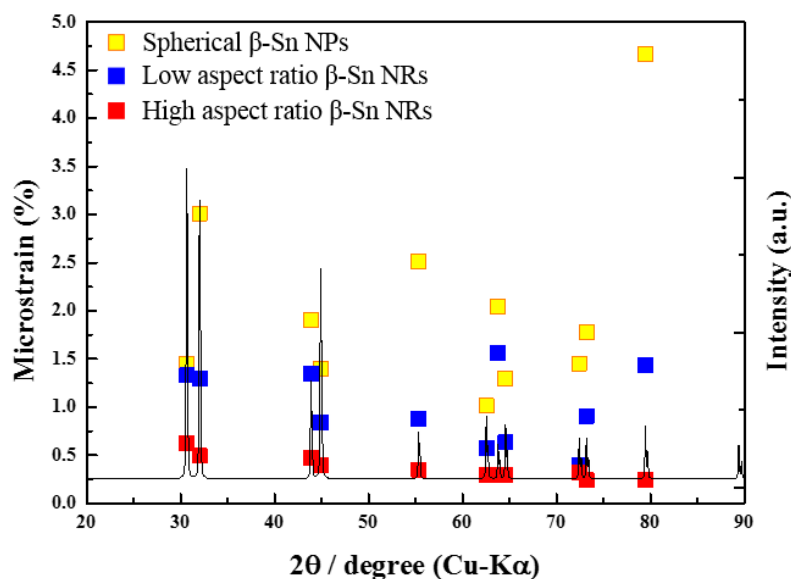


Figure 3.2. The calculated XRD based micro-strains of each crystallographic planes of spherical, low aspect ratio, and high aspect ratio β -Sn NPs for different crystal planes. XRD pattern shown is the simulated pattern of β -Sn with JCPDS 04-0673.

3.3.2. Electrochemical Measurement

Cyclic voltammetry (CV), cycle tests, and C-rate tests were performed in order to investigate the electrochemical properties and reactions, and the effect of high and low aspect ratio of β -Sn NRs during the discharge/charge process in LIB half-cell. Figure 3.3 shows CV test of the first three (3) charge/discharge cycles with a potential window of 0.01 – 3.0 V (sweep direction is from 3 V to 0.01 V as indicated by the black arrow) at a scan rate of $0.1 \text{ mV} \cdot \text{s}^{-1}$. The starting potential used is similar to the measured open circuit potential (OCP), i.e. 2.82 V and 2.94 V for high and low aspect ratio β -Sn NRs respectively. Cyclic voltammogram results of both high and low aspect ratio β -Sn NRs show irreversible peaks at 0.019, and 0.391 V, during the first discharge that disappears in the subsequent cycles. This corresponds to both the formation of SEI layer and the alloying of Lithium with Sn to form Li_xSn alloys ($\text{Sn} + x\text{Li}^+ + xe^- \rightarrow \text{Li}_x\text{Sn}$). It can also be observed that the reduction peak on both low and high aspect ratio at 0.88 V and 0.818 V respectively on the first cycle shifted to 1.18 and 1.15 V respectively for

the succeeding cycles. This can be attributed to the electron-insulating phase, e.g. SnO₂, SEI, and Li₂O, that covers the conducting active material,²⁷ i.e. Sn. After the first discharge, the cathodic peaks at 0.56, 1.23, and 1.43 V, and the anodic peaks at 0.6 (Li₇Sn₃), 0.5 (Li₅Sn₂ and Li₁₃Sn₅), 0.4 (Li₇Sn₂), and 0.3 V (Li₂₂Sn₅) corresponds to the dealloying and alloying of β-Sn respectively.²⁸⁻³² While the reversible and overlapping curves of the second and third cycles correspond to a stable cycling performance of the anode material. It can also be observed that the total current is larger for high aspect ratio NRs compared to that of the low aspect ratio NRs. In electrochemistry, there are only two factors that affect the total current, i.e. scan rate, and polarization and ohmic resistance. It is widely known that as the scan rate increases, the total current also increases due to the increase in the flux on to the electrode. Since the scan rate is the same for both high and low aspect ratio NRs, i.e. 0.1 mV·s⁻¹, the increase in the total current which is greatly affected by the flux, can be related to the decrease in the polarization and ohmic resistance. Polarization and ohmic resistance are factors of both Li⁺ diffusion and e⁻ migration. Though lower aspect ratio NRs have higher Li⁺ diffusion, the void spaces in-between particles restricts the flow of electrons and thus decreases the total current. On the other hand, high aspect ratio NRs, due to the longer length, the 1D flow of e⁻ was enhanced and thus results to a higher total current.³³⁻³⁵

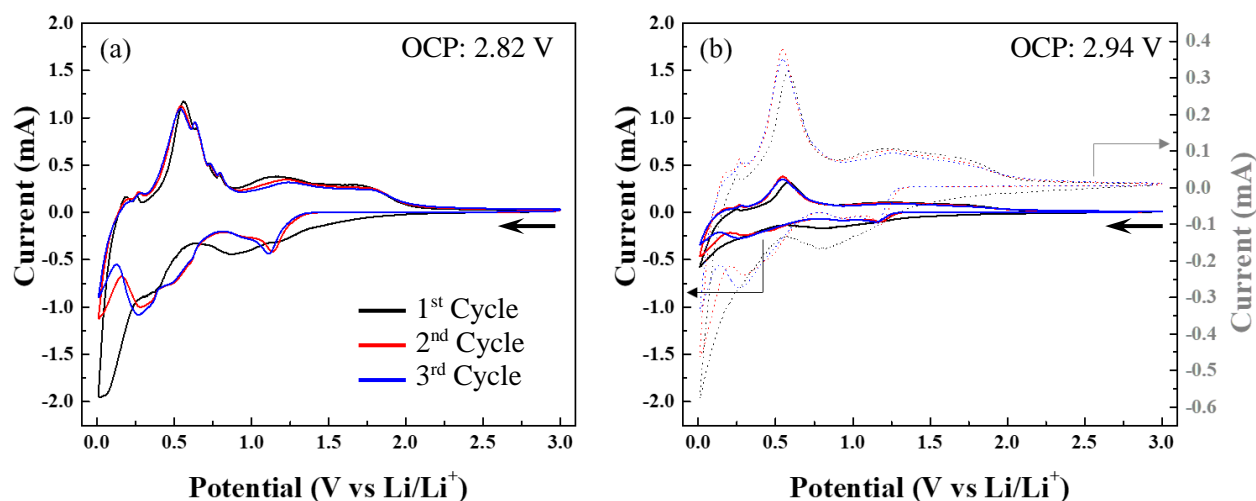


Figure 3.3. Cyclic voltammograms at a scan rate of $0.1 \text{ mV} \cdot \text{s}^{-1}$ between 0.1 and 3.0 V vs Li/Li^+ : (a) high aspect ratio and (b) low aspect ratio β -Sn NRs. The dotted line corresponds to the magnified trend of the low aspect ratio β -Sn NRs.

β -Sn is known to have poor cycling stability due to large volumetric change. However, varying the morphology is a known method to greatly improve the cycling stability. Figure 3.4 shows the capacity and cycle stability of high (red) vs low (black) aspect ratio β -Sn NRs electrodes. Spherical β -Sn NPs electrode (blue) were also examined as a reference to show the instability of β -Sn NPs. As expected, it was observed that rod-like morphology, as indicated by both high and low aspect ratio β -Sn NRs electrodes, have better stability than spherical β -Sn NPs electrode. The higher stability can be attributed to the 1D morphology that can improve the capacity retention by buffering large volumetric expansion and facilitating strain relaxation.⁷ The results agree with the microstrain analysis shown in Figure 3.2. However, it can be observed that low aspect ratio β -Sn NRs electrode has better stability, *i.e.*, the capacity stabilizes after ~ 20 cycles. Whereas the capacity of high aspect ratio β -Sn NRs electrode continuously degrades very slowly upon successive cycles. The slow continuous capacity fading can be attributed to another factor, *vis.* the formed SEI layer, which is greatly affected by the surface crystallographic plane of the active material.^{1-6,16-20,36}

To further analyze the electrochemical difference between high and low aspect ratio β -Sn NRs electrodes, the impedance of both high and low aspect ratio β -Sn NRs electrodes was also measured (Figure 3.5a), and the corresponding solution, SEI, and charge transfer resistivities, as well as the Li^+ diffusion from the Warburg impedance coefficient, were calculated (Table 3.1). The diffusion coefficient, D_{Li} , was calculated using the Warburg impedance coefficient, σ , formula:³⁷⁻³⁹

$$\sigma = \frac{RT}{n^2 F^2 A \sqrt{2}} \left(\frac{1}{C_{\text{Li}} D_{\text{Li}}^{0.5}} \right)$$

and thus:

$$D_{\text{Li}} = \frac{R^2 T^2}{2 \sigma^2 n^4 F^4 A^2 C_{\text{Li}}^2}$$

where R is the ideal gas constant ($8.314 \text{ J mol}^{-1} \text{ K}^{-1}$), T is the temperature in Kelvin, F is the Faraday's constant ($96485.33289 \text{ C mol}^{-1}$), A is the electrode surface area, n is the number of electrons associated with the alloying of Li with Sn ($\text{Sn} + 4.4 \text{ Li}^+ + 4.4 \text{ e}^- \rightarrow \text{Li}_4.4\text{Sn}$), and C_{Li} is the concentration of Li^+ in the electrolyte. The σ was calculated as the slope of the relationship between real resistance (Z') and the inverse square root of angular speed ($\omega^{-1/2}$) low frequency region (Figure 3.5b).

It was observed that the solution resistivity (R_{S}) was almost equal on both high and low aspect ratio β -Sn NRs electrodes. However, the low aspect ratio β -Sn NRs electrode has slightly lower SEI resistivity (R_{SEI}) but with much higher charge transfer resistivity (R_{CT}). Considering the morphology of β -Sn NRs, the higher aspect ratio is expected to have lower R_{CT} due to the 1D flow of e^- , which allow the ease of charge transfer along the rod. The smaller the particles, i.e. spherical and low aspect ratio NRs, have more void spaces in between the particles

compared to that of the high aspect ratio NRs. According to Roy and Srivastava,⁴⁰ the electronic transport on small particles has random walk of electrons along the grain boundaries, through carbon binders or additives, and carbon coating on the particles. The grain boundaries and voids between particles and the random walk of e^- restricted the electronic transport and thus reduces both the battery performance and electrical conductivity, which leads to higher R_{CT} . On the other hand, Li^+ diffusion depends on the size of the particle. The smaller the particle size, the larger the surface area and thus increases Li flux. However, larger surface area also increases the electrode-electrolyte interface that triggers secondary reactions, i.e. electrolyte decomposition to form the SEI layer that increases ohmic resistance and at the same time can prevent or block the migration of Li^+ .⁴⁰⁻⁴³ Based on the calculated Li^+ diffusion coefficient, after the formation of SEI layer (after the 3rd discharge), which is merely based on the Warburg impedance coefficient, it was found that Li^+ diffusion in low aspect ratio β -Sn NRs electrode is faster by an order of magnitude compared to that of higher aspect ratio β -Sn NRs. After 100 cycles (Figure S3.2), the impedance of that of the low aspect ratio did not increase abruptly. Further, it is comparable to that of the impedance of high aspect ratio NRs after the 3rd discharge. The higher charge transfer resistivity but better Li^+ diffusion on shorter NRs after the 3rd discharge and 100 cycles can be attributed to other factor, vis. the formed SEI layer, which will be further explained in the succeeding paragraphs.

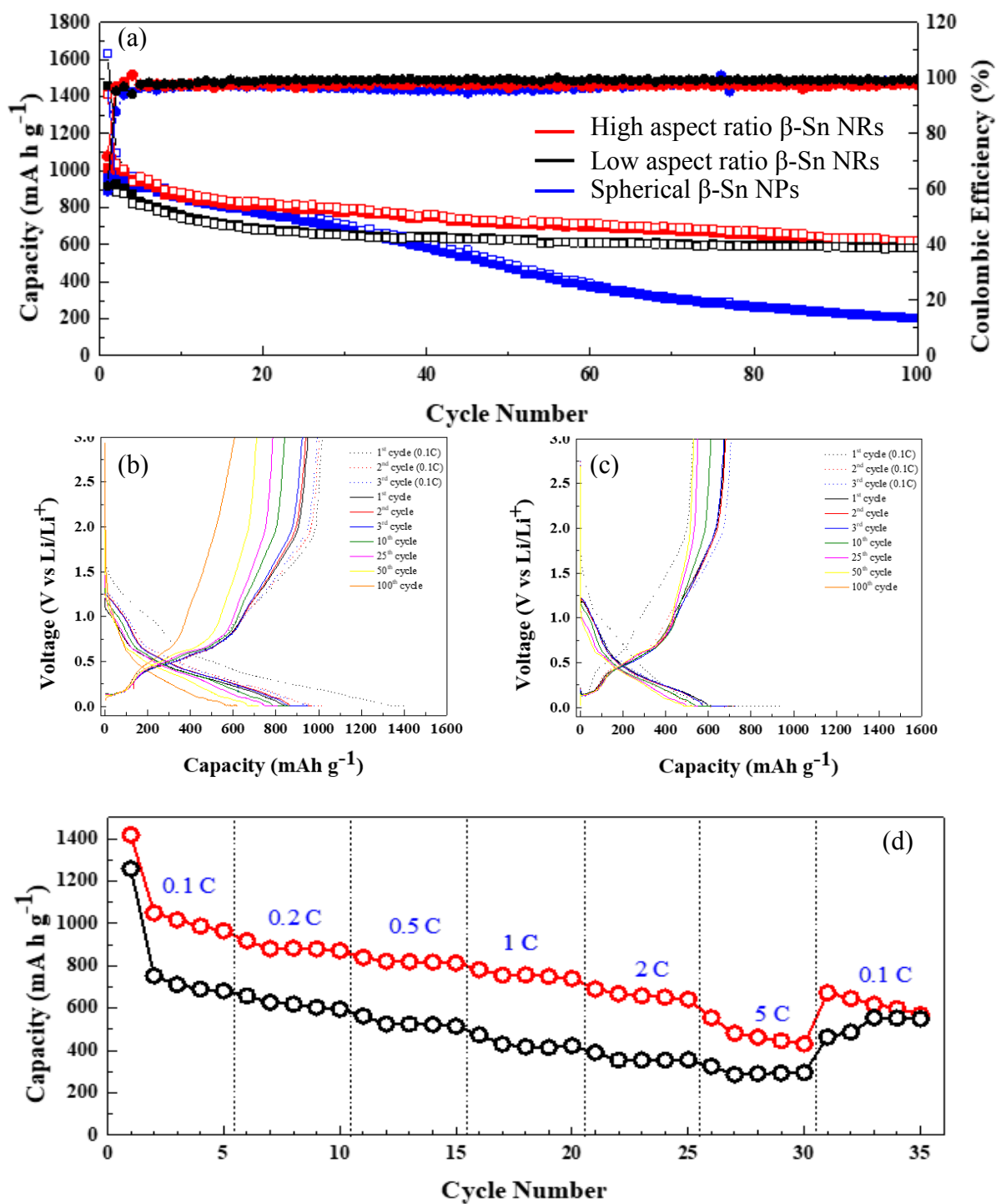


Figure 3.4. (a) Cyclic test of high and low aspect ratio β -Sn NRs and spherical β -Sn electrodes, charge-discharge curve of (b) high and (c) low aspect ratio β -Sn NRs electrodes using 0.2C with voltage window of 0.1 V to 3.0 V, and (d) rate performance of high (red) and low (black) aspect ratio β -Sn NRs electrodes.

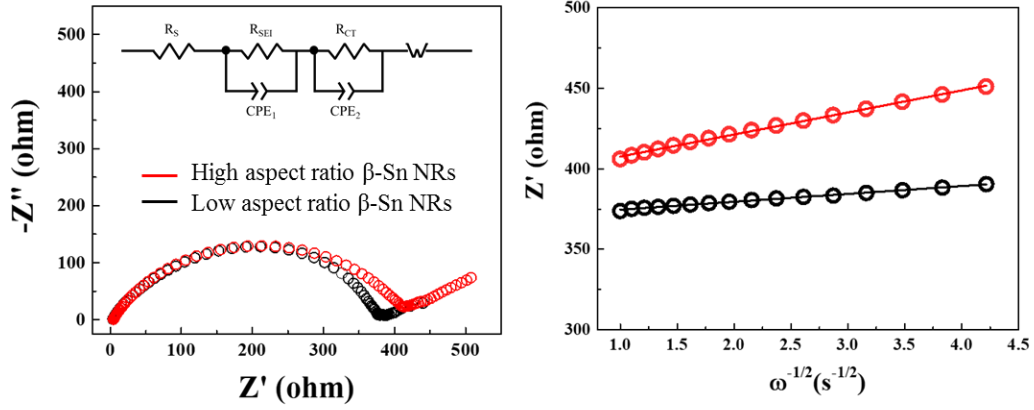


Figure 3.5. (a) Nyquist plot after the 3rd discharge with the inset of the equivalent circuit model for the determination of the resistance values, and (b) relationship between real resistance (Z') and inverse square root of angular speed ($\omega^{-1/2}$) at low frequency region, of the high and low aspect ratio β -Sn NRs.

Table 3.1. Calculated resistivity values (top) and diffusion coefficient (bottom) in Figure 3.5a and 3.5b respectively.

	High aspect ratio NRs	Low aspect ratio NRs
R_s (Ω)	3.5	3.3
R_{SEI} (Ω)	382	370
R_{CT} (Ω)	0.05	0.5
Diffusion Coefficient ($cm^2 s^{-1}$)	2.13E-13	1.67E-12
Slope	13.7	4.89
R^2	0.9978	0.9962

R_s – solution resistance, R_{SEI} – SEI resistance, R_{CT} – charge transfer resistance, R^2 – goodness of the fit.

3.3.3. Ex-situ analysis of Sn NRs after electrochemical test

TEM images and XPS analysis of the electrodes were examined after the 3rd discharge to determine the effect of Li⁺ intercalation and the type of the initially formed SEI layers. Based on the TEM images of high (Figure 3.6a) and low (Figure 3.6b) aspect ratio β -Sn NRs, the rod-like morphology was still maintained after 3 cycles which indicates that rod-like morphology is stable enough to accommodate the large volumetric change of β -Sn upon charge and discharge cycles. Based on the SAED analysis (Figure 3.6c and 3.6d), the fully lithiated phase after the 3rd discharge indicates that Sn forms an alloy of Li₂₂Sn₅ with Li. The formation of the Li₂₂Sn₅ alloy agrees well with the CV curve (Figure 3.3) as indicated by the reduction peak at 0.3V. However, after 100 cycles (Figure S3.3 and S3.4), it can be observed that the morphology of the low aspect ratio NRs deviates from the initial rod-like morphology. SEM (Figure S3.3) images show that the rod-like morphology looks compressed and aggregated, however, a closer examination under TEM (Figure S3.4) revealed that the rod-like morphology looks aggregated spherical particles and thus lose its initial morphology, as been expected. Though the morphology collapsed after 100 cycles, the produced anode material is already stable with a coulombic efficiency of almost 100% for low aspect ratio NRs, hence the stability can be attributed to another factor, vis. SEI layer.

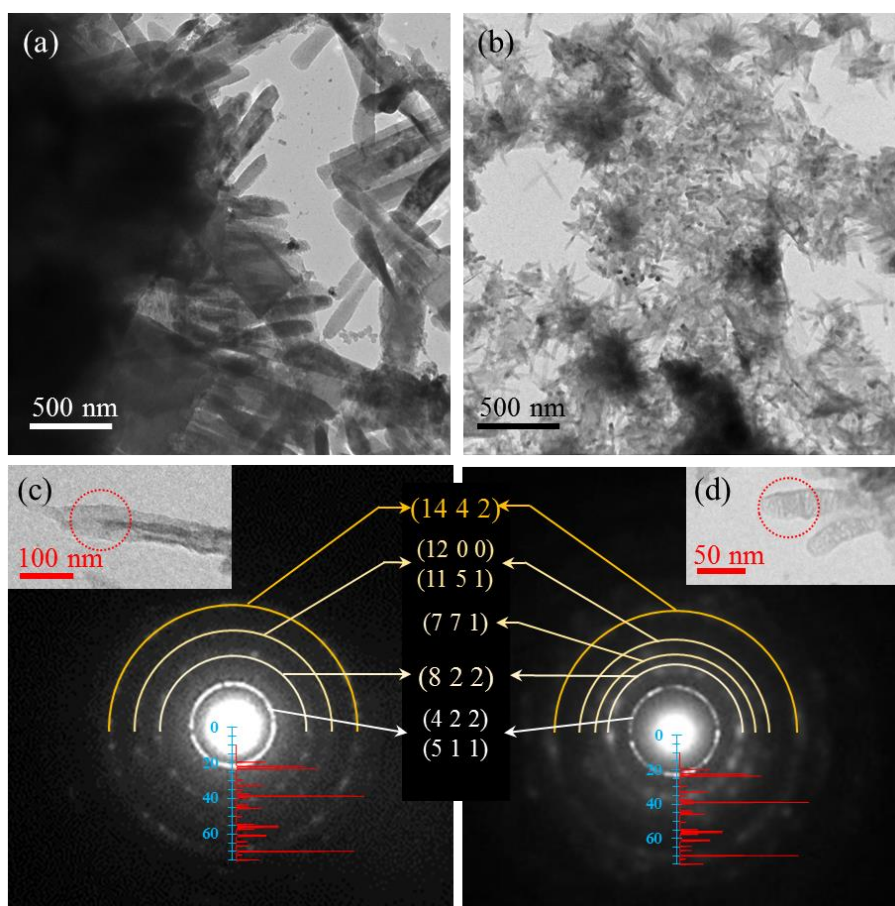


Figure 3.6. (a, b) TEM images and (c, d) SAED pattern of (a, c) high and (b, d) low aspect ratio NRs after the 3rd discharge. Inset pictures and curves in (c) and (d) indicates the TEM images of the area of analyses and the simulated XRD pattern of $\text{Li}_{22}\text{Sn}_5$ (JCPDS 00-018-0753) respectively.

XPS analysis, on the other hand, was conducted (Figure 3.7 and Table 3.2) to analyze the SEI layer formed at the surface of the anode material before and after the 3rd discharge. Based on the F 1s spectrum, the low aspect ratio β -Sn NRs (Figure 3.7d) has richer LiF compound than other F containing compounds. While high aspect ratio β -Sn NRs (Figure 3.7j) on the other hand has less LiF compared to the other F containing compounds. The LiF and the other F containing compounds are attributed to the components of the formed SEI layer after the 3rd discharge, since before the electrochemical test (Figures 3.7a and 3.7g) there are no peaks corresponding to F containing compounds. The higher amount of other F containing

compounds for high aspect ratio NRs than LiF compared to that of low aspect ratio NRs agrees well with both the C 1s (Figures 3.7e and 3.7k) and O1s (Figures 3.7f and 3.7l). The F containing compounds as indicated by the 287 and 292 eV (-CH₂-CH₂-O- and -CF₂-CH₂-), and 535 eV (O-F_x) peaks^{2,18} on both C 1s (Figures 3.7e and 3.7k) and O1s (Figures 3.7f and 3.7l) after the 3rd discharge respectively are relatively more intense for high aspect ratio β -Sn NRs compare to that of low aspect ratio β -Sn NRs. While the other peaks of the C 1s spectrum of both high (Figure 3.7b) and low (Figure 3.7h) aspect ratio NRs before cycling at 284, 285, 286, and 289.5 eV, correspond to C-C, C-H, C-O, and C=O peaks respectively.^{2,18} The C-C peak can be attributed to the added conductive carbon, while the C-H, C-O, and C=O peaks are from PVP, CMC, and SBR binders respectively. The O1s spectrum on the other hand of both low (Figure 3.7c) and high (Figure 3.7l) aspect ratio β -Sn NRs before cycling contain peaks at 530.5, 531.5, and 533 eV which corresponds to the SnO_x, C-O, and C=O peaks respectively.^{2,18} The SnO_x peaks were from the surface oxide on β -Sn NRs, while the C-O and C=O peaks come from the PVP, CMC, and SBR binders which agrees with the C 1s spectrum. After the 3rd discharge, based on the C 1s spectrum (Figures 3.7e and 3.7k), aside from the additional 2 peaks as indicated by F containing compounds, it can also be observed that the intensity of the C=O peak at 533 eV increases with respect to other initial C1s peaks, i.e. C-C, C-H, and C-O peaks. This might be due to the formation of carbonate-rich SEI layer, vis. Poly(VC) and Li₂CO₃. The O 1s spectrum (Figures 3.7f and 3.7l), on the other hand, aside from the additional one (1) peak at 535 eV, the broadening and increase in the intensity of the peak at 530.5 eV with respect to the other components, correspond to the formation of Li₂O, Poly(VC), and/or Li₂CO₃. The formation of Li₂CO₃ and Poly(VC) agrees well with the C 1s spectrum (Figures 3.7e and 3.7k) while Li₂O is due to the presence of SnO_x at the surface of β -Sn NRs. Based on our XPS analysis, it was found that these F containing SEI layer in high aspect ratio β -Sn NRs only contains 21.9% LiF compared to 75.2% LiF in low aspect ratio β -Sn NRs. Based on our

XPS analysis, the higher stability and higher Li⁺ diffusion on low aspect ratio β -Sn NRs compared to that of high aspect ratio Sn NRs can be attributed to the LiF-rich F containing SEI layer. This agrees well with other studies that use FEC additive in the electrolyte to produce a LiF-rich F containing SEI layer.^{2,5,6,16-20} In our case, the higher LiF-rich F containing SEI layer obtained in low aspect ratio NRs comes from the higher total specific surface area of the active (001) plane of the rod tip, i.e. ~ 9 times that of the high aspect ratio β -Sn NRs. The (001) active surface allows the formation of LiF which helps stabilize the formed SEI layer. Our results indicate the controlled exposed surface crystallographic planes of β -Sn combined with nanorod morphology can lead to stable cycling of the anode via producing stable SEI, good microstrain relaxation, and high ionic and electronic conductivity.

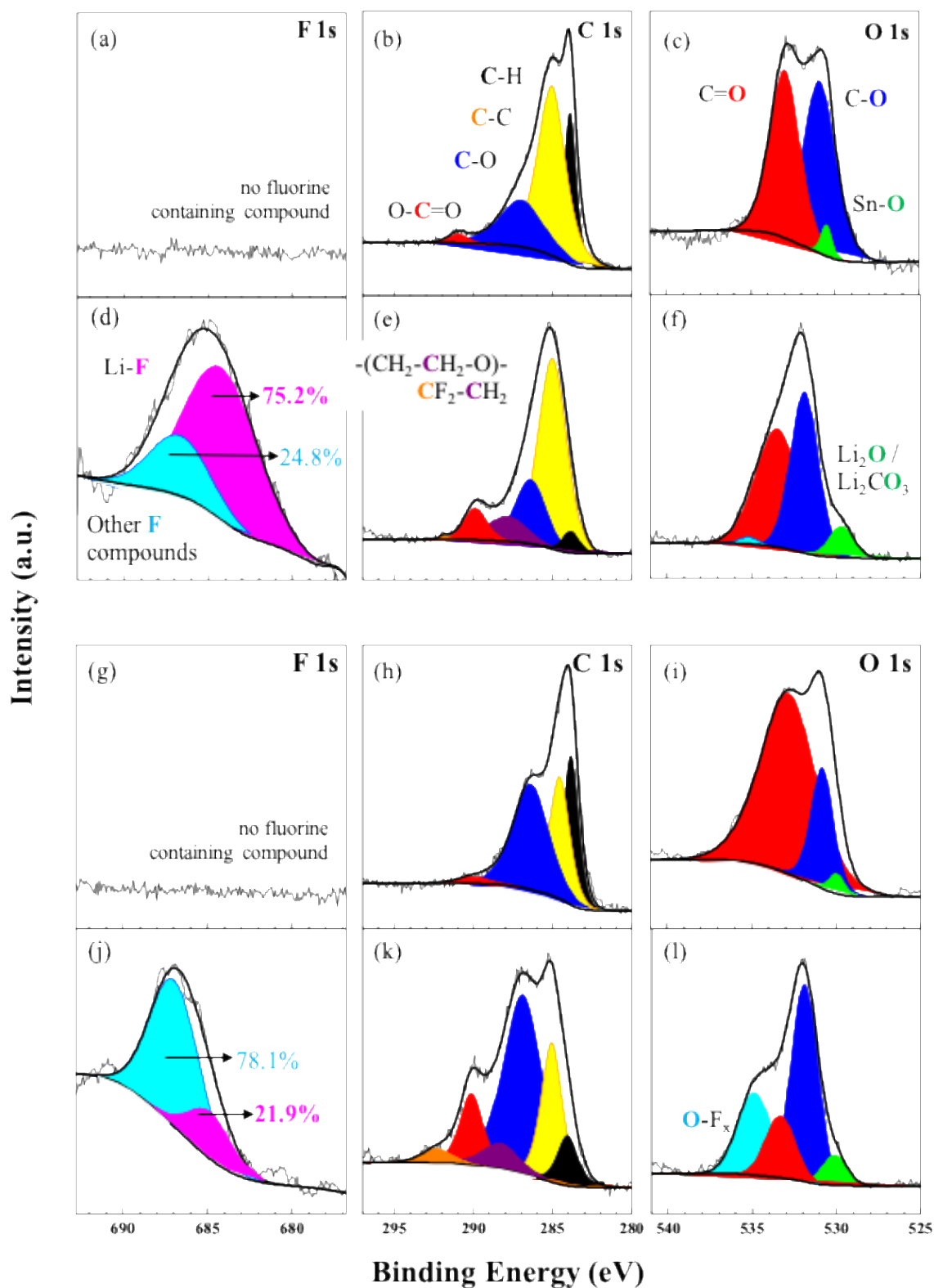


Figure 3.7. XPS analysis of (a-f) low and (g-l) high aspect ratio NRs before cycling (a-c, g-i), and after 3rd discharge (d-f, j-l).

Table 3.2. Corresponding XPS binding energy (eV) of low and high aspect ratio NRs before cycling and after the 3rd discharge.

		Low aspect ratio NRs		High aspect ratio NRs	
		before cycle	after 3rd discharge	before cycle	after 3rd discharge
C 1s	C-H	283.915	284.003	283.848	283.846
	C-C	285.076	285.176	284.576	284.849
	C-O	286.973	286.557	286.383	286.703
	O-C=O	290.953	290.019	290.016	289.919
	-(CH ₂ -CH ₂ -O)-	---	288.052	---	288.103
	CF ₂ -CH ₂	---	292.025	---	292.114
O 1s	C=O	532.986	533.527	532.821	533.13
	C-O	530.921	531.907	530.809	531.703
	Sn-O	530.498	---	529.970	---
	Li ₂ O / Li ₂ CO ₃	---	529.729	---	529.919
	O-Fx	---	535.217	---	534.687
F 1s	LiF	---	684.947 (75.2%)	---	685.259 (21.9%)
	Other F compounds	---	686.995 (24.8%)	---	687.189 (78.1%)

The percentage in the parenthesis shows the amount of F in different compound calculated from the XPS peak area shown in Figure 3.7.

3.3.4. Mechanism of LiF-rich SEI layer on Low Aspect Ratio NRs

SEI layer is one of the important factors that dictate the stability and cyclability of the electrodes in LIBs. It can either cause the continuous capacity fading due to the continuous electrolyte decomposition or it can make a passivation type layer that prevents the further electrolyte degradation at the surface of the active material.^{1,2,18,32} Based on the XPS analysis of the SEI layer formed at the surface of the anode, it can be observed that LiF dominates the fluorine-containing SEI compounds in low aspect ratio NRs. This LiF serves as a passivation layer that likely prevents the further degradation of the electrolyte that continuously results to the capacity fading^{1,3} and at the same time enhances the Li⁺ conductivity.^{1,2} Aside from LiF, the formation of Poly (VC), Li₂CO₃² and the Li₂O⁴⁴ as SEI layers is also contribute to the flexibility

and stability of the produced anode material, while other SEI compounds, *i.e.*, ROCOOLi, $\text{Li}_x\text{PO}_y\text{F}_z$, and C-F, is likely to cause the further degradation of the electrolyte and the continuous capacity fading of high aspect ratio β -Sn NRs. Figure 3.8 shows the mechanism that explains the higher stability of low aspect ratio β -Sn NRs electrodes than that of the high aspect ratio β -Sn NRs electrodes due to the formation of stable and higher Li^+ diffusion SEI layer, *vis.* LiF, Poly(VC), Li_2CO_3 and Li_2O . Poly(VC) can be attributed to the additional 2% VC added to the electrolyte, while the formation of LiF and Li_2CO_3 can be attributed to the surface crystallographic plane of β -Sn NRs, *i.e.* low surface energy (100) and high surface energy (001) yields Li_2CO_3 and LiF respectively¹ as shown in Figure 3.8b-d. Figure 3.8a shows that the β -Sn NRs has low surface energy (200) facets and grows along the [001] which indicates that the tip of the β -Sn NRs has (001). High aspect ratio β -Sn NRs is expected to have more exposed (200) plane compared to (001) than that of low aspect ratio β -Sn NRs. The higher amount of exposed (001) yields to a higher amount of LiF that passivates the surface of the electrode and thus prevents the further electrolyte degradation and have a better capacity stability. This also explains the higher Li^+ diffusion in low aspect ratio β -Sn NRs electrode compared to that of high aspect ratio β -Sn NRs electrode as shown in Figure 3.4 and Table 3.1, wherein the formation of LiF allows the ease of Li^+ transfer in the SEI layer. After 100 cycles, the impedance of that of the low aspect ratio also did not show much increase as shown in Figure S3.2, *i.e.* comparable to that of high aspect ratio NRs after the 3rd discharge. This small increase in the impedance might be due to the LiF-rich F-containing SEI layer, since LiF is known to prevent the further electrolyte degradation that increases the battery's internal resistance.^{1,3}

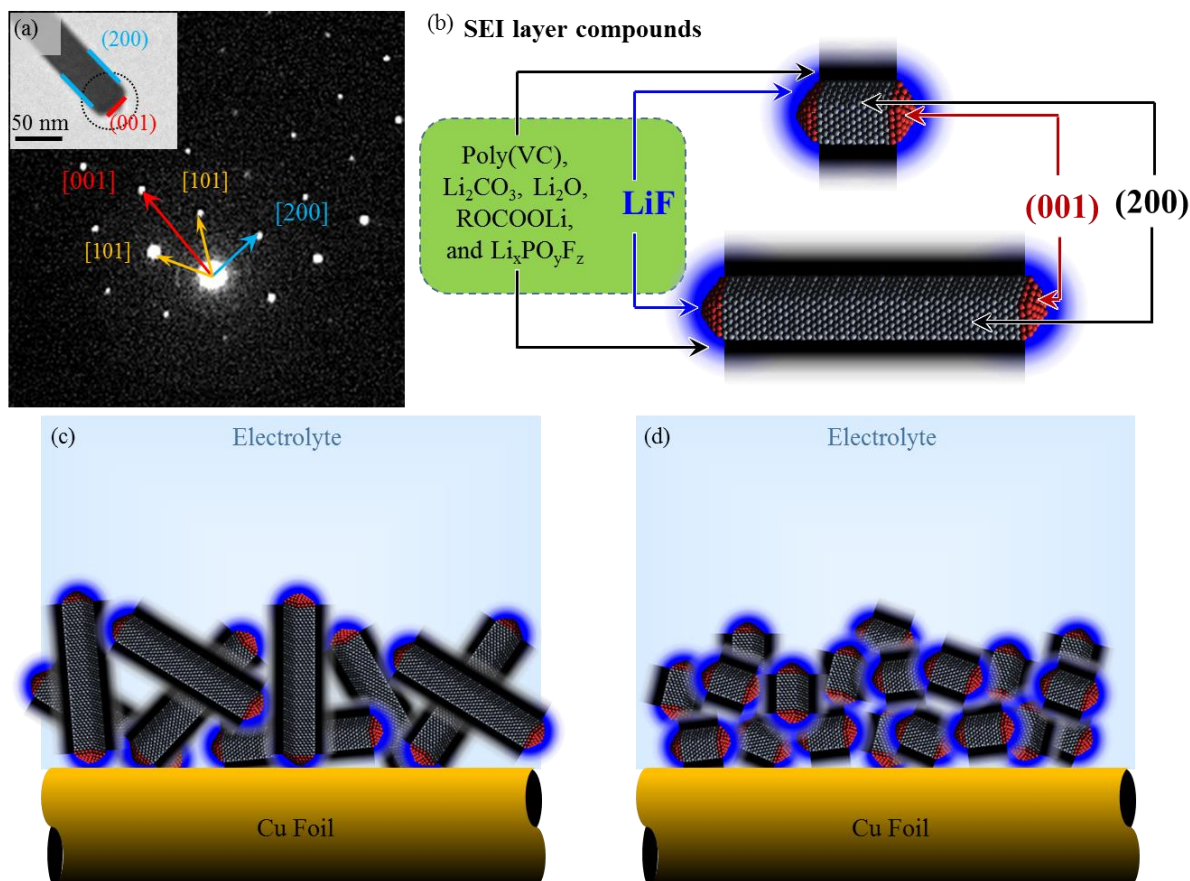


Figure 3.8. (a) SAED analysis of β -Sn NRs indicating the growth direction and surface planes, (b) the type of SEI layer compound formed on the surface of β -Sn NRs with respect to the surface crystallographic plane, and schematic illustrations of the SEI layer formed on (c) high and (d) low aspect ratio β -Sn NRs.

3.4. Conclusion

The chemically synthesized single crystal β -Sn NRs have low surface energy (200) facets with highly active (001) tip is a potential anode material for lithium-ion battery. β -Sn NRs have better cycle stability due to the rod-like morphology, which buffers large volumetric change, compared to that of the spherical NPs. However, it was found that low aspect ratio β -Sn NRs is more stable than that of the high aspect ratio β -Sn NRs, where it slowly decreases with continuous charge and discharge cycles. The high stability of low aspect ratio β -Sn NRs can be attributed to the LiF-rich F containing SEI layer, which is similar to the SEI formed when

electrolyte with FEC-additive was used, as indicated by the XPS analysis. The formation of LiF-rich F containing SEI layer is due to higher amount of exposed reactive (001), i.e. tip of the rod, in low aspect ratio β -Sn NRs. The presence of LiF-rich F-compound agrees well with the impedance test, wherein, low aspect ratio β -Sn NRs have higher Li^+ diffusion by an order of magnitude.

Acknowledgment

Authors thank Prof. S. Tadanaga and Dr. N. C. Rosero Navarro (Hokkaido Univ.) for the fruitful discussions. This work is partially supported by Hokkaido University. LMZDJ and IVBM thank the financial support of Center for Engineering Education Development (CEED) of Hokkaido Univ. for the stay in Taoyuan and Sapporo, respectively. WRL thanks Hokkaido Univ. for the support for his stay in Sapporo. We also thank Mr. T. Tanioka (Hokkaido Univ.) for TEM measurement and Mr. K. Suzuki (Hokkaido Univ.) for fruitful discussion in XPS measurement.

References

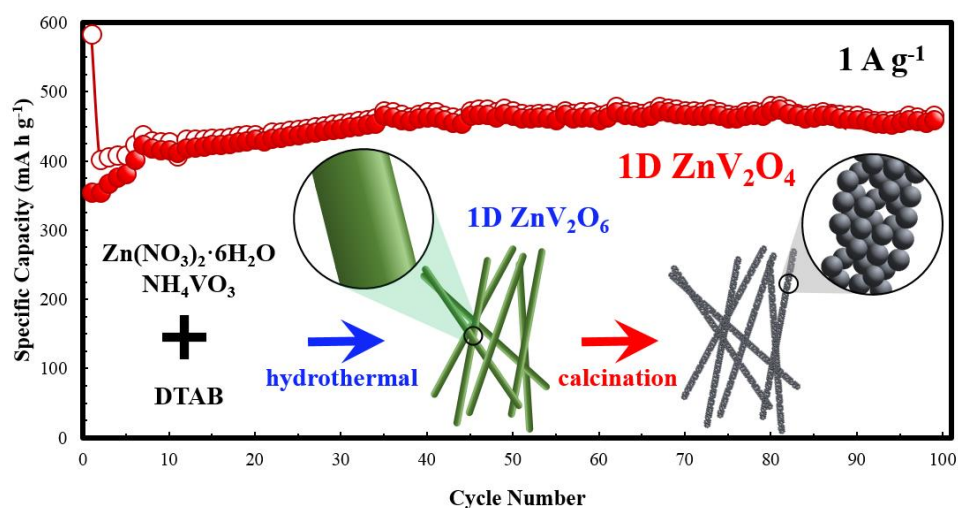
1. Qiao, R.; Lucas, I. T.; Karim, A.; Syzdek, J.; Liu, X.; Chen, W.; Persson, K.; Kostecki, R.; Yang, W., Distinct Solid-Electrolyte-Interphases on Sn (100) and (001) Electrodes Studied by Soft X-Ray Spectroscopy. *Adv. Mater. Interfaces* **2014**, *1*, 1300115-1300121.
2. Seo, D. M.; Nguyen, C. C.; Young, B. T.; Heskett, D. R.; Woicik, J. C.; Lucht, B. L., Characterizing Solid Electrolyte Interphase on Sn Anode in Lithium Ion Battery. *J. Electrochem. Soc.* **2015**, *162*, A7091-A7095.
3. Lucas, I. T.; Syzdek, J.; Kostecki, R., Interfacial processes at single-crystal β -Sn electrodes in organic carbonate electrolytes. *Electrochem. Commun.* **2011**, *13*, 1271-1275.
4. Tokur, M.; Algul, H.; Uysal, M.; Cetinkaya, T.; Alp, A.; Akbulut, H., Electrolytic coating of Sn nano-rods on nickel foam support for high performance lithium ion battery anodes. *Surf. Coat. Technol.* **2016**, *288*, 62-68.
5. Eom, K.; Jung, J.; Lee, J. T.; Lair, V.; Joshi, T.; Lee, S. W.; Lin, Z.; Fuller, T. F., Improved stability of nano-Sn electrode with high-quality nano-SEI formation for lithium ion battery. *Nano Energy* **2015**, *12*, 314-321.
6. Yang, Z.; Gerwirth, A. A.; Trahey, L., Investigation of Fluoroethylene Carbonate Effects on Tin-based Lithium-Ion Battery Electrodes. *ACS Appl. Mater. Interfaces* **2015**, *7*, 6557-6566.
7. Wang, B.; Luo, B.; Li, X.; Zhi, L., The dimensionality of Sn anodes in Li-ion batteries. *Mater. Today* **2012**, *15*, 544-552.

8. Huang, L.; Wei, Q.; Sun, R.; Mai, L., Nanowire electrodes for advanced lithium batteries. *Front. Energy Res.* **2014**, *2*, 43: 1-13.
9. Wang, J.; Fan, F.; Liu, Y.; Jungjohann, K. L.; Lee, S. W.; Mao, S. X.; Liu, X.; Zhu, T., Structural Evolution and Pulverization of Tin Nanoparticles during Lithiation-Delithiation Cycling. *J. Electrochem. Soc.* **2014**, *161*, F3019- F3024.
10. Dasgupta, N. P.; Sun, J.; Liu, C.; Brittan, S.; Andrews, S. C.; Lim, J.; Gao, H.; Yan, R.; Yang, P., 25th anniversary article: semiconductor nanowires-synthesis, characterization, and applications. *Adv. Mater.* **2014**, *26*, 2137–2184.
11. Chan, C. K.; Peng, H.; Liu, G.; Mcilwrath, K.; Zhang, X. F.; Huggins, R. A.; Cui, Y., High-performance lithium battery anodes using silicon nanowires. *Nat. Nanotechnol.* **2008**, *3*, 31–35.
12. Szczech, J. R.; Jin, S., Nanostructured silicon for high capacity lithium battery anodes. *Energy Environ. Sci.* **2011**, *4*, 56–72.
13. Huang, J.Y.; Zhong, L.; Wang, C. M.; Sullivan, J. P.; Xu, W.; Zhang, L. Q.; Mao, S. X.; Hudak, N. S.; Liu, X. H.; Subramanian, A.; Fan, H.; Qi, L.; Kushima, A.; Li, J., In situ observation of the electrochemical lithiation of a single SnO₂ nanowire electrode. *Science* **2010**, *330*, 1515–1520.
14. Mai, L. Q.; Wei, Q. L.; Tian, X. C.; Zhao, Y. L.; An, Q. Y., Electrochemical nanowire devices for energy storage. *IEEE Trans. Nanotechnol.* **2014**, *13*, 10–15.
15. Mai, L.; Dong, Y.; Xu, L.; Han, C., Single nanowire electrochemical devices. *Nano Lett.* **2010**, *10*, 4273–4278.
16. Jaumann, T.; Balach, J.; Langklotz, U.; Sauchuk, V.; Fritsch, M.; Michaelis, A.; Telteviskij, V.; Mikhailova, D.; Oswald, S.; Klose, M.; Stephani, G.; Hauser, R.; Eckert, J.; Giebeler, L., Lifetime vs. rate capability: Understanding the role of FEC and VC in high-energy Li-ion batteries with nano-silicon anodes. *Energ. Stor. Mater.* **2017**, *6*, 26-35.
17. Xu, K., Electrolytes and Interphases in Li-ion Batteries and Beyond. *Chem. Rev.* **2014**, *114*, 11503-11618.
18. Markevich, E.; Salitra, G.; Aurbach, D., Fluoroethylene Carbonate as an Important component for the Formation of an Effective Solid Electrolyte Interphase on Anodes and Cathodes for Advance Li-ion Batteries. *ACS Energy Lett.* **2017**, *2*, 1337-1345.
19. Markevich, E.; Salitra, G.; Fridman, K.; Sharabi, R.; Gershtinsky, G.; Garsuch, A.; Semrau, G.; Schmidt, M.; Aurbach, D., Fluoroethylene Carbonate as an Important Component in Electrolyte Solutions for High-Voltage Lithium Batteries: Role of Surface Chemistry on the Cathode. *Langmuir* **2014**, *30*, 7414-7424.
20. Shin, H.; Park, J.; Sastry, A. M.; Lu, W., Effects of Fluoroethylene Carbonate (FEC) on Anode and Cathode Interfaces at Elevated Temperatures. *J. Electrochem. Soc.* **2015**, *162*, A1683-A1692.
21. Peled, E.; Tow, D. B.; Merson, A.; Galdklich, A.; Burstein, L.; Golodnitsky, D., Composition, depth profiles and lateral distribution of materials in the SEI built on HOPG-TOF SIMS and XPS studies. *J. Power Sources* **2001**, *97-98*, 52-57
22. De Juan, L. M. Z.; Nguyen, M. T.; Yonezawa, T.; Tokunaga, T.; Tsukamoto, H.; Ishida, Y., Structural Control Parameters for Formation of Single-Crystalline β -Sn Nanorods in Organic Phase. *ACS Cryst. Growth Des.* **2017**, *17*, 4554-4562.
23. Lin, Y.-M.; Abel, P. R.; Heller, A.; Mullins, C. B., α -Fe₂O₃ Nanorods as Anode Materials for Lithium Ion Batteries, *J. Phys. Chem. Lett.*, **2011**, *2* (22), 2885-2891
24. Yao, X.; Kong, J.; Zhao, C.; Zhou, D.; Zhou, R.; Lu, X., Zinc ferrite nanorods coated with polydopamine-derived carbon for high-rate lithium ion batteries, *Electrochim. Acta*, **2014**, *146*, 464-471
25. Zhang, J.; Huang, T.; Liu, Z.; Yu, A., Mesoporous Fe₂O₃ nanoparticles as high performance anode materials for lithium-ion batteries, *Electrochem. Commun.*, **2013**, *29*, 17-20
26. Zhao, K.; Wen, M.; Dong, Y.; Zhang, L.; Yan, M.; Xu, W.; Niu, C.; Zhou, L.; Wei, Q.; Ren, W.; Wang, X.; Mai, L., Thermal Induced Strain Relaxation of 1D Iron Oxide for Solid

- Electrolyte Interphase Control and Lithium Storage Improvement, *Adv. Energy Mater.* **2016**, 1601582: 1- 10.
27. Dong, W.; Xu, J.; Wang, C.; Lu, Y.; Liu, X.; Wang, X.; Yuan, X.; Wang, Z.; Lin, T.; Sui, M.; Chen, I-W.; Huang, F., A Robust and Conductive Black Tin Oxide Nanostructure Makes Efficient Lithium-Ion Batteries Possible, *Adv. Mater.*, **2017**, 29, 1700136: 1-9.
 28. Li, S.; Wang, Z.; Liu, J.; Yang, L.Y.; Guo, Y.; Cheng, L.; Lei, M.; Wang, W., Yolk-Shell Sn@C Eggshell-like Nanostructure: Application in Lithium-Ion and Sodium-Ion Batteries. *ACS Appl. Mater. Interfaces* **2016**, 8, 19438-19445
 29. Chen, X.; Guo, J.; Gerasopoulos, K.; Langrock, A.; Brown, A.; Ghodssi, R.; Culver, J. N.; Wang, C., 3D tin anodes prepared by electrodeposition on a virus scaffold. *J. Power Sources* **2012**, 211, 129-132.
 30. Xu, Y.; Liu, Q.; Zhu, Y.; Liu, Y.; Langrock, A.; Zachariah, M. R.; Wang, C., Uniform Nano-Sn/C Composite Anodes for Lithium Ion Batteries. *ACS Nano. Lett.* **2013**, 13, 470-474.
 31. Qin, J.; He, C.; Zhao, N.; Wang, Z.; Shi, C.; Liu, E.; Li, J., Graphene Networks Anchored with Sn@Graphene as Lithium Ion Battery Anode. *ACS Nano* **2014**, 8, 1728-1738.
 32. Winter, M.; Besenhard, J. O., Electrochemical lithiation of tin and tin-based intermetallics and composites. *Electrochim. Acta.* **1999**, 45, 31-50.
 33. Bard, A. J.; Faulkner, L. R., *Electrochemical Methods Fundamentals and Applications*, second edition, John Wiley & Sons, Inc., New York, NY, **2001**, Chapter 6, pp. 226-256
 34. Elgrishi, N.; Rountree, K. J.; McCarthy, B. D.; Rountree, E. S.; Eisenhart, T. T.; Dempsey, J. L., A Practical Beginner's Guide to Cyclic Voltammetry, *J. Chem. Educ.*, **2018**, 95, 197-206
 35. Huang, Y.; Li, X.; Luo, J.; Wang, K.; Zhang, Q.; Qui, Y.; Sun, S.; Liu, S.; Han, J.; Huang, Y., Enhancing Sodium-ion Storage Behaviors in TiNb₂O₇ by Mechanical Ball Milling, *ACS Appl. Mater. Interfaces*, **2017**, 9 (10), 8696-8703
 36. Veith, G. M.; Doucet, M.; Sacci, R. L.; Vacaliuc, B.; Baldwin, J. K.; Browning, J. F., Determination of the Solid Electrolyte Interphase Structure Grown on a Silicon Electrode Using a Fluoroethylene Carbonate Additive, *Sci. Rep.* **2017**, 7, 6326: 1-15.
 37. Maggay, I. V. B.; De Juan, L. M. Z.; Nguyen, M. T.; Yonezawa, T.; Chang, B. K.; Chan, T. S.; Liu, W.-R., ZnV₂O₄: A potential anode material for sodium-ion batteries, *J. Taiwan Inst. Chem. Eng.*, **2018**, DOI: 10.1016/j.jtice.2018.03.052.
 38. Takami, N.; Satoh, A.; Hara, M.; Ohsaki, T., Structural and Kinetic Characterization of Lithium Intercalation into Carbon Anodes for Secondary Lithium Batteries, *J. Electrochem. Soc.*, **1995**, 142 (2), 371-379.
 39. Ong, T. S.; Yang, H., Lithium Intercalation into Mechanically Milled Natural Graphite: Electrochemical and Kinetic Characterization, *J. Electrochem. Soc.*, **2002**, 149 (1), A1-A8.
 40. Roy, P.; Srivastava, K., Nanostructured anode materials for lithium ion battery, *J. Mater. Chem. A*, **2015**, 3, 2454-2484
 41. Wang, Y.; Li, H.; He, P.; Hoson, E.; Zhou, H., Nano active materials for lithium-ion batteries, *Nanoscale*, **2010**, 2, 1294-1305
 42. Jiang, C.; Hosono, E.; Zhou, H., Nanomaterials for lithium ion batteries, *Nano Today*, **2006**, 1 (4), 28-33
 43. Hu, Y.-S.; Kienle, L.; Guo, Y.-G.; Maier, J., High Lithium Electroactivity of Nanometer-Sized Rutile TiO₂, *Adv. Mater.*, **2006**, 18, 1421-1426.
 44. Nie, A.; Gan, L.-Y.; Cheng, Y.; Asayesh-Ardakani, H.; Li, Q.; Dong, C.; Tao, R.; Mashayek, F.; Wang, H.-T.; Schwingenschlögl, U.; Klie, R. F.; Yassar, R. S., Atomic-scale Observation of Lithiation Reaction Front in Nanoscale SnO₂ Materials, *ACS Nano*, **2013**, 7, 6203-6211.

CHAPTER 4

POROUS ZnV_2O_4 NANOWIRE FOR STABLE AND ENHANCED CAPACITY ANODE AT HIGH CURRENT DENSITY CHARGE-DISCHARGE IN LITHIUM-ION BATTERY



Abstract	135
4.1.Introduction	135
4.2.Experimental Section	
4.2.1. Materials Preparation	139
4.2.2. Characterizations	140
4.2.3. Electrochemical Test	140
4.2.4. Ex-situ Characterizations	142
4.3.Results and Discussion	
4.3.1. Formation of 1D ZnV_2O_4	142
4.3.2. Proposed mechanism in the formation of porous ZnV_2O_4	150
4.3.3. Electrochemical test	151
4.4.Conclusion	160
References	162

Abstract

A two-step fabrication, i.e. hydrothermal reaction followed by calcination, was used to produce porous ZnV_2O_4 . Despite the porous structure, the porous ZnV_2O_4 nanowires (NWs) are single crystal with $\{220\}$ facets and wire direction along $\langle 111 \rangle$. Based on the electrochemical test, these porous ZnV_2O_4 NWs have better cycling stability and higher specific capacity, i.e. 460 mA h g^{-1} after 100 cycles and 149 mA h g^{-1} after 1000 cycles using 1 and 5 A g^{-1} current densities respectively, compared to other morphologies, i.e. spherical and coral-like morphologies. As ternary transition metal oxide, the produced porous ZnV_2O_4 NWs undergoes gradual phase transformation until the 35th cycle as been evident in the dQ/dV curves of different cycles without compromising the resulting capacity. The occurred phase transformation, which opposed the other ZnV_2O_4 , led to the formation of both ZnO and V_2O_3 . After 100 cycles using 1 A g^{-1} , it was found that 1D morphology were kept with shorter length. On the other hand, the CV curves at different scan rates indicate a pseudo-capacitive electrochemical behavior of the porous ZnV_2O_4 .

3.1. Introduction

Global warming and the increasing energy demand are the two main issues globally. As the energy supply increases so as the amount of carbon dioxide being emitted from the burning of the fossil fuel and thus enhances global warming. To mitigate these problems, a need to resolve to both renewable energy and electric vehicles (EV) is indispensable. However, the full utilization of both renewable energy and EVs are still immature and still needs further improvements, with energy storage devices as one of the issues that need to be addressed.¹⁻⁷ Among the different energy storage devices Lithium-ion battery (LIB) is the most appealing due to its high specific energy and specific power that opens up a wide range of applications. One of the current drawbacks of the commercially produced battery is the type of anode

material, i.e. carbon with a theoretical specific capacity of only 372 mA h g^{-1} , that restricts its applicability in high energy and power applications. Conversion type is one of the promising anode material due to its high theoretical capacities ranging between 650 and 1000 mA h g^{-1} . The high theoretical capacities can be attributed to the materials ability to transfer more than one electron per atom, e.g. 2-3 e^- , are exchanged for a typical oxide, during the redox reaction with Li^+ . Conversion type materials, though with higher specific gravimetric capacity than that of graphite, it still much lower compared to that of alloying material. However, in terms of volumetric capacity and volumetric expansion during Li^+ uptake, conversion type materials are superior compared to alloying materials.^{7,8}

Ternary transition metal oxides (TMOs) as a conversion anode type of material, have gathered much attention due to its high reversible capacity, low cost, natural abundance, and hypotoxicity.⁹⁻¹¹ However, TMOs are known to have low electrical conductivity caused by insulating property due to the intrinsic high band gaps, poor ionic conductivity and ion diffusion kinetics, high voltage hysteresis, and large volume expansion and complete structural reorganization that all leads to poor capacity retention. Thus numerous studies have been conducted to enhance the electrochemical properties and hence the capacity cycling stability. Three approaches have been considered to address these issues: (a) coat TMOs with a stable carbon layer,^{12,13} (b) synthesize bicomponent-active TMOs to allow the stepwise volumetric change to improve the electrochemical cycling,⁹ and (c) to fabricate nanostructure TMOs.^{14,15} Coating TMOs with a stable carbon layer is an effective way to enhance e^- transfer and thus improving high-rate and cycling properties. However, incorporating carbon can sometimes lead to the decrease in the overall Li-storage due to the low specific capacity of carbon, e.g. Zn_2GeO_4 can deliver higher capacity after 40 cycles compared to its carbon coated counterpart, i.e. $\text{Zn}_2\text{GeO}_4/\text{g-C}_3\text{N}_4$.^{13,16} Hence producing nanoparticles with an ideal nanostructure is

desirable. One dimensional (1D) nanoparticles gathered much attention due to: (a) high surface to volume ratio, (b) 1-D geometry that enhances e^- transfer and conduction, and (c) nanometer-sized diameter for short Li^+ diffusion and facilitate strain relaxation.¹⁷⁻¹⁹ High surface to volume ratio due to the nanometer size enhances: (a) the reaction kinetics that can further improve the cell capacity and capacity retention, and (b) the ability to use high charge/discharge rates. Hence, having a porous geometry that further enhances the surface to volume ratio of the 1D nanoparticle is an ideal structure to improve the electrochemical property of the material.^{16,20,21} Li et al. compared the electrochemical performance of Zn_2GeO_4 nanorods (ZGONRs) with that of its porous counterpart Zn_2GeO_4 nanofibers (p-ZGONFs). They observed that p-ZGONFs have much better capacity stability with good capacity retention at different current densities.¹⁶

ZnV_2O_4 , a TMO with spinel structure is a potential anode material for LIBs. Compounds with spinel structure have the general formula of AB_2X_4 . A and B are the cations occupying the tetrahedral (8a) sites and octahedral (16d) sites respectively of the cubic structure with space group symmetry $Fd\bar{3}m$, while X, is the anion occupying the 32e sites, forming a cubic-close-packed array.¹¹ Theoretically, spinel structures are known to be crystallographically porous with 56 empty tetrahedral sites and 16 empty octahedral sites, since A and B cations only occupy one-eighth (1/8) of the tetrahedral sites and one-half (1/2) of the octahedral sites respectively. Hence spinel structure is expected to easily accommodate small guest ions, e.g. Li^+ , within its interstitial spaces. However, the short distances and coulombic interactions between the guest ions and the A and B cations, due to the shared faces (at least two) of the empty tetrahedral and octahedral sites with the occupied tetrahedral and octahedral sites, can hinder the simultaneous insertion of the guest ions. Instead, Li^+ insertion occurs following the reduction of the A and B cations, accompanied by an internal phase change transforming the

A[B₂]O₄ structure to a rock-salt structure, [LiA]_{16c}[B₂]_{16d}O₄, wherein the square brackets indicates octahedral sites.²²⁻²⁴

ZnV₂O₄ is one of the promising anode materials for LIB, wherein both Zn and V can store Li⁺ by alloying and redox reaction respectively. Zn can form different alloys with Li (LiZn \rightleftharpoons LiZn₂ \rightleftharpoons Li₂Zn₅) while V can have a multistep oxidation to a higher valence state, e.g. V²⁺ to V^{4.36+}, since V metal typically has multiform valence state.²⁹ V can also form an amorphous oxide matrix during the phase transformation that can act as a buffer carrier that preserves the architecture and provides a conductive backbone due to its mixed-valence state.²⁶ Zheng et al. fabricated a hierarchical ZnV₂O₄ microsphere which exhibited high rate performance and good cycling stability with a reversible capacity of 638 mA h g⁻¹ that was maintained after 280 cycles at a current of 100 mA g⁻¹.²⁸ Xiao et al. produced a chew-like ZnV₂O₄ hollow spheres with specific capacity of 524 mA h g⁻¹ after over 50 cycles.²⁹ Zhu et al. examined nanophase ZnV₂O₄ with 660 mA h g⁻¹ after 30 cycles using 50 mA g⁻¹ current density.³⁰ Zheng et al. produced ZnV₂O₄-CMK nanocomposite with improved capacity and cycling stability of 536 mA h g⁻¹ after 100 cycles compared to that of its counterpart in the absence of CMK.³¹ On the other hand, our previous report shows that ZnV₂O₄ is also a potential anode material for sodium-ion battery, wherein both Zn and V participated in the Na⁺ uptake.¹¹ However, though there are already several studies that utilized ZnV₂O₄ as anode material for LIB, 1D ZnV₂O₄ as anode material for LIB has not yet been reported and hence been the focus of this study.

In this research, we fabricate a porous 1D ZnV₂O₄ via a two-step process, i.e. hydrothermal synthesis followed by calcination. Hydrothermal synthesis allows the formation of wire-like morphology, while calcination at 600 °C using 3% H₂/N₂ for 4 h yields to porous ZnV₂O₄ nanowires (NWs). These ZnV₂O₄ NWs exhibited better capacity, i.e. 460 mA h g⁻¹ after 100

cycles, and 149 mA h g^{-1} after 1000 cycles, at high current density, i.e. 1 A/g and 5 A/g respectively, compared to that of the spherical and coral-like particles, which were obtained by varying the calcination conditions. This study is also the first study that examine ZnV_2O_4 compound at high current density of 5 A g^{-1} for 1000 cycles. Both high specific capacity and good capacity retention of the porous ZnV_2O_4 NWs can be attributed to both the 1D morphology and high surface area due to the porous structure of the wires, which are advantageous to improve both the cycle stability at numerous charge/discharge cycles and Li^+ flux respectively.

3.2. Experimental Section

3.2.1. Materials Preparation

Spinel compound ZnV_2O_4 were synthesized using the hydrothermal method. Zinc nitrate hexahydrate ($\text{Zn}(\text{NO}_3)_2 \cdot 6\text{H}_2\text{O}$, Junsei Chemical Co. Ltd.) and ammonium vanadate (V) (NH_4VO_3 , Junsei Chemical Co. Ltd.) were used as the precursors, while dodecyl trimethylammonium bromide (DTAB, Tokyo Chemical Industry Co., Ltd.) served as capping ligand. Distilled water, on the other hand, was used as a solvent. All chemicals were used without further purification.

ZnV_2O_4 NWs were prepared via two-step synthesis. 0.1729 g of $\text{Zn}(\text{NO}_3)_2 \cdot 6\text{H}_2\text{O}$, 0.0544 g of NH_4VO_3 , and 0.06 g of DTAB were mixed in 10 mL distilled water under vigorous stirring for 2 h at $75 \text{ }^\circ\text{C}$. The mixture was then transferred to a 20 mL Teflon-lined stainless-steel autoclave and kept in a muffle furnace at $200 \text{ }^\circ\text{C}$ for 24 h . The obtained powder was then purified by further dispersion in 40 mL water and 1-propanol, as it was centrifuged several times, using 8000 rpm for 15 minutes . The obtained product was dried under vacuum for not less than 12 h before it was calcined at $600 \text{ }^\circ\text{C}$ using $3\% \text{ H}_2/\text{N}_2$ for 4 h .

On the other hand, spherical and coral-like morphologies were obtained using the same hydrothermal synthesis as that of the porous NWs. The variation on the morphology was obtained by changing the calcination condition. Spherical and coral-like morphologies were obtained by increasing the calcination temperature to 700 °C and successive calcination (3 times) at 600 °C respectively under 3% H₂/N₂ for 4 h.

3.2.2. Characterizations

The crystallinity and phase structure of the produced product were characterized using X-ray diffraction (XRD, Rigaku Miniflex II desktop X-ray diffractometer, Cu K α , 1.5418 Å, radiation) and the oxidation states of both Zn and V were identified using X-ray photoelectron spectroscopy (XPS, JEOL Photoelectron Spectrometer (ESCA), JPS-9200, monochromatic Al-K α). The morphology of the of the produced product, the corresponding elemental mapping, and crystal structure were examined using both scanning electron microscope (SEM, JEOL JSM-6510LA) and transmission electron microscope (TEM, JEOL JEM-2000FX, 200 kV), while the crystal growth and surface plane were analyzed using a scanning transmission electron microscope (STEM, JEOL JEM-ARM200F, 200 kV).

3.2.3. Electrochemical Test

The electrochemical tests were conducted using the HS Flat Cell from Hohsen Corp. as illustrated in Figure 4.1, using lithium metal as the counter electrode. The ZnV₂O₄ electrode was prepared by coating the ZnV₂O₄ slurry onto a 10 μm copper foil (The Nilaco Corporation). The ZnV₂O₄ slurry was composed of 70 w/w% active material, i.e. ZnV₂O₄ NWs, 20 w/w% carbon black (Super C65, Timcal America Inc.), 6 w/w% carboxymethylcellulose (CMC, MTI

Corporation), and 4 w/w% styrene-butadiene rubber (SBR, MTI Corporation). The coated electrode was initially dried at 70 °C for 5 min before it was punched into a 14 mm disk. The residual water was removed by further drying under vacuum at 120 °C for 12 h to remove the residual water. The HS Flat Cell was assembled in an N₂-gas filled glovebox with O₂ content < 3 ppm. Celgard membrane disk (Celgard[®] 2325), and LiPF₆ in ethylene carbonate and dimethyl carbonate (1.0 M LiPF₆ in EC/DMC=50/50 v/v, battery grade, Sigma-Aldrich Co.) were used as separator and electrolyte respectively. The discharge/charge and C-rate test were both examined using the Electrofield EF-7100P. The voltage range was from 0.01 V to 3.0 V at room temperature. The impedance of the cell was examined using potentiostat/ galvanostat device (SI 1260 and 1287, Solartron).

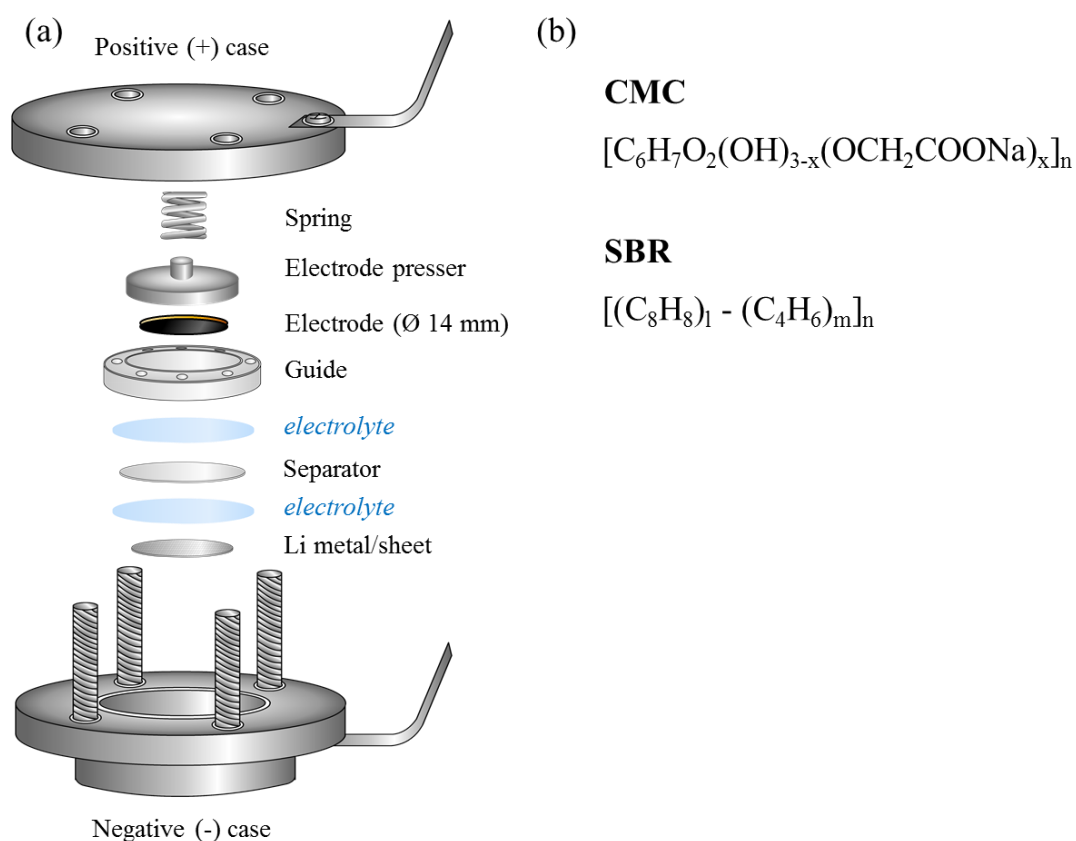


Figure 4.1. (a) Schematic diagram of HS Flat Cell, (b) are the chemical formula of the CMC and SBR binders used.

3.2.4. Ex-situ Characterizations

To further characterize and explain what occurs in the anode material during the charge/discharge test, ex-situ analysis of the working electrode was done. The working electrode was obtained by opening the HS Flat Cell inside the N₂-filled glovebox with the O₂ content of <3 ppm before it was washed for several times using hexane to remove the excess electrolyte. The crystallinity and phase structure of the porous ZnV₂O₄ NWs electrode were characterized using X-ray diffraction (XRD, Rigaku Miniflex II desktop X-ray diffractometer, Cu K α , 1.5418 Å, radiation), while the morphology was examined using a scanning electron microscope (SEM, JEOL JSM-6510LA).

3.3. Results and Discussion

3.3.1. Formation of 1D ZnV₂O₄

Hydrothermal synthesis is one of the mostly used techniques in the formation of particles with different morphologies. In this study, we utilize the hydrothermal method in the formation of zinc vanadium oxide (ZVO) with wire-like morphology using Zn(NO₃)₂•6H₂O and NH₄VO₃ as precursors in the presence of DTAB. After the hydrothermal synthesis, it was found that the XRD pattern of the produced particles (blue pattern) corresponded to ZnV₂O₆ with JCPDS # 00-023-0757 as shown in Figure 4.2. After calcination under 3% H₂/N₂ at 600 °C for 4h, these particles were reduced to ZnV₂O₄ of which the XRD pattern (red pattern) was well aligned with the reference pattern of the ZnV₂O₄ (JCPDS # 01-075-0318), as indicated in Figure 4.2.

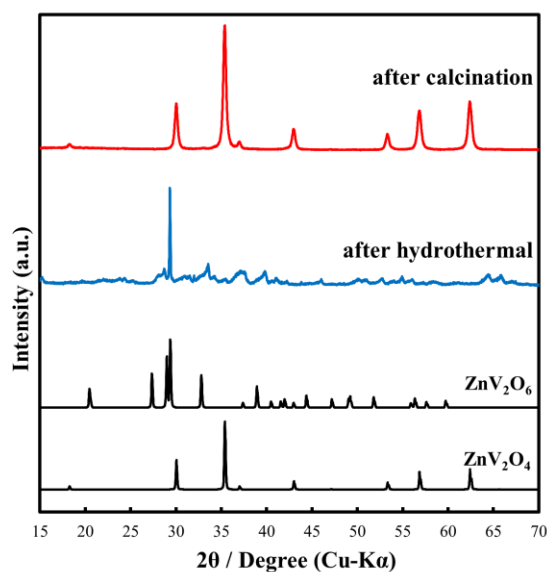


Figure 4.2. XRD patterns of the samples synthesized in the presence of DTAB: after hydrothermal (blue) and after calcination (red) with the corresponding XRD patterns of ZnV_2O_6 (JCPDS # 00-023-0757) and ZnV_2O_4 (JCPDS # 01-075-0318).

The morphology of the produced particles was analyzed in TEM and STEM. It was found that the particles produced after the hydrothermal process have a wire-like structure as shown in Figure S4.1. The SAED analysis of the wire-like structure agrees well with the XRD result, wherein the compound is analyzed as ZnV_2O_6 . After calcination, the single crystal NWs become porous as shown in Figure 4.3. Based on the SAED pattern, even though these NWs have porous structure, these NWs are still single crystal with the $\langle 111 \rangle$ direction along the wire and $\{220\}$ facets.

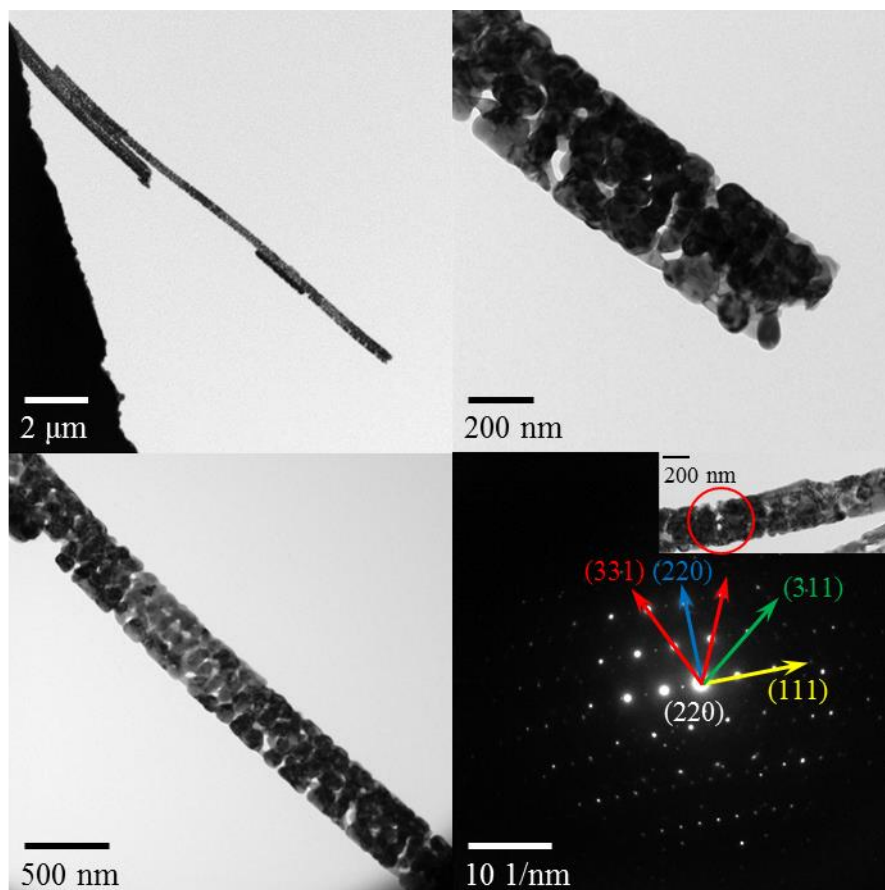


Figure 4.3. TEM images of the 1D ZnV_2O_4 : (a) whole 1D ZnV_2O_4 , (b) tip of the 1D ZnV_2O_4 , (c) along the wire, (d) SAED of the 1D ZnV_2O_4 with inset of the examined area.

ZnV_2O_4 , a spinel compound, has Zn atoms occupying the tetrahedral (8a) sites and V atoms occupying the octahedral (16d) sites as shown in Figure 4.4a. Based on the HAADF-STEM image in Figure 4.4b, the surface of the NW is a single crystal with (220) as the surface crystallographic plane as indicated by the distance between the lattice fringes, that is 2.97 Å. This result agrees well with the TEM and SAED result, wherein the NWs have {220} facets. Figures 4.4c and 4d shows the HAADF-STEM and ABF-STEM respectively of the surface of the NW, with superimposed two-dimensional atomic arrangement of the Zn, V, and O atoms viewed at (220), and hexagonal (red) arrangement of 6 Zn atoms and 4 V atoms surrounding the central V atom as shown in Figure 4.4a. Based on the HAADF-STEM in Figure 4.4c, there are a total of 10 atoms surrounding the central atoms. These 10 atoms can be attributed to 6 Zn

atoms and 4 V atoms as indicated by the brighter and less bright contrasts respectively. The 6 O atoms that surround the central V atom, on the other hand, were located in the dark area of the HAADF-STEM image. This agrees well with the ABF-STEM image (Figure 4.4d), wherein the central atoms were surrounded by 4 spheres (2 relatively larger spheres and 2 relatively smaller spheres) which are not evident and are located in the dark areas of the HAADF-STEM image. Both the relatively larger and smaller spheres are all attributed to O atoms, where the relatively larger sphere is composed of 2 O atoms, hence a total of 6 O atoms surrounds the central V atom. The red hexagons were superimposed on both HAADF-STEM and ABF-STEM images for ease of visualization.

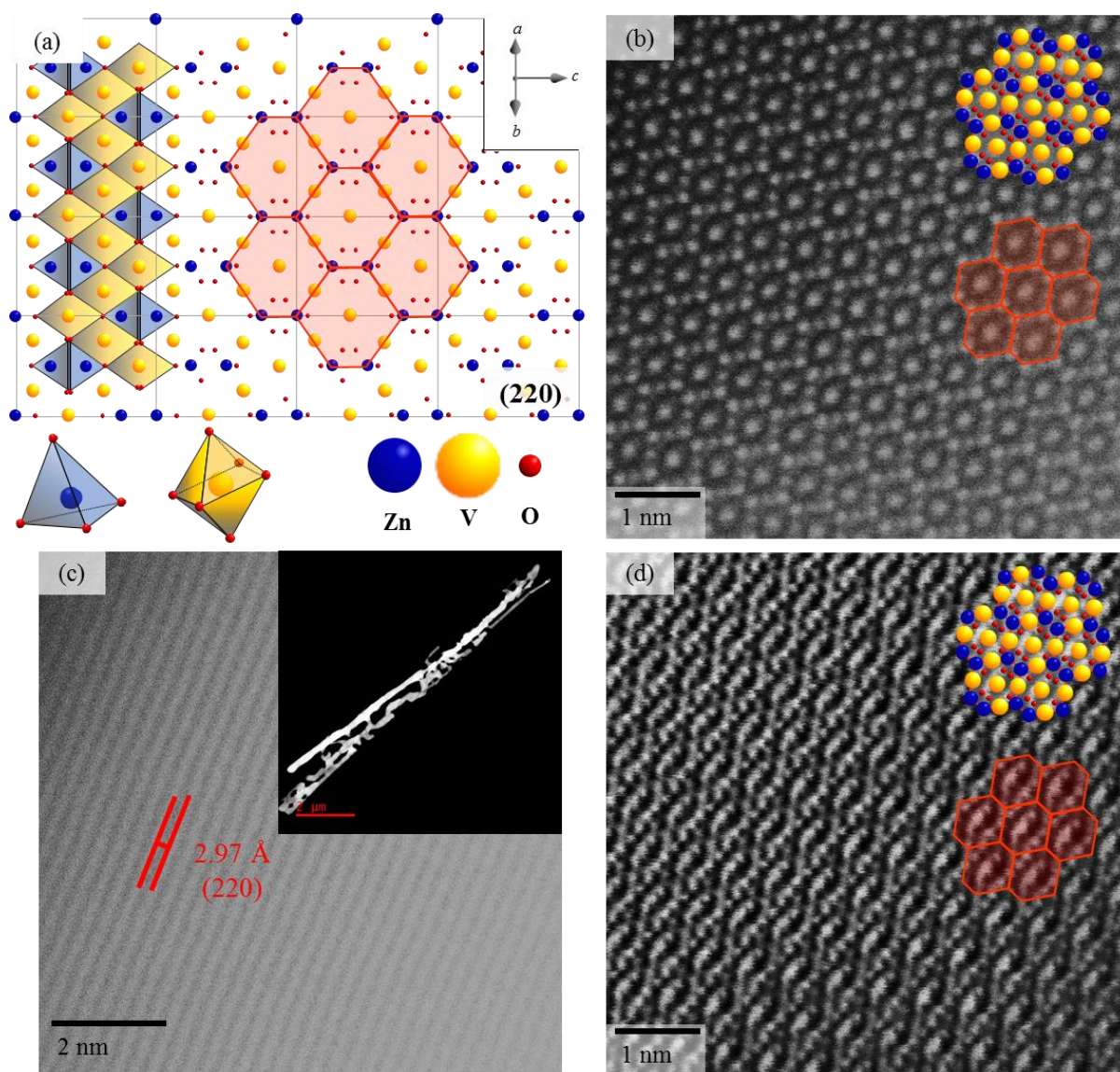


Figure 4.4. (a) Two-dimensional crystal structure of ZnV_2O_4 illustrating the distribution of Zn (blue), V (yellow), and O (red) atoms viewed along the $[220]$, where Zn and V occupy the tetrahedral (8a) and octahedral (16d) sites respectively. The red hexagon indicates the 4 V atoms and 6 Zn atoms surrounding the V atom. (b and c) HAADF-STEM images of the rod indicating the distance between the (b) lattice fringes, i.e. 2.97 \AA , corresponding to the (220) plane and (c) the distribution of the atoms at the surface of the rod. (d) the corresponding ABF-STEM image of (c). The superimposed images in (c) and (d) illustrates both the red hexagons indicated in (a) and the atomic arrangement of Zn, V, and O.

In order to get an insight on the purity of the produced porous ZnV_2O_4 , XPS analysis was performed as shown in Figure 4.5. Figure 4.5a indicates that Zn, V, O, and C are all present in the sample. The presence of C in the sample can be attributed to the added DTAB during the hydrothermal synthesis and the used C tape (substrate) to examine the sample under XPS. The deconvoluted narrow scan of V 2p (Figure 4.5b) indicates that there are two valence states of V present in the sample, i.e. V^{3+} (95.47%) and V^{5+} (4.53%). The peaks at 515.735 eV and 523.368 eV corresponds to the V 2p_{3/2} and 2p_{1/2} of V^{3+} , while that at 517.179 eV and 524.827 eV are attributed to V 2p_{3/2} and 2p_{1/2} of V^{5+} respectively. The spin-orbit splitting between the measured V 2p_{3/2} and 2p_{1/2} are 7.633 eV and 7.648 eV for V^{3+} and V^{5+} respectively, which agrees well with the standard value of 7.64 eV.^{11,25,32,33} The presence of a small amount of V^{5+} can be attributed to the surface oxidation and/or the incomplete reduction of ZnV_2O_6 during calcination.^{1,17,24} The presence of the peak at 520.201 eV can be designated to the satellite peak due to the existence of both V^{3+} and V^{5+} .²⁵ On the other hand, the deconvoluted peak of Zn 2p (Figure 4.5c) indicates two peaks at 1021.88 eV and 1045.04 eV corresponding to Zn 2p_{3/2} and Zn 2p_{1/2} respectively of Zn^{2+} . The difference between these two peaks is 23.16 eV which agrees with the standard value of 22.97 eV.^{11,32,33} The deconvolution of O 1s (Figure 4.5d) depicted two peaks at 530.196 eV and 533.392 eV which can be attributed to the oxide anions and the C-OH (and carbonate, C-O-O) respectively from the oxidized carbon species.^{11,32,33} The formation of the oxidized carbon species (C-OH and carbonate, C-O-O) are already present after the hydrothermal reaction, as shown in Figure S4.2d, for the XPS analysis of ZnV_2O_6 NWs. Aside from the oxidized carbon, the peak at 530.527 eV can also be attributed to the oxide anions as that of the porous ZnV_2O_4 NWs. The wide scan in Figure S4.2a indicates the presence of Zn, V, O, and C in the ZnV_2O_6 NWs after the hydrothermal synthesis. The peaks at 1045.59 eV and 1022.42 eV of the deconvoluted Zn 2p (Figure S4.2c) peaks with the spin-orbit splitting of 23.17 eV indicates the presence of Zn^{2+} . The V 2p peaks (Figure S4.2b) on

the other hand depicts that both V^{3+} (7.83%) and V^{5+} (92.17%) valence states are present in the ZnV_2O_6 NWs after the hydrothermal synthesis.

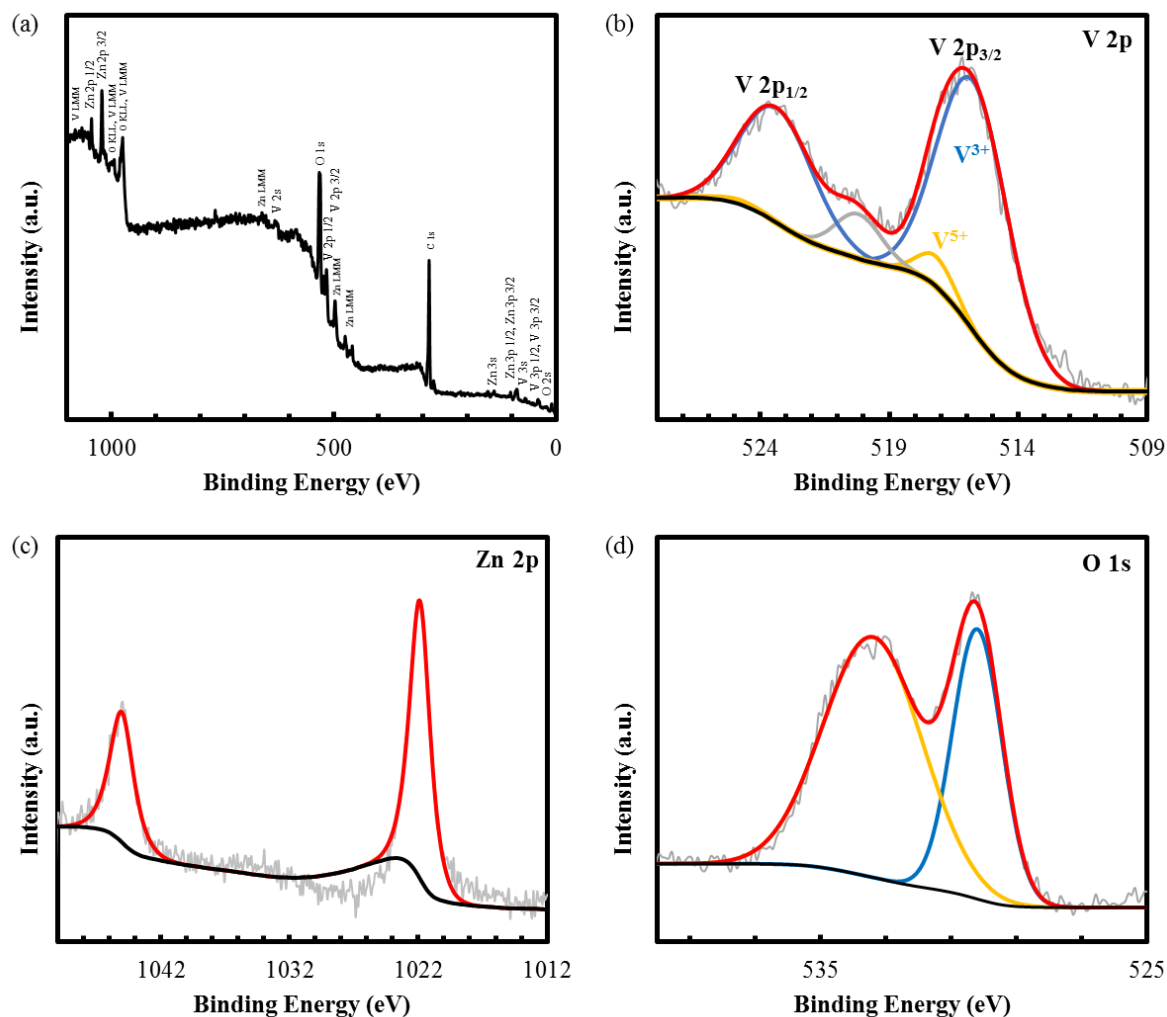


Figure 4.5. XPS spectra of porous ZnV_2O_4 NWs: (a) wide scan, and narrow scans of (b) V 2p, (c) Zn 2p, and (d) O 1s.

To determine the effect of the added DTAB, a similar method was performed in the absence of DTAB. It was found that in the absence of DTAB, ZnV_2O_6 and ZnV_2O_4 were still formed after hydrothermal synthesis and calcination respectively as indicated by the XRD peaks in Figure S4.3, and still with wire-like morphology as indicated by the SEM images as shown in Figure S4.4. However for the wire-like morphology to be obtained, it will take around

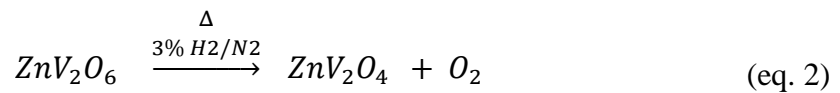
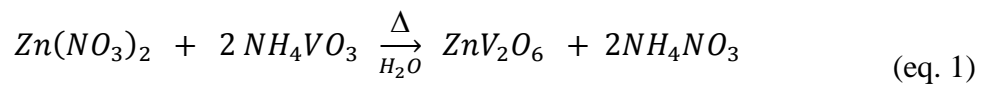
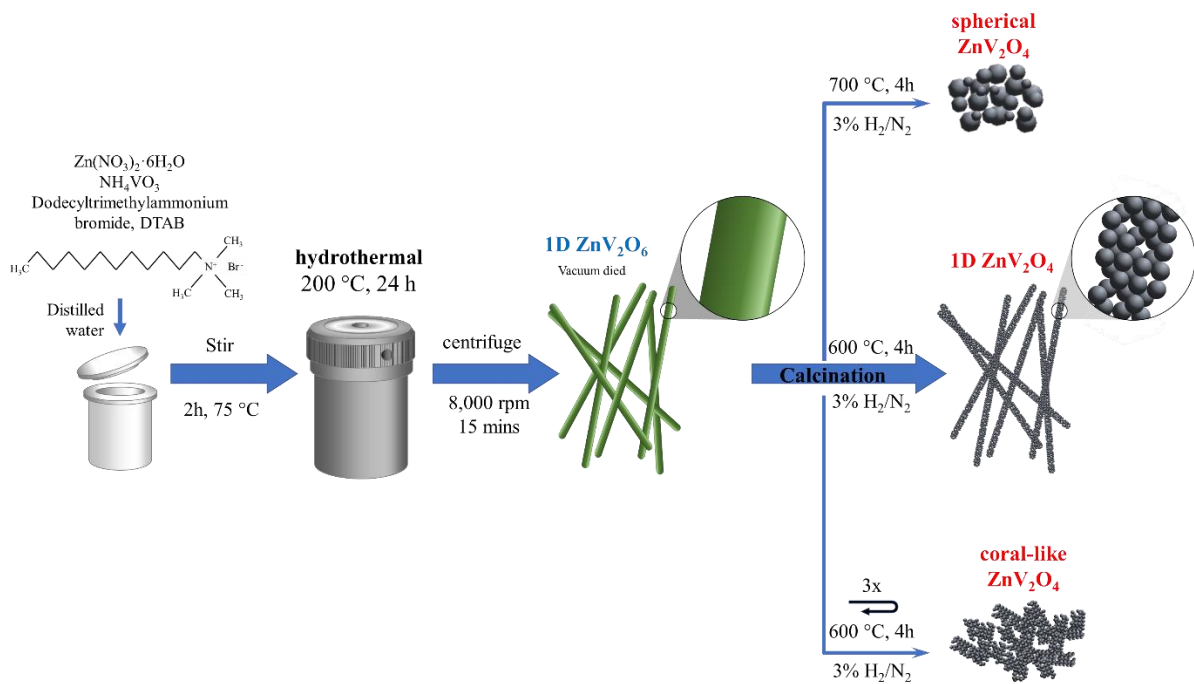
7 days for the hydrothermal synthesis to finish. This result agrees well with the results of Sun et al., wherein they found that meso/nanowires can be formed after 48 h, but it still needs >96 h to allow the splitting of the meso/nanowires into thinner NWs.¹⁹ The thinner NWs produced without DTAB have almost the same size as that of the NWs produced in the presence of DTAB using 24 h hydrothermal synthesis. From the results of Sun et al., they observed that before the NWs were produced, they obtained both microflowers and microsheets after 3 h and 12 h of hydrothermal reaction time respectively.¹⁹ The formation of the $\text{ZnV}_2\text{O}_6/\text{Zn}_2\text{V}_2\text{O}_7$ microsheets were also observed in our process in the presence of DTAB after 6 h hydrothermal reaction time as shown in the XRD pattern and SEM image in Figure S4.5. Hence, the role of the used DTAB in the hydrothermal synthesis can be ascribed to increase the reaction rate / speed up the reaction rather than to aid in the formation of the wire-like morphology. DTAB is known to have a catalytic effect, e.g. phase transfer catalysis for the pharmaceutical industry, and catalyst, additives, and auxiliaries in both polymers and agrochemical industry.³⁴ However, the applicability of DTAB as a catalyst in speeding up the morphological changes for hydrothermal synthesis has not yet been observed, and hence the verification of its catalytic effect is yet to be understood.

On the other hand, varying the calcination condition also affect the morphology of the produced particles. Increasing the calcination temperature to 700 °C for 4 h using 3% H_2/N_2 resulted in spherical particles as shown in Figure S4.6a. On the other hand, repetitive calcination, vis. 3 times, at 600 °C using 3% H_2/N_2 for 4 h per calcination each time resulted in a broken wire structure that resembles a coral-like morphology as shown in Figure S4.6b. Based on the HAADF-STEM and ABF-STEM of both spherical and coral-like particles, both morphologies are still single crystal ZnV_2O_4 with {220} facets as shown in Figures S4.7a-f.

3.3.2. Proposed mechanism in the formation of porous ZnV₂O₄

In this study, porous ZnV₂O₄ NWs were formed via two-step synthesis, i.e. hydrothermal followed by calcination, as shown in scheme 1. Zn(NO₃)₂•6H₂O and NH₄VO₃ were used as precursors in the hydrothermal synthesis in the presence of DTAB. The 24 h hydrothermal reaction at 200 °C, already produces green colored particles that are characterized to be single crystal ZnV₂O₆ with wire-like morphology due to the catalytic effect of DTAB. On the other hand, calcination at 600 °C for 4 h under 3% H₂/N₂ results in a porous structure due to the reduction/removal of oxygen. These porous NWs are characterized as single crystal ZnV₂O₄. Varying the calcination temperature to 700 °C for 4 h under 3% H₂/N₂, and repetitive calcination at 600 °C for 4 h per calcination process under 3% H₂/N₂ result to a change in morphology, i.e. spherical and coral-like morphology, which are observed to be a single crystal with {220} facets. The proposed chemical reactions that occurred during hydrothermal and calcination were shown in eq. (1) and (2). During the hydrothermal synthesis, 1 mol of Zn(NO₃)₂ reacts with 2 mol NH₄VO₃ to form ZnV₂O₆ and 2 mol NH₄NO₃. The produced NH₄NO₃ is soluble in H₂O and was removed during the purification process, hence only ZnV₂O₆ was left after the purification process. On the other hand, in the calcination process, the ZnV₂O₆ was reduced to ZnV₂O₄ through the removal of O₂ hence promoted the formation of porous structure. Calcination at 600 °C is necessary for the conversion of ZnV₂O₆ to ZnV₂O₄, lower temperature resulted in a non-completing reduction. However, higher temperature, i.e. 700 °C, or longer times of calcination caused the breakage of the wire structure and formation of spherical or coral-like structure, respectively. This is possibly due to the high reduction speed at high temperature or the thermal instability of the formed ZnV₂O₄ NWs structure under longtime calcination, respectively.

Scheme 1. Mechanism in the formation of porous ZnV_2O_4 with different morphologies with respect to the calcination condition.



3.3.3. Electrochemical Test

The electrochemical test of the produced porous ZnV_2O_4 NWs was examined as an anode material for LIB as shown in Figure 4.6. The cycling behavior of porous ZnV_2O_4 NWs at a current density of 1 A g^{-1} is shown in Figure 4.6a while the corresponding voltage-capacity profile is shown in Figure 4.6c. It can be observed that the initial discharge capacity of 584 mA h g^{-1} decreases to 402 mA h g^{-1} on the 2nd cycle with a coulombic efficiency of 60.75%. The large decrease in the capacity after the 1st cycle can be attributed to the formation of the SEI layer. After the 2nd cycle, it can be observed that the capacity increases to 409 mA h g^{-1} on the 5th cycle and then it gradually increases on the succeeding cycles until 473 mA h g^{-1} on the 35th

cycle. After that, the capacity almost stabilizes with minimal fluctuations. This result indicates that the produced porous ZnV_2O_4 NWs have high capacity and good cycling stability. The continuous increase in the capacity during the 2nd to 35th cycle might be due to an active process, i.e. phase transformation, leading to an instable state of Li^+ insertion and extraction.²⁹⁻
³² On the other hand, to determine the rate performance of the porous ZnV_2O_4 NWs, different current densities were applied as shown in Figure 4.6b and its corresponding voltage-capacity profile in Figure 4.6d. It can be observed that the produced porous ZnV_2O_4 NWs have good rate performance, with stable average discharge capacities of 814, 736, 622, 500, 340, 132 mA h g^{-1} at different current densities of 0.1, 0.2, 0.5, 1, 2, and 5 A g^{-1} respectively. It is also worth noting that when the current density was returned to 0.1 A g^{-1} after being cycled at 5A g^{-1} , the porous ZnV_2O_4 NWs electrode has an average retention rate of 109.67% with a discharge capacity of 808 mA h g^{-1} , indicating the strong tolerance for the rapid Li^+ insertion and extraction.

To better understand what occurs on the electrode during the charge-discharge process, the dQ/dV plots at different cycles were analyzed as shown in Figure 4.7 and S4.8. It can be observed that on the 1st cycle, a broad peak at 0.5 – 1.0 V can be observed. This broad peak can be attributed to the formation of the SEI layer, which is responsible for the irreversible capacity loss, and the phase transformation. Ternary metal oxides are known to undergo a phase transformation to form a structure with an active metal oxide embedded in an amorphous metal oxide. In the case of Z-V-O ternary metal oxide, Zn serves as the active material that forms an alloy with Li^+ to form $\text{LiZn} \rightleftharpoons \text{LiZn}_2 \rightleftharpoons \text{Li}_2\text{Zn}_5$,²⁹ while V forms an amorphous lithiated vanadium oxide that can serve as buffer carrier to preserve the surface architecture and to have a stable cycling stability.²⁶ In addition, V can also accommodate Li^+ to increase the working electrode's specific capacity through a redox reaction, i.e. reduction to lower valence state.^{27,29-}

³² It can be observed that after the 1st cycle, the broad peak at 0.5 – 1.0 V can no longer be observed, while the peaks at ca. 0.55 and 0.96 V increases in the subsequent cycles. These 2 peaks correspond to the alloying of Zn and reduction of V respectively.^{10,12,29,32} The growing peaks at ca. 0.55 and 0.96 V during the first 35 cycles can be attributed to the continuous phase transformation, while the overlapping curves after the 35th cycle can be attributed to the stable transformed anode material. On the other hand, the protuberances at about 1.1 and 2.25 V during delithiation that increases as the cycle rate increases until the 35th cycle (Figure S4.8) can be attributed to the dealloying of Li_xZn_y to form ZnO and the oxidation of V^{+z} to higher valence state.^{10,12,29,32} The observed increase in the peak during delithiation agrees well with the growing peaks in the lithiation process. Hence, based on these result, the formed porous ZnV_2O_4 NWs have a continuous phase transformation until the 35th cycles without compromising the resulting specific capacity to form an architecture with stable capacity.

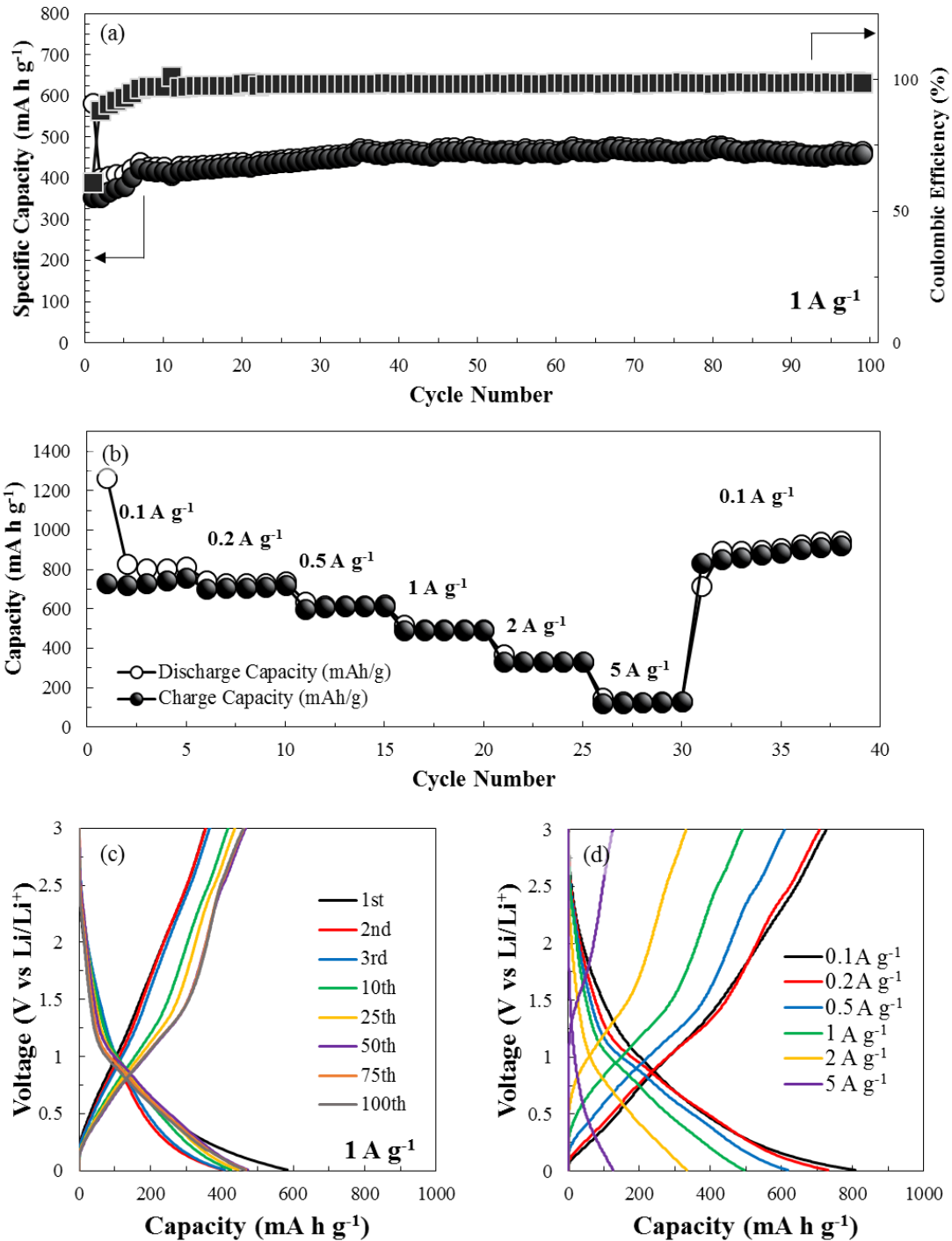


Figure 4.6. Electrochemical test of porous ZnV₂O₄ NWs: (a) charge/discharge profile with a current density of 1 A g⁻¹, (b) rate performance, and voltage-capacity profiles associated with (c) charge/discharge profile with a current density of 1 A g⁻¹ and (d) various current rates.

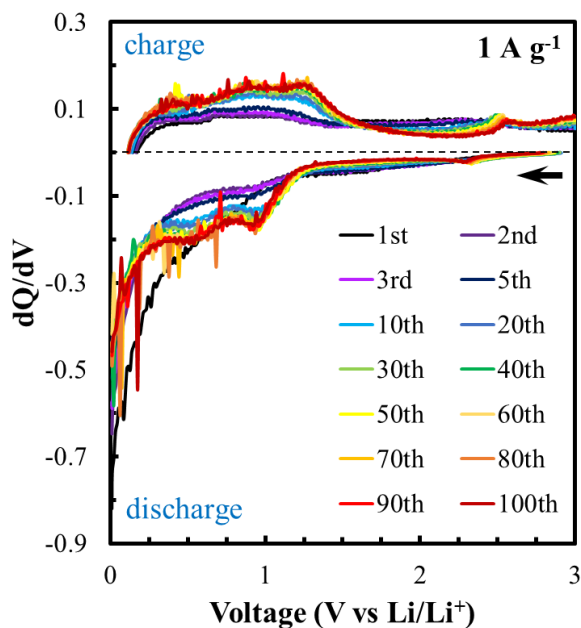


Figure 4.7. Plots of dQ/dV of the porous ZnV_2O_4 NWs cycled at 1 A g^{-1} at different cycle number.

To further analyze the electrochemical properties of the produced porous ZnV_2O_4 , the electrochemical impedance of the cell were obtained as shown in Figure 4.8, which is comprised of a semicircle and a straight sloping line at high and low-frequency regions respectively. It can be observed that the fresh sample has a higher resistance in the middle frequency compared to that of the measured cycled samples. During the charge/discharge process, V stores Li^+ through the redox reaction i.e. oxidizes at higher oxidation state during the charged process.^{22,29} The presence of the mixed-valence state of V acts as a conductive skeleton that enhances the electrochemical performance,²⁶ hence can be attributed to the decrease in resistance in the middle frequency from the fresh to the cycled samples. This phenomenon was also observed by Yu et al. when they utilize zinc pyrovanadate nanoplates as anode material for LIB.¹² On the other hand, the increase in the resistance in the middle frequency from the 10th cycle to the 100th cycle is to be expected due to the repeated cycles.

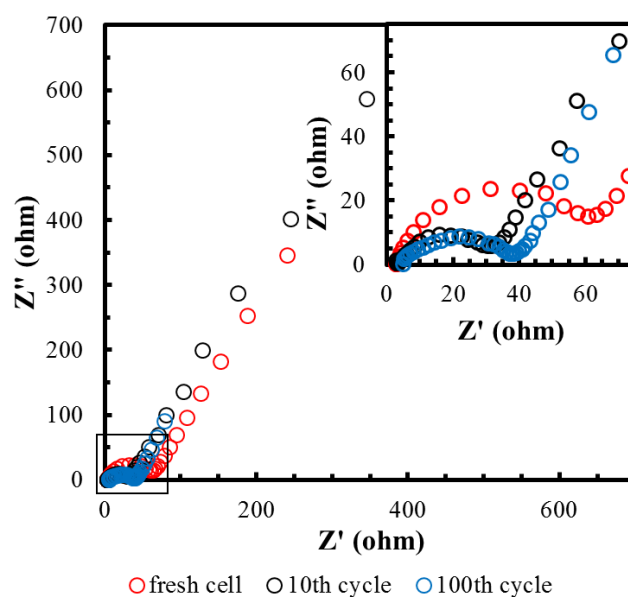


Figure 4.8. Nyquist plot of the porous ZnV_2O_4 : fresh cell (red), after 10 cycles (black), and after 100 cycles (blue) in the frequency range of 10^{+5} to 0.01 Hz.

It is known for ternary vanadium oxide, vis. zinc vanadium oxide, to form a stable architecture during phase transformation with V forming an amorphous oxide to serve as buffer carrier to preserve the morphology. Yang et al.²⁶ reported that the ZVO nanosheets can still be maintained after 10 cycles but with smaller dimensions, and in the study by Sun et al.¹⁹ wherein the 1D morphology of ZnV_2O_6 were maintained even after 80 cycles. However, instead of having an amorphous vanadium oxide and crystalline ZnO, based on the XRD pattern (Figure S4.9) on the electrode after 100 cycles, the peaks for ZnV_2O_4 are still present with additional peaks from both V_2O_3 and ZnO. According to Zhu et al.,³⁰ the $[\text{B}]_2\text{O}_4$ sublattice of the spinel structure ($\text{A}[\text{B}]_2\text{O}_4$) is the most active Li^+ insertion/extraction site, that can accommodate a maximum of 2 Li^+ . Though in some selected conditions, the said sublattice can accept more Li^+ and form $\text{Li}_x\text{V}_2\text{O}_4$ while keeping the spinel framework intact. However, the presence of both ZnO and V_2O_3 after 100 cycles indicates that phase transformation occurs. Hence both intact spinel framework and phase transformation occur simultaneously in the porous ZnV_2O_4

NWs electrode due to the gradual phase transformation which is attributed to the high current density used.

To further investigate the Li^+ storage mechanism and evaluate the rate behavior of the porous ZnV_2O_4 NWs, the CV curves at different scan rates were employed as shown in Figure 4.9a. It can be observed that all the peaks observed agree well with that of the peaks observed in the dQ/dV plots (Figure 4.7 and S4.8), which corresponds to the alloying/dealloying of Zn and reduction/oxidation of V during the charge/discharge process respectively. It can also be observed that as the scan rate increases, the CV curves deviate from the original position, hence can be attributed to the increase in polarization and ohmic resistance.^{25,35} In order to determine the capacitive behavior of the porous ZnV_2O_4 NWs, the relationship between the scan rate and the peak currents of the CV curves were analyzed as indicated by eq. (3).

$$i = av^b \quad (\text{eq. 3})$$

Where i and v correspond to measured current and the scan rate respectively. The b -value can be estimated using the slope of the $\log(v) - \log(i)$ plot as shown in Figure 4.9b. If the b -value $\cong 0.5$, the electrochemical behavior is governed by the diffusion process, however, if b -value $\cong 1.0$, the behavior is based on capacitive behavior. Based on the calculated b -value, i.e. 0.9298, the electrochemical behavior of porous ZnV_2O_4 NWs electrode is pseudo-capacitive. The high surface area due to the porous morphology of the ZnV_2O_4 NWs are propitious to the capacitive behavior, hence results to high cycle stability.^{25,35}

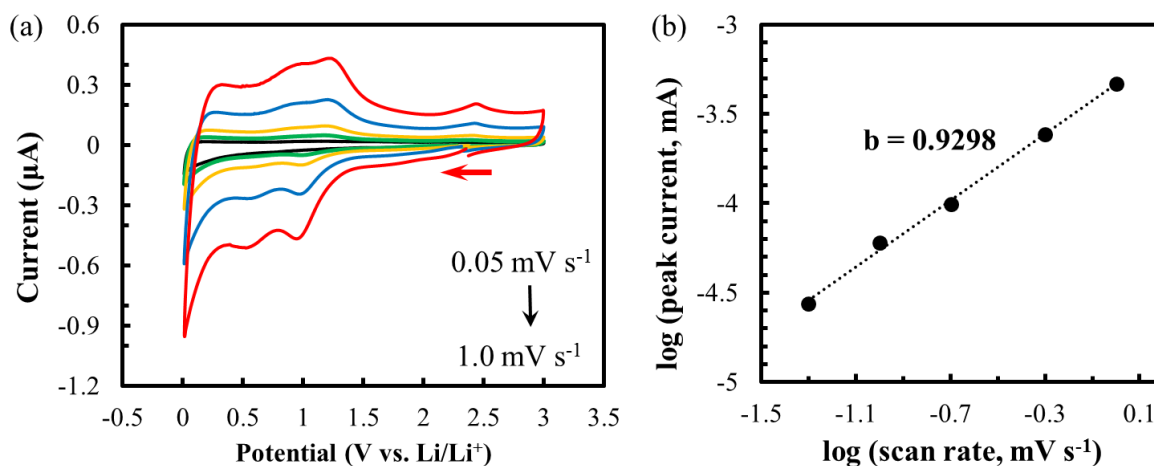


Figure 4.9. (a) CV curves of porous ZnV₂O₄ at different scan rates from 0.05 to 1.0 mV s⁻¹ with voltage window of 0.01 – 3.0 V. (b) log (v) – log (i) plot of (a). The sweep direction is from 3 to 0.01 V as indicated by the red arrow.

To determine the change in the morphology after 100 cycles, the SEM image of the electrode was examined under SEM as shown in Figure 4.10. It was observed that after 100 cycles, the 1D morphology was maintained, though with a shorter length. Based on the EDS analysis of the 1D particle after 100 cycles, Zn, V, and O are still well distributed along the rod with measured at% of V almost equal to twice of that of at% of Zn, hence the ratio between the Zn and V are still maintained which agrees well with the XRD result. The presence of the 1D morphology can be ascribed to the intact spinel framework, while the decrease in length might be the result of phase transformation as indicated by the presence of both ZnO and V₂O₃.

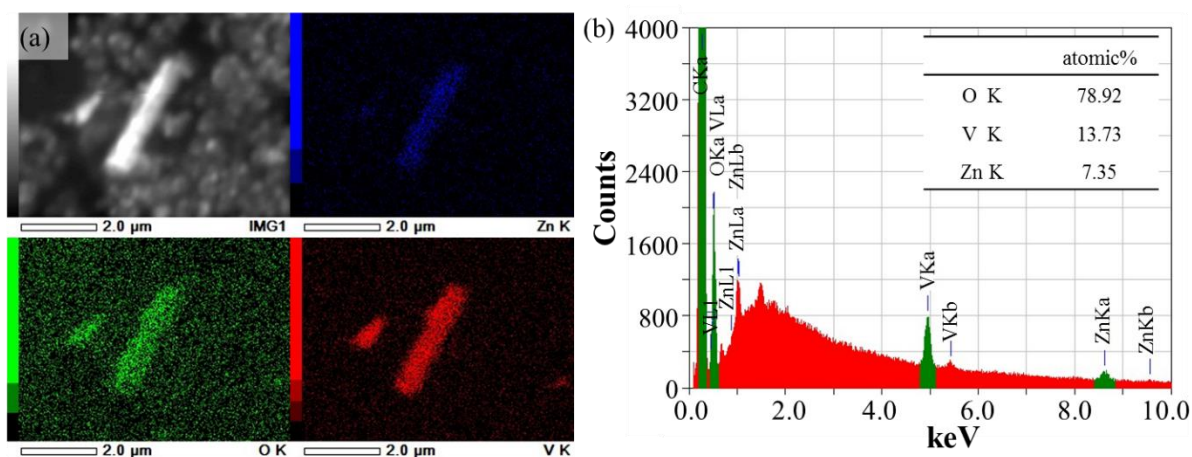


Figure 4.10. (a) SEM image of the porous ZnV₂O₄ NWs after 100 cycles, and the corresponding EDS mapping for (b) Zn, (c) V, and (d) O, and EDS spectrum with inset of the atomic %.

On the other hand, to determine the advantage of the porous NW morphology over the other morphologies, vis. spherical particle and coral-like morphology, the cycle test of the ZnV₂O₄ particles with different morphologies were examined under 5 A g⁻¹ as shown in Figure 4.11. It can be observed that even though all morphologies have stable capacity until the 1000th cycle, the porous NWs have the highest capacity, i.e. 149 mA h g⁻¹ after 1000 cycles. Figure S4.10 shows the comparison of this study with the other reported zinc vanadium oxide particles as an anode material for LIB. It can be observed that in comparison with the other zinc vanadium compounds, ZnV₂O₄ have the lower specific capacity, however, in comparison with the other ZnV₂O₄ morphologies, the produced ZnV₂O₄ NWs have much higher specific capacity at different current density. The high specific capacity over the other morphologies can be attributed to its porous 1D structure. The same phenomenon was observed by Sun et al. when they compare the electrochemical properties of ZnV₂O₆ NW with other morphologies as anode material for LIB.¹⁹ The improved electrochemical property can be attributed to the both porous, that provides a more active site for Li⁺ diffusion, and 1D morphologies, that provide a 1D flow

of e^- and ions. Thus we obtained the highest specific capacity among published data for the compound ZnV_2O_4 .

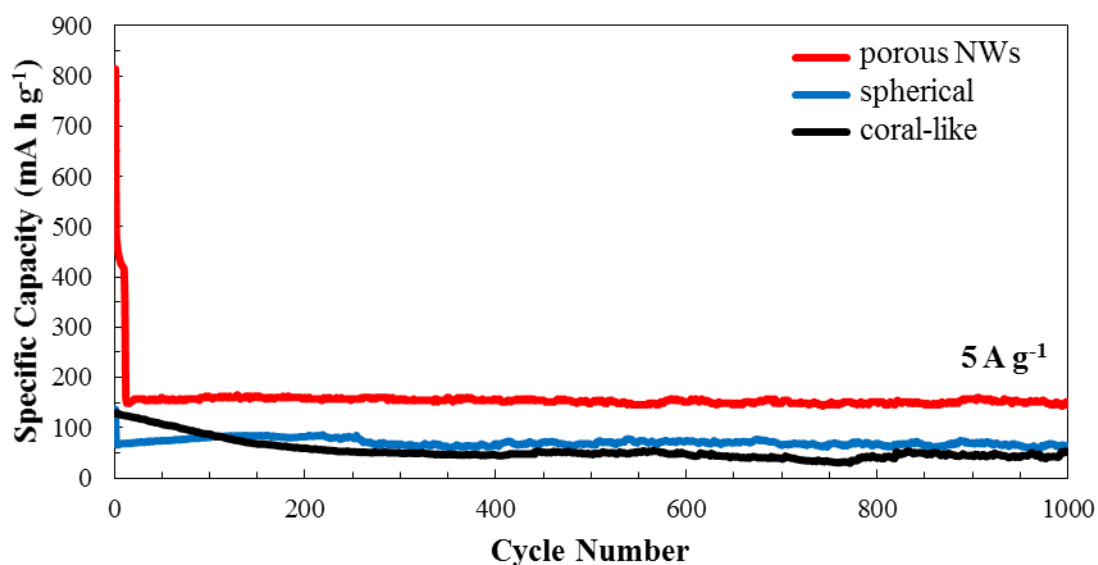


Figure 4.11. Charge/discharge profiles (current density of 5 A g^{-1}) of ZnV_2O_4 with different morphologies: (red) porous NWs, (blue) spherical, (black) and coral-like.

3.4. Conclusion

The porous ZnV_2O_4 NWs were synthesized via two-step process, i.e. hydrothermal followed by calcination. After the hydrothermal method, ZnV_2O_6 NWs were obtained while reduction occurs during the calcination process resulting in a porous ZnV_2O_4 NWs. These porous ZnV_2O_4 NWs are still single crystal with $\{220\}$ facets and $\langle 111 \rangle$ along the wire, despite its porous structure. The added DTAB in the hydrothermal synthesis could speed up the reaction to form ZnV_2O_6 NWs rather than as a shape-directing agent. On the other hand, the electrochemical properties of these porous ZnV_2O_4 NWs exhibit a stable and high specific capacity of 460 mA h g^{-1} after 100 cycles and 149 mA h g^{-1} after 1000 cycles using 1 and 5 A g^{-1} current densities respectively. The porous ZnV_2O_4 NWs have higher specific capacity compared to that of spherical and coral-like morphology, which were obtained by varying the calcination condition.

In comparison with the previously reported ZnV_2O_4 , the produced porous NWs show better specific capacity and cycling stability with the occurrence of phase transformation until the 35th cycle as indicated by the dQ/dV curves. While the analysis of the CV curves at different scan rates indicates that the governing electrochemical behavior of porous ZnV_2O_4 NWs is pseudo-capacitive which can also be attributed to the stable cycling stability. On the other hand, the 1D morphology can still be obtained after 100 cycles, which can be attributed to both the intact spinel structure of ZnV_2O_4 and the stable form after phase transformation. The partial and gradual phase transformation in porous ZnV_2O_4 NWs until the 35th cycle might be due to the applied high current density, i.e., 1 A g^{-1} .

Acknowledgment

This work is partially supported by Hokkaido University and Grants-in-Aid for Scientific Research ((B) 18H01820 to TY, and for Young Researcher (B) 17K14072 to MTN) from JSPS, Japan. A part of this study was conducted at Hokkaido University and was supported by the “Nanotechnology Platform” Program of the Ministry of Education, Culture, Sports, Science, and Technology (MEXT), Japan. TY also thanks partial supports by the Cooperative Research Program of “Network Joint Research Center for Materials and Devices” (20181111) and JSPS A3 Foresight Program “Organic/inorganic Nanohybrid Platforms for Precision Tumor Imaging and Therapy”. The authors thank Prof. W.-R. Liu (Chung Yuan Christian University, Taiwan) for fruitful discussions, Mr. T. Tanioka and Ms. R. Kurishiba (Hokkaido University) for their support in TEM observation and Mr. H. Tsukamoto (Hokkaido University) for this support in cyclic voltammetry set-up and measurement. LMZDJ would like to thank R. D. Corpuz (Mindanao State University – Iligan Institute of Technology, Philippine) and I. V. B. Maggay (Chung Yuan Christian University, Taiwan) for the fruitful discussions.

References

1. An, X.; Yang, H.; Wang, Y.; Tang, Y.; Liang, S.; Pan, A.; Cao, G., Hydrothermal synthesis of coherent porous V_2O_3 /carbon nanocomposites for high-performance lithium- and sodium-ion batteries, *Sci. China Mater.*, **2017**, 60(8), 717-727
2. Kim, H.; Seo, D.-H.; Kim, H.; Park, I.; Hong, J.; Park, K.-Y.; Kang, K., Multicomponent Effects on the Crystal Structures and Electrochemical Properties of Spinel-Structured M_3O_4 ($M = Fe, Mn, Co$) Anodes in Lithium Rechargeable Batteries, *Chem. Mater.*, **2012**, 24, 720-725
3. Meister, P.; Jia, H.; Li, J.; Kloepsch, R.; Winter, M.; Placke, T., Best Practice: Performance and Cost Evaluation of Lithium ion Battery Active Materials with Special Emphasis on Energy Efficiency, *Chem. Mater.*, **2016**, 28, 7203-7217
4. Mohanty, D.; Li, J.; Abraham, D. P.; Huq, A.; Payzant, A.; Wood, D. L. III; Daniel, C., Unraveling the Voltage-Fade Mechanism in High-Energy-Density Lithium-Ion Batteries: Origin of the Tetrahedral Cations for Spinel Conversion, *Chem. Mater.*, **2014**, 26, 6272-6280
5. Han, J.-T.; Huang, Y.-H.; Goodenough, J. B., New Anode Framework for Rechargeable Lithium Batteries, *Chem. Mater.*, **2011**, 23, 2027-2029
6. Lin, M.; Ben, L.; Sun, Y.; Wang, H.; Yang, Z.; Gu, L.; Yu, X.; Yang, X.-Q.; Zhao, H.; Yu, R.; Armand, M.; Huang, X., Insight into Atomic Structure of High-Voltage Spinel $LiNi_{0.5}Mn_{1.5}O_4$ Cathode Material in the First Cycle, *Chem. Mater.*, **2015**, 27, 292-303
7. Andre, D.; Hain, H.; Lamp, P.; Maglia, F.; Stiaszny, B., Future high-energy density anode materials from an automotive application perspective, *J. Mater. Chem. A*, **2017**, 5, 17174-17198
8. Li, H.; Huang, X.; Chen, L., Anodes based on oxide materials for lithium rechargeable batteries, *Solid State Ionics*, **1999**, 123(1-4), 189-197
9. Ge, X.; Li, Z.; Wang, C.; Yin, L., Metal-Organic Frameworks Derived Porous Core/Shell Structured $ZnO/ZnCo_2O_4/C$ Hybrids as Anodes for High-Performance Lithium-Ion Battery, *ACS Appl. Mater. Interfaces*, **2015**, 7, 26633-26642
10. Chen, N.; Wang, C.; Hu, F.; Bie, X.; Wei, Y.; Chen, G.; Du, F., Brannerite-Type Vanadium-Molybdenum Oxide $LiVMoO_6$ as a Promising Anode Material for Lithium-Ion Batteries with High Capacity and Rate Capability, *ACS Appl. Mater. Interfaces*, **2015**, 7, 16117-16123
11. Maggay, I. V. B.; De Juan, L. M. Z.; Nguyen, M. T.; Yonezawa, T.; Chang, B. K.; Chan, T.-S.; Liu, W.-R., ZnV_2O_4 : A potential anode material for sodium-ion batterie, *J. Taiwan Inst. Chem. Eng.*, **2018**, 88, 161-168
12. Yu, Y.; Niu, C.; Han, C.; Zhao, K.; Meng, J.; Xu, X.; Zhang, P.; Wang, L.; Wu, Y.; Mai, L., Zinc Pyrovanadate Nanoplates Embedded in Graphene Networks with Enhanced Electrochemical Performance, *Ind. Eng. Chem. Res.*, **2016**, 55, 2992-2999
13. Li, X. D.; Feng, Y.; Li, M. C.; Li, W.; Wei, H.; Song, D. D., Smart Hybrids of Zn_2GeO_4 Nanoparticles and Ultrathin $G-C_3N_4$ Layers: Synergistic Lithium Storage and Excellent Electrochemical Performance, *Adv. Funct. Mater.*, **2015**, 25, 6858-6866
14. Poizot, P.; Laruelle, S.; Grugeon, S.; Dupont, L.; Tarascon, J.-M., Nano-sized transition-metal oxides as negative-electrode materials for lithium-ion batteries, *Nature*, **2000**, 407, 496-499
15. Qu, B.; Hu, L.; Li, Q.; Wang, Y.; Chen, L.; Wang, T., High Performance Lithium-ion Battery Anode by Direct Growth of Hierarchical $ZnCo_2O_4$ Nanostructures on Current Collectors, *ACS Appl. Mater. Interfaces*, **2014**, 6, 731-736
16. Li, H.-H.; Wu, X.-L.; Zhang, L.-L.; Fan, C.-Y.; Wang, H.-F.; Li, X.-Y.; Sun, H.-Z.; Zhang, J.-P.; Yan, Q., Carbon-Free Porous Zn_2GeO_4 Nanofibers as Advanced Anode Materials for

- High-Performance Lithium Ion Batteries, *ACS Appl. Mater. Interfaces*, **2016**, 8, 31722-31728
17. De Juan, L. M. Z.; Maggay, I. V. B.; Nguyen, M. T.; Liu, W.-R.; Yonezawa, Y., β -Sn Nanorods with Active (001) Tip Induced LiF-Rich SEI Layer for Stable Anode Material in Lithium Ion Battery, *ACS Appl. Nano. Mater.*, DOI:10.1021/acsanm.8b00664
 18. De Juan, L.M.Z.; Nguyen, M.T.; Yonezawa, T.; Tokunaga, T.; Tsukamoto, H.; Ishida, Y., Structural Control Parameters for Formation of Single-Crystalline β -Sn Nanorods in Organic Phase, *Crystal Growth & Design*, **2017**, 17, 4554-4562
 19. Sun, Y.; Li, C.; Wang, L.; Wang, Y.; Ma, X.; Ma, P.; Song, M., Ultralong monoclinic ZnV_2O_6 nanowires: their shape-controlled synthesis, new growth mechanism, and highly reversible lithium storage in lithium-ion batteries, *RSC Adv.*, **2012**, 2, 8110-8115
 20. Gao, J.; Lowe, M. A.; Abruña, Sponge Nanosized Mn_3O_4 as a High-Capacity Anode Material for Rechargeable Lithium Batteries, *Chem. Mater.*, **2011**, 23, 3223-3227
 21. Zeng, P.; Wang, X.; Ye, M.; Ma, Q.; Li, J.; Wang, W.; Geng, B.; Fang, Z., Excellent lithium ion storage property of porous MnCo_2O_4 nanorods, *RSC Adv.*, **2016**, 6, 23074-23084
 22. Thackeray, M. M., Spinel Electrodes for Lithium Batteries, *J. Am. Ceram. Soc.*, **1999**, 82 (12), 3347-3354
 23. Arrebola, J. C.; Caballero, A.; Hernán, L.; Morales, J., Improving the Performance of Lithium-ion Batteries by Using Spinel Nanoparticles, *J. Nanomater.*, **2008**, 2008, 659397: 1-10
 24. Yuvaraj, S.; Selvan, R. K.; Lee, Y. S., An overview of AB_2O_4 - and A_2BO_4 -structured negative electrodes for advanced Li-ion batteries, *RSC Adv.*, **2016**, 6, 21448-21474
 25. Maggay, I. V. B.; De Juan, L. M. Z.; Lu, J.-S.; Nguyen, M. T.; Yonezawa, T.; Chan, T.-S.; Liu, W.-R., Electrochemical properties of novel FeV_2O_4 as an anode for Na-ion batteries, *Sci. Rep.*, **2018**, 8, 8839: 1-11
 26. Yang, G.; Li, S.; Wu, M.; Wang, C., Zinc pyrovanadate nanosheets of atomic thickness: excellent Li-storage properties and investigation of their electrochemical mechanism, *J. Mater. Chem. A*, **2016**, 4, 10974-10985
 27. Yan, N.; Xu, Y.; Li, H.; Chen, W., The preparation of FeVO_4 as a new sort of anode material for lithium ion batteries, *Mater. Lett.*, **2016**, 165, 223-226
 28. Zheng, C.; Zeng, L.; Wang, M.; Zheng, H.; Wei, M., Synthesis of hierarchical ZnV_2O_4 microsphere and its electrochemical properties, *CrystEngComm*, **2016**, 16, 10309-10313
 29. Xiao, L.; Zhao, Y.; Yin, J.; Zhang, L., Chewlike ZnV_2O_4 Hollow Spheres: Nonaqueous Sol-Gel Synthesis, Formation Mechanism, and Lithium Storage Properties, *Chem. Eur. J.*, **2009**, 15, 9442-9450
 30. Zhu, X.; Jiang, X.; Xiao, L.; Ai, X.; Yang, H.; Cao, Y., Nanophase ZnV_2O_4 as stable and high capacity Li insertion electrode for Li-ion battery, *Current Applied Physics*, **2015**, 15, 435-440
 31. Zheng, L.; Xiao, F.; Wang, J.; Gao, S.; Ding, X.; Wei, M., ZnV_2O_4 -CMK nanocomposites as an anode material for rechargeable lithium-ion batteries, *J. Mater. Chem.*, **2012**, 22, 14284-14288
 32. Sambandam, B.; Soundharranjan, V.; Song, J.; Kim, S.; Jo, J.; Pham, D. T.; Kim, S.; Mathew, V.; Kim, J., $\text{Zn}_3\text{V}_2\text{O}_8$ porous morphology derived through a facile and green approach as an excellent anode for high-energy lithium ion batteries, *Chem. Eng. J.*, **2017**, 328, 454-463
 33. Butt, F. K.; Cao, C.; Wan, Q.; Li, P.; Idrees, F.; Tahir, M.; Khan, W. S.; Ali, Z.; Zapata, M. J. M.; Safdar, M.; Qu, X., Synthesis, evolution and hydrogen storage properties of ZnV_2O_4 glomerulus nano/ microspheres: A prospective material for energy storage, *Int. J. Hydrogen Energy*, **2014**, 39, 7842-7851

34. SACHEM Inc. Dodecyltrimethylammonium Bromide (DOTAB) dry.
<https://sacheminc.com/dodecyltrimethylammonium-bromide-DOTAB-dry/>
35. Huang, Y.; Li, X.; Luo, J.; Wang, K.; Zhang, Q.; Qui, Y.; Sun, S.; Liu, S.; Han, J.; Huang, Y., Enhancing Sodium-ion Storage Behaviors in TiNb_2O_7 by Mechanical Ball Milling, *ACS Appl. Mater. Interfaces*, **2017**, 9, 8696-8703

CHAPTER 5

GENERAL CONCLUSION

One-dimensional (1D) nanomaterials (NMs), e.g. nanowires (NWs), nanorods (NRs), and nanofibers (NFs), are promising materials with wide range of applications. 1D NMs are known to have high surface area, 1D flow of electrons and ions, ability to restrain mechanical degradation, and have geometrical advantages for in-situ electrochemical probing, which makes them a suitable electronic material, vis. energy storage devices. The commonly used method in the production of 1D NMs is by the template-assisted method, however, the removal of the template can damage the produce 1D NMs. Hence both solution and hydrothermal synthesis of single crystal 1D NMs are widely used methods due to lower cost and feasibility for mass production. This thesis aims to study template-free solution synthesis approaches for growing of 1D NMs: the formation mechanism and their potential application as anode materials for rechargeable Lithium-ion battery (LIB). Materials of interest include β -Sn and spinel oxides, vis. ZnV_2O_4 , for their good performance as anode materials for LIB.

This study first focused on new synthesis approach to grow β -Sn NRs. The capping property of the ligand or the difference in the surface energy of the material's crystallographic planes can direct the formation of 1D NMs. The former is the basis for the colloidal synthesis of 1D NMs whereas the latter is an important factor to grow different morphology in materials with anisotropic crystal structure. β -Sn has an anisotropic crystal structure, i.e. tetragonal. However, when β -Sn nanoparticles (NPs) were chemically produced at high temperature, the spherical

shape was formed despite using different capping ligands. This can be attributed to the low melting point of bulk β -Sn, i.e. 232 °C. Hence, this study proposed to grow 1D β -Sn NMs based on lowering the synthesis temperature in a viscous synthesis solution to manipulate the kinetics of the particle nucleation and growth. The results demonstrated that single crystalline β -Sn NRs growing along [001] direction with tunable aspect ratios were successfully formed at below room temperature. When the synthesis temperature was decreased from 26 °C to 10 °C, the morphology of the produced particle varied from spherical to rod-like with 2.5 aspect ratio. A further decrease in the synthesis temperature to 5, 0, -10, and -15 °C increases the aspect ratio to 4.8, 11.1, 15.8, and 22.9, respectively. On the other hand, varying the viscosity of the solution by varying the amount of K90 PVP showed that as the viscosity increases, the aspect ratio of the produced rod-like morphology also increases. Hence, both temperature and viscosity can influence the movement of the particles and thus their kinetic energy. Higher kinetic energy particles/ions can attach easily on any surface planes of the nuclei, while lower kinetic energy particle/ions have a preferred attachment on high surface energy planes. The preferred attachment resulted in rod-like morphology leaving the low surface energy planes, i.e. {200} for β -Sn, on its facets. Besides it was found that PVP can bridge two or more particles together, wherein the higher the molecular weight, MW, of the PVP, the longer the polymeric chain and thus can bridge more particles together to form higher aspect ratio NRs. Therefore, in order to grow high aspect ratio β -Sn NRs, both high MW of ligand that bridges more particles together, and slow particle mobility (lower temperature, more viscous solution), i.e. still enough for lattice realignment, are necessary.

The formed β -Sn NPs with different aspect ratios through the variation of the synthesis temperature was examined under the electrochemical test, i.e. as anode material for LIB. Due to the promising properties of the rod-like morphology, it was observed that β -Sn NRs exhibited

better cycling stability compared to that of the spherical β -Sn NPs. This is due to the strain relaxation effect of the NRs that can buffer large volumetric change. However, a closer examination on the effect of Sn NRs with different aspect ratios revealed that lower aspect ratio NRs have better cycling stability, i.e. almost 100% coulombic efficiency, compared to that of higher aspect ratio NRs. It is found that the higher stability of the low aspect ratio NRs relates to the formed LiF-rich solid electrolyte interface, SEI, layer. For β -Sn, (100) and (001) plane can dictate the produced SEI layer, i.e. mainly LiCO_3 with electrolyte uptake and LiF with other organic molecules respectively. LiF is known to prevent the further degradation of the electrolyte and improve the ionic conductivity from the solution to the electrode, and hence desirable. Based on our calculation, since β -Sn NRs have (001) tip and (100) side facets, lower aspect ratio NRs have 9 times specific surface area of the active (001) surface compared to that of the high aspect ratio NRs, hence should have higher amount of LiF F-containing SEI layer that contributes to the cycle stability. This result agrees well with our XPS result, wherein low aspect ratio NRs have higher LiF F-containing SEI compounds compared to that of the high aspect ratio NRs. This result also agrees well with impedance analysis, wherein, the low aspect ratio NRs have lower SEI resistance and an order of magnitude higher Li^+ diffusion compared to that of the high aspect ratio NRs. These results elucidate the reason for the better performance of low aspect ratio NRs compared to that of the high aspect ratio NRs in addition to the morphology effect in comparison to that of the spherical NPs.

Unlike that of Sn, i.e. alloying type anode material, spinel structured materials such as ZnV_2O_4 , is a conversion type anode material. Spinel structure materials are known to be crystallographically porous, i.e. with 56 empty tetrahedral sites and 16 empty octahedral sites, and are expected to easily accommodate small guest ions such as Li^+ within its interstitial space. However, the short distances and coulombic interactions between the guest ions and the ions

on tetrahedral and octahedral sites prevent the simultaneous occupation, and hence Li^+ can be introduced chemically and electrochemically instead. Zn can form an alloy with Li ($\text{LiZn} \rightleftharpoons \text{LiZn}_2 \rightleftharpoons \text{Li}_2\text{Zn}_5$), while V undergoes redox reaction upon lithiation and delithiation. Conversion anode materials are known to have lower gravimetric capacities compared to that of the alloying materials but with better volumetric capacities and less volumetric change. However, conversion type anode material still experienced large volumetric change that is detrimental as anode material for lithium-ion battery, hence 1D nanostructure is preferable to buffer large volumetric change as that of Sn. In this study, 1D ZnV_2O_4 , a spinel compound, was produced via two-step fabrication, i.e. hydrothermal method followed by calcination at $600\text{ }^\circ\text{C}$ under $3\%\text{H}_2/\text{N}_2$. Zinc nitrate and ammonium vanadate with 1:2 mole ratio serve as the reactants in the formation of fibrous like ZnV_2O_6 using the hydrothermal synthesis. These fibrous ZnV_2O_6 were reduced to form porous ZnV_2O_4 NWs for the first time. Despite its porous structure, the formed ZnV_2O_4 NWs exhibited single crystal property with $\{220\}$ facets and $\langle 111 \rangle$ along the wire. By varying the calcination condition used in the synthesis, it is found that spherical ZnV_2O_4 NPs were synthesized.

The electrochemical property of these porous ZnV_2O_4 NWs was examined. It was found that when porous ZnV_2O_4 NWs were cycled using 1 A g^{-1} current density, there is a decrease in the initial capacity which is attributed to the formation of the SEI layer. However, on the succeeding cycles after the 2nd cycle, the specific capacity increases until the 35th cycles. The increase in the capacity can be attributed to the occurrence of the phase transformation that gradually occurs upon successive cycles. This phase transformation is evident in the XRD pattern of the electrode after 100 cycles, wherein aside from the ZnV_2O_4 peaks, the peaks from both ZnO and V_2O_3 were evident indicating that phase transformation occurred in the sample. On the other hand, based on the CV curves at various scan rates, it was deduced that the

electrochemical behavior of the porous ZnV_2O_4 NWs were pseudo-capacitive.

ZnV_2O_4 with both spherical and NWs morphologies showed good cycle stability when being used as anode materials for LIB, though it was observed that the NW structure resulted to a higher capacity at high current density, i.e. 5 A/g for over 1000 cycles. The better specific capacity and performance at high current density can be attributed to the porous structure of the wire which is propitious for high current density application due to the increase in the surface area that increases the Li^+ flux.

This research deals with the synthesis and application of 1D NMs as anode material for LIB, wherein: (a) new approach in the synthesis and formation of Sn NRs were shown and proposed, (b) first study on the combined effect of both the 1D morphology and the formed SEI layer, i.e. the LiF-rich F-containing SEI layer induced by the (001) tip of the rod, of Sn NRs as anode material for LIB was presented, and (c) first synthesis and application of 1D ZnV_2O_4 as anode material for LIB with good stability at high current density were demonstrated.

Appendix I. Supporting Information for Chapter 2

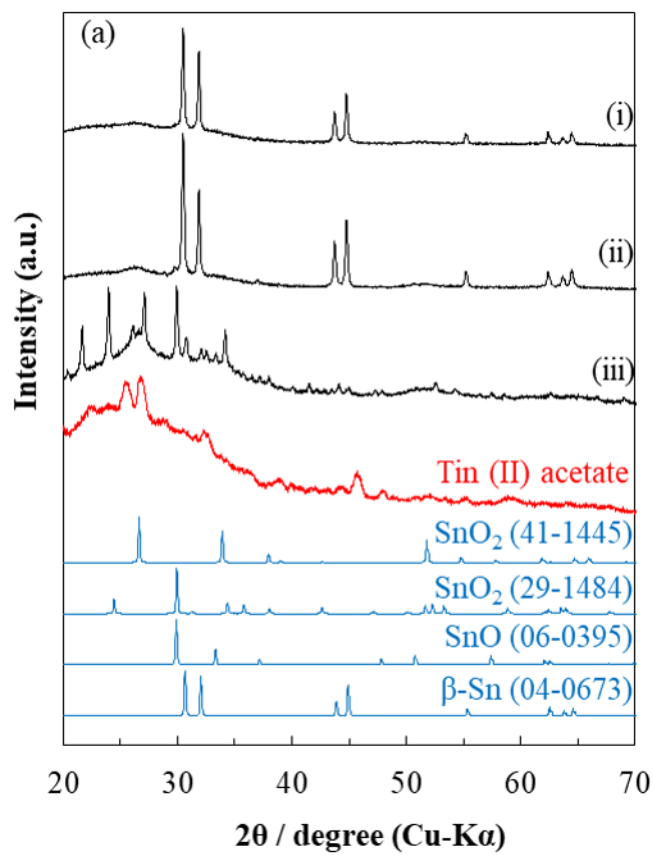


Figure S2.1 XRD patterns of the nanoparticles obtained using 3.0728 g poly(vinylpyrrolidone) (PVP) at -15 °C for: (i) 44 hours, (ii) 4 hours, and (iii) 15 minutes reaction time.

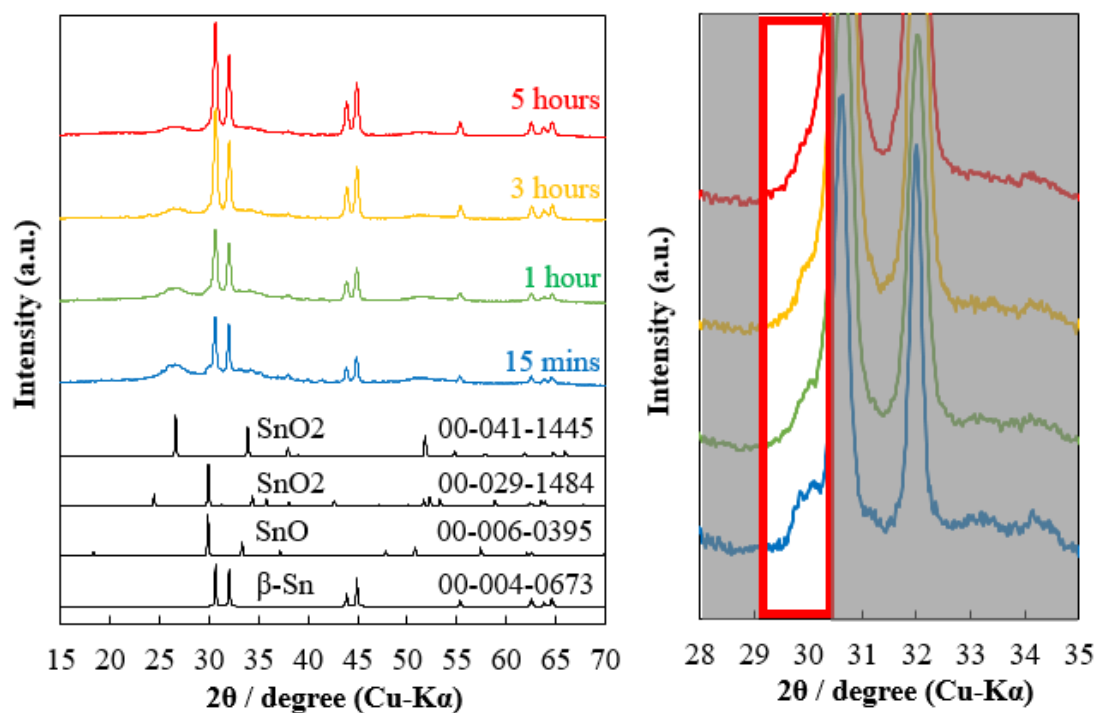


Figure S2.2. XRD patterns of the nanoparticles obtained using 3.0728 g poly(vinylpyrrolidone) (PVP) at -10 °C for 15 min, 1 hour, 3 hours, and 5 hours reaction time.

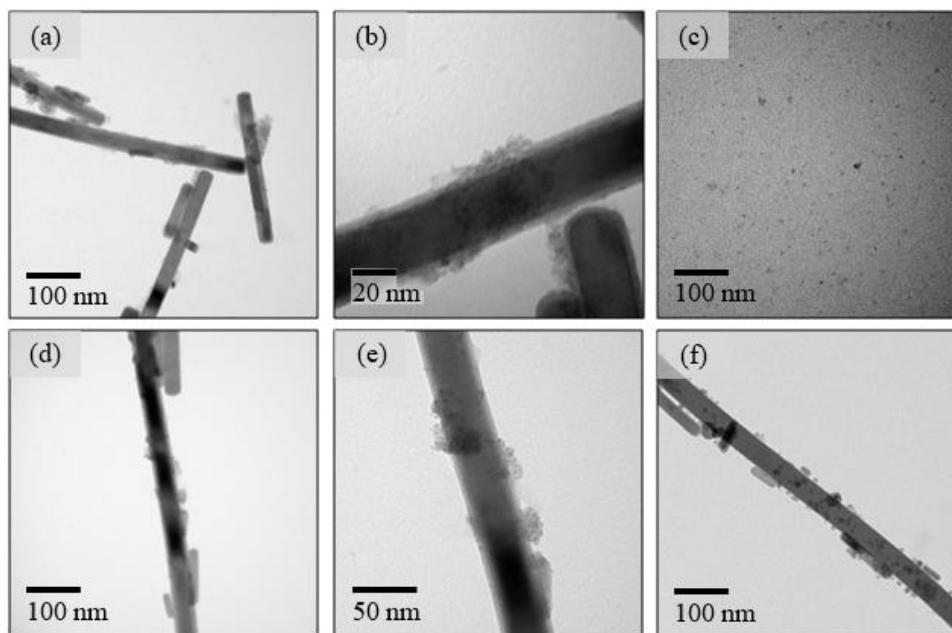


Figure S2.3. TEM images of nanoparticles obtained using 3.0728 g poly(vinylpyrrolidone) (PVP) K90 at -10 °C after (a, b, c) 1 hour, (d, e) 3 hours and (f) 5 hours reaction time.

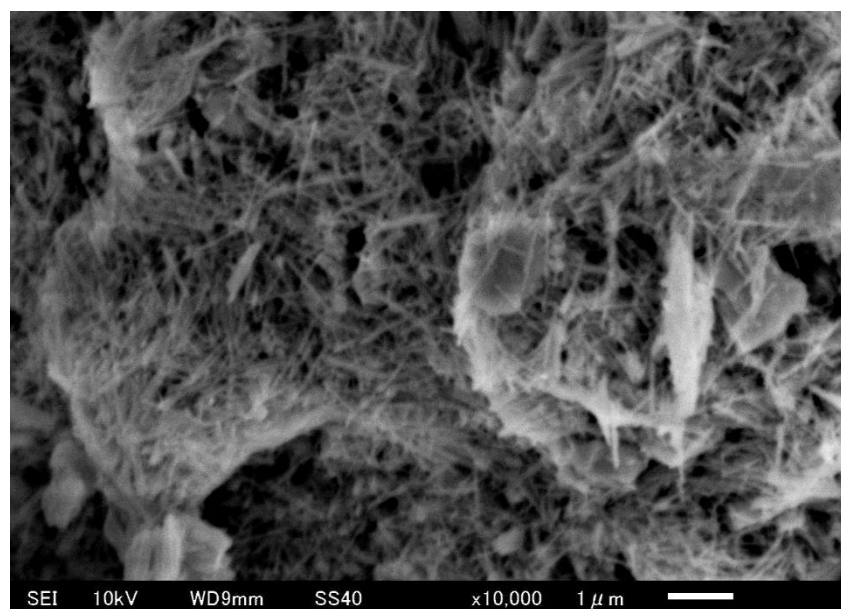
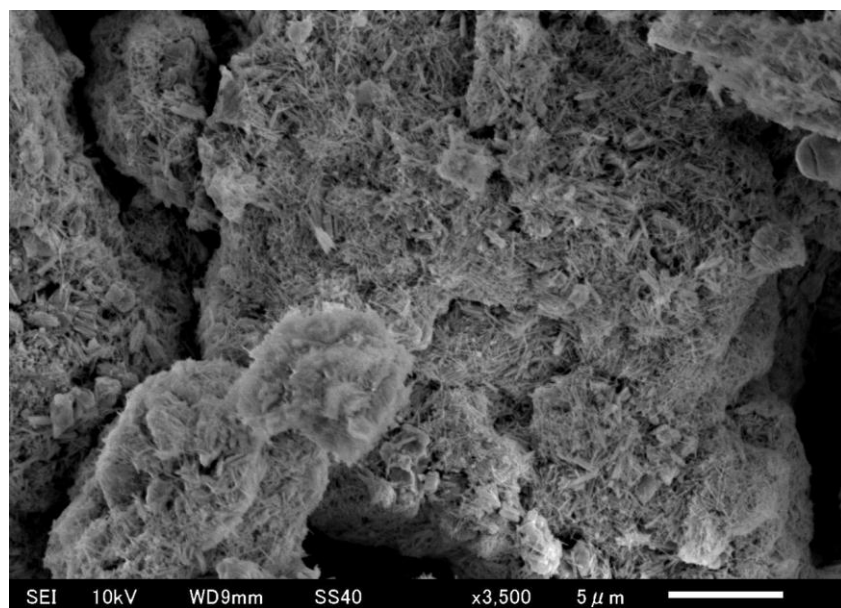


Figure S2.4. SEM image of particles produced using 3.0728 g poly(vinylpyrrolidone) (PVP) at 0 °C.

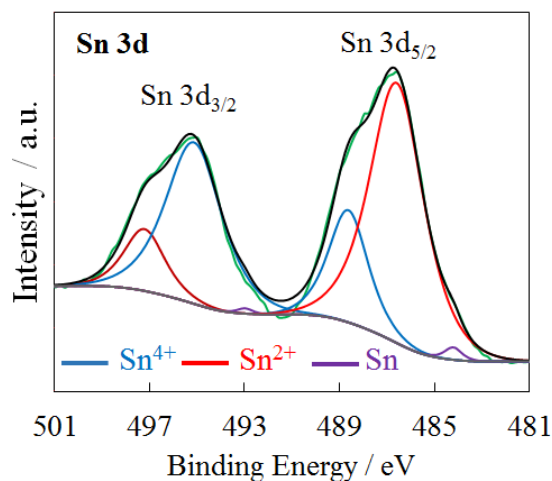


Figure S2.5. XPS spectra of Sn NRs produced using 3.0728 g poly(vinylpyrrolidone) (PVP) at 0 °C after 5 hours reaction time: wide scan (a) and narrow scans of Sn 3d (b, c), O 1s (d, e), and C 1s (f, g); where b, d, and f correspond to the spectra before Ar etching and c, e, and g correspond to after Ar etching.

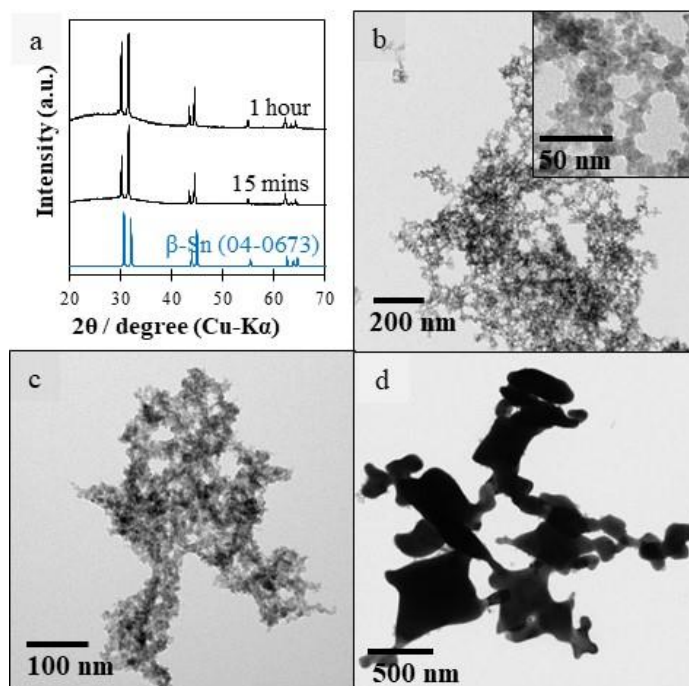


Figure S2.6. XRD pattern (a) of nanoparticles obtained after 15 min and 1 hour reaction time. TEM image of β-Sn particles synthesized at -25 °C without poly(vinylpyrrolidone) (PVP): (b) after 15 min reaction time; (c, d) after 1 hour reaction time.

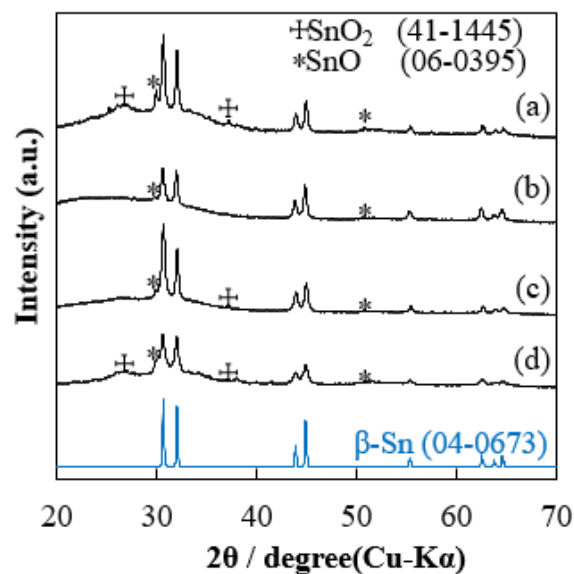


Figure S2.7. XRD pattern of β -Sn particles produced at 0 °C using different amounts of poly(vinylpyrrolidone) (PVP) K90: (a) 6.1456 g, (b) 3.0728 g, (c) 1.5364 g, (d) 0.3073 g.

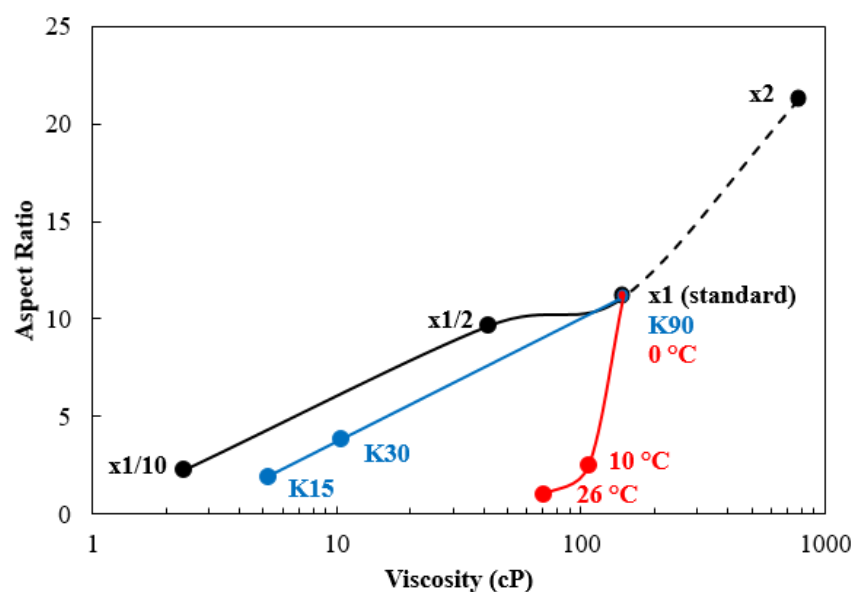


Figure S2.8. Plot of viscosity vs. aspect ratio of the produce NPs/NRs. The blue, red, and black markers and lines corresponds to the change in the MW of poly(vinylpyrrolidone), PVP, (at 0 °C and 3.0728 g of PVP), synthesis temperature (using 3.0728 g of PVP K90), and the amount of PVP (at 0 °C and using PVP K90) respectively.

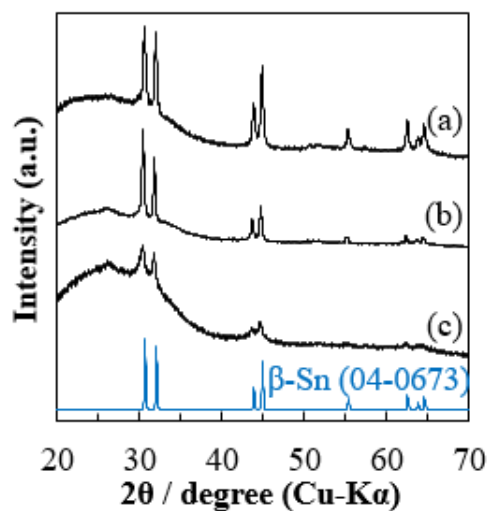


Figure S2.9. XRD pattern of β -Sn particles produce using 3.0728 g of different MW of poly(vinylpyrrolidone) (PVP): (a) 630,000 MW, (b) 40,000 MW, and (c) 10,000 MW, synthesized at 0 °C.

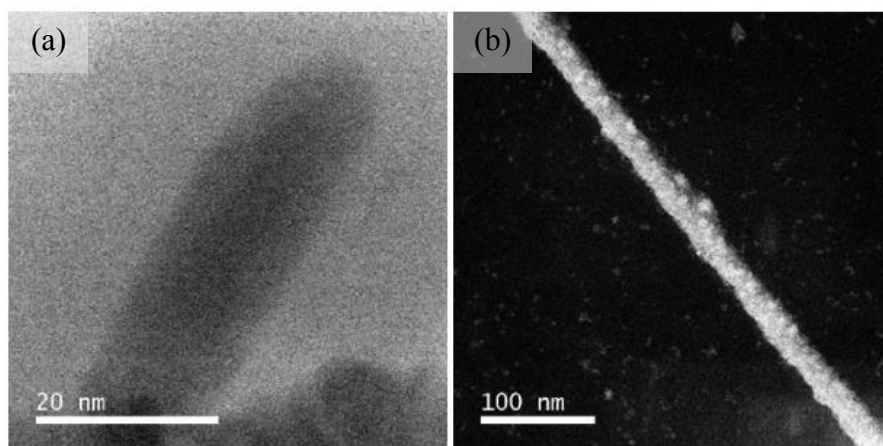


Figure S2.10. TEM image of β -Sn particles synthesized at -15 °C using 3.0728 g of poly(vinylpyrrolidone) (PVP) K90: (a) A big grain sized particle, and (b) a rod like particle made of many small crystals.

Appendix II. Supporting Information for Chapter 3.

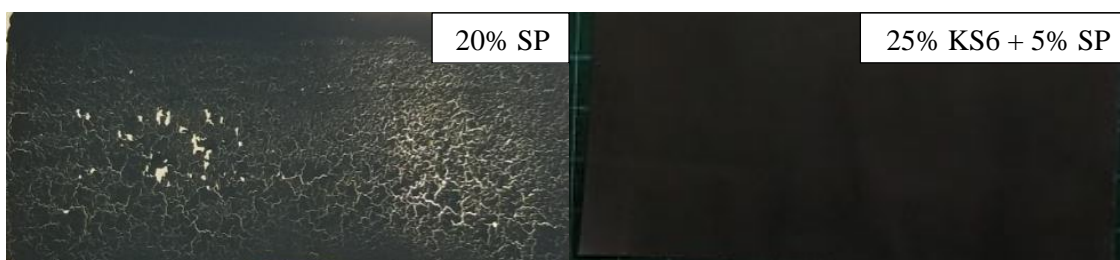


Figure S3.1. Images of the coated Cu foil after drying at 80°C with a slurry containing, (left) 20 w/w% Super-P, and (right) 25 w/w% KS6 + 5 w/w% Super P.

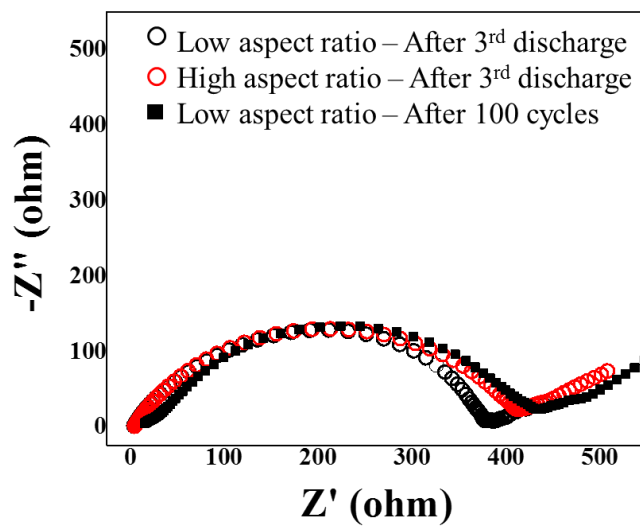


Figure S3.2. Nyquist plot after the 3rd discharge of the high and low aspect ratio β -Sn NRs after the 3rd discharge and after 100 cycles of the low aspect ratio β -Sn NRs.

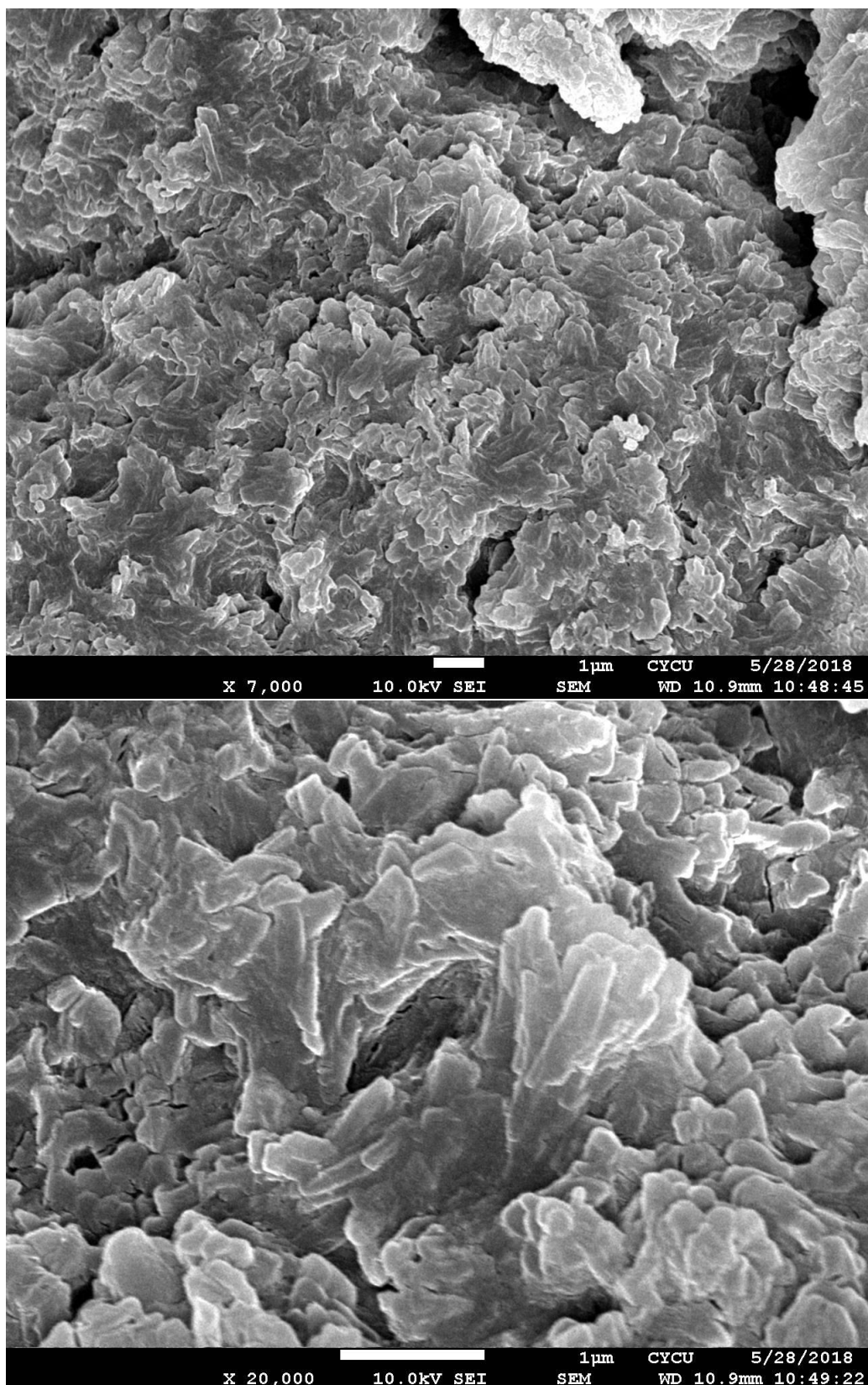


Figure S3.3. SEM image of the low aspect ratio NRs after 100 cycles.

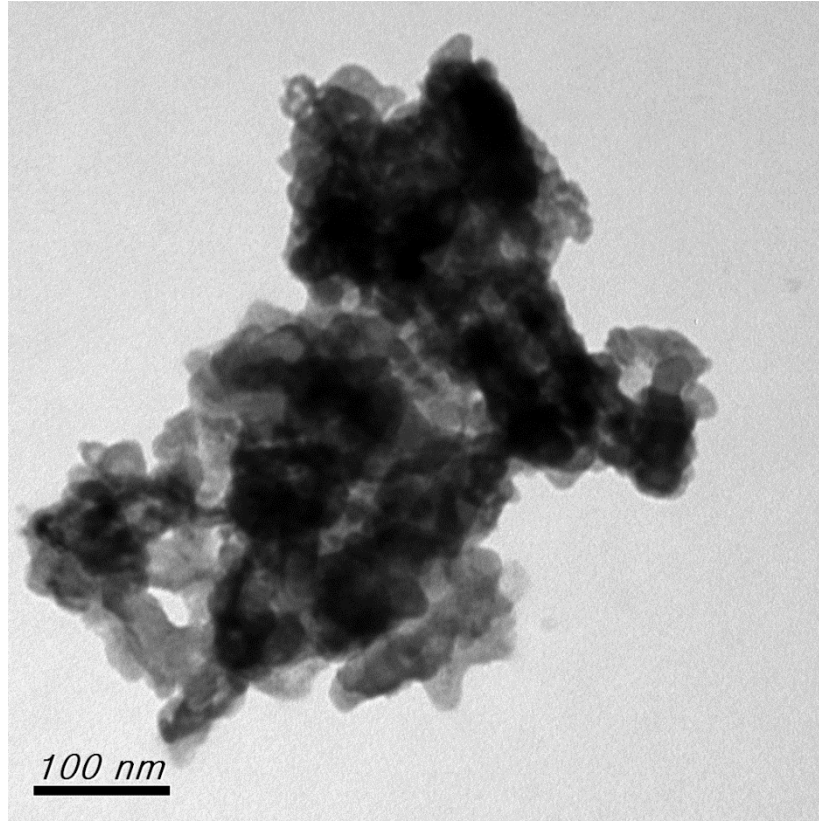


Figure S3.4. TEM image of the low aspect ratio NRs after 100 cycles.

Calculation of the total area ratio of the (001) tip surface between low aspect ratio Sn NRs, $S_{T(001) low}$, and high aspect ratio Sn NRs, $S_{T(001) high}$.

The mass of the active material used was the same for high and low aspect ratio NRs, and hence the volume of the active material should be the same.

$$V_{low} = V_{high}$$

Total volume, V , of both low and high aspect ratio Sn NRs can be calculated using the formula:

$$V = \frac{m}{\rho} = n * S_{(001)} * l = S_{T(001)} * l$$

where n is the number nanorods, $S_{(001)}$ is the surface area of the (001) tip, l is the length of the rod, and $S_{T(001)}$ is the total surface area of the (001) tip per given volume.

Thus, the total area ratio of the (001) tip surface between low aspect ratio Sn NRs, $S_{T(001) low}$, and high aspect ratio Sn NRs, $S_{T(001) high}$, can be roughly estimated as:

$$\begin{aligned} S_{T(001) low} * l_{low} &= S_{T(001) high} * l_{high} \\ \frac{S_{T(001) low}}{S_{T(001) high}} &= \frac{l_{high}}{l_{low}} = \frac{202.1 \text{ nm}}{22 \text{ nm}} \\ \boxed{\frac{S_{T(001) low}}{S_{T(001) high}} &= \sim 9} \end{aligned}$$

Appendix III. Supporting Information for Chapter 4.

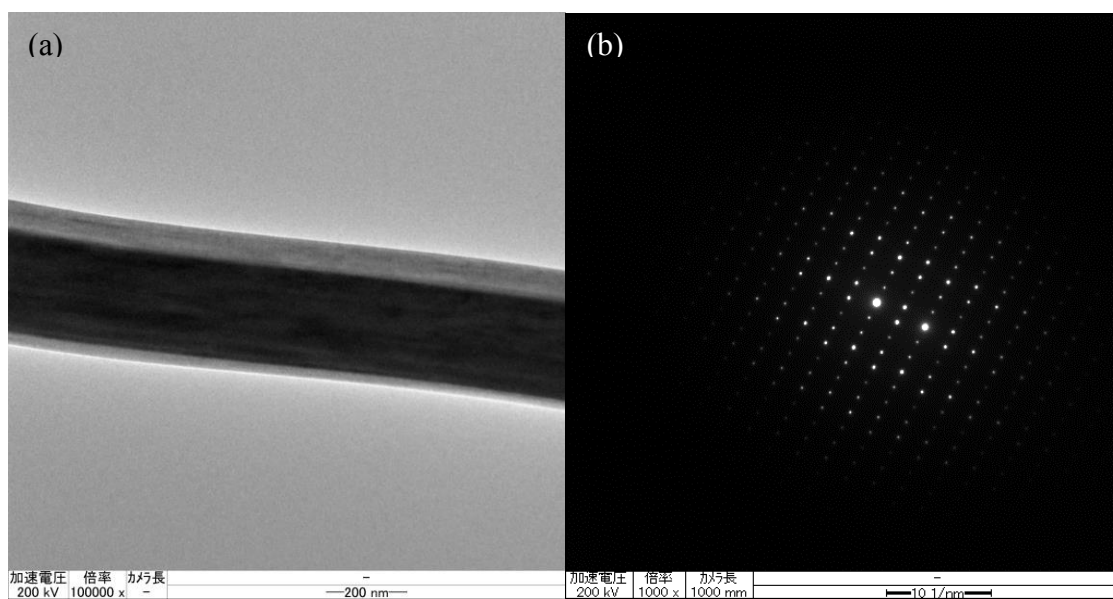


Figure S4.1. (a) TEM image and (b) SAED pattern of a ZnV_2O_6 NW produced after hydrothermal synthesis.

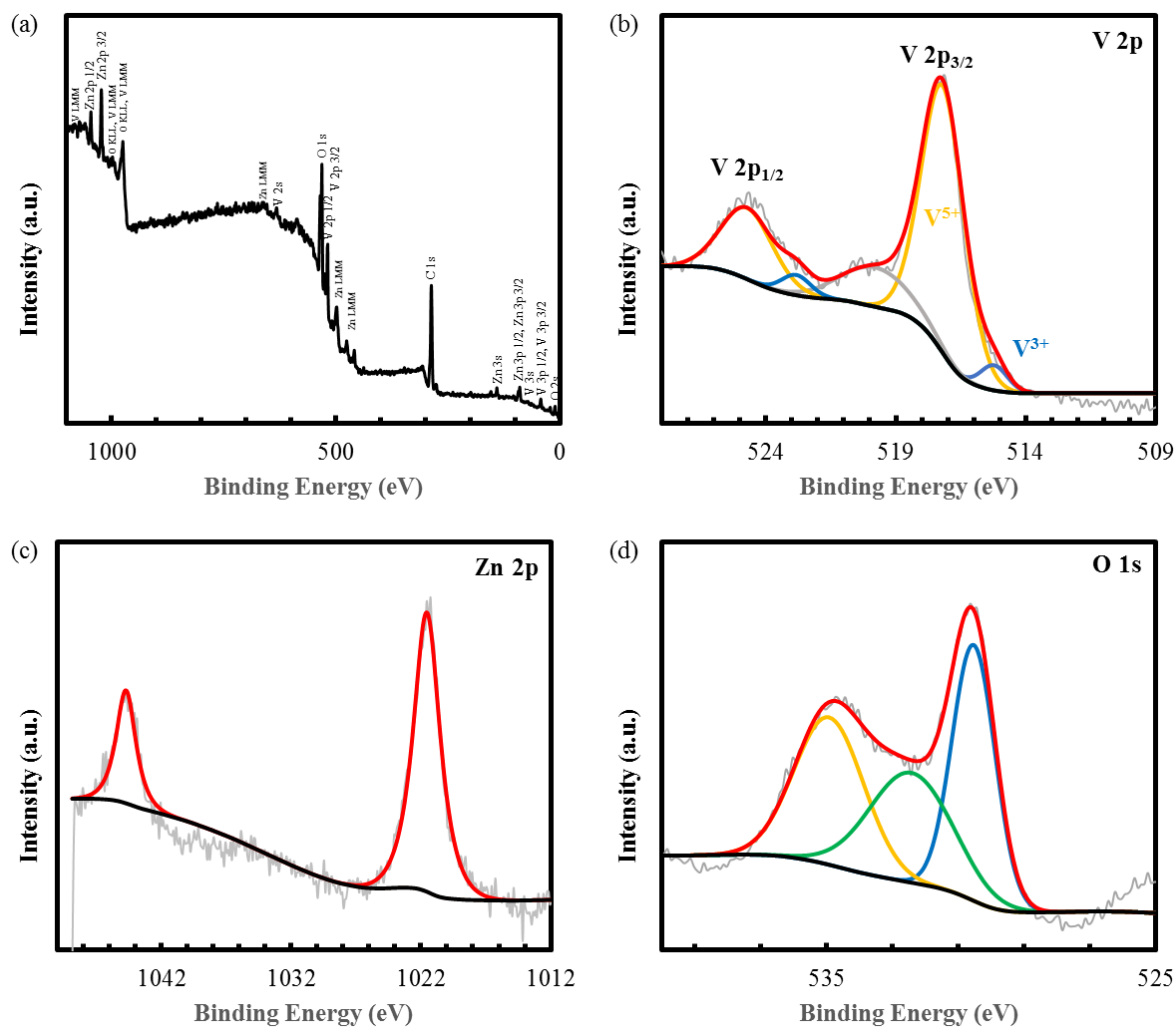


Figure S4.2. XPS spectra of ZnV₂O₆ NWs: (a) wide scan, and narrow scans of (b) V 2p, (c) Zn 2p, and (d) O 1s.

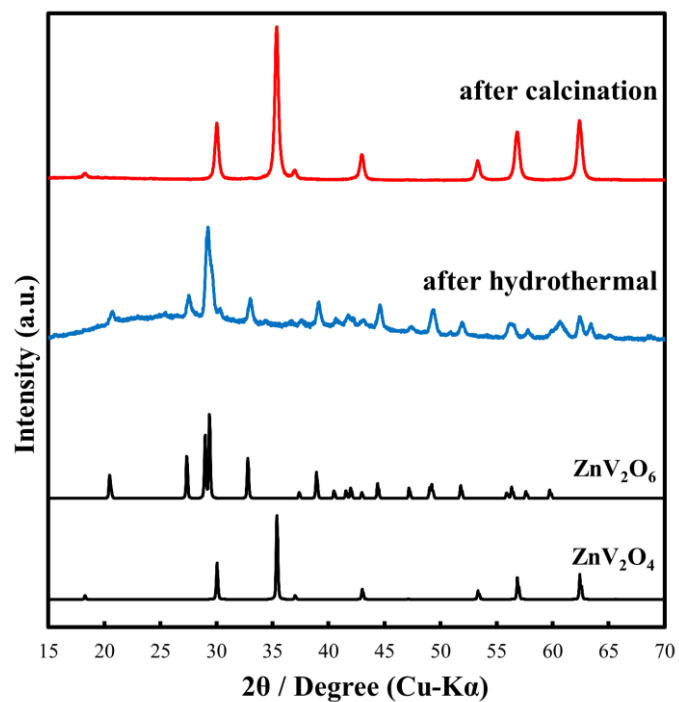


Figure S4.3. XRD patterns of the samples synthesized in the absence of DTAB: after hydrothermal (blue) and after calcination (red) with the corresponding XRD patterns of ZnV_2O_6 and ZnV_2O_4 with JCPDS # 00-023-0757 and 01-075-0318 respectively.

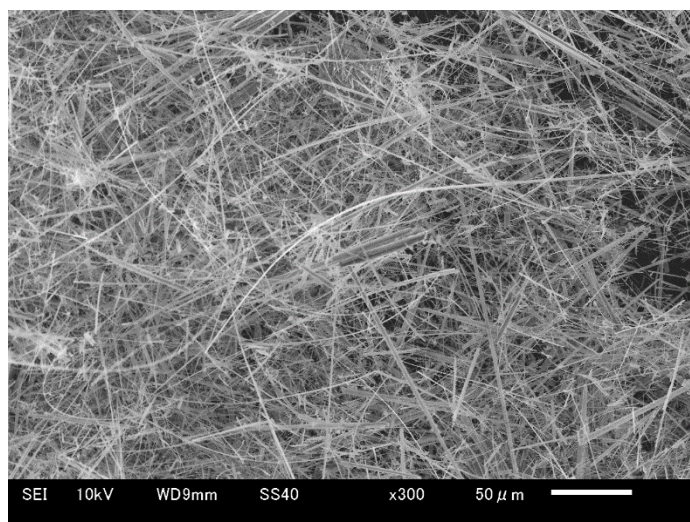


Figure S4.4. SEM images of the ZnV_2O_4 sample prepared in the absence of DTAB.

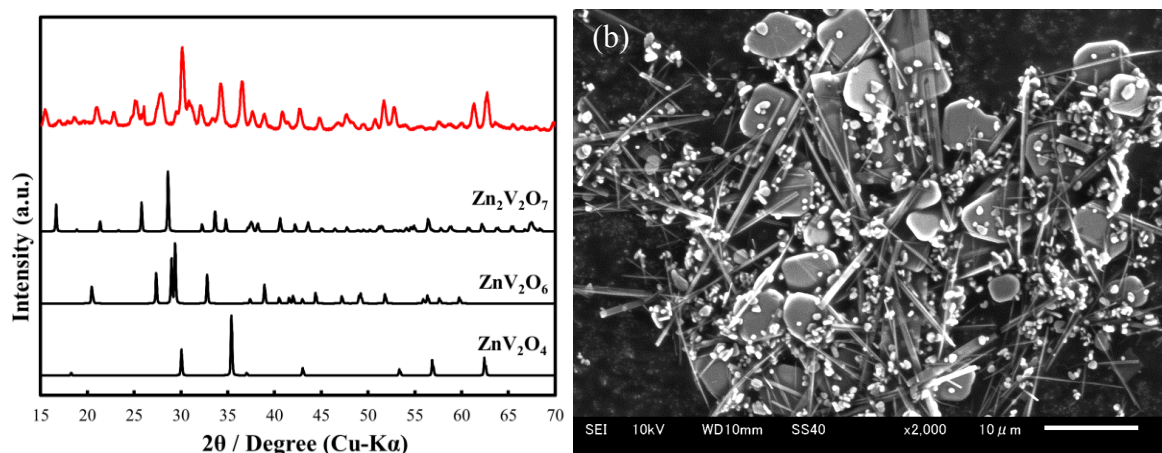


Figure S4.5. (a) XRD pattern and (b) SEM images of the microsheets produced after 6 h hydrothermal reaction. The corresponding XRD patterns of $\text{Zn}_2\text{V}_2\text{O}_7$ (JCPDS #00-038-0251), ZnV_2O_6 (JCPDS # 00-023-0757) and ZnV_2O_4 (JCPDS # 01-075-0318).

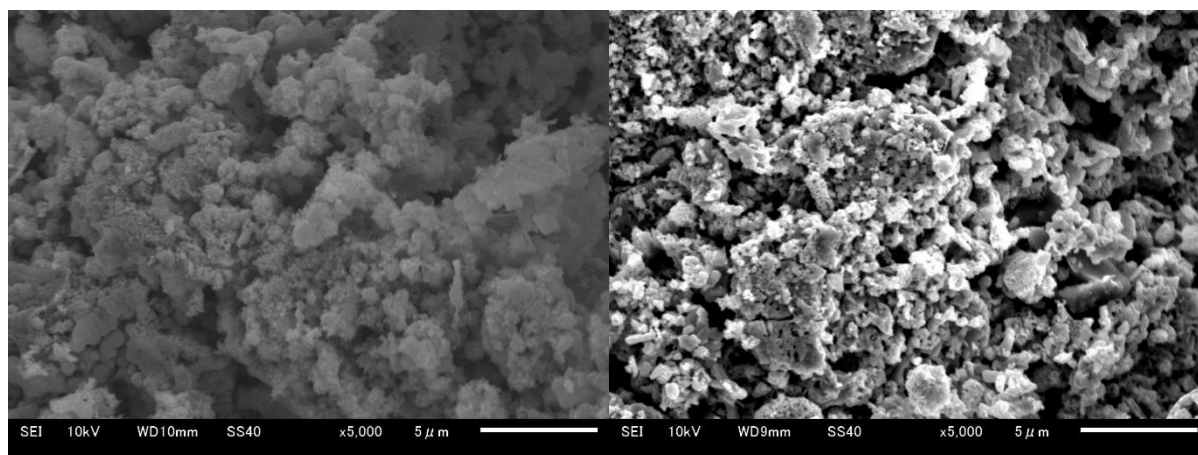


Figure S4.6. SEM images of the (a) spherical ZnV_2O_4 and (b) coral-like ZnV_2O_4 .

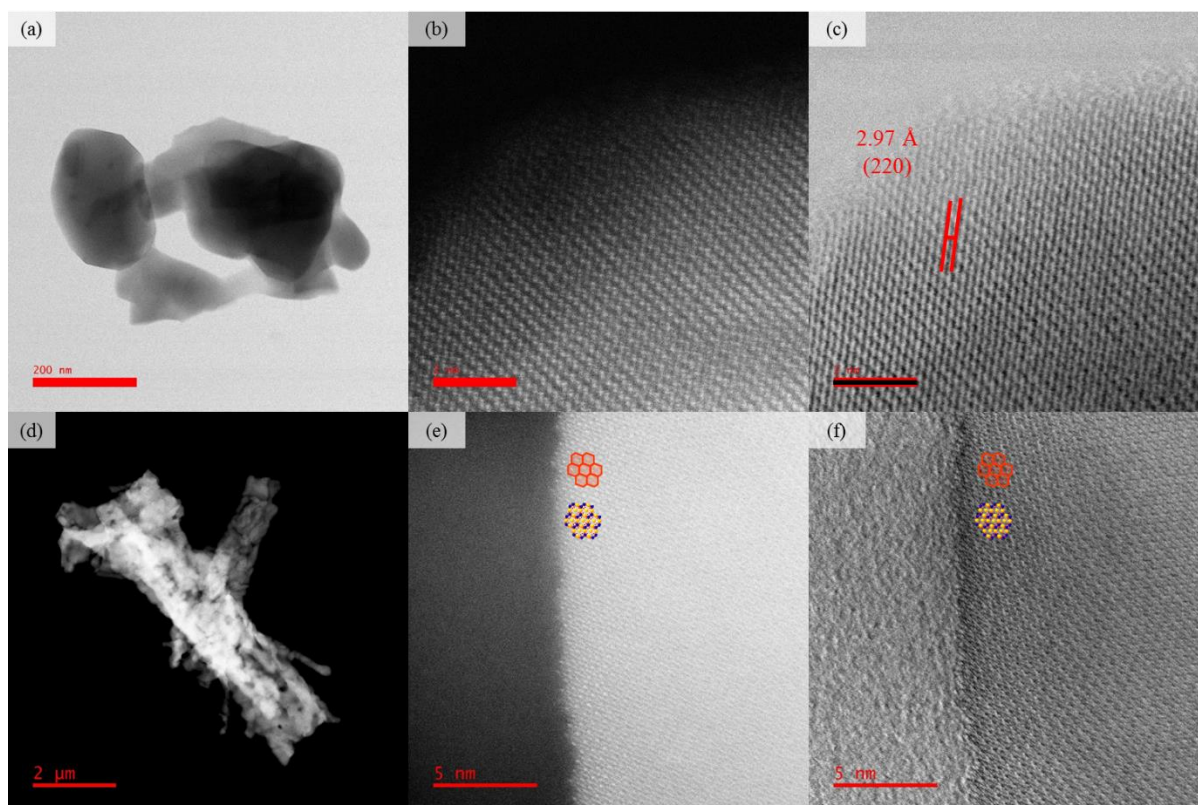


Figure S4.7. (a,d) STEM images, (b,e) HAADF-STEM and (c,f) ABF-STEM images of particles with (a-c) spherical and (d-f) coral-like morphology. The superimposed images in (e,f) illustrate both the red hexagons indicated in (Figure S6a) and the two-dimensional atomic arrangement of Zn, V, and O.

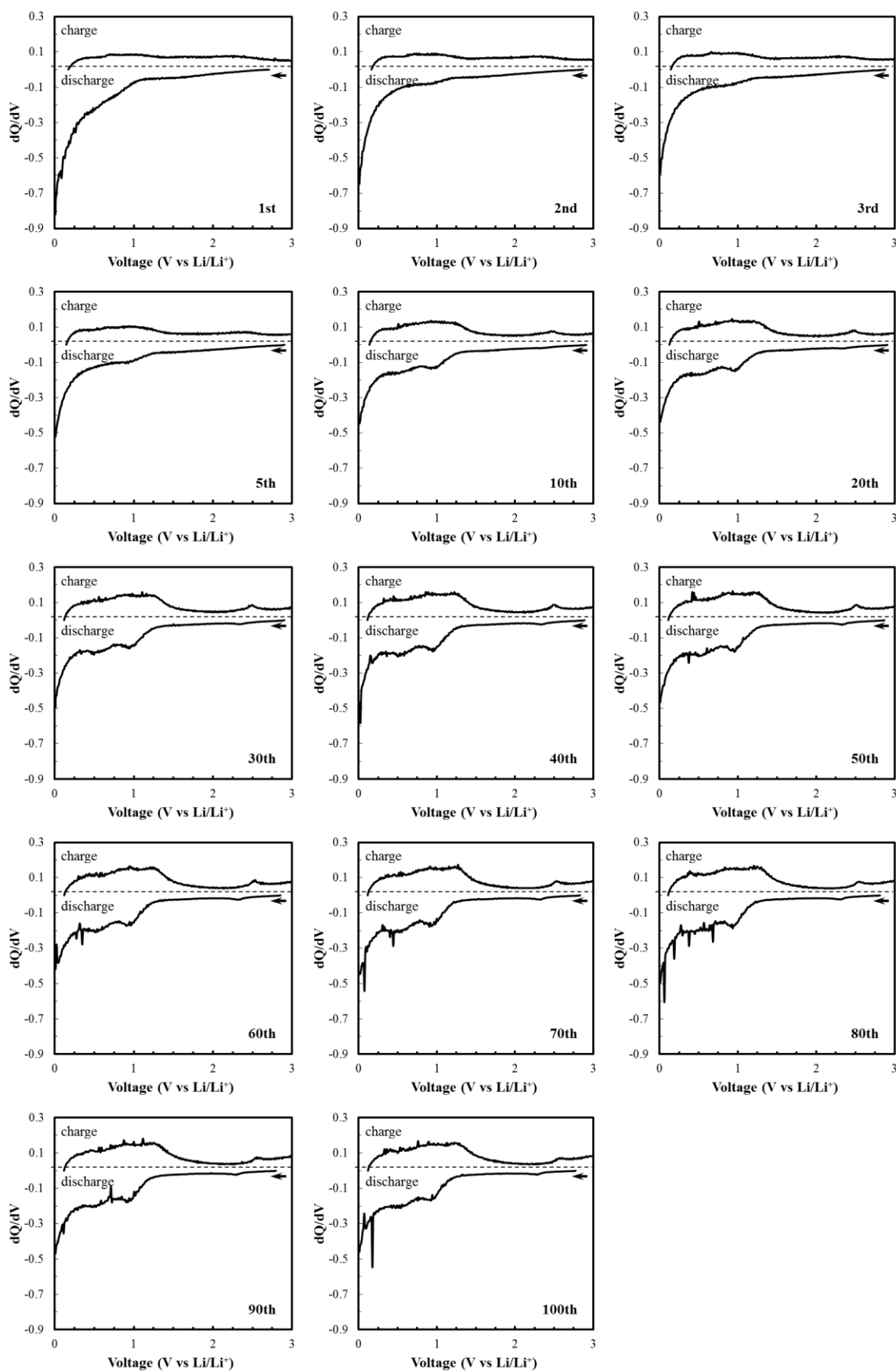


Figure S4.8. Plots of dQ/dV at different cycles of the porous ZnV_2O_4 cycled at 1 A g^{-1} .

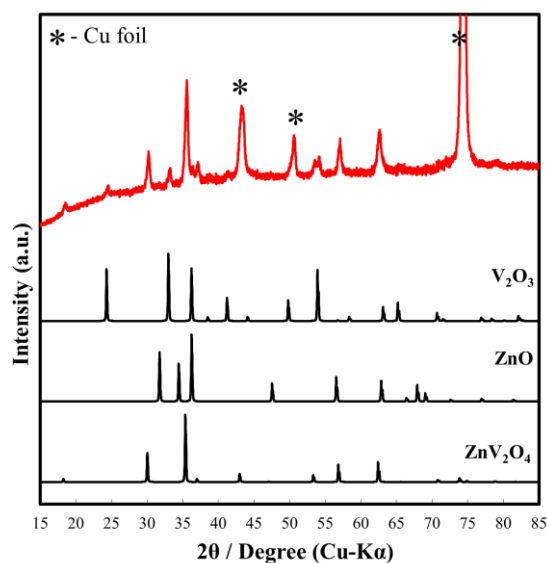


Figure S4.9. XRD patterns of the porous ZnV_2O_4 NWs electrode and the corresponding XRD patterns of ZnV_2O_4 (JCPDS # 01-075-0318), ZnO (JCPDS # 00-005-0664), and V_2O_3 (JCPDS # 00-034-0187).

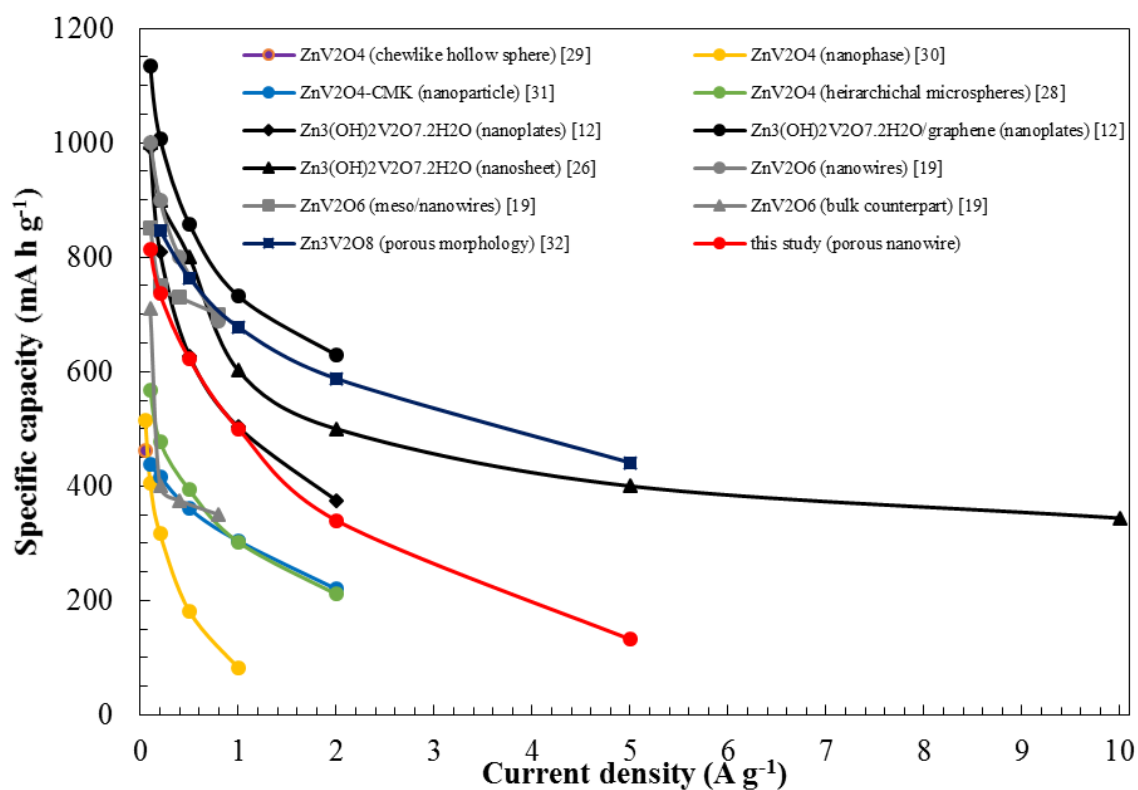


Figure S4.10. Specific capacities of other reported zinc vanadium oxide particles as anode material for LIB in comparison with this study.